



# THE ISO HANDBOOK

Volume III:

**LWS –**

## **The Long Wavelength Spectrometer**

Cécile Gry<sup>1</sup>, Bruce Swinyard<sup>2</sup>, Andrew Harwood<sup>2</sup>, Norman Trams<sup>3</sup>, Sarah Leeks<sup>4</sup>, Tanya Lim<sup>2</sup>, Sunil Sidher<sup>2</sup>, Christopher Lloyd<sup>2</sup>, Stefano Pezzuto<sup>5</sup>, Sergio Molinari<sup>5</sup>, Rosario Lorente<sup>1</sup>, Emmanuel Caux<sup>6</sup>, Edward Polehampton<sup>7</sup>, Josephine Chan<sup>2</sup>, Gerard Hutchinson<sup>2</sup>, Thomas Müller<sup>8</sup>, Martin Burgdorf<sup>9</sup>, and Timothy Grundy<sup>2</sup>

**SAI-99-077/Dc, Version 2.1**

June, 2003

<sup>1</sup> ISO Data Centre, Science Operations and Data Systems Division, Research and Scientific Support Department of ESA, Villafranca del Castillo, P.O. Box 50727, E-28080 Madrid, Spain

<sup>2</sup> Rutherford Appleton Laboratory, Chilton, Didcot OX11 0QX Oxfordshire, UK

<sup>3</sup> Science Operations and Data Systems Division of ESA/ESTEC, Keplerlaan 1, Postbus 299, 2200 AG Noordwijk, The Netherlands

<sup>4</sup> Herschel Science Centre, Research and Scientific Support Department of ESA, ESTEC, Keplerlaan 1, Postbus 299, 2200 AG Noordwijk, The Netherlands

<sup>5</sup> IFSI-CNR, Via Fosso del Cavaliere 100, 00133 Roma, Italy

<sup>6</sup> CESR, BP4346, 31028 Toulouse Cedex 4, France

<sup>7</sup> Max-Planck-Institut für Radioastronomie, Auf dem Hügel 69, 53121 Bonn, Germany

<sup>8</sup> Max-Planck-Institut für Extraterrestrische Physik, Giessenbachstrasse, 85748 Garching, Germany

<sup>9</sup> SIRTf Science Center, California Institute of Technology, 220-6, Pasadena, CA91125, USA

## Document Information

Document:	The ISO Handbook
Volume:	III
Title:	LWS – The Long-Wavelength Spectrometer
Reference Number:	SAI/99-077/Dc
Issue:	Version 2.1
Issue Date:	June 2003
Authors:	C. Gry, B. Swinyard, A. Harwood et al.
Editors:	T. Müller, J. Blommaert & P. García-Lario
Web-Editor:	J. Matagne

## Document History

The ISO Handbook, Volume III: LWS – The Long Wavelength Spectrometer, is based on the following documents:

- The ISOLWS Data Users Manual (SAI/95-219/Dc, Issue 5.0 June 1, 1998), N. Trams, using inputs from: M. Burgdorf, C. Gry, T. Lim, S. Pezzuto, A. Harwood, S.J. Leeks, P.E. Clegg, B. Swinyard, K. King, S. Lord, S. Unger.
- The LWS observer’s manual (Issue 1.0, March 1994, LWS/PEC/2038.01), prepared by the LWS consortium and written by: P.E. Clegg, A. Heske, N.R. Trams.
- The Addendum to the LWS OBSERVER’S MANUAL (SAI/96-166/Dc, Version 1.0, 5 August 1996), N.R. Trams, P.E. Clegg and B.M. Swinyard.

and many articles and reports which are referenced in the corresponding sections and listed in the Bibliography.

## Document Change Record

Date	Revision	Comments
31/12/99	Draft 1.0	Initial Draft for comments
11/02/00	Version 1.0	First Version of the ISO Handbook, Volume IV: LWS – The Long-Wavelength Spectrometer related to OLP 8.6 data products
November 2000	Version 1.1	update
June 2001	Version 1.2	update, related to OLP 10.0 data products
August 2002	Version 2.0	update, now Volume III
June 2003	Version 2.1	update, printed version

## Acknowledgements

The following pages list the many people and teams who have contributed to the development, the operations, the science planning, the data-analysis and the calibration of the LWS.

The information contained in this handbook results from their work.

### **LWS Instrument Principal Investigator:**

Peter Clegg (QMW London)

### **The LWS was conceived and built in the following institutes:**

Rutherford Appleton Laboratory (**RAL**), Didcot, UK

Queen Mary and Westfield College (**QMW**), London, UK

University College London (**UCL**), London, UK

Laboratoire d'Astronomie Spatiale (**LAS**), Marseille, F

Centre d'Etude Spatiale des Rayonnements (**CESR**), Toulouse, F

Istituto di Fisica dello Spazio Interplanetario (**IFSI**), Roma, I

Naval Research Laboratory (**NRL**), USA.

## LWS Instrument Consortium

Peter Ade	QMW London
Jean-Paul Baluteau	Obs. Marseille
Mike Barlow	UCL London
Jean-Claude Berges	LAS Marseille
Emmanuel Caux	CESR Toulouse
Cecilia Ceccarelli	IFSI Frascati
Ricardo Cerulli	IFSI Frascati
Sarah Church	UC Berkley
Peter Clegg	QMW London
Francis Cotin	CESR Toulouse
Pierre Cox	Obs. Marseille
Paul Cruvellier	LAS Marseille
Gary Davis	U. Saskatchewan
Roger Emery	RAL Didcot
Jackie Fischer	NRL Washington
Ian Furniss	UCL London
Bill Glencross	UCL London
Matt Greenhouse	NASM Washington
Matt Griffin	QMW London
Cécile Gry	LAS Marseille
Martine Joubert	CNES Paris
Ken King	RAL Didcot
Rene Liseau	Obs. Stockholm
Dario Lorenzetti	IFSI Frascati
David Naylor	U. Lethbridge
Brunella Nisini	IFSI Frascati
Alain Omont	Obs. Grenoble
Renato Orfei	IFSI Frascati
Daniel Péquinot	Obs. Paris
Dominique Pouliquen	LAS Marseille
N'Guyen Quang Rieu	Obs. Paris
David Robinson	QMW London
Michel Saisse	LAS Marseille
Paolo Saraceno	IFSI Frascati
Guy Serra	CESR Toulouse
Howard Smith	NASM Washington
Luigi Spinoglio	IFSI Frascati
Bruce Swinyard	RAL Didcot
Bill Towlson	UCL London
Glenn White	QMW London

## The LWS Standing Committee for Science

<b>Name</b>	<b>Representing</b>
Peter Clegg	(PI, Chairman)
Roger Emery	(UK)
Martine Joubert	(France)
Paolo Saraceno	(Italy)
Howard Smith	(USA)

## Specialist Astronomy Groups

<b>Group</b>	<b>Leader</b>
Solar System (SS)	David Naylor/Gary Davis
The ISM (ISM)	Jean-Paul Baluteau
Pre-Main-Sequence Evolution (Pre-MS)	Paolo Saraceno
Post-Main-Sequence Evolution (Post-MS)	Mike Barlow
Extragalactic Studies (Xgal)	Howard Smith

## LWS Consultants

<b>SAG</b>	<b>Consultant</b>	<b>Affiliation</b>	<b>Programme</b>
SS	Simon Calcutt	U. Oxford	
	Daniel Gautier	Obs. Paris	
	Glenn Orton	JPL Pasadena	
ISM	Per Annestad	U. Arizona	IB. Study of ionised regions
	Joseph Cassinelli	U. Wisconsin	IV. Abundance gradients
	José Cernicharo	IEM-CSIC	IA Neutral interstellar gas
	Ed Churchwell	U. Wisconsin	IV. Abundance gradients
	Alain Léger	IAS Orsay	IIA. Interstellar cirrus
	Steve Miller	UCL London	IA Neutral interstellar gas
	Jonathan Tennyson	UCL London	IA Neutral interstellar gas
Pre-MS	Helen Walker	RAL Didcot	IA. Interstellar cirrus
	Phillipe André	Saclay	
	Martin Cohen	UC Berkeley	
Post-MS	Francesco Palla	Obs. Arcetri	
	Martin Cohen	UC Berkeley	
XGal	Jim Cohen	NRAL Jodrell Bank	
	Chris Skinner	UCL London	
	Helen Walker	RAL Didcot	
	Matt Malkan	UC Los Angeles	
	Jonathan McDowell	SAO Boston	
Calibration	Chris Skinner	UCL London	
	Gordon Stacey	U. Cornell	
	Steven Lord	IPAC/Caltech	
	Sean Colgan	NASA/Ames	
	Michael Haas	NASA/Ames	

## Development Phase

Peter Ade	QMW	Detector development, Guaranteed time programme
Phillipe André	Saclay	Scientific consultant
Per Annestad	U. Arizona	Scientific consultant
Jean-Paul Baluteau	LAS	French Project Scientist, Guaranteed time programme
Mike Barlow	UCL	Guaranteed time programme
Jean-Claude Berges	LAS	Design of optics and mechanical assembly
Mark Buckley	RAL	Diagnostics software development
Martin Burgdorf	ESA	Preparation of PV phase
John Cathrew	RAL	Product assurance
Simon Calcutt	U. Oxford	Scientific consultant
Joseph Cassinelli	U. Wisconsin	Scientific consultant
Emmanuel Caux	CESR	Warm electronics development, Guaranteed time programme
Cecilia Ceccarelli	IFSI	On-Board software development, Guaranteed time programme
José Cernicharo	IEM-CSIC	Scientific consultant
Ricardo Cerulli	IFSI	Digital processing unit electronics engineering
Jean-Paul Chabaud	CESR	Warm electronics development
Sarah Church	QMW	Detector characterisation
Ed Churchwell	U. Wisconsin	Scientific consultant
Peter Clegg	QMW	Principal Investigator LWS, Guaranteed time programme
Jim Cohen	NRAL Jodrell Bank	Scientific consultant
Martin Cohen	UC Berkeley	Scientific consultant
Sean Colgan	NASA/Ames	Scientific consultant
Francis Cotin	CESR	Warm analogue electronics management
Pierre Cox	Obs. Marseille	Guaranteed time programme
Paul Cruvellier	LAS	Director of LAS
Gary Davis	MSSL	Fabry-Pérot development manager, Guaranteed time programme
Christophe Deletrez	CESR	FPU simulator electronics engineering
Trevor Dimbylow	RAL	RTA/QLA Software design
Brian Diplock	RAL	Mechanical engineer, Cold vibration facility engineering
Auriel Donkin	RAL	Project office administration
Duncan Drummond	RAL	EGSE electronics/software engineering
Eric Dunford	RAL	Head of RAL Space Science Department, Liaison with SERC/PPARC
Roger Emery	RAL	Project scientist, Guaranteed time programme
David Ewart	RAL	AIT test controller, Scientific consultant
Jacqueline Fischer	NRL	Guaranteed time programme
Ian Furniss	UCL	Fabry-Pérot design scientist, Guaranteed time programme
Daniel Gautier	Obs. Paris	Scientific consultant
Bill Glencross	UCL	Fabry-Pérot development, Guaranteed time programme
Peter Gray	RAL	Optics design
Matt Griffin	QMW	Detector development, Guaranteed time programme
Phil Griffiths	RAL	Product assurance
Cécile Gry	LAS	Guaranteed time programme
Michael Haas	NASA Ames	Scientific consultant
Andrew Harwood	RAL	Software development, QLA and pipeline
Phil Hingston	RAL	AIV operations
John Holmes	MSSL	Fabry-Pérot assembly development
Martine Joubert	LAS	French Project Scientist, Optics development management, Guaranteed time programme
Ken King	RAL	EGSE Development, Operations scientist, Guaranteed time programme

Alain Léger	IAS Orsay	Scientific consultant
Kate Lidiard	RAL	Optics design engineering
Tanya Lim	RAL	Diagnostics software development, Scientific consultant
René Liseau	IFSI / Obs. Stockholm	Guaranteed time programme
Judy Long	RAL	Project office administration, Party organisation
Steve Lord	IPAC	Scientific consultant
Dario Lorenzetti	IFSI	Guaranteed time programme
Matt Malkan	UC Los Angeles	Scientific consultant
Jonathan McDowell	SAO Boston	Scientific consultant
Steve Miller	UCL	Scientific consultant
Sergio Molinari	IFSI	Operations preparation, Scientific consultant
David Naylor	U. Calgary	Fabry-Pérot development, Guaranteed time programme
Brunella Nisini	IFSI	Guaranteed time programme
Keith Norman	MSSL	Fabry-Pérot development manager
Alain Omont	Obs. Grenoble	Guaranteed time programme
Renato Orfei	IFSI	DPU electronic design, development management, Guaranteed time programme
Glenn Orton	JPL	Scientific consultant
Francesco Palla	Obs. Arcetri	Scientific consultant
Tom Patrick	MSSL	Fabry-Pérot wheel mechanical design
Daniel Péquignot	Obs. Paris	Guaranteed time programme
Dominique Pouliquen	LAS	Optics design engineering
Mark Price	QMW	Detector testing
N'Guyen Quang Rieu	Obs. Paris	Guaranteed time programme
Alan Rogers	RAL	LWS Project Management
David Robinson	QMW	Detector development management, Product Assurance, Quality Assurance
Tony Rush	RAL	Product Assurance, Quality Assurance
Michael Saisse	LAS	Optics Design
Paolo Saraceno	IFSI	Italian Project Scientist, Guaranteed time programme
Lakshmi Sastry	RAL	Software engineering
Guy Serra*	CESR	Warm electronics development, Guaranteed time programme
Roger Sidey	Custon Development	Fabry-Pérot wheel motor design
Sunil Sidher	RAL	Software engineering calibration pipeline, Scientific consultant
Chris Skinner*	UCL	Scientific consultant
Alan Smith	RAL	AIV facility development, operations and management
Howard Smith	NRL	US Project Scientist, Guaranteed time programme
Luigi Spinoglio	IFSI	Guaranteed time programme
Phil Spurrett	RAL	AIV testing
Gordon Stacey	U. Cornell	Scientific consultant
Bruce Swinyard	RAL	Instrument testing and calibration, PV phase preparation, Guaranteed time programme
Jonathan Tennyson	UCL	Scientific consultant
Damien Texier	ESA	Preparation of LIDT
Bill Towlson	UCL	Fabry-Pérot Development
Norman Trams	ESA	Operations preparation, Scientific consultant
Derek Vickers	QMW	Detector/Focal Plane engineering
Helen Walker	RAL	Scientific consultant
Yvonne Windsor	BNSC	BNSC executive
Glenn White	QMW	Guaranteed time programme

## Operations Phase

Peter Ade	QMW	Science analysis
Christiane Armand	LAS	LIDT member, wavelength calibration
Jean-Paul Baluteau	LAS	Science analysis
Mike Barlow	UCL	Science analysis
Mark Buckley	RAL	Software development, calibration analysis
Martin Burgdorf	ESA	LIDT member, calibration uplink, photometric calibration
Emmanuel Caux	CESR	Calibration analysis, Science analysis, Parallel and serendipity mode concept and implementation
Cecilia Ceccarelli	U. Grenoble	Science analysis
Peter Clegg	QMW	Principal Investigator LWS, Science analysis
Martin Cohen	UC Berkely	Calibration analysis
Carlos Correia	QMW	Calibration analysis, Science analysis
Pierre Cox	Obs. Marseille	Science analysis
Gary Davis		Fabry-Pérot calibration analysis, Science analysis
Anna di Giorgio	IFSI	LIDT member, wavelength calibration, Science analysis
Roger Emery	RAL	LWS Project Scientist, Science Analysis
David Ewart	RAL	LIDT member, trend analysis, RTA/QLA expert
Jacqueline Fischer	NRL	Science analysis
Ian Furniss	UCL	Science analysis
Bill Glencross	UCL	Science analysis
Matt Greenhouse	Smithsonian NASM	Science analysis
Griffin Matt	QMW	Instrument commissioning, Calibration analysis, Science analysis
Cécile Gry	LAS/ESA	LIDT member, wavelength calibration, grating profile, Science analysis
Andrew Harwood	RAL	OLP software development
Martine Joubert		Science analysis
Ken King	RAL	Project manager
Sarah Leeks	QMW	Detector analysis, Science analysis
Tanya Lim	RAL/ESA	LIDT deputy leader, photometric calibration, RSRF, Science analysis
René Liseau	Obs. Stockholm	Science analysis
Xiao-Wei Liu	UCL	Calibration analysis, Science analysis
Judy Long	RAL	Project office administration, Party organisation
Steve Lord	IPAC	Calibration analysis, ISAP development, Science Analysis
Dario Lorenzetti	IFSI	Science analysis
Rosario Lorente	ESA	Calibration analysis, grating profile
Nigel Minchin	QMW	Calibration analysis, blues performer, Science analysis
Sergio Molinari	IFSI/IPAC	LIDT member, photometric calibration, beam characterisation, Science analysis
David Naylor	U. Lethbridge	Science analysis
Brunella Nissini	IFSI	Science analysis
Graeme Oldham	QMW	Calibration analysis, Science analysis
Alain Omont	Obs. Grenoble	Science analysis
Tom Patrick	MSSL	Diagnostic wheel engineering
Daniel Péquinet	Obs. Paris	Science analysis
Stefano Pezzuto	IFSI	LIDT member, Fabry-Pérot calibration, Science analysis
Mark Price	QMW	LIDT member, detector calibration, trend analysis
N'Guyen Quang Rieu	Obs. Paris	Science analysis

Paolo Saraceno	IFSI	Science analysis
Sunil Sidher	RAL	LIDT member, calibration analysis, community support, LIA/ISAP development, Science analysis
Alan Smith	RAL	Operations support
Howard Smith	NASM	Calibration analysis, Science analysis
Luigi Spinoglio	IFSI	Science analysis
Bruce Swinyard	RAL	UK LWS team leader, Instrument comissioning, Calibration analysis, LIA/ISAP development, Science analysis
Roger Sylvester	UCL	Calibration analysis, Science analysis
Damien Texier	ESA	LIDT leader, trend analysis
Elisabetta Tommasi	IFSI	LIDT member, wavelength calibration, Science analysis
Norman Trams	ESA	LIDT/SOC member, Fabry-Pérot calibration
Sarah Unger	RAL/IPAC	ISAP development, Community support, Science analysis
Glenn White	QMW	Science analysis

## Post-Operations Phase

Martin Burgdorf	ESA	Photometric calibration
Susana Cabinero Rodríguez	RAL	Serendipity mode analysis
Emmanuel Caux	CESR	Transient correction
Josephine Chan	RAL	Scientific validation, Photometric calibration
Peter Clegg	QMW	LWS Principal Investigator
Roger Emery	RAL	LWS Project Scientist
David Ewart	RAL	Computer systems support
Cécile Gry	ESA	Handbook editor, Grating resolution element
Andrew Harwood	RAL	OLP software development
Gerard Hutchinson	RAL	LIA development, Fabry-Pérot calibration
Ken King	RAL	UKIDC manager
Sarah Leeks	QMW	Detector characterisation
Tanya Lim	RAL/ESA	Parallel and serendipity mode calibration, RSRF, LWS project manager
Chris Lloyd	RAL	Beam characterisation, de-fringing
Judy Long	RAL	Project office administration, Party organisation
Steve Lord	IPAC	ISAP development, Calibration analysis
Phillippe Marty	CESR	Transient correction, LIA development
Sergio Molinari	IPAC	ISAP/LIA development
Huw Morris	RAL	Computer system manager
Thomas Müller	ESA	Calibration analysis
Edward Polehampton	RAL/Oxford	Fabry-Pérot calibration
Sunil Sidher	RAL	LIA development, Photometric calibration
Bruce Swinyard	RAL	LWS project manager, Photometric calibration, optical modelling
Florence Vivares	CESR	Parallel and serendipity mode pipeline development



# Contents

<b>List of Figures</b>	<b>xvii</b>
<b>List of Tables</b>	<b>xix</b>
<b>1 Introduction</b>	<b>1</b>
1.1 Purpose . . . . .	1
1.2 Structure . . . . .	1
1.3 How to Contact Us . . . . .	1
1.4 LWS Publications . . . . .	2
1.4.1 Acknowledgements and guidelines . . . . .	2
1.4.2 Inventory of ISO publications . . . . .	2
<b>2 Instrument Overview</b>	<b>5</b>
2.1 Introduction . . . . .	5
2.2 Overall Design . . . . .	5
2.3 The LWS Optics . . . . .	5
2.4 The Grating Spectrometer . . . . .	8
2.5 The Fabry-Pérot Spectrometers . . . . .	14
2.6 The LWS Detectors . . . . .	17
2.6.1 LWS readout electronics (integrating amplifiers) . . . . .	20
2.6.1.1 The ramps . . . . .	22
2.6.2 Particle hits . . . . .	23
<b>3 Instrument Modes and Observing Templates</b>	<b>25</b>
3.1 Summary of the Observing Modes . . . . .	25
3.2 Description of the Observing Modes: the Astronomical Observation Templates (AOTs) . . . . .	26
3.2.1 Medium-resolution wavelength range (AOT L01) . . . . .	26
3.2.2 Medium-resolution line spectrum (AOT L02) . . . . .	27
3.2.3 Narrow-band photometry (AOT L02) . . . . .	27
3.2.4 High-resolution wavelength range (AOT L03) . . . . .	27
3.2.5 High-resolution line spectrum (AOT L04) . . . . .	27
3.2.6 Parallel and serendipity modes . . . . .	27
3.3 History of AOT Changes throughout the Mission . . . . .	28

<b>4</b>	<b>Data Processing</b>	<b>31</b>
4.1	Processing Overview . . . . .	31
4.2	Quality Check of the Data . . . . .	35
4.3	Derive-SPD Processing Steps . . . . .	35
4.3.1	Introduction . . . . .	35
4.3.2	Construction of ramps and discarding unusable readouts . . . . .	36
4.3.3	Conversion of readouts to voltages . . . . .	36
4.3.4	Flag saturated ramps . . . . .	37
4.3.5	First level deglitching . . . . .	37
4.3.5.1	Introduction to glitches and spikes . . . . .	37
4.3.5.2	Detection method . . . . .	37
4.3.5.3	Patterns expected from spikes and glitches . . . . .	39
4.3.5.4	Glitch handling . . . . .	40
4.3.6	Extraction of ramp slopes and conversion to photocurrent . . . . .	41
4.3.7	Illuminator processing . . . . .	42
4.4	Auto-Analysis Processing Steps . . . . .	42
4.4.1	Absolute responsivity correction and responsivity drift correction . . . . .	42
4.4.1.1	Grouping of data . . . . .	43
4.4.1.2	Absolute responsivity correction . . . . .	43
4.4.1.3	Responsivity drift correction . . . . .	47
4.4.2	Dark current/background straylight subtraction . . . . .	48
4.4.3	Grating scan wavelength calibration . . . . .	49
4.4.4	Grating spectral responsivity calibration . . . . .	50
4.4.5	Spectral bandwidth correction . . . . .	50
4.4.6	Fabry-Pérot scan wavelength calibration . . . . .	50
4.4.7	Fabry-Pérot throughput correction . . . . .	51
4.4.8	Velocity correction to wavelength . . . . .	51
4.4.9	Write LSNR data product (only in OLP versions earlier than 8) . . . . .	52
4.4.10	Calculation of uncertainties . . . . .	52
4.4.10.1	Grating continuum flux error estimation . . . . .	52
4.4.10.2	Fabry-Pérot continuum flux error estimation . . . . .	52
4.5	Processing of the Parallel and Serendipity Modes . . . . .	54
4.5.1	Dark current subtraction and drift removal . . . . .	54
<b>5</b>	<b>Calibration and Performance</b>	<b>57</b>
5.1	Introduction . . . . .	57
5.2	Absolute Flux Calibration and Grating Relative Response . . . . .	57
5.2.1	Absolute flux calibration . . . . .	59
5.2.2	Relative spectral response function . . . . .	60
5.3	Fabry-Pérot Flux Calibration . . . . .	61
5.4	Dark Current Determination . . . . .	62
5.5	In-orbit Sensitivity of the LWS – Detector Performance . . . . .	63

5.6	Photometric Accuracy . . . . .	65
5.6.1	Calibration sources used for photometric purposes . . . . .	65
5.6.2	LWS photometric stability checked with observations of Mars . . . . .	66
5.6.3	Comparison with IRAS fluxes . . . . .	67
5.6.3.1	Sample selection . . . . .	67
5.6.3.2	Corrections applied . . . . .	68
5.6.3.3	Results . . . . .	69
5.6.4	Checking the Fabry-Pérot photometric accuracy . . . . .	71
5.7	The Strong Source Correction . . . . .	71
5.7.1	The reason for the correction . . . . .	71
5.7.2	The correction . . . . .	72
5.7.3	Future . . . . .	73
5.8	Quarter-Second Processing . . . . .	75
5.8.1	LW5: quarter- versus half-second processing . . . . .	75
5.8.2	Summary of processing for various strength sources . . . . .	77
5.9	Instrumental Field of View: The Beam Profile . . . . .	77
5.9.1	The beam profile . . . . .	78
5.9.2	Asymmetry . . . . .	79
5.9.3	Flux correction for extended sources . . . . .	81
5.9.4	Extended source flux per unit area . . . . .	81
5.9.5	Effect of the ISO PSF at large distances: check of the straylight around Jupiter . . . . .	83
5.10	Grating Wavelength Calibration . . . . .	85
5.10.1	Basic principles and calibration strategy . . . . .	85
5.10.2	Calibration sources and types of observations . . . . .	85
5.10.3	Detector angles . . . . .	85
5.10.4	Time dependence . . . . .	85
5.10.5	Assessment of the achieved wavelength accuracy . . . . .	87
5.11	Grating Resolution and Characterisation of the Line Profiles . . . . .	88
5.11.1	Preparation of the data . . . . .	88
5.11.2	Stability of the line profiles . . . . .	89
5.11.3	Characteristics of the profiles. Comparison to Gaussians. . . . .	90
5.11.4	Effect of a lower spectral sampling . . . . .	92
5.12	Fabry-Pérot Wavelength Calibration . . . . .	92
5.12.1	Introduction . . . . .	92
5.12.2	Strategy of calibration . . . . .	92
5.12.2.1	The line fitting algorithms . . . . .	93
5.12.3	Calibration for OLP Version 10 . . . . .	93
5.12.4	Monitoring the Fabry-Pérot wavelength calibration . . . . .	94
5.12.4.1	Results for FPS . . . . .	96
5.12.4.2	Results for FPL . . . . .	96
5.12.5	Fabry-Pérot wavelength accuracy . . . . .	96
5.13	Fabry-Pérot Resolution and Line Profiles . . . . .	99

5.14	Accuracy of the Parallel and Serendipity Mode Calibration . . . . .	99
5.14.1	Prime mode observations coincident with parallel observations . . . . .	99
5.14.2	Comparison with prime mode from stabilisation periods . . . . .	100
5.14.3	Comparison between overlapping parallel rasters . . . . .	101
5.14.4	Comparison with other instruments . . . . .	102
<b>6</b>	<b>Caveats and Unexpected Effects</b>	<b>105</b>
6.1	Glitches . . . . .	105
6.2	Response to Off-axis and Extended Sources: Fringes in the Data . . . . .	105
6.3	Response to Off-axis and Extended Sources: Spectrum Fracturing . . . . .	107
6.4	Dark Current Subtraction . . . . .	109
6.5	Differences between Overlapping Sub-spectra . . . . .	109
6.6	Spurious Features Introduced by the RSRF . . . . .	109
6.7	The Near-IR Leak . . . . .	110
6.8	‘Detector Warm-up Features’ in the Long Wavelength Detectors . . . . .	112
6.9	Transients and Memory Effects . . . . .	113
6.9.1	Description . . . . .	113
6.9.2	The correction procedure . . . . .	115
6.10	Detector Non-linearity: the Strong Source Correction . . . . .	119
6.10.1	Does your data require the correction? . . . . .	119
6.10.2	Getting the correction applied to your data . . . . .	120
6.11	57.16 $\mu\text{m}$ SW2 Feature in the Fabry-Pérot Spectra . . . . .	120
6.12	FP Wavelength Calibration . . . . .	120
6.13	Removal of the Grating Resolution Element in FP Observations . . . . .	120
6.14	Use of ‘Non-prime Data’ in FP Observations . . . . .	122
6.15	Side Order Contamination in FP Data . . . . .	123
6.16	Responsivity Drift in Long FP Observations . . . . .	125
<b>7</b>	<b>Guide to Instrument Related Data Products</b>	<b>127</b>
7.1	Inventory and Naming Convention . . . . .	127
7.2	Product Files – Description of Content and Use . . . . .	129
7.2.1	Timing information in the products: the ITK . . . . .	129
7.2.2	General FITS header keywords for LWS data . . . . .	129
7.2.3	Transparent data . . . . .	129
7.2.4	Edited Raw Data (ERD files) . . . . .	130
7.2.4.1	LSTA: The LWS Compact Status History . . . . .	130
7.2.4.2	LIER: LWS illuminator ERD file . . . . .	135
7.2.4.3	LGER: LWS grating ERD file . . . . .	136
7.2.4.4	LSER: LWS short-wavelength Fabry-Pérot ERD file . . . . .	137
7.2.4.5	LLER: LWS long-wavelength Fabry-Pérot ERD file . . . . .	138
7.2.4.6	LWHK: LWS housekeeping ERD file . . . . .	139
7.2.5	Standard Processed Data (SPD product files) . . . . .	143
7.2.5.1	LSPD: LWS standard processed data . . . . .	143

7.2.5.2	LIPD: LWS illuminator processed data file . . . . .	147
7.2.5.3	LWGH: LWS Glitch History file . . . . .	148
7.2.5.4	LPSP: LWS parallel Standard Process Data . . . . .	149
7.2.5.5	LSSP: LWS serendipity Standard Process Data . . . . .	149
7.2.6	LSPD and LIPD status words . . . . .	150
7.2.6.1	Detector status word . . . . .	150
7.2.6.2	Mechanism status word . . . . .	151
7.2.7	Auto-Analysis results (AAR product files) . . . . .	151
7.2.7.1	LSAN: LWS Auto-Analysis results . . . . .	151
7.2.7.2	LSNR: LWS Auto-Analysis results without responsivity correction . . . . .	154
7.2.7.3	LIAC: LWS illuminator summary file . . . . .	154
7.2.7.4	LSCA: LWS scan summary file . . . . .	155
7.2.7.5	LGIF: LWS Group Information File . . . . .	156
7.2.7.6	LPAA: LWS parallel Auto-Analysed data . . . . .	157
7.2.7.7	LSAA: LWS serendipity Auto-Analysed data . . . . .	157
7.2.7.8	LPAD: LWS parallel averaged data . . . . .	158
7.2.8	LSAN status words . . . . .	159
7.3	Calibration Files . . . . .	159
7.3.1	SPD calibration files . . . . .	160
7.3.1.1	LCDT: Discard times file . . . . .	160
7.3.1.2	LCAL: Readout limits for the analogue electronics . . . . .	161
7.3.1.3	LCVC: Detector voltage conversion file . . . . .	162
7.3.1.4	LCGA: Analogue amplification gains . . . . .	162
7.3.1.5	LCJF: JF4 amplifier parameters . . . . .	163
7.3.1.6	LCDB: Saturation voltage thresholds for slope fitting . . . . .	164
7.3.1.7	LCD1: First level deglitching parameters . . . . .	165
7.3.1.8	LCGH: Glitch History file parameters . . . . .	166
7.3.1.9	LCD2: Second level deglitching parameters . . . . .	166
7.3.1.10	LCFP: Parameters for electronic filters . . . . .	166
7.3.1.11	LCD3: Third level deglitching parameters . . . . .	166
7.3.2	Auto-Analysis calibration files . . . . .	167
7.3.2.1	General information . . . . .	167
7.3.2.2	LCIR: Illuminator reference file . . . . .	168
7.3.2.3	LCGW: Grating position to wavelength conversion parameters . . . . .	169
7.3.2.4	LCGR: Grating relative response file . . . . .	170
7.3.2.5	LCFW: Fabry-Pérot wavelength calibration parameters . . . . .	171
7.3.2.6	LCGB: Grating spectral bandwidth correction factors . . . . .	171
7.3.2.7	LCDK: Fixed dark current calibration file . . . . .	172
7.3.2.8	LCTP: Fabry-Pérot throughput correction calibration file . . . . .	172

<b>8 Getting Started with LWS Data</b>	<b>173</b>
8.1 Retrieving and Reading the Data . . . . .	173
8.2 Analysing the Data . . . . .	174
8.2.1 LWS data reduction recipes . . . . .	174
8.2.2 The ISO Spectral Analysis Package (ISAP) . . . . .	174
8.2.3 The LWS Interactive Analysis (LIA) . . . . .	174
8.3 Analysing Parallel/Serendipity Mode Data . . . . .	177
8.4 Where to Find the Calibration Parameters . . . . .	177
8.5 Useful Web Addresses . . . . .	178
<b>A List of Acronyms</b>	<b>179</b>
<b>Bibliography</b>	<b>183</b>
<b>Index</b>	<b>187</b>

# List of Figures

2.1	The LWS with optical path overlay . . . . .	6
2.2	Mirror 2 . . . . .	7
2.3	Photograph of the LWS . . . . .	7
2.4	The LWS grating . . . . .	9
2.5	The LWS spectral range . . . . .	10
2.6	LWS flight model filters . . . . .	11
2.7	LWS flight model detector responses . . . . .	11
2.8	Grating efficiency measurements . . . . .	13
2.9	The construction of a Fabry-Pérot etalon . . . . .	15
2.10	FP finesse and transmission as a function of reflectance . . . . .	16
2.11	Drawing of the LWS detector block . . . . .	19
2.12	Integrating amplifier circuit . . . . .	21
2.13	LWS ramps . . . . .	22
2.14	The effect of a bias boost . . . . .	23
2.15	An example of a glitched ramp . . . . .	24
3.1	Modes of the LWS . . . . .	26
4.1	Data processing overview . . . . .	32
4.2	Schematic overview of Derive-SPD . . . . .	33
4.3	Overview of Auto-Analysis . . . . .	34
4.4	Illuminator flash sequence . . . . .	46
4.5	Comparison of OLP 8 and OLP 10 illuminator processing . . . . .	47
5.1	Uranus model . . . . .	58
5.2	Relative Spectral Response Function (RSRF) . . . . .	60
5.3	Derivation of the FPS throughput with Mars ‘mixed-mode’ observations . . . . .	61
5.4	Derivation of the FPL throughput with Mars ‘mixed-mode’ observations . . . . .	62
5.5	Martian rotational modulation detected at 3% level . . . . .	67
5.6	Comparison of IRAS and LWS fluxes at 100 $\mu\text{m}$ for a wide range of fluxes . . . . .	68
5.7	Ratio of the IRAS flux to LWS flux at 100 $\mu\text{m}$ for various source types . . . . .	69
5.8	LWS versus IRAS flux comparison at 100 $\mu\text{m}$ for three different samples . . . . .	70
5.9	LWS versus IRAS flux comparison at 60 $\mu\text{m}$ . . . . .	70
5.10	A curved ramp . . . . .	72

5.11	Modelled versus observed photocurrents of Saturn for LW3 . . . . .	73
5.12	Strong source corrected spectrum . . . . .	74
5.13	A curved half-second ramp . . . . .	75
5.14	Ramps hitting the ADC rail . . . . .	76
5.15	LW5 Sagittarius B2 with quarter- and half-second processing . . . . .	76
5.16	Offset positions of the Mars beam profile observations . . . . .	77
5.17	The mean beam profile for each detector . . . . .	79
5.18	FWHM vs. detector for the four alignments . . . . .	80
5.19	Correction factor for extended sources versus wavelength . . . . .	81
5.20	Comparison of LWS and IRAS 100 $\mu\text{m}$ fluxes in Trumpler 14 and 16, and Galactic Centre . . . . .	83
5.21	Model of the point spread function as sampled with the LWS . . . . .	84
5.22	Main LWS grating wavelength standards . . . . .	87
5.23	Deviation of the measured line center . . . . .	88
5.24	Measured grating profiles . . . . .	91
5.25	Gap between plates versus encoded position for FPS and FPL . . . . .	95
5.26	Monitoring data for FPL . . . . .	97
5.27	Velocity residuals for ORION CO lines . . . . .	98
5.28	L01 full grating spectrum of a background position . . . . .	100
5.29	Comparison between serendipity and grating rest observation . . . . .	101
5.30	Parallel map in the Galactic Centre region . . . . .	102
5.31	Comparison between map fluxes and raster fluxes . . . . .	103
6.1	Example of a remaining glitch in the calibrated data . . . . .	106
6.2	Example of fringes in the spectrum of an extended source . . . . .	107
6.3	Example of spectrum fracturing . . . . .	109
6.4	Double-peaked feature in SW1 . . . . .	110
6.5	Example of features due to the near-IR leak in the spectrum of Aldebaran . . . . .	111
6.6	Straylight features on LW detectors . . . . .	113
6.7	Examples of transients in fixed-grating observations . . . . .	114
6.8	Variation of transient effect correction parameters with time . . . . .	116
6.9	Result of the transient correction for an extended source . . . . .	117
6.10	Result of the transient correction for a non-extended source . . . . .	118
6.11	Example of ‘saggy’ sub-spectra . . . . .	119
6.12	Stability and systematic errors in the FP wavelength calibration . . . . .	121
6.13	Example of the raw data recorded on a ‘non-prime’ detector . . . . .	122
6.14	Location of the FP ‘useful’ data on the grating profile . . . . .	123
6.15	Comparison of prime and co-added non-prime data . . . . .	124
6.16	FP transmission for orders at wavelengths from $\lambda_2$ to $\lambda_{-3}$ . . . . .	124
6.17	Grating profile with the contribution from the two FP side orders . . . . .	125

# List of Tables

2.1	Detector parameters . . . . .	12
2.2	Detector angles and wavelengths . . . . .	14
2.3	Detector types, wavelength ranges and in-orbit bias voltages . . . . .	18
2.4	Bias levels and voltages per detector type . . . . .	19
4.1	The LWS grating rest position wavelengths . . . . .	54
5.1	Typical accuracies of the LWS . . . . .	58
5.2	Observations of Uranus used to derive the RSRF . . . . .	59
5.3	The three illuminator sequence types . . . . .	60
5.4	LWS dark current values . . . . .	63
5.5	In-orbit sensitivity of the LWS instrument . . . . .	64
5.6	Sources used for the photometric calibration . . . . .	66
5.7	Sources and lines used for the FP photometric accuracy . . . . .	71
5.8	In-orbit detector responsivities . . . . .	74
5.9	Effective aperture of the detectors . . . . .	80
5.10	Extended source corrections and effective beam sizes . . . . .	82
5.11	Comparison of LWS observations of Jupiter with the ISO PSF model . . . . .	84
5.12	Lines from astronomical sources used for grating wavelength calibration . . . . .	86
5.13	Detector angles adopted for wavelength calibration . . . . .	86
5.14	Grating wavelength coefficients . . . . .	87
5.15	LWS wavelength calibration accuracy . . . . .	88
5.16	Grating profile parameters and comparison to Gaussian profiles . . . . .	90
5.17	Lines and sources used to calibrate the FP's . . . . .	94
5.18	FPS and FPL wavelength calibration coefficients . . . . .	94
5.19	Lines and sources used to monitor FP's calibration . . . . .	94
5.20	FPS rms calibration errors . . . . .	96
5.21	FPL rms calibration errors . . . . .	96
5.22	FP resolving power . . . . .	99
5.23	L01 observations concurrent with parallel observations . . . . .	100
6.1	Characteristics of the near-IR leak . . . . .	112
6.2	Mean transient correction parameter values for Uranus . . . . .	116
6.3	Detectors within each FP's nominal range. . . . .	122

7.1	General header keywords for products . . . . .	131
7.2	TDATA AOT-VAR message contents . . . . .	132
7.3	TDATA message-1 contents . . . . .	132
7.4	LWS Compact Status record structure . . . . .	133
7.5	Meaning of the LSTASTAT field . . . . .	133
7.6	LWS sample list . . . . .	134
7.7	LWS illuminator ERD file record structure . . . . .	135
7.8	LWS grating scan ERD file record structure . . . . .	136
7.9	LWS FPS scan ERD file record structure . . . . .	137
7.10	LWS FPL ERD file record structure . . . . .	138
7.11	LWS housekeeping ERD file record structure . . . . .	139
7.12	Detector biases in the housekeeping . . . . .	140
7.13	Amplifier parameters in the housekeeping frames . . . . .	141
7.14	Grating parameters in the housekeeping frames . . . . .	141
7.15	FP parameters in the housekeeping . . . . .	142
7.16	LWS SPD file record structure . . . . .	144
7.17	LWS SPD file header keywords . . . . .	145
7.18	LSPD statistics keywords . . . . .	146
7.19	LWGH file record structure . . . . .	148
7.20	LWS Glitch History file keywords . . . . .	148
7.21	LPSP file record structure . . . . .	149
7.22	LSSP file record structure . . . . .	149
7.23	LSPD and LIPD detector status word . . . . .	150
7.24	LSPD mechanism status word . . . . .	151
7.25	LWS Auto-Analysis product file record structure . . . . .	152
7.26	LWS Auto-Analysis file keywords . . . . .	153
7.27	LIAC product file record structure . . . . .	154
7.28	LSCA product file record structure . . . . .	155
7.29	LGIF product file record structure . . . . .	156
7.30	LPAA product file record structure . . . . .	157
7.31	LSAA product file record structure . . . . .	157
7.32	LPAD product file record structure . . . . .	158
7.33	LSAN and LSNR status word . . . . .	159
7.34	LCDT calibration file keywords . . . . .	160
7.35	LCAL calibration file keywords . . . . .	161
7.36	LCJF calibration file keywords . . . . .	163
7.37	LCDB calibration file keywords . . . . .	164
7.38	LCD1 calibration file keywords . . . . .	165
7.39	LCGH calibration file keywords . . . . .	166
7.40	Auto-Analysis calibration files general keywords . . . . .	167
7.41	LCIR calibration file record structure . . . . .	168
7.42	LCGW calibration file record structure . . . . .	169

7.43 LCGW keywords . . . . .	169
7.44 LCGR calibration file structure . . . . .	170
7.45 LCGR keywords . . . . .	170
7.46 LCFW calibration file keywords . . . . .	171
7.47 LCGB calibration file record structure . . . . .	171
8.1 Instrumental and astronomical calibration parameters . . . . .	178



# Chapter 1

## Introduction

### 1.1 Purpose

The LWS Handbook is one in a series of five<sup>1</sup> documents that explain the operations of the Infrared Space Observatory (ISO) and its four instruments, the data received from the instruments and the processing carried out on the data. Volume I gives an overview of the entire ISO mission and it explains the operations of the ISO satellite while the remaining four explain the individual instruments (CAM, LWS, PHT and SWS). The LWS document is intended to provide all information necessary to understand the offered LWS standard data products, as processed by Version 10 of the Off-Line Processing (OLP) system, retrievable from the Legacy ISO Data Archive (IDA) at:

<http://www.iso.vilspa.esa.es/>

Therefore, it gives a full description of the instrument, the automatic processing pipeline, the calibration steps applied and the data products. In order to further reduce data through interactive analysis there are two software packages available with reduction tools written in IDL. Links to these are provided in Chapter 8.

This volume of the ISO Handbook serves as the reference for both the processing as well as the correct interpretation of LWS data as available from the ISO Data Archive.

### 1.2 Structure

Users who have not previously worked with LWS data should use **Chapter 8** as an entry point to this document as this chapter gives information on how to retrieve LWS data from the ISO Data Archive and what the standard data reduction recipes are. New users should refer to the observing modes in **Chapter 3** and they may also wish to gain an overview of the LWS product file types given in **Chapter 7**. **Chapters 2** and **4** give background information on the instrument design and data processing, for those users who want to gain a deeper knowledge of the instrument and the data processing, e.g. while troubleshooting specific problems within their data. The calibration is detailed in **Chapter 5** and typical accuracies are given in section 5.1. **Chapter 6** contains a description of all known problems that can occur with LWS data and this chapter should be an entry point for experienced users.

### 1.3 How to Contact Us

To supplement this handbook, LWS experts can be contacted at the ESA ISO Data Centre in VILSPA:

---

<sup>1</sup>Originally six documents were planned with Volume I on the *ISO Mission* and II on the *ISO Satellite* but both have now been merged in Volume I in Version 2.0.

<http://www.iso.vilspa.esa.es/> → ISO Explanatory Library → LWS  
 or at the LWS UK Data Centre:  
<http://jackal.bnsc.rl.ac.uk/isouk/>

Any question regarding LWS data products or their interactive analysis can be addressed by e-mail to:

[helpdesk@iso.vilspa.esa.es](mailto:helpdesk@iso.vilspa.esa.es).

## 1.4 LWS Publications

### 1.4.1 Acknowledgements and guidelines

Any paper published based on **ISO data** should contain the following text, as a footnote to the title.

*Based on observations with ISO, an ESA project with instruments funded by ESA Member States (especially the PI countries: France, Germany, the Netherlands and the United Kingdom) and with the participation of ISAS and NASA.*

Should the journal in question not permit footnotes to the title, the above text should appear as a footnote the first time ISO is mentioned.

The preferred reference for the ISO mission is:

*The Infrared Space Observatory (ISO) mission*, Kessler, M.F. et al. 1996, A & A 315, L27

Any paper published based on **LWS data** should acknowledge the instrument with the following reference:

*The ISO Long-Wavelength Spectrometer*, Clegg, P.E. et al 1996, A&A 315, L38

If you have used the **LWS Interactive Analysis (LIA)** to reduce your LWS data please write in the acknowledgments:

*LIA is a joint development of the ISO-LWS Instrument Team at Rutherford Appleton Laboratories (RAL, UK - the PI Institute) and the Infrared Processing and Analysis Centre (IPAC/Caltech, USA).*

If you have used the **ISO Spectral Analysis Package (ISAP)** to reduce your LWS or SWS data please write in the acknowledgments:

*The ISO Spectral Analysis Package (ISAP) is a joint development by the LWS and SWS Instrument Teams and Data Centres. Contributing institutes are CESR, IAS, IPAC, MPE, RAL and SRON.*

### 1.4.2 Inventory of ISO publications

In order to offer a complete bibliographic information to the ISO Data Archive users, we try to keep track of all publications involving ISO data, and of all observations used for these publications. As a result, in IDA next to any selected observation, the button ‘Articles’ provides the references of the publications involving this particular observation and a link to their Astrophysics Data System (ADS) entry<sup>2</sup>. Your contribution in this matter can greatly help keeping an information as comprehensive as possible and we therefore ask you to kindly provide the following information for each of your publications:

- complete reference of the article (or preprint)
- list of TDT numbers and instrument modes of the observations that you have exploited for the publication.

---

<sup>2</sup><http://adswww.harvard.edu/>

You can send the information either by e-mail to:  
**helpdesk@iso.vilspa.esa.es**

or by normal mail to:

**ISO Project Scientist  
(ISO Preprints)  
ESA Satellite Tracking Station  
Villafranca del Castillo  
P.O. Box 50727  
28080 Madrid**



## Chapter 2

# Instrument Overview

### 2.1 Introduction

The Long Wavelength Spectrometer (LWS, Clegg et al. 1996, [9]) was one of the four instruments on board the Infrared Space Observatory which operated between November 1995 and April 1998. The LWS covered the spectral range between 43 and 197  $\mu\text{m}$  at medium ( $\Delta\lambda/\lambda \sim 150\text{--}200$ ) resolution using a diffraction grating and at high resolution ( $\Delta\lambda/\lambda \sim 6800\text{--}9700$ ) with either of the two Fabry-Pérot's additionally placed in the beam. ISO was operated as an observatory and LWS users had the option of using any combination of four observing modes defined as standard astronomical observation templates (AOTs). These consisted of wavelength range scanning or line scanning, using either the grating alone or with the Fabry-Pérot. A sub-mode of the grating line scanning mode where the grating did not move from the rest position was also defined for narrow-band photometry. The LWS was equipped with ten photoconductive detectors overlapping in wavelength range, five operating in second order and five in first order. A Ge:Be detector was used for the shortest wavelength range (43–51  $\mu\text{m}$ ), five Ge:Ga detectors for the 50–121  $\mu\text{m}$  range and four stressed Ge:Ga detectors for the longest wavelength range (108–197  $\mu\text{m}$ ).

### 2.2 Overall Design

The LWS consisted of three main components, the focal plane unit (FPU), operating at liquid-helium temperatures, and two warm units: the analogue processing unit (APU), which was driving the various mechanisms and powering the detectors in the FPU, as well as processing the resulting signals, and the digital processing unit (DPU), which commanded the LWS via the APU and interfaces with the spacecraft computer.

The FPU itself consisted of three main subsystems: the optical subsystem, the detector subsystem and the Fabry-Pérot subsystem. The optical subsystem comprised a collimator, a grating, and re-focusing optics which fed the detector subsystem. The Fabry-Pérot subsystem, which was situated in the parallel part of the beam, consisted of a Fabry-Pérot wheel carrying two Fabry-Pérot interferometers. The wheel could be set in any of four positions: in one of these, the beam passed through the subsystem unhampered whilst in another, the beam was completely obscured. In the remaining two positions, one or other Fabry-Pérot was placed in the beam and modulated it spectrally.

### 2.3 The LWS Optics

Radiation from an astronomical source entered the ISO telescope, which was a 60 cm diameter ( $D$ ) Ritchey-Chrétien system with an overall focal ratio of  $f/15$  ( $F_t/D$ , where  $F_t$  is the effective telescope

focal length). The telescope plate scale is given by  $1/F_t$  and is  $22.9''/\text{mm}$ ; i.e. an object of  $22.9''$  on the sky had a linear size of 1 mm in the focal plane of the telescope. The radiation was divided into four beams, one for each ISO instrument, by a pyramidal mirror near the Cassegrain focus. Figure 2.1 shows the path radiation took through the LWS, superimposed on a photograph of the instrument taken before the integration of the Fabry-Pérot subsystem. After entering the LWS it was reflected from Mirror 1 onto Mirror 2, which was coincident with the telescope focus. The size of Mirror 2 thus precisely defined the Field of View (FOV) on the sky for the LWS. At these extreme infrared wavelengths the spatial resolution of the ISO telescope was completely determined by diffraction, with an achievable spatial resolution of  $\sim 83''$  ( $\theta = 1.22 \lambda/D$ ) at the longest wavelength ( $\lambda$ ). Although this lowers with decreasing wavelength, the LWS was designed to detect this longest wavelength with reasonable efficiency yet have a nearly constant FOV on the sky. A study of the intensity received from a point source as a function of the focal plane aperture size by Duncan 1983, [14] showed that the diameter of the central Airy diffraction disc ( $d = 2.44 \lambda(F_t/D)$ ) can be reduced to about 65% before significant losses occur. Note that the energy within the central spot of the Airy disc is 84%, whilst Figure 5 of Duncan 1983, [14] shows that this only reduces to  $\sim 72\%$  with an iris set to 0.65 of the Airy disc diameter. For the longest LWS wavelength this gave a diameter of  $d = 4.65 \text{ mm}$  ( $d = 0.65 \times 2.44 \lambda(F_t/D)$ ), which was the criterion used to set the size of Mirror 2. The maximum geometrical FOV for the LWS was given by  $d \times 1/F_t \sim 106''$ .

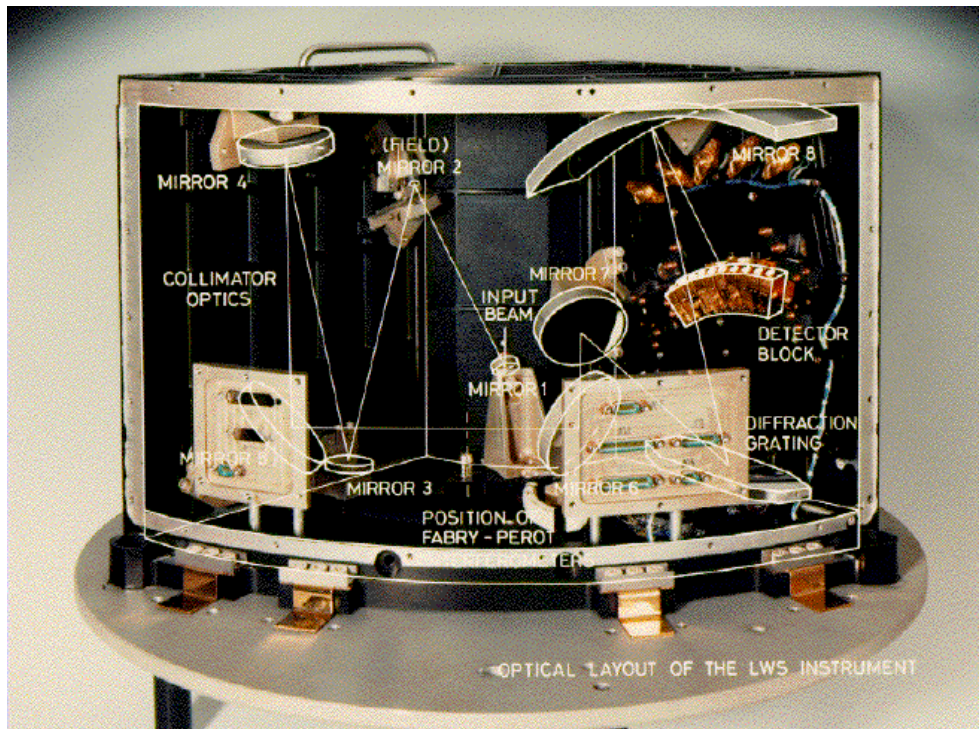


Figure 2.1: Photograph of the LWS with an overlay of the optical path (note the FP wheel is not shown) by S. Adams (QMW).

In practice the beam size was determined by the aperture size at the detector feed horn entrance which also determined the spectral resolution achievable. This will be addressed again in the next section which describes the grating. This unavoidable linkage between the spectral and spatial performance of the LWS makes it a particularly difficult instrument to understand and hence its output data products are also difficult to interpret. To further confuse these issues, internal stops and diffraction losses within the instrument also modify the FOV. The beam size on the sky, while in-flight, was  $\sim 80''$  (see Section 5.9). This was measured by scanning a point source across the FOV in-flight.

Unfortunately Mirror 2 was stepped, as shown in Figure 2.2, with a much larger diameter annular surface parallel to the mirror surface. The intention was that this surface should have been black, to absorb all of the straylight from around the target source. The blackening method chosen was to anodise this annular ring with nickel dye to a thickness of  $55\ \mu\text{m}$ , which proved not to be efficient enough at long wavelengths (see Ungar et al. 1990, [44] for a study of black paints for ISO). The step,  $h$ , between the front and annular planes was  $\sim 1.5\ \text{mm}$ , so in effect, at the longer wavelengths, radiation from sources extended with respect to the beam (or non-centred point sources) would partly reflect off the annular surface and interfere with that from the desired path from the front of Mirror 2. This interference is seen as fringing in the spectra as described in Section 6.2.

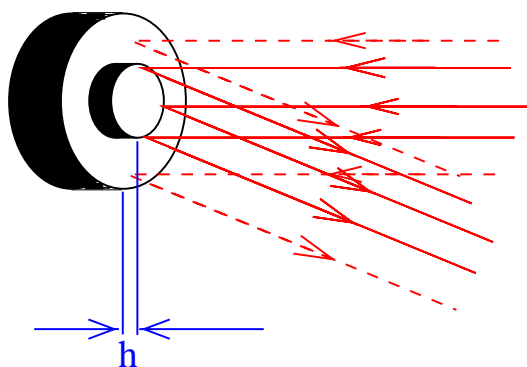


Figure 2.2: *The unintentionally stepped Mirror 2. Dashed lines show the undesired optical path with consequent phase delay  $\sim 2h$ .*

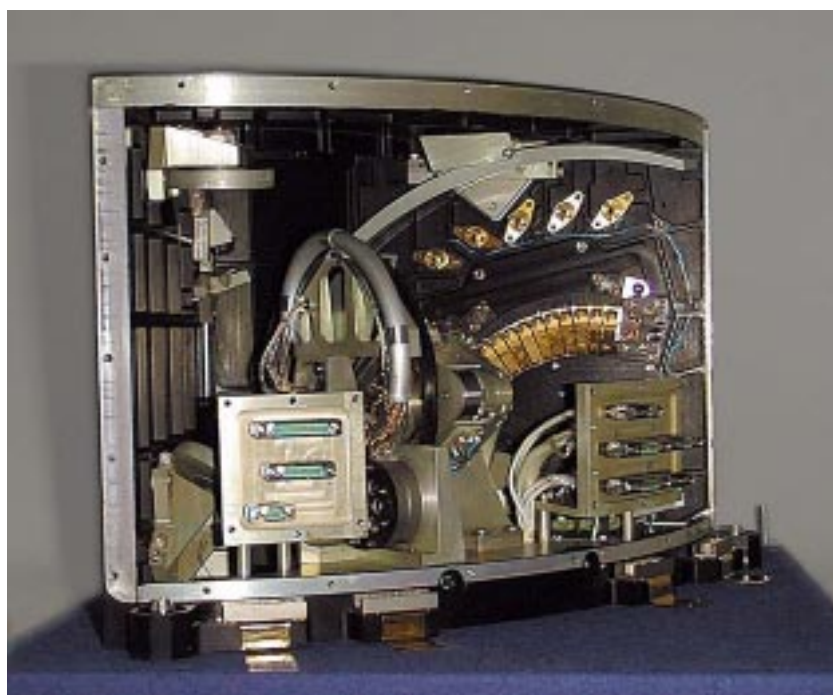


Figure 2.3: *The LWS (photographed by S. Adams, QMW)*

Following reflection from Mirror 2, the radiation then met Mirrors 3 and 4, which made a powered reverse Cassegrain that collimated the beam. The collimator focal length (500 mm) was necessarily large to reduce the angular spread of the parallel beam, which limited the attainable resolution of the Fabry-Pérot (the Fabry-Pérot Spectrometers are discussed in Section 2.5). Because the focal length was large, mirrors (5, 6 and 7) were used to fold the beam to adhere with the space constraints on board ISO. Between Mirror 5 and Mirror 6 the radiation passed through the interchange wheel. This wheel was driven by a pinion engaging gear-teeth on the rim of the wheel: a new type of cryogenic motor was especially developed to drive the wheel. The wheel could be set to four positions: a hole for grating-only medium resolution mode, the long wavelength Fabry-Pérot or the short wavelength Fabry-Pérot for high resolution modes and a blanking plate for dark current measurements (this was never used in operation). The Fabry-Pérot mechanism can be seen in Figure 2.3, which shows the complete instrument. Mirror 7 then directed the parallel radiation onto the diffraction grating, which had an off-centre rotationally symmetric Schmidt profile to correct for the spherical aberration. The basic action of the grating was to disperse different wavelengths from the source spatially. The grating was rotated to cover a range of wavelengths.

The dispersed radiation from the grating was focused by the large spherical condensing Mirror 8 (see Figure 2.1, focal length 97.5 mm) onto the cylindrical surface of the ten element detector array which was aligned along the dispersion direction.

## 2.4 The Grating Spectrometer

In its rest position, the grating normal was at  $60^\circ$  to the incident beam (see Figure 2.4). By rotating the grating, by means of a servo-controlled drive mechanism, between  $-7^\circ$  and  $+7^\circ$  (the physical limits of its motion), the centre of the grating response function was scanned over a wavelength band, for SW4 this ranged from  $64$  to  $86 \mu\text{m}$ ; it is shown in the upper panel of Figure 2.5. Considering each detector in turn, a contiguous coverage from  $45$  to  $180 \mu\text{m}$  was achieved by rotating the grating from  $-3.5^\circ$  to  $+3.5^\circ$ . By using the extended range of operation ( $-7^\circ$  to  $+7^\circ$ ) — at the cost of a small increase in power dissipated in the focal plane — the spectral range was extended to cover  $43$ – $197 \mu\text{m}$ , whilst giving significant overlap between the spectral coverage of adjacent-wavelength detector channels. In order to maximise the sensitivity of the instrument at all wavelengths, the extended scanning range has been used in normal operation. The wavelength ranges used for each detector, along with the overlaps, are indicated in the upper panel of Figure 2.5 (note that the limitations on the detector wavelength ranges, as discussed below, are taken into account). The nominal well calibrated ranges are shown in yellow. The extended range gave important verification when looking for weak line features and afforded redundancy in the instrument if there had been a catastrophic failure in one detector.

The grating diffracts radiation of wavelength  $\lambda$  in first order at the same angle as wavelength  $\lambda/2$  in second order and as wavelength  $\lambda/n$  in  $n^{\text{th}}$  order. With this constraint it was not possible to utilise the full wavelength coverage afforded by the range of possible scan angles. To ensure that only the required narrow band of wavelengths is detected at a particular grating angle, and not the wavelengths in different orders, filters with well-defined passbands were placed in front of the detectors. The transmission of the filters, measured by Ade (private communication), is shown in Figure 2.6. The resulting nominal wavelength limits for each band are given in Table 2.3. They take into account the following limitations:

- Ge:Be (the detector type used for SW1) has a long wavelength cut-off at  $51 \mu\text{m}$  (see Figure 2.7).
- For SW1, 2 and 3 the short wavelength end was limited by the requirement on the filters to reject third order when observing the longest wavelength in second order.
- For LW1 an unstressed Ge:Ga detector was used, which has a long wavelength cut-off (see Figure 2.7).

Clearly these factors resulted in a small loss in redundancy over the LWS range. The detectors are discussed in Section 2.6.

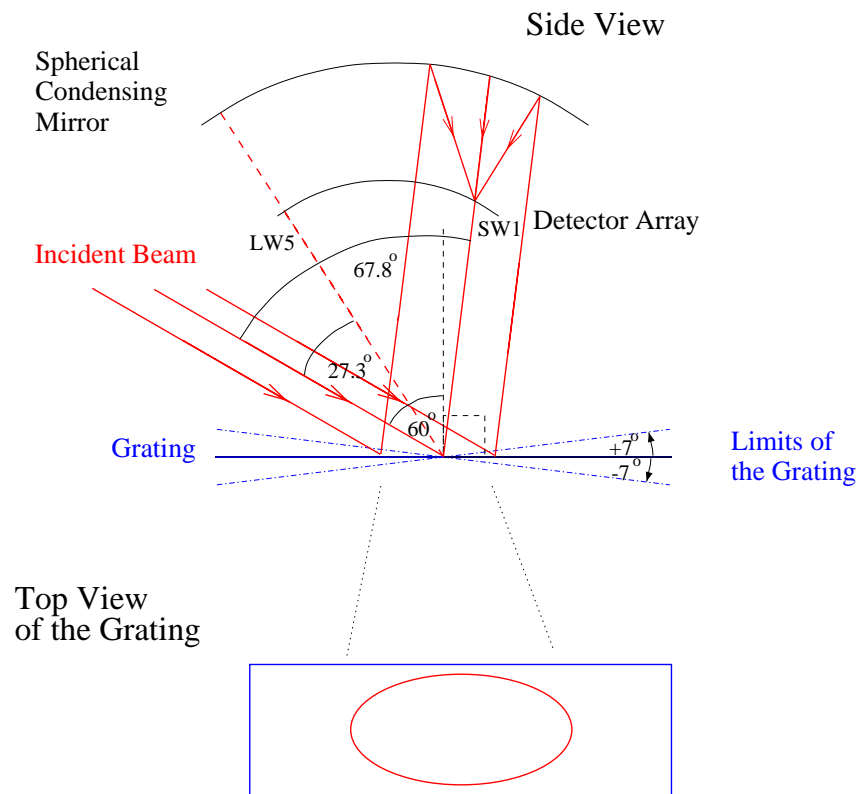


Figure 2.4: The side view shows an incident beam (red line), diffracted by the grating at its rest position (solid blue line, limits of rotation shown by dashed blue line). The shorter wavelength radiation went to SW1 and the longer to LW5, via the spherical condensing mirror. The middle panel indicates the elliptical footprint of the beam. The bottom diagram shows the angle of the incident beam to the normal. The diffracted beam was also normal to the grating (for one wavelength), in its rest position, because a blaze angle of  $30^\circ$  was chosen for optimum performance.

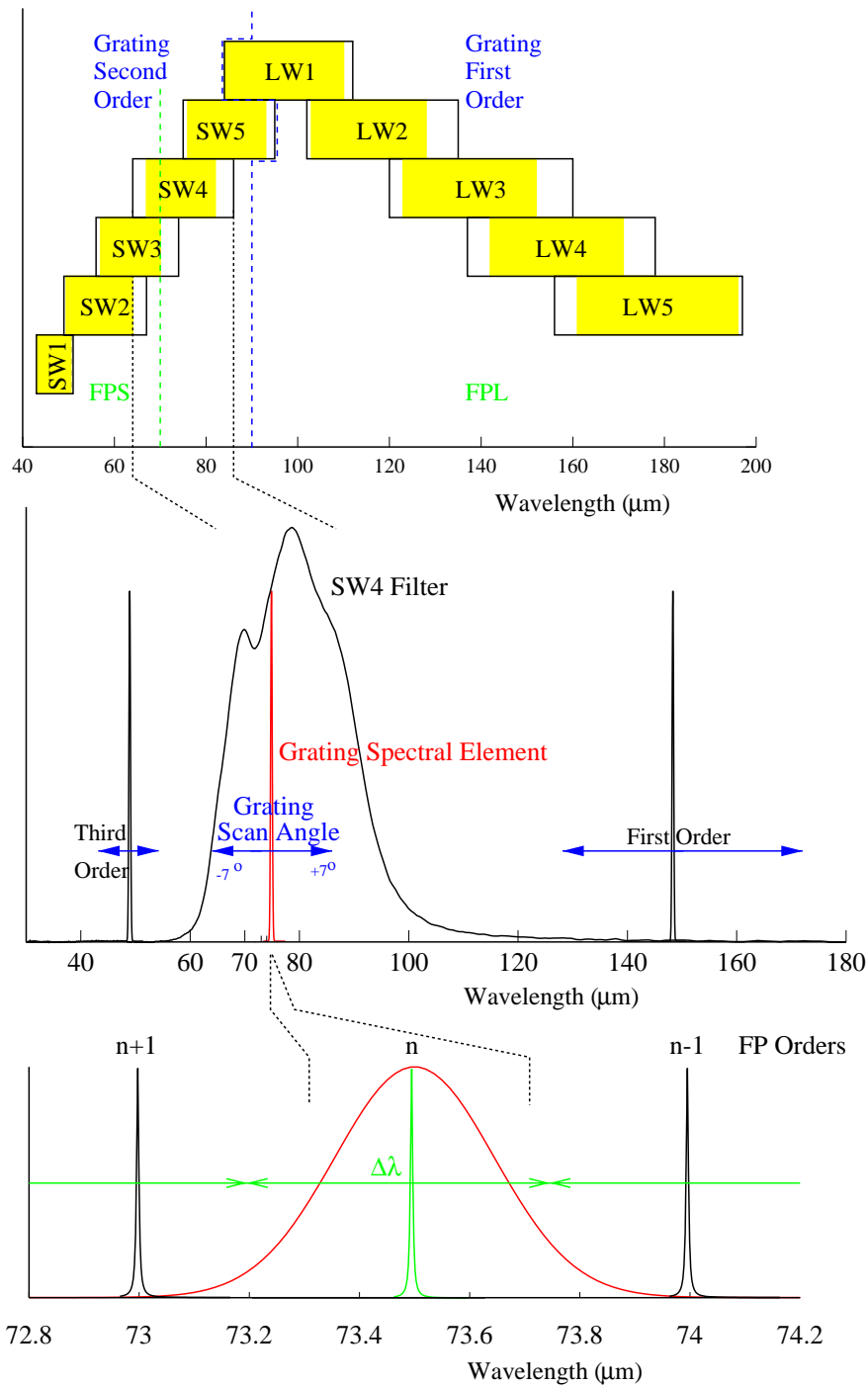


Figure 2.5: The top plot shows the range covered by each of the ten detectors, by rotating the grating to its extremes, along with the grating order and the FP wheel used. The yellow regions indicate the nominal wavelength ranges. The second plot shows the second order grating spectral element (red) at a grating angle of  $-1.36^\circ$ . It also shows the adjacent orders of this radiation and the detector filter which prevented these orders from reaching the detector. The final plot shows the  $n^{\text{th}}$  order Airy profile of the FP with the superimposed grating spectral element, also the range of wavelengths which could be covered by changing the mesh separation is indicated by the green arrows. The neighbouring peaks that fell outside of the grating response are indicated.

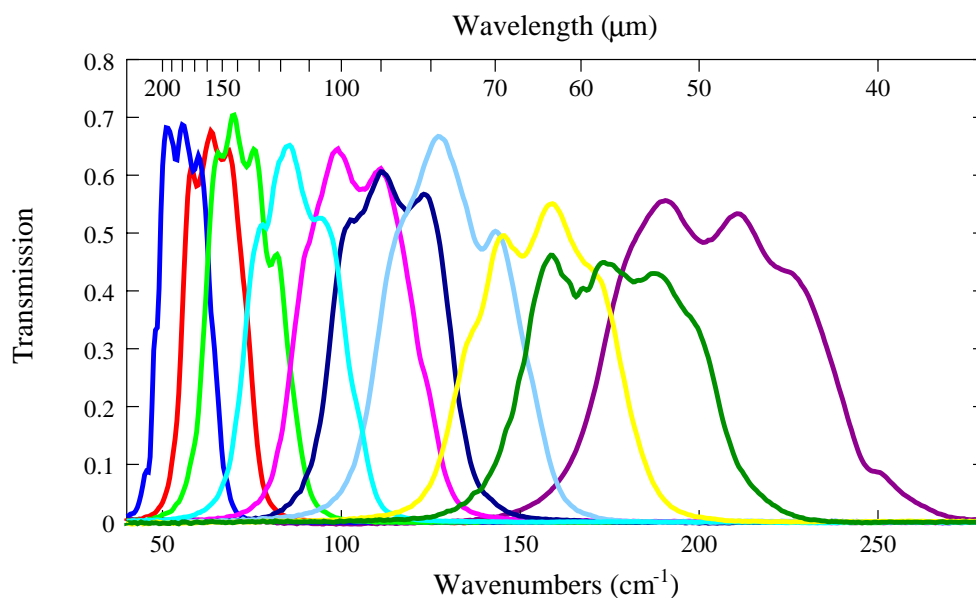


Figure 2.6: *The LWS flight model filters measured by Ade (private communication). They are in sequential order SW1 to LW5 (from right to left), see also Table 2.1.*

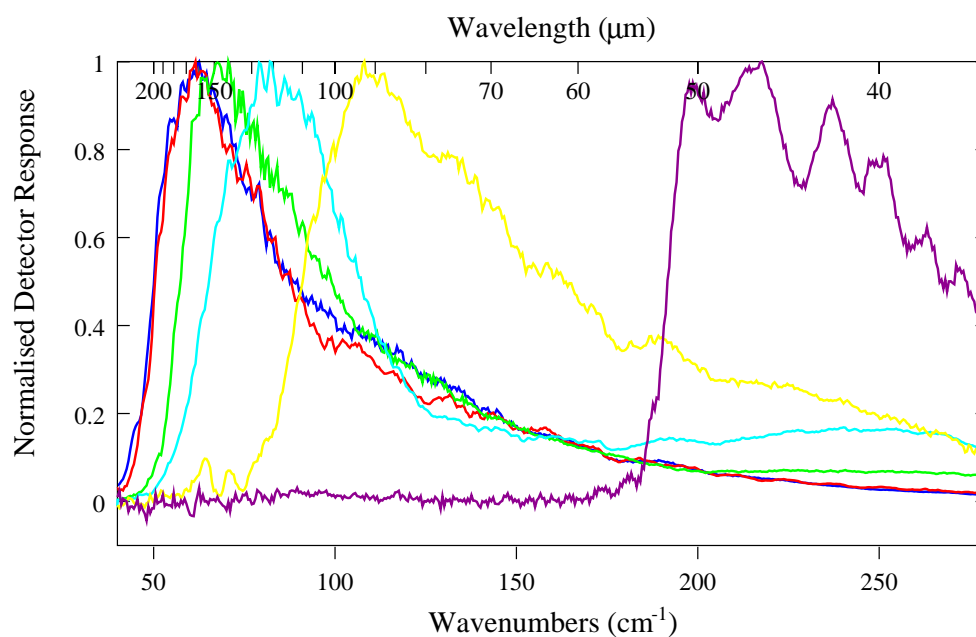


Figure 2.7: *The LWS flight model detector responses measured by Ade (private communication). LW5 is shown by the blue curve, LW4 red, LW3 green, LW2 cyan, SW2–LW1 yellow and SW1 magenta.*

The central panel in Figure 2.5 shows the nominal wavelength range covered by SW4, as determined by its filter. When the grating was in its rest position, the central wavelength falling on this detector was  $75\ \mu\text{m}$ . With the grating at an angle of  $-1.36^\circ$  its spectral response function (red) fell at  $73.5\ \mu\text{m}$ . The lower panel shows the range of the wavelengths that fell on the detector at this angle, as given by the grating spectral element (red).

Table 2.1: *Theoretical and measured LWS detector aperture sizes in the dispersion direction, Y, and the non-dispersion direction, X. Also the serial numbers of the detectors, bandpass filters and edge filters used on the LWS are listed.*

Det	Y		X		Detector	Bandpass	Edge Filter
	Measured	Design	Measured	Design	Serial	Filter Serial	Serial
	$[\mu\text{m}]$	$[\mu\text{m}]$	$[\text{mm}]$	$[\text{mm}]$	Number	Number	Number
SW1	494	500	1.34	1.29	7	325	8
SW2	529	530	1.32	1.29	9	321	50
SW3	529	540	1.30	1.29	13	319	6
SW4	617	610	1.34	1.29	11	313	12
SW5	640	650	1.35	1.29	12	309	9
LW1	580	570	1.34	1.29	10	306	2
LW2	617	620	1.35	1.29	55	302	1
LW3	652	650	1.34	1.29	56	328	5
LW4	700	690	1.32	1.29	58	296	4
LW5	758	750	1.30	1.29	57	292	3

The re-imaged size of the beam,  $W$ , at the detector array was determined by the focal ratios of the collimator ( $f_{col} = 15$ ) and the condenser ( $f_{con} = 1.5$  in the dispersion direction and  $f_{con} = 3$  in the non-dispersion direction as dictated by the anamorphic magnification, see below) and the size of the focal plane aperture, M2 ( $d$ ) such that:

$$W = d \frac{f_{con}}{f_{col}} \quad (2.1)$$

This gives a theoretical aperture size in the non-dispersion direction — which is the same for all detectors and for all grating angles — of 0.93 mm. These were set to be larger than this,  $\sim 1.30$  mm, to allow for diffraction and detector misalignment.

Equation 2.1 gives the aperture size in the dispersion direction to be 0.465 mm. However, there is a modification of the beam cross-section which is referred to as anamorphic magnification (AMAG; the ratio of the diameter in the non-dispersion direction to that in the dispersion direction). It occurred because the radiation was not specularly reflected with respect to the plane of the grating, hence the emergent beam was elliptical. (The incident beam was circular and it made an elliptical footprint on the grating, but this was due to purely geometrical effects.) This AMAG reduced the image size such that a detector aperture of 0.7 mm was actually required for the dispersion direction.

AMAG was smallest for the most positive scan angles (long wavelength end) of each detector range, so to ensure good efficiency the positive scan angle limit was used to determine the beam size and consequently the aperture size for each detector in the dispersion direction. The final measured and designed aperture sizes for the detectors are given in Table 2.1 along with the serial numbers of the actual detectors, bandpass filters and edge filters that flew on ISO.

For the LWS the AMAG is typically equal to two. As the parallel beam had a width of 34 mm, the beam was typically dispersed over 68 mm. The grating was ruled with 7.9 lines per mm, hence the number

of lines covered by the beam in the dispersion direction was  $\sim 540$ . For the above configuration, the chromatic resolving power ( $mN$ , where  $m$  is the order and  $N$  is the number of lines) is  $\sim 1080$  in second order and  $\sim 540$  in first. However, in reality the chromatic resolution depends on the detector location (as different detectors view the grating at different angles) and also on the scan angle of the grating. The LWS beam size is wavelength dependent. An effective aperture radius for each detector has been defined by Lloyd 2000, [27] (see Section 5.9) and is listed in Table 5.9.

This array was therefore capable of simultaneously detecting ten spectral elements within the LWS spectral region. However, the packing density of the detectors was sparse (limited by the size of the detector mounts), so to get complete spectral coverage the grating had to be scanned to move the wavelengths sequentially across each detector. By having ten detectors rather than one, the whole spectrum could be obtained in a tenth of the time. Because of the wide spectral coverage of the LWS, it was necessary to use the grating in first order for wavelengths from  $94.6\text{--}196.9\ \mu\text{m}$  and second order for wavelengths  $43\text{--}94.6\ \mu\text{m}$ , to maximise its efficiency. The grating efficiency measurements, as performed by Petti 1989, [31], are shown in Figure 2.8. Because of the two orders used in the LWS, it was necessary to interleave the long wavelength detectors between the short wavelength detectors to make optimum use of the limited space available whilst maintaining the maximum spectral range. Accordingly, the detectors are labelled SW1 through SW5 for the short wavelength set and LW1 to LW5 for the long wavelength set. The detectors in their different positions saw the grating at different angles. The diffracted beam for detector SW1 emerged at an angle of  $+7.9^\circ$  with respect to the grating normal, as shown in the top part of Figure 2.4. A simplistic way to determine where the detectors were located in the LWS is to refer to the angle between the incident beam and the direction of the detector from the grating, as tabulated in Table 2.2.

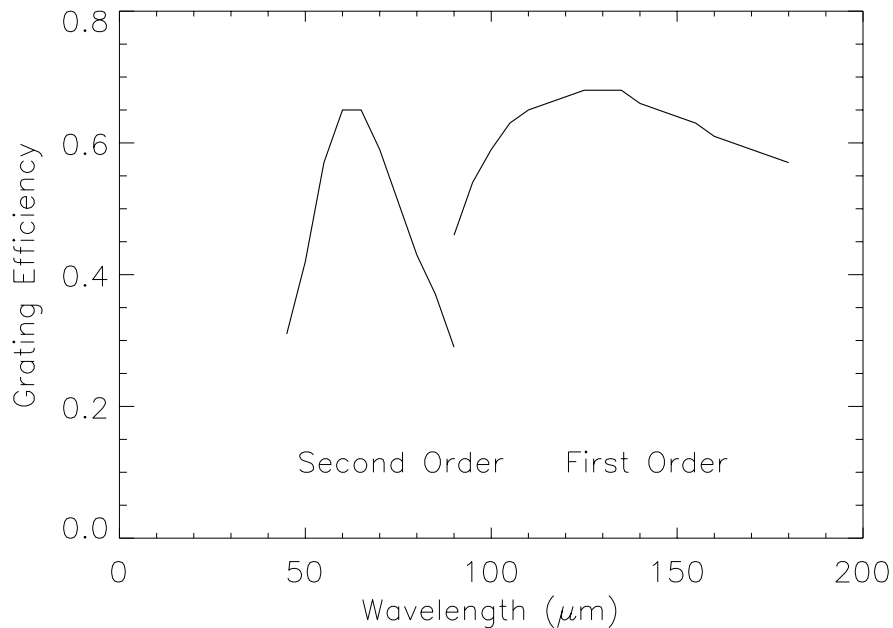


Figure 2.8: *The efficiency of the LWS grating.*

Table 2.2: *The angles (ground and in orbit) between the incident beam on the grating and the detectors (these angles are shown in Figure 2.4 for SW1 and LW5) and the corresponding wavelengths for the grating in the nominal position.*

Detector	Detector Angles [°]		Wavelength [μm]	
	Ground	In Orbit	Ground	In Orbit
SW1	67.938	67.80	46.0711	46.2220
LW1	63.411	63.26	102.092	102.425
SW2	58.889	58.74	56.0389	56.2033
LW2	54.370	54.29	122.042	122.218
SW3	49.885	49.71	65.9272	66.1173
LW3	45.340	45.27	141.659	141.809
SW4	40.825	40.73	75.6000	75.6989
LW4	36.308	36.275	160.487	160.554
SW5	31.785	31.72	84.7346	84.7977
LW5	27.256	27.32	178.090	177.971

## 2.5 The Fabry-Pérot Spectrometers

The resolving power for the grating-only mode was typically  $\sim 200$ . To enhance this, Fabry-Pérot (FP) etalons were used to further select only a narrow portion of the spectrum within the grating passband. Although inherently capable of very high resolving power ( $10^4 - 10^5$ ) the FP interferometers, as used in ISO, were limited by the grating performance (see Figure 2.5) and by the ohmic losses in the FP plates, as discussed below.

An FP consists of two parallel partially reflecting plates between which multiple reflection occurs, creating constructive interference for the transmitted beam.

The construction of the Fabry-Pérot etalons is shown in Figure 2.9. The Moving Plate is suspended on Leaf-Springs between the Back Plate and the Fixed Plate. Each corner of the moving plate carries a loudspeaker-like Drive Coil which operates in a gap surrounding a permanent magnet in the Back Plate. The position of each corner, relative to the Fixed Plate, is determined by measuring the charge on the Capacitance Micrometer, formed by pads on the Moving and Fixed Plates. The position of each corner is controlled by a servo-mechanism which supplies sufficient current to the Drive Coil to make the measured charge equal to a control value. Initially, the two plates of the etalon are made parallel by applying offset signals to two of the three drive circuits. The moving etalon is then scanned as a whole by applying the same additional driving signal to all three coils.

The fixed and moving plates carry the reflecting elements, made of free-standing nickel meshes supplied by Heidenhain: these meshes are affixed to the Mesh-Mounting Frames which are attached to the plates. The meshes consist of a rectangular grid of rectangular section: the thickness of the meshes is  $3\ \mu\text{m}$ , the width of the ‘bars’ of which the meshes are composed is  $6\ \mu\text{m}$ , and the periods of the grid are  $19\ \mu\text{m}$  for the long wavelength Fabry-Pérot and  $15.5\ \mu\text{m}$  for the short wavelength Fabry-Pérot. The narrow tolerance allowed on these dimensions is critical to the performance of the instrument.

For monochromatic input, the transmitted intensity,  $T_r(\lambda, d)$ , has a series of maxima dependent on the wavelength,  $\lambda$ , and plate separation,  $d$ , as prescribed by the function (Born & Wolf 1970, [1]):

$$T_r(\lambda, d) = \frac{\mathcal{T}^2}{(1 - \mathcal{R})^2 + 4\mathcal{R}^2 \sin^2(\delta/2)}, \quad (2.2)$$

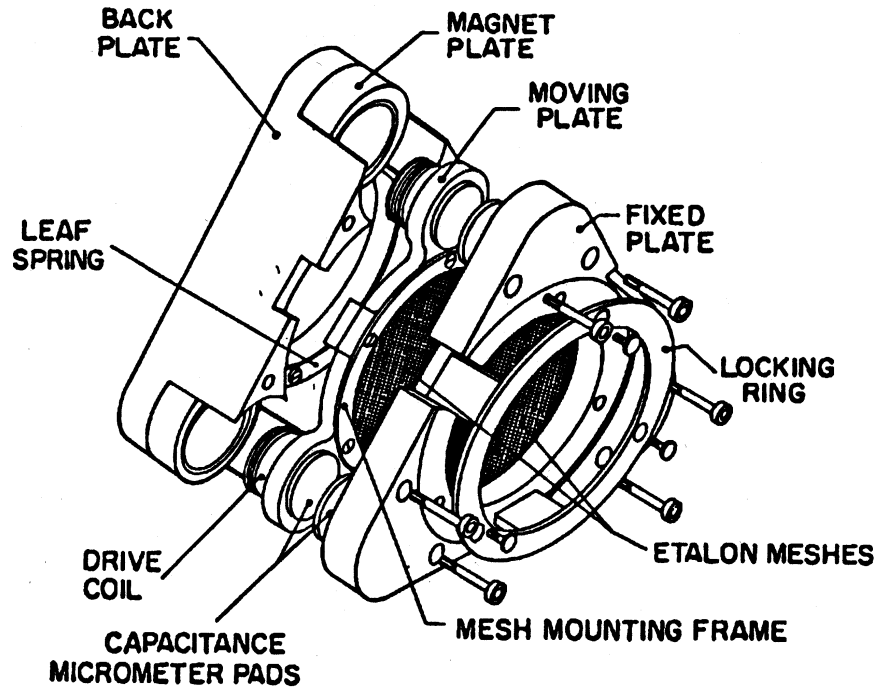


Figure 2.9: *The construction of a Fabry-Pérot etalon.*

where  $\delta$  is the phase difference between adjacent transmitted rays and  $\mathcal{R}$  and  $\mathcal{T}$  are the single plate reflected and transmitted intensities respectively. This can be simplified by defining the parameter  $F$  such that:

$$F = \frac{4\mathcal{R}}{(1 - \mathcal{R})^2}, \quad (2.3)$$

giving:

$$T_r(\lambda, d) = \frac{\mathcal{T}^2}{(1 - \mathcal{R})^2} \frac{1}{(1 + F \sin^2(\frac{\delta}{2}))} \quad (2.4)$$

To take into account the intensity absorbed by the plates,  $\mathcal{A}$ , we apply:

$$\mathcal{R} + \mathcal{T} + \mathcal{A} = 1 \quad (2.5)$$

Now using Equation 2.5 in Equation 6.2 and rearranging we have:

$$T_r(\lambda, d) = \left(1 - \frac{\mathcal{A}}{(1 - \mathcal{R})}\right)^2 \left(\frac{1}{1 + F \sin^2(\frac{\delta}{2})}\right), \quad (2.6)$$

where the first term on the right hand side expresses the wavelength dependent FP efficiency and the second factor is called the Airy Function.

The sharpness of the fringes is given by the Full Width Half Maximum (FWHM). A useful parameter to use is the reflective finesse,  $\mathcal{F}$ , which is the ratio of the separation of successive orders divided by the

FWHM of the transmitted peaks. Using this definition and writing the phase difference of the  $m^{\text{th}}$  peak as  $\delta = 2m\pi \pm \frac{\epsilon}{2}$  where  $\epsilon$  is the phase shift from the line peak to its half power point, we see that:

$$\mathcal{F} = \frac{\pi\sqrt{F}}{2} = \frac{\pi\sqrt{\mathcal{R}}}{1-\mathcal{R}} \quad (2.7)$$

For a high resolving power, a finesse as large as possible was required. However, measurements by Davis et al. 1995, [12] indicate that the plate absorption was  $\sim 1\%$ . As can be seen from Figure 2.10, for a 1% absorption and 97% reflectance (which corresponds to a finesse of 100), the transmission is 44%. Increasing the reflectivity to 98% increases the resolving power but decreases the transmission to 25%. For 99% reflectivity (and 1% absorption) the finesse is very high, 312, however there is very little transmission.

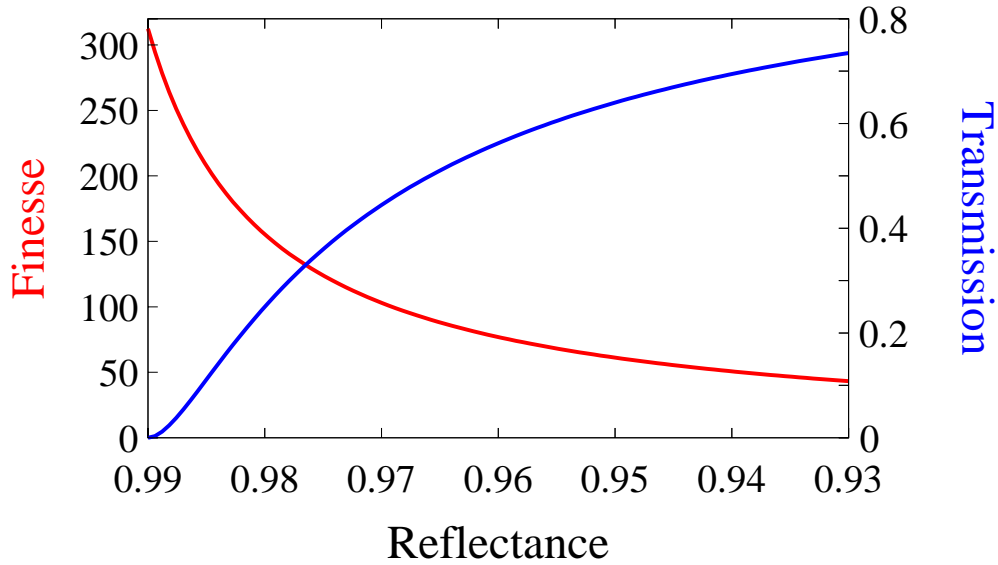


Figure 2.10: *FP finesse (red) and transmission (blue) as a function of reflectance for an absorption of 1%.*

With metal mesh reflection plates, the reflectivity is wavelength dependent (Davis et al. 1995, [12]). Typically the reflectivity changes from about 0.96 to 0.98 for a frequency change of a factor of two. It is therefore impossible to cover the whole LWS range with both high finesse and good transmission. For this reason two FPs were used in the LWS: The Short wavelength FP (FPS) to cover the wavelength range of 47–70  $\mu\text{m}$  and the Long wavelength FP (FPL) for the range 70–196.6  $\mu\text{m}$ .

In wavenumber space, evenly separated peaks are produced by an FP. To avoid spectral contamination it was required that when a particular order is scanned across the grating response function of width  $\Delta\sigma$ , by varying the plate separation,  $d$ , no other FP orders would overlap with it (shown at the bottom of Figure 2.5). So for orders separated by  $\Delta\sigma$  wavenumbers it is required that the distance between the two meshes is:

$$d \leq \frac{1}{2\Delta\sigma} \quad (2.8)$$

Since the grating resolving power is constant in wavelength terms, the criterion for setting the FP gaps ( $d$ ) needs to be determined for the shortest wavelength observed. The wavelengths of 45  $\mu\text{m}$  ( $222\text{ cm}^{-1}$ )

and  $90\ \mu\text{m}$  ( $111\ \text{cm}^{-1}$ ) were used<sup>1</sup> for FPS and FPL, respectively. The spectral resolution of the grating in wavenumber units is  $2\ \text{cm}^{-1}$  and  $1\ \text{cm}^{-1}$  respectively at the short wavelength extremes of FPS and FPL. This results in a basic mesh separation of  $2.7\ \text{mm}$  for FPS and  $5.0\ \text{mm}$  for FPL from Equation 2.8. The actual motion required to scan the whole LWS range using the ten detectors was reduced to a small interval of  $\sim d/n$ , the displacement required to move the  $n^{\text{th}}$  peak to the  $(n+1)^{\text{th}}$  peak. For the LWS this was at most  $\sim 35\ \mu\text{m}$  for FPS and  $\sim 100\ \mu\text{m}$  for FPL.

The order of radiation at wavelength  $\lambda_1$  is found from  $d = \frac{n\lambda_1}{2}$ , so that:

$$n = \frac{2d}{\lambda_1}, \quad (2.9)$$

hence at their shortest operational wavelengths FPS was used in the  $120^{\text{th}}$  and FPL in  $111^{\text{th}}$  order. At their longest wavelengths they worked in orders 77 and 50 for FPS and FPL respectively. This gave a range in resolving power for the FP of  $\sim 5000$  to  $12000$ .

Other factors can limit the resolving power of an FP, such as the Jacquinot criterion (a limit induced by imperfect collimation), flatness criterion (limited by imperfect flatness of the plates) and even non-parallelism between the plates. All of these factors were made to be small, compared to the basic wire grid limitations discussed above.

The bottom panel of Figure 2.5 shows the expanded range for one particular grating setting for SW4 with the FPS in the beam. With the grating at an angle of  $-1.36^\circ$ , radiation of a wavelength  $73.5\ \mu\text{m}$  falls on SW4. The Fabry-Pérot etalons could be scanned such that any spectral region within the grating bandwidth can be selected without contamination from higher or lower FP orders. A high resolution scan therefore required that the grating was stepped across the range of SW4 and within each step the FP was scanned across the grating spectral band. High resolution observations of the first order wavelengths were made in the same way, but using FPL with detectors LW1–5.

In this mode it was only possible in principle to use the output from one detector at a time, since it would be unlikely that the FP position and the grating position would be correct for any of the other four detectors in the FPS range<sup>2</sup>. It is therefore apparent that the LWS was very efficient when recording medium spectral resolution with the grating, but inefficient when observing the whole spectrum at high resolution. Indeed, for line work using the Fabry-Pérots, most scans were performed just around the known lines, which were evident from the grating spectra.

## 2.6 The LWS Detectors

The LWS used photoconductive detectors which could provide background photon noise limited sensitivities when operated at the available temperatures in ISO. An understanding of the operation of these devices is important as any non-ideal characteristics will affect the data interpretation.

In a semiconductor at very low temperatures, the electrons fill the valence band. If the energy of a photon (wavelength  $\lambda$ ) incident on a photoconductor is greater than or equal to the energy gap ( $\Delta E_g$ ) between the valence band and the acceptor states, then an electron can be promoted to the acceptor states (and thus a hole is available for conductivity). Hence for an electron to be excited:

$$\frac{hc}{\lambda} \geq \Delta E_g, \quad (2.10)$$

where  $h$  is Planck's constant and  $c$  is the speed of light. If the photon's energy is not as large as the energy gap then the photon cannot be absorbed; the material is transparent. This produces a limit on the longest wavelength detectable.

<sup>1</sup>In the planning stages of the FPs they were designed to be used such that FPS covered the grating second order wavelengths and FPL the first order.

<sup>2</sup>It is however possible to recover this non-prime data, which proves useful sometimes for high flux data.

By applying an electric field across a small cuboid of photoconductive material the conduction electrons will move towards the positive potential thus creating a small current in the external circuit. By measuring this current the number of photons falling on the detector can be determined. In an intrinsic semiconductor, electrons are excited from the valence band to the conduction band. Doping a semiconductor produces smaller energy gaps in the detector and hence the wavelength range of the detector can be extended. Doped semiconductors are extrinsic and come in two types,  $n$  and  $p$ . In  $n$  type semiconductors, a substituted impurity atom in the lattice structure donates an electron which is loosely bound to this positive impurity centre. For a uniformly doped device we therefore get energy levels just below the conduction band, called donor impurity levels. Bound electrons in these levels are promoted to the conduction band by the absorption of an appropriate long wavelength infrared (IR) photon because of the now much reduced band gap. For  $p$  type semiconductors, the substituted impurity atom accepts an electron, thus effectively creating a hole loosely bound to the negative impurity centre. This creates energy levels just above the valence band called acceptor states. When an IR photon is absorbed, an electron from the valence band is promoted into this acceptor level but is still bound. This however leaves a free positive hole in the valence band which will, with the aid of an electric field across the detector, migrate towards the negative potential and thus produce a current. A good description of the physics and range of available photodetectors is given by Bratt 1977, [2]. The LWS photoconductors are all  $p$  type. The long wavelength cut-off, as indicated in Equation 2.10, for Germanium doped with Gallium (Ge:Ga) detectors is at  $115\ \mu\text{m}$ . Until recently, Ge:Ga photodetectors represented the longest wavelength sensitive photodetectors available. However, it was found that by putting the detector under mechanical uniaxial stress the band gap could be effectively decreased, affording detection out to just beyond  $200\ \mu\text{m}$  (see for example Wang et al. 1987, [45]). Hence, the four longest wavelength channels in the LWS (LW2–LW5) are all stressed.

The LWS detector sub-system, shown in Figure 2.11, had three types of detectors: the shortest wavelength detector ( $43\text{--}50\ \mu\text{m}$ ), denoted SW1, was a germanium doped with beryllium detector, Ge:Be; detectors SW2, SW3, SW4, SW5 and LW1 were unstressed germanium doped with gallium, Ge:Ga(u), covering the total wavelength range of  $50\text{--}110\ \mu\text{m}$ ; the long wavelength detectors, LW2–5, encompassed the range of  $110\text{--}197\ \mu\text{m}$  and were stressed germanium doped with gallium, Ge:Ga(s). Figure 2.7 showed the spectral response of these detectors. SW1 had a bias voltage of 600 mV, SW2 had a bias of 200 mV. The other Ge:Ga(u) detectors had a bias voltage of 150 mV. LW2 and LW5 had the lowest bias voltages, at 40 mV, and the LW3 and LW4 values were 60 mV; this information is given in full in Table 2.3. Each detector was a 1 mm sided cube.

Table 2.3: *The ten detectors, their names, types, nominal wavelength ranges and bias voltages.*

Detector	Type	Wavelength Range [ $\mu\text{m}$ ]	In-orbit Bias Voltage [mV]
SW1	Ge:Be	43–50.5	600 (500 prior to rev.191)
SW2	Ge:Ga(u)	49.5–64	200 (150 prior to rev.191)
SW3	Ge:Ga(u)	57–70	150
SW4	Ge:Ga(u)	67–82	150
SW5	Ge:Ga(u)	76–93	150
LW1	Ge:Ga(u)	84–110	150
LW2	Ge:Ga(s)	103–128	40
LW3	Ge:Ga(s)	123–152	60
LW4	Ge:Ga(s)	142–171	60
LW5	Ge:Ga(s)	161–197	40

Table 2.4: Voltage values (in mV) corresponding to the various bias levels per detector type.

Detector type	Ge:Be (SW1)	Ge:Ga(u) (SW2-LW1)	Ge:Ga(s) (LW2-LW5)
Level			
0	0	0	0
1	250	50	25
2	400	100	40
3	500	150	60
4	600	200	70
5	700	250	80
	1000	300	
bias boost	2V	1V	0.2V
bias boost	3V	2V	0.4V

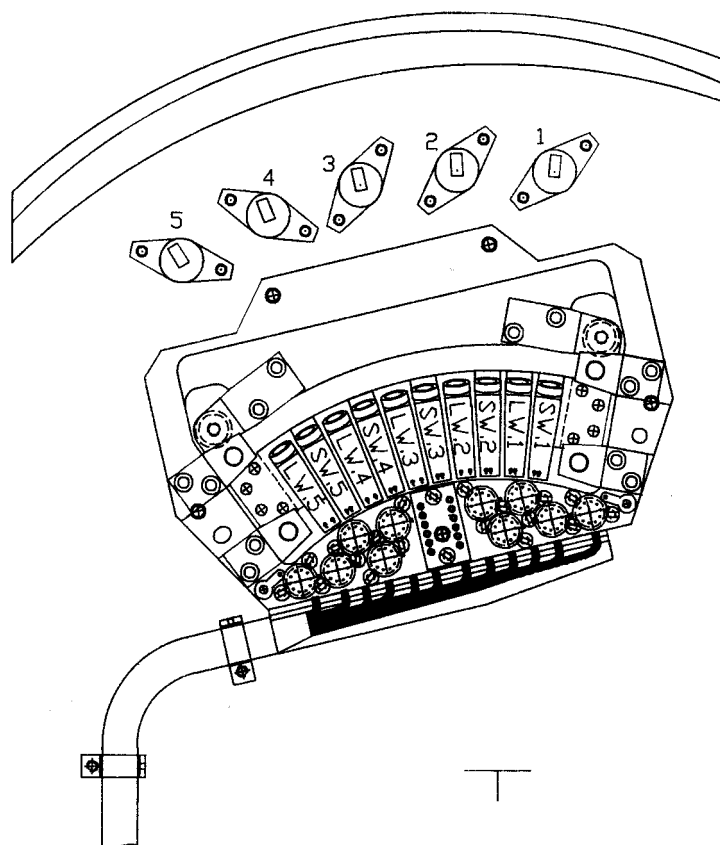


Figure 2.11: A schematic of the detectors and the illuminators.

Each detector was mounted in an integrating cavity to increase its absorption efficiency and is fed by a horn designed to couple efficiently with the radiation leaving the spherical mirror (8 of Figure 2.1).

The reduction in the energy band gap produced by a screw stressing the detectors, also makes them more sensitive to residual thermal energy, as the phonons can have enough energy to excite carriers into the acceptor states. This produces a larger dark current than in an unstressed detector. Under very low photon backgrounds, shot noise from this dark current limits the inherent sensitivity of these devices. The free carrier number density drops exponentially with temperature (the Boltzmann distribution is proportional to  $e^{-\Delta E/kT}$ ), so cooling the detectors below 3 K quickly reduces the number of thermally excited carriers and hence the dark current. It was found empirically (Church 1993, [8]) that by reducing the temperature of the stressed detectors to the lowest available temperature on board ISO, which was that of the helium tank at 1.8 K, the dark current could be reduced to an acceptable level. However, it was found that when the unstressed detectors were operated at temperatures less than 2.5 K the detectors would become unstable and spontaneously spike. This spiking increased in severity as the temperature was reduced to 1.8 K, making the detectors unusable (Church 1993, [8]). This spontaneous spiking phenomenon is thought (Teitsworth, Westervelt & Haller 1983, [43]; Teitsworth & Westervelt 1986, [42]) to be caused by trapped space charge near the injecting contact causing local electric field breakdown within the detector with a subsequent ‘avalanche’ of carriers. It is due to this spiking that the unstressed detectors (Ge:Be and Ge:Ga) are cooled only to 3.0 K, and not to 1.8 K as the stressed detectors, causing the mounting to be more complicated. At 3.0 K the detectors can be operated nearly as well as at 1.8 K because the dark current is only a factor of  $\sim 3$  higher (Church 1993, [8]). Operating the two types of detectors at different temperatures was achieved by mounting them on separate bars. The unstressed detectors were mounted on the upper bar, which accommodated a heater and a thermometer operating in a servo loop and it had a weak thermal link to the lower bar. The stressed detectors were attached to this lower bar, which was thermally shorted to the helium tank with a high-conductance copper strap.

### 2.6.1 LWS readout electronics (integrating amplifiers)

Each of the ten LWS detectors was read out by an integrating amplifier. This choice of readout was dictated by the very high impedance of the detectors under the ultra-low photon backgrounds experienced in flight, see Price 1993, [35] and Leeks 2000, [24] for more details. An integrating amplifier is, in principle, a resistor capacitor (RC) circuit. The readout circuit is shown in Figure 2.12. The voltage across the resistor in response to an input is given by:

$$V(t) = V_o \left[ 1 - e^{-t/RC} \right], \quad (2.11)$$

where  $V_o$  is the voltage supply,  $t$  the time of build up of the voltage  $V(t)$  on the capacitor,  $R$  is the resistance and  $C$  is the capacitance. For  $t \ll RC$  then, expanding the exponential to first order, Equation 2.11 becomes:

$$V(t) = \frac{It}{C} \quad (2.12)$$

and differentiating with respect to  $t$  gives:

$$\frac{dV}{dt} = \frac{I}{C}, \quad (2.13)$$

so by measuring the voltage build up in a known capacitor, the current  $I$  can be recovered. This is the essence of the Infrared Labs. JF4 integrating amplifier as used in the LWS.

For a photoconductor under low photon flux, the photon noise is negligible so the dominant noise processes are Generation-Recombination (GR) noise [rms noise current,  $i_{ngr} = (4eGI)^{1/2}$ ] and electron shot noise [rms noise current,  $i_{ns} = (2eI)^{1/2}$ ] for a post detection bandwidth of 1 Hz. Here  $I$  is the total current flowing in the detector circuit,  $e$  is the electronic charge and  $G$  is the photoconductive gain (see Bratt 1977, [2] for a detailed description). Since these two mechanisms are uncorrelated the total noise current is given by their quadratic sum:

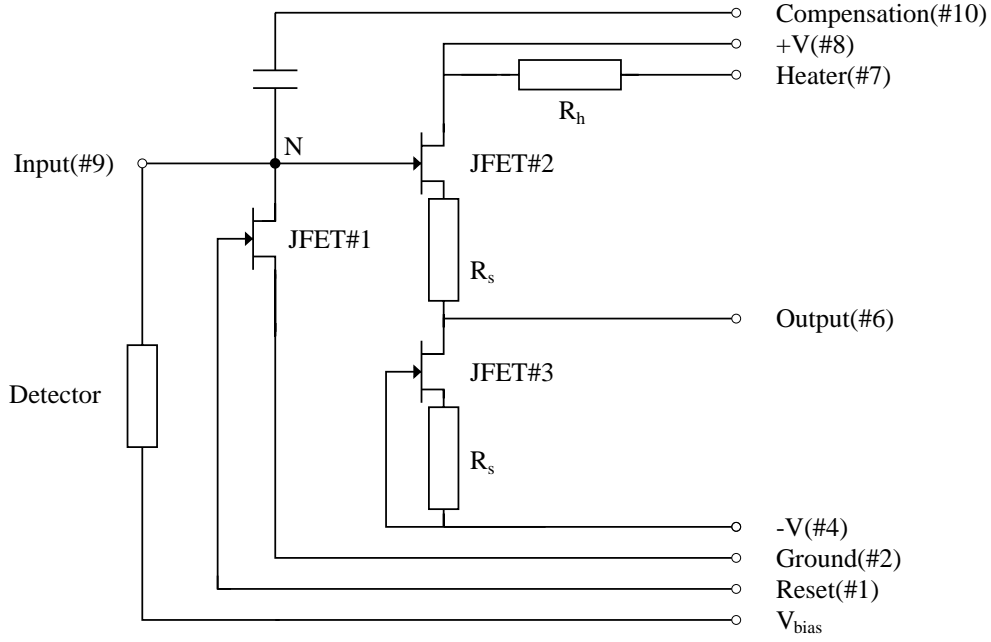


Figure 2.12: The integrating amplifier readout circuit for an LWS detector.  $R_s$  are source resistors for the JFETs and  $R_h$  is the heater resistor.  $N$  is the integrating node.

$$i_{ntot} = [2eI_d(1 + 2G)]^{1/2} \quad (2.14)$$

where  $I_d$  is known as the dark current (the current flowing in the absence of photons).

For the LWS the average photoconductive gain,  $G$ , is 0.66 (see Table 4 of Swinyard et al. 2000, [41] for the individual values of  $G$ ), giving  $i_{ntot} = 2.2 (eI_d)^{1/2}$ . The responsivity for the detector circuit,  $S$ , gives the current,  $I$ , which flows in the detector when illuminated by an infrared signal of power  $P$ , such that:

$$S = \frac{I}{P} = \frac{e\eta G\lambda}{hc} \quad (2.15)$$

where  $\eta$  is the Responsive Quantum Efficiency,  $h$  is Planck's constant,  $c$  is the speed of light and  $e$  is the charge on one electron. The NEP ( $i_{ntot}/S$ ) is then:

$$\text{NEP} = \frac{2.2 hc}{\eta G \lambda} \left( \frac{I_d}{e} \right)^{1/2} \quad (2.16)$$

Hence for dark currents of  $\sim 100$  electrons/s ( $I_d/e$ ) and an  $\eta G$  product of 0.1, an NEP of  $\sim 5 \cdot 10^{-19}$  W Hz $^{-1/2}$  at 100  $\mu\text{m}$  is achieved.

Note that the read noise of the integrating amplifier was measured to be  $\sim 10$  electrons regardless of the integration time, which is significantly less than the dark current.

The integration amplifier therefore gives a photon-noise-limited performance. It is like a trans-impedance amplifier but with an infinite feedback resistance so that there is no Johnson noise from the feedback resistor to limit the performance of the detector circuit. This made the integrating amplifier very suitable for the LWS.

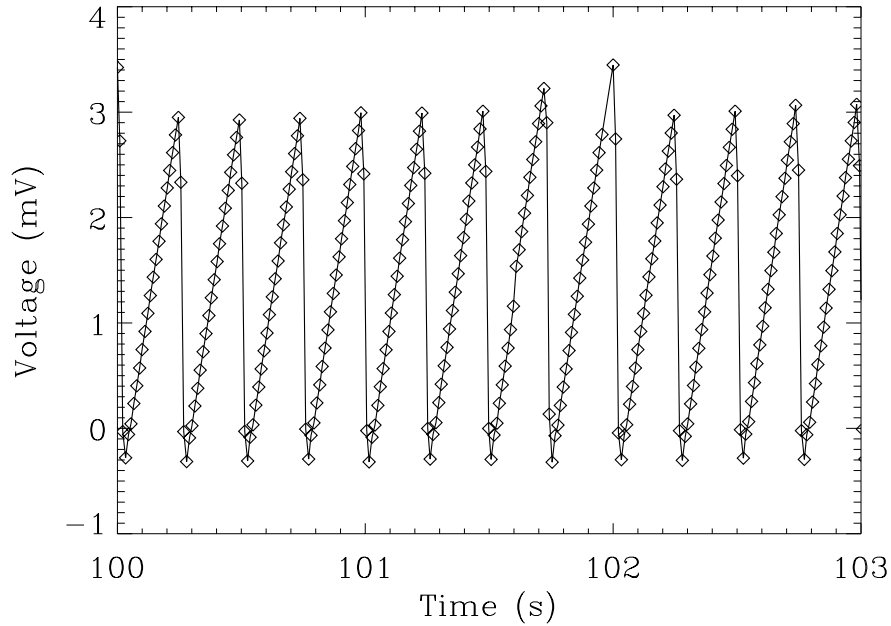


Figure 2.13: This figure shows 12 one quarter second ramps from an observation of W28 A2 on detector SW3. The data points are shown by the diamonds.

### 2.6.1.1 The ramps

The integrating amplifiers used typically had a gain of 0.9 and a capacitance of 7.5 pF. The photons incident at a detector produced a flow of charge which accumulated at the input capacitor. The voltage produced as this capacitor charges was non-destructively read out 88 times per second (sampled every 11.4 ms) through the JFET#2 (see Figure 2.12). After an appropriate time this capacitor was discharged by applying a reset pulse through reset JFET#1 at the gate of JFET#2 and also applying a compensation pulse which is adjusted to neutralise any residual charge left from the reset. After the reset the build up of voltage began again. JFET#3 balances out the offset voltage of JFET#1 so that the voltage at output #6 represents that measured at the gate of JFET#2 alone.

Two different integration times (0.5 s or 0.25 s) were available with the LWS; for strong signals the output was less noisy and more non-linear hence the shorter integration time was more suitable. Ideally, for very strong sources, the integration time would have been reduced even further. However, the *dead-time* (the time taken for the signal to settle down after a reset) was  $\sim 50$  ms and so reducing the integration time to less than 250 ms would have lowered the overall on-source efficiency and given very few data points in the ramps for statistical evaluation.

The resetting of the circuit produces a series of ‘ramps’, where one ramp was the voltage build up between two resets representing the signal collected during the interval. Figure 2.13 shows twelve such one quarter second ramps for SW3 (22 data points per ramp; half-second ramps have 44 points). One full grating spectrum has typically 2500 ramps. The build up of charge caused a drop in the effective bias voltage (this is called de-biasing) which in turn caused a change in the responsivity. This effect was quite large in strong sources and it produced a non-linear response to the input signal. Effectively for the same increase in input the output does not increase by as much so the ramps are curved.

The ramps represent the incoming photon flux from the astrophysical object observed and are converted

to photocurrents in the second stage of the automatic data processing (see Section 4.1).

### 2.6.2 Particle hits

ISO was subjected to particle hits, while in orbit about the Earth, from energetic protons and high energy electrons. The effect of these charged particle impacts on a detector is to generate electron hole pairs from which the intrinsically generated electrons neutralise the compensation donor impurities and thus increase the mobility and hence responsivity. For laboratory dosage of high energy gammas (60 keV,  $\sim 1000$  hits/s) it was possible to saturate the responsivity after  $\sim 100$  s, with typical observed responsivity changes between factors of 10 and 50. Clearly any gain change of the detectors needed to be carefully monitored if any sense was to be made of the astronomical data. The most dramatic effect of particle hits was when passing through the Van Allen belts.

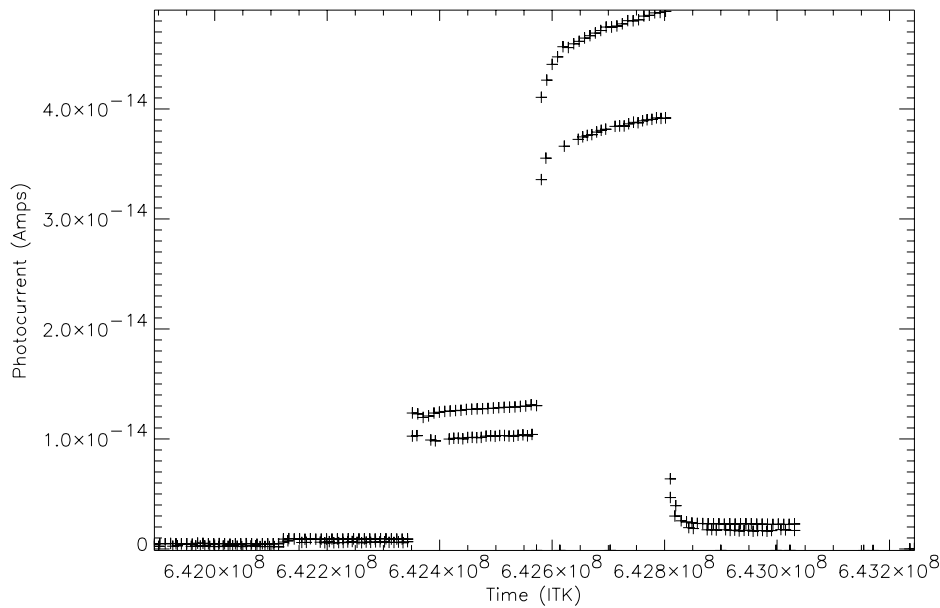


Figure 2.14: Photocurrents from SW<sub>4</sub> of an illuminator before (upper data) and after (lower) a bias boost.

The responsivity of the detectors increased due to the particle hits: to re-normalise the responsivity, the bias current was increased to beyond the breakdown voltage for each detector. This bias boosting causes impact ionisation of the neutral impurities and therefore largely restores the pre-irradiation values of donor and acceptor levels. Operationally, bias boosting was applied on exit from the Van Allen belts. Figure 2.14 shows the reduction of the responsivity of LW<sub>4</sub> after a second bias boost which was performed about half way through the 24 hour orbit. The data are from an illuminator flash before and after a bias boost half way through an orbit.

This boost was required to restore the responsivity of the detectors which also increased during the orbit as the satellite was constantly bombarded by galactic cosmic rays (H and He nuclei). However the dark currents were not affected by the cosmic rays, they remained constant during an orbit (Swinyard et al. 2000, [41]). These cosmic ray hits, about one every eight seconds, also caused the readout signal to jump (this is termed a glitch) as shown in Figure 2.15. It was found that a glitch changed the responsivity for the rest of that integration and the following ones, hence these data could not be used. The part of the integration before the glitch could, however, still be used to find the photocurrent caused by the

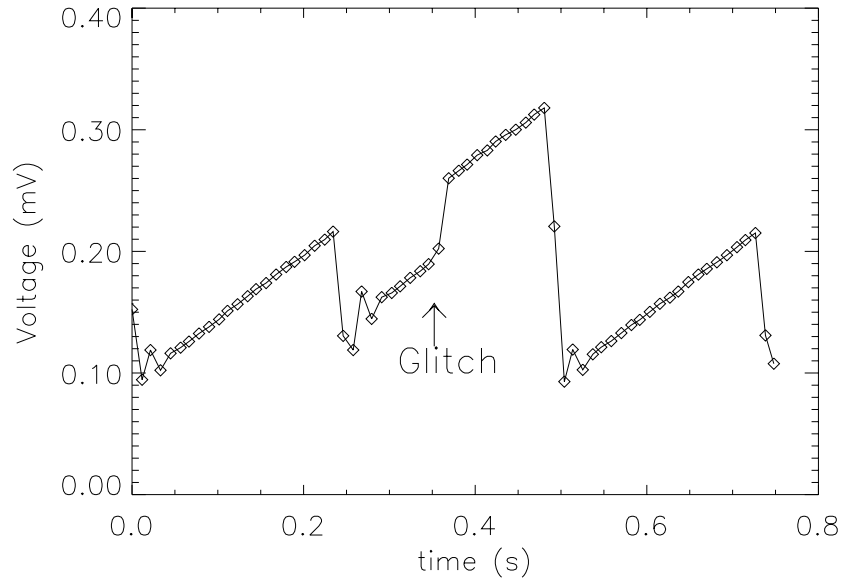


Figure 2.15: *Three moderate strength integration ramps are shown; the middle one shows a glitch.*

incident photons. The longer the individual integrations, the greater the number of resets required to recover from a glitch. To reduce the number of unusable integrations, and hence the amount of observing time wasted, the length of them was reduced, from the pre-flight specification of two seconds, to one half-second (one quarter-second for strong sources, see also Section 5.7). It was then found that only two integrations after the glitched one were affected and should not be used. This still presented the high possibility of there being no good data for a particular wavelength if they were collected consecutively, hence ‘fast scanning’ became the standard. This was where just one integration per wavelength interval was recorded and the grating was scanned to cover the required wavelength range, producing one ‘scan’. This was repeated to produce several scans which could be co-added.

The change in responsivity between the bias boosts was monitored by the use of IR illuminators. The five illuminators (labelled 1 to 5 in Figure 2.11), which are located in front of the detectors, output a known IR signal which is used to monitor the responsivity changes. The data of these illuminators are used to correct for the drift in responsivity with time during an orbit and an individual observation as discussed in Section 4.1.

## Chapter 3

# Instrument Modes and Observing Templates

### 3.1 Summary of the Observing Modes

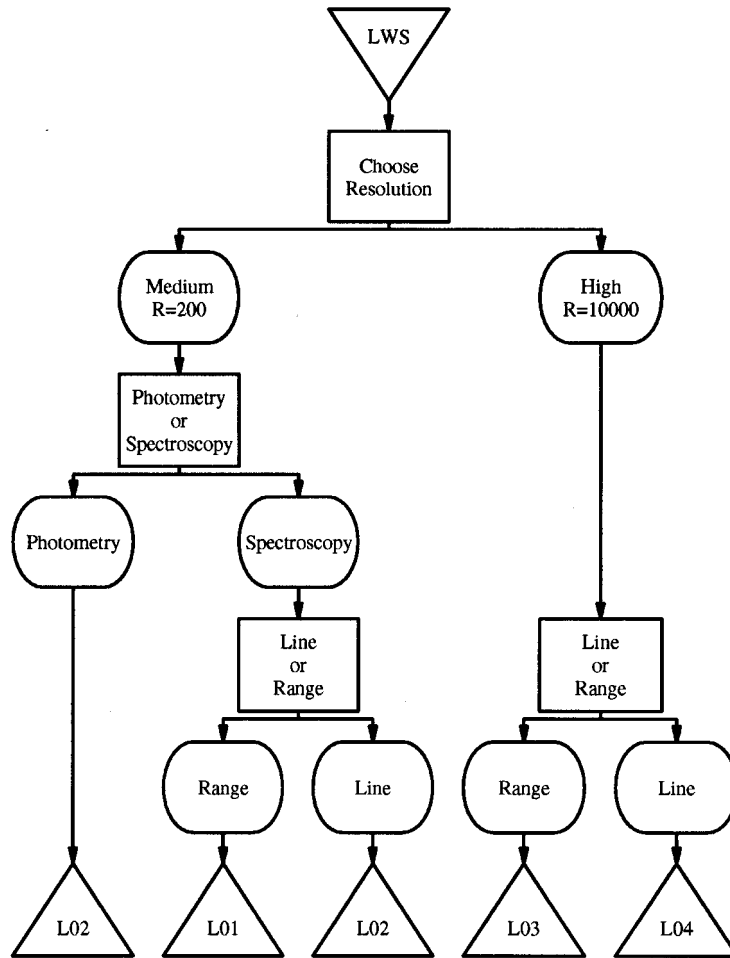
Four different observing modes were available to users, via the so-called ‘Astronomical Observation Templates’ (AOTs), which allowed to operate the instrument only in a few standardised ways, giving the observer the choice of the wavelength ranges, the sampling intervals, and the exposure times. These observing modes are described in Section 3.2 and summarised in Figure 3.1.

Two extra observing modes have been implemented later in the mission to systematically make use of the time when LWS was not the prime instrument: the parallel mode when another instrument was used and the serendipity mode when the satellite was slewing to another target. Unlike the four AOTs, these observing modes were not available to the users but were used in a systematic way.

Grating mode, in which only the grating was used, provided moderate spectral resolving power of about  $0.29 \mu\text{m}$  in the short-wavelength channels (SW1–SW5) and  $0.6 \mu\text{m}$  in the long-wavelength channels (LW1–LW3, LW5) corresponding to a resolving power of between 100 and 300 depending on the wavelengths being investigated. Because of the multiplexing described in Section 2.4, usable data were obtained from all ten detectors simultaneously. Whether or not these data are useful to the observer depends upon the range of wavelengths selected.

Fabry-Pérot mode, in which one of the two Fabry-Pérots was used in combination with the grating, provided high spectral resolving power between 8 000 and 10 000. Radiation in different orders of the Fabry-Pérot falls on detectors other than the prime detector (i.e. that selected for the wavelength of interest), and in some cases data from the non-prime detectors have proven quite useful although the grating position had not been set to have its peak transmission at the orders falling on these detectors. Automatic recovery of this non-prime detector data is foreseen.

In both grating and Fabry-Pérot modes, scans were carried out at one of two standard lengths of detector integration ramp, 0.25 s and 0.5 s. The total integration time per spectral point was then achieved by varying the number of these ramps. It was originally intended that spectra be scanned by carrying out a number of integrations at each setting of the grating or Fabry-Pérot until the total required integration time had been built up. In order to minimise the low-frequency end of  $1/f$  noise, a fast-scanning mode was also implemented, in which only one integration was performed at each position of the grating or Fabry-Pérot. The total integration time was then built up by repeatedly scanning. In fact during the mission this method has been recommended for all observations. Early observations have proven that in this way one could avoid that all integration ramps at one wavelength were affected by the same particle hit.

Figure 3.1: *Modes of the LWS.*

## 3.2 Description of the Observing Modes: the Astronomical Observation Templates (AOTs)

### 3.2.1 Medium-resolution wavelength range (AOT L01)

The medium-resolution wavelength range (L01) mode allowed for a grating range scan covering a wavelength range specified by the user up to the full range of 43–197 microns. The spectrum is composed of 10 sub-spectra with the sub-spectra being generated by the grating scanning over the 10 LWS detectors simultaneously. In practice this mode was almost always used for a range scan covering the entire LWS range. The spectral sampling allowed was 1, 1/2, 1/4 or 1/8 of a resolution element and the scanning speed was always such that only one ramp per sampling interval was taken, with signal-to-noise built up by taking more than one scan.

### 3.2.2 Medium-resolution line spectrum (AOT L02)

This Medium-Resolution Line Spectrum (L02) mode allowed for a grating range scan of up to  $\pm 7$  spectral elements around up to ten wavelengths specified by the observer. Data were recorded from all ten detectors while the specified ranges are being scanned. The observer had the choice of the spectral sampling interval, between 1, 1/2, 1/4 and 1/8 of a resolution element.

### 3.2.3 Narrow-band photometry (AOT L02)

This mode was produced by specifying zero-width scan in the medium-resolution line-spectrum AOT (L02). By consequence the grating was not scanned but remained at a fixed position. This produced an under-sampled medium-resolution spectrum by providing ten photometric points — one in each detector — at 46.2  $\mu\text{m}$ , 56.2  $\mu\text{m}$ , 66.1  $\mu\text{m}$ , 75.7  $\mu\text{m}$ , 84.8  $\mu\text{m}$ , 102.4  $\mu\text{m}$ , 141.8  $\mu\text{m}$ , 160.6  $\mu\text{m}$  and 178.0  $\mu\text{m}$ .

### 3.2.4 High-resolution wavelength range (AOT L03)

This AOT consisted in a Fabry-Pérot scan covering a wavelength range specified by the user, up to the full range of the LWS (46–196.7  $\mu\text{m}$ ). Although the wavelength range specified by the user covered only one detector, data were recorded for all detectors together. The observer had the choice of the spectral sampling interval, between 1, 1/2, 1/4 and 1/8 of a resolution element.

Note that as a full spectral scan with the Fabry-Pérot took a very long time, a significant part of the spectrum has been recorded at high resolution (with L03) only for four objects: Orion BN/KL, Sgr B2, Sgr A and Jupiter.

### 3.2.5 High-resolution line spectrum (AOT L04)

This AOT produced up to ten Fabry-Pérot scans over a small interval around wavelengths specified by the observer. For each line the grating is fixed, hence all the data resides within one grating element. Although the grating position was optimised only for the wavelength of the specified line and hence for only one detector at a time (the *prime* detector), data is recorded from all detectors. The observer had the choice of the spectral sampling interval, between 1, 1/2, 1/4 and 1/8 of a resolution element.

### 3.2.6 Parallel and serendipity modes

When another instrument was the prime instrument, the LWS operated in parallel mode and when no AOT was active the LWS operated in a serendipity mode. This mainly refers to those times when ISO was slewing. The actual configuration of the LWS instrument for the parallel and serendipity modes is identical. These modes were not used until revolution 237 and continued until the end of the ISO mission with a gap between revolutions 380 and 442 when LWS was switched off due to a problem with the interchange wheel.

While not observing as prime instrument, some of the data in the LWS housekeeping was not necessary and the LWS parallel and serendipity modes were implemented by replacing this data with detector signal values calculated on board. The space available provided for two values from each detector to be placed in each telemetry format every two seconds. For this reason the instrument was not scanning but was used in the Narrow-Band Photometry mode (see Section 3.2.3 and the detector integration time on board was adjusted to provide 1 s integrations in these modes rather than the 1/2 or 1/4 s used during prime observations.

### 3.3 History of AOT Changes throughout the Mission

The following lists — per revolution number, i.e. chronologically — the changes made to the AOT logic during the mission.

#### From revolution 49 (in the Performance-Verification phase)

1. New responsivities, taken from Saturn observations and SCP checkout observations, in the uplink tables.
2. Improved wavelength accuracy in the uplink tables.
3. The maximum commandable grating position increased from 3700 to 3740 as a result of performing the grating limits test in revolution 8.
4. The bias levels for the detectors were lowered by 1 (see Table 2.4). For LW2 the bias level was lowered by 2. The default HOLD mode sampling was set to 0.5 s ramps.
5. 4, 2 and 1 s ramps were not used any more (Grating AOTs). 1 s ramps were still available for use in FP observations.

#### From revolution 55

- The optimum offsets were set for the FPS parallelisation as determined from 2nd order data in revolutions 35 and 47. For FPL approximate offsets were given, based on results for first order measurements from revolutions 31 and 35.

#### From revolution 61

1. The maximum commandable grating position decreased from 3740 to 3700 as a result of performing tests of further data from grating scans.
2. Improved FP wavelength accuracy in the uplink tables.

#### From revolution 69

1. New responsivities, taken from Pallas observations, in the uplink tables.
2. New detector dark current, taken from Peter Clegg, in the uplink tables.
3. New power and noise levels, calculated by Matt Griffin, in the uplink tables. The NEPs were changed correspondingly.
4. Improved FPS wavelength accuracy in the uplink tables. FP scan range: 46.795–197.049  $\mu\text{m}$ .

#### From revolution 90

1. New noise levels, recalculated by Matt Griffin, in the uplink tables. The NEPs were changed correspondingly.
2. Mini-scan overlap increased to 5 spectral elements, Overlap between FPs raised to 1.8  $\mu\text{m}$ .
3. Maximum wavelength changed to 196.974  $\mu\text{m}$ .
4. 1 s ramps were not used any more in FP AOTs. So only 1/4 and 1/2 second ramps were allowed. The usage of 1/4 second ramps was inhibited for source strengths below 10000 Jy.

**From revolution 100**

- Closed flashes, which are needed for dark current subtraction and absolute response correction, were used instead of open illuminator flashes.

**From revolution 150**

1. FPS cut-off changed to 70  $\mu\text{m}$ .
2. Update of Cal-U file L-FPSCAN: Start and end FP offsets added for each microscan.

**From revolution 191**

1. Implementation of the new values for the responsivities of the SW1, SW2 and LW5 detectors.
2. Implementation of the new transmission profiles generated from Ceres and NGC 7027.
3. New detector dark current, taken from illuminator flashes, in the uplink tables.
4. Detector bias levels were set to (4, 4, 3, 3, 3, 3, 2, 3, 3, 2) for the sequence of detectors SW1–SW5 and LW1–LW5 (for the voltage values corresponding to these levels see Table 2.4)
5. New power and noise levels, recalculated by Matt Griffin, in the uplink tables.
6. Improved wavelength accuracy in the uplink tables.
7. L-FPSCAN: Correction of the wrong values of the offsets for the FPS microscan corresponding to the 93.225–93.616 interval plus change in the cut-off wavelength between FPS and FPL.
8. Maximum wavelength changed to 196.989  $\mu\text{m}$ .
9. Wrong interpolation in LWS FPL offsets corrected.

**From revolution 237**

1. Use of LWS serendipitous/parallel mode; the HOLD mode was set to use 1 s ramps so that the LWS parallel mode can operate correctly.
2. Changes to ensure a constant detector temperature throughout a revolution.

**From revolution 277**

1. L-FPSCAN: implementation of new micro scans lengths, with a maximum FPL offset change of 5 between two steps.
2. L-OPTIC: Correction of the wrong values of the grating mode relative transmission efficiency.
3. L-SETNGS: Increase of the scan width for the L04 AOTs (2 resolution elements added for both FPS & FPL).

**From revolution 336**

1. Illuminator flashes avoided during the middle of an observation.
2. Improved wavelength accuracy in the uplink tables for grating and FPL.

**From revolution 411**

1. New LWS illuminator flash scheme (Change ILL1LEVEL1 ... ILL5LEVEL2 to 180).

2. An increase of the time required to make the wheel movements.
3. The 1st illuminator flash leaves the wheel in the grating positions and now the 2nd illuminator flash must leave it in the opaque position.
4. Use of the FPL for the opaque configuration of grating AOTs.
5. LWS parallel mode stopped.

**From revolution 526**

- LWS parallel mode restored.

**From revolution 584**

- Improved wavelength accuracy in the uplink tables for revolution 349 onwards. This resulted in re-derived FP coefficients.

**From revolution 764**

- LWS parallel mode now also after 2nd illuminator flash of Ground Station Handover.

# Chapter 4

## Data Processing

### 4.1 Processing Overview

The ISO data for each instrument is processed automatically through a pipeline (Off-Line Processing software or OLP) consisting of three stages: Derive-ERD extracts the observation-relevant data from the telemetry stream; Derive-SPD processes the raw detector readouts into photocurrent and removes glitches due to particle impacts; Auto-Analysis performs the astronomical calibration of the data to produce a spectrum in flux units versus wavelength units.

The three separate stages were designed to allow observers to choose at which stage to start their own reduction. For the three scientifically validated LWS AOTs it is expected that the final Auto-Analysis Results (AAR) product is the starting point for reduction (see Section 8), but in some cases (see Chapter 6) an observer may wish to start with SPD data and process this to AAR through LWS interactive analysis (LIA – see Section 8.2.3).

The files produced at each stage of the data processing are listed and described in Chapter 7. A global overview of the three stages is given in Figure 4.1.

The ISO processing is an automated process where the end products (Edited Raw Data, Standard Processed Data and Auto-Analysis Results) are quality checked (see Section 4.2). The following is a brief overview of the three steps in the processing. The algorithms used in the last two steps (Derive-SPD and Auto-Analysis) are described in more detail in Sections 4.3 and 4.4.

**TDF first scan/Derive-ERD** The telemetry data from the satellite is transmitted to the Ground Station in blocks called ‘formats’, each format containing the data for a 2 second period. These data are stored in the Ground Segment as so-called Telemetry Distribution Files (TDFs). The TDFs contain the raw scientific data from the Prime Instrument and satellite and instrument housekeeping information for a complete revolution. They are, thus, the prime input for the ISO data processing system. The first step in the ISO processing for an observation is to extract from a TDF the raw data relevant to that observation. This is carried out in two stages:

- ‘TDF first scan’ reads the TDF (and other ancillary files) to create a set of pointers to relevant events in the observation, such as: the start and end of the observation, the start and end of LWS illuminator flashes, the start and end of mechanism (grating or FP) scans. This is stored in the ‘Compact Status History’ (LSTA) file.
- Using the Compact Status History, ‘Derive-ERD’ extracts the information for the observation into the set of Edited Raw Data (ERD) files for the observation. The data extracted includes the instrument science data, instrument housekeeping data and relevant satellite information (e.g housekeeping, pointing and orbital information). The ERD produced is a complete set of the data required to process an observation, but, as no conversion from engineering values has

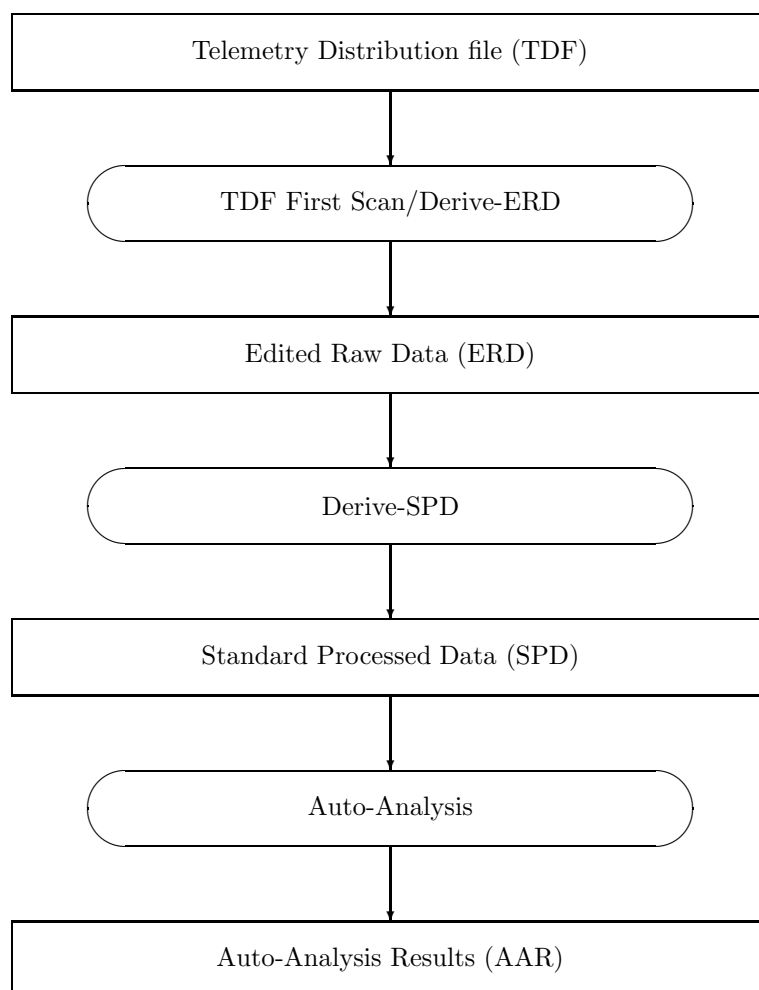


Figure 4.1: *Overview of the ISO data processing.*

been made, it requires a detailed knowledge of the instrument to process and is therefore not recommended as a starting point.

**Derive-SPD (SPL)** In the second stage of the ISO data processing most of the instrument specific peculiarities are removed and some basic calibrations are performed. In Figure 4.2 a schematic overview of the Derive-SPD process is given.

The output of this process (Standard Processed Data or SPD) contains only scientific data, still in engineering units (i.e. not wavelength or flux calibrated), and in chronological order. Derive-SPD processes a Target Dedicated Time (TDT) which can consist of more than one AOT. The individual data types (i.e. different AOTs or subsystems in the instrument) can be identified using

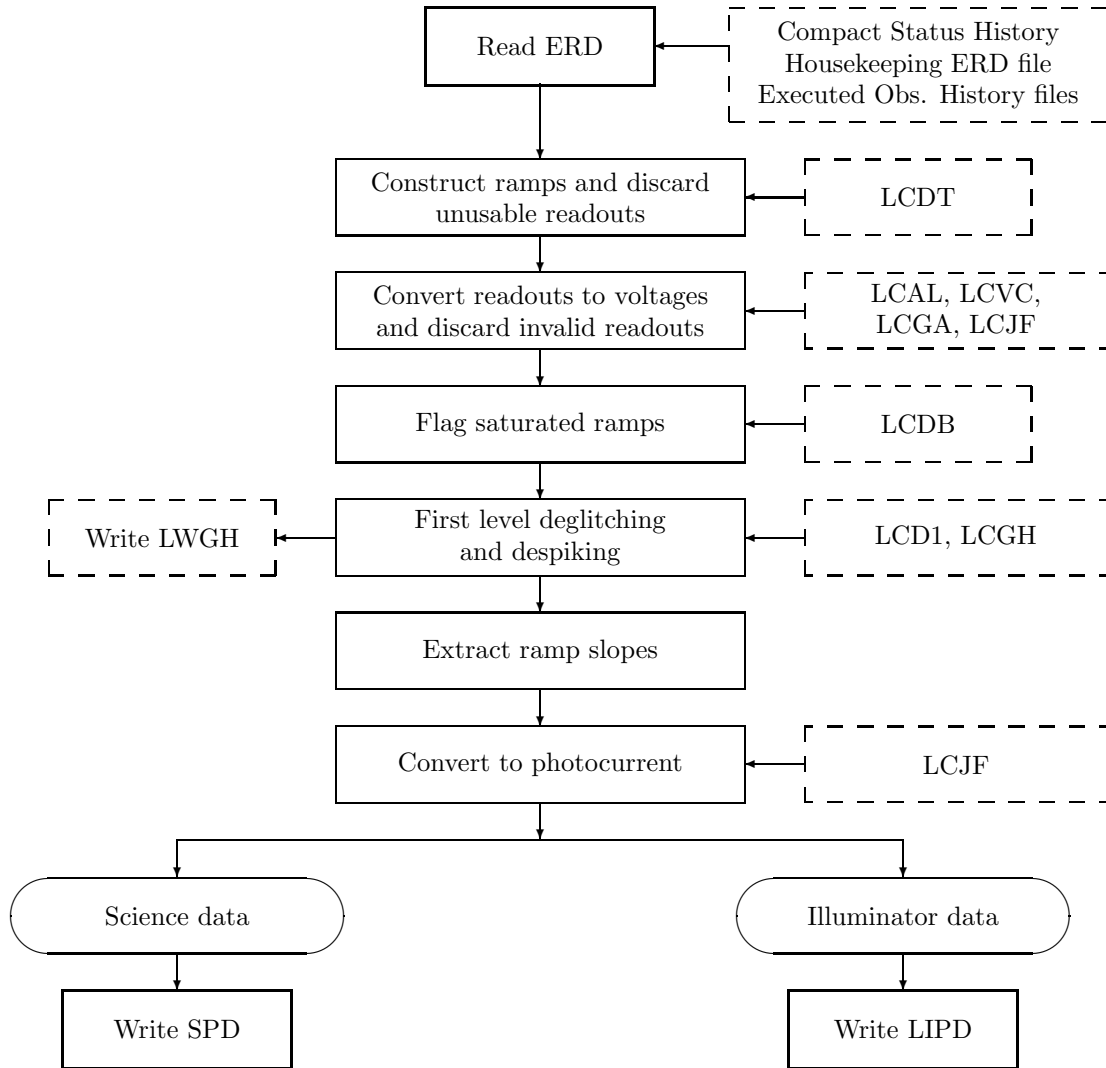


Figure 4.2: Schematic overview of Derive-SPD. The names in the dashed boxes indicate auxiliary or calibration files.

LWS Compact Status History. This file is produced by TDF first scan. Derive-SPD processes the raw detector readouts into photocurrent by fitting the raw data ramps. It also removes glitches due to particle impacts. Derive-SPD also processes the measurements of the internal illuminators into a calibration file that is used by Auto-Analysis.

**Auto-Analysis (AAL)** This final stage in the ISO processing performs all the astronomical calibrations of the data. The main output of this stage is the LSAN file, containing the flux and wavelength calibrated spectrum for a single AOT. The AAL process corrects for the spectral responsivity (absolute responsivity and responsivity drift), removes the dark current, performs the wavelength and the flux calibrations, including the correction for the spectral resolution element (or spectral bandwidth). Three new files are produced by Auto-Analysis.

A schematic overview of the Auto-Analysis process is given in Figure 4.3.

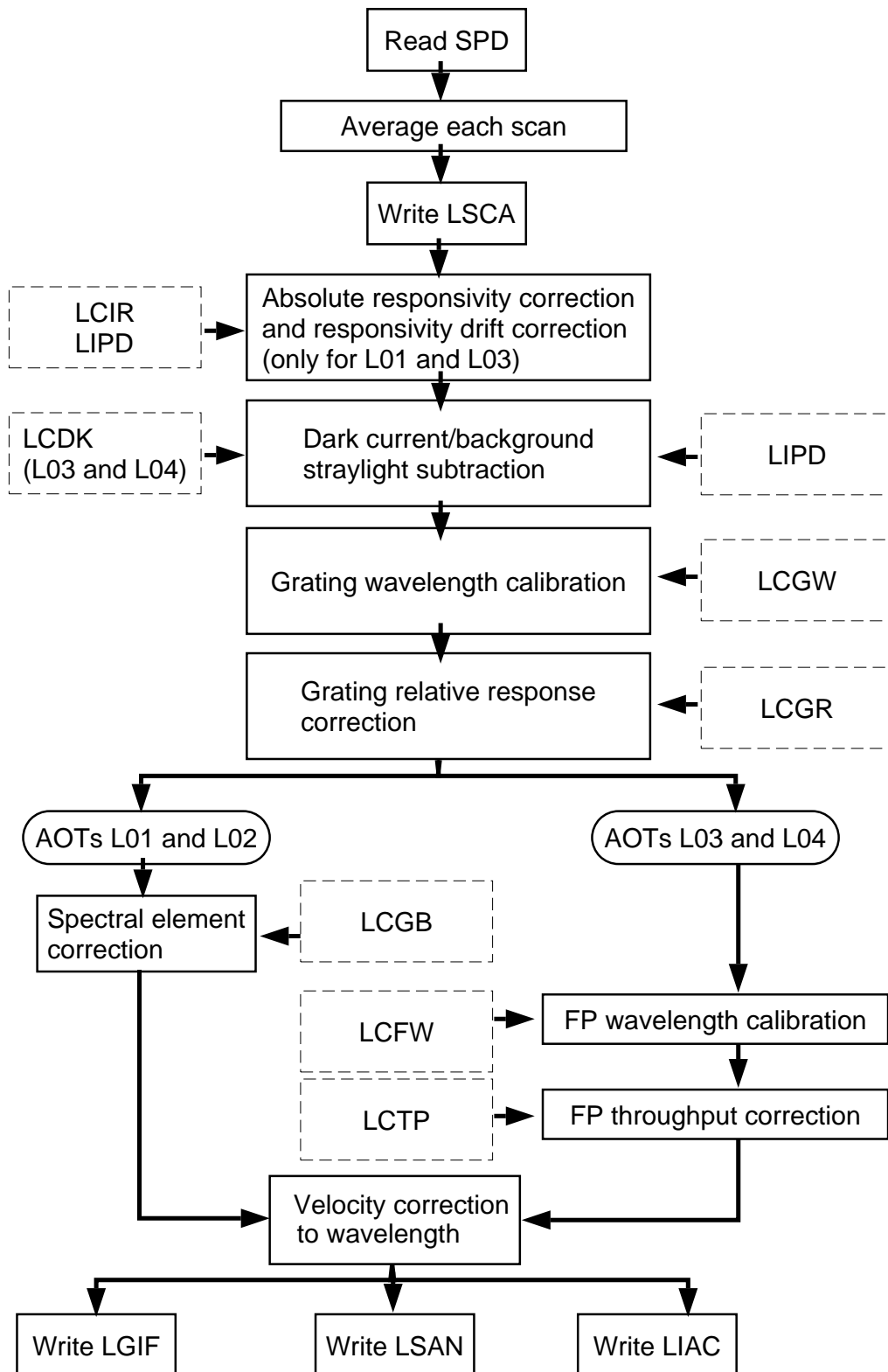


Figure 4.3: Overview of Auto-Analysis. The files in dashed boxes are the calibration files used by AA.

Auto-Analysis does not include:

- averaging of repeated spectral scans
- joining together of spectra on adjacent detectors
- generation of maps for raster scans
- subtraction of the local astronomical background
- correction for the effective aperture of an extended source

## 4.2 Quality Check of the Data

The LWS data products for AOTs L01, L02 and L04 have been Quality Checked. This was to ensure that no corrupted data is distributed. The quality check was performed at three levels.

**Level 1** Here the OLP operators checked the products of the processing for obvious errors like:

- Instrument failures or telemetry drops during the observation
- Absence of a spectrum
- A non-physical (i.e. negative) spectrum
- A flat spectrum (i.e. all values equal)

If an anomaly was detected at this level, it was passed to Level 2

**Level 2** Here the instrument team investigated whether the failure was due to an instrument failure, or a peculiar behaviour of the instrument and decided if the observation was still scientifically valid. If this was not the case the observation was passed to Level 3.

**Level 3** Here the astronomers in the ISO team investigate whether the observation needed to be rescheduled (when ISO was still in operation !), or whether the observation would most likely fail again (for instance due to very high backgrounds, or proximity to a very bright source).

The data observers got for the AOTs L01, L02 and L04 should therefore not contain any obvious errors (as listed above). For LWS the products of AOT L03 (FP wavelength range) have not been scientifically validated and have therefore not been Quality Checked.

## 4.3 Derive-SPD Processing Steps

### 4.3.1 Introduction

The inputs to Derive-SPD (SPL) are the Compact Status History file (LSTA), science ERD files, the housekeeping ERD file (LWHK), the executed observation history files (EOHI and EOHA), and various calibration files. The science ERD files consist of LGER for grating scan data, LLER for FPL scan data, LSER for FPS scan data, and LIER for illuminator flash data.

The outputs of SPL are the standard processed data file (LSPD), the illuminator processed data file (LIPD), and the Glitch History file (LWGH). The LWGH file is for information only, and is not used during any further processing steps.

SPL is driven by the contents of the Compact Status History file (CSH) for the selected observation. The LWS CSH file is named LSTA. The LSTA file identifies the regions of data taken in an observation with the grating, FP, or illuminator.

### 4.3.2 Construction of ramps and discarding unusable readouts

The first stage of SPL reads in all records from the currently open science ERD file that correspond to one ramp of data for all ten detectors. The LSTA file specifies which of the science ERD files the data is read from.

The start of a ramp is indicated by a detector readout which has its most significant bit set. The expected number of readouts per ramp is then read in from the housekeeping ERD file (LWHK).

The time key of each readout is checked as it is read in to identify any periods of missing data and to adjust the ramp contents appropriately.

After the ramp has been read in, some of the readouts have to be discarded for the following reasons:

- Readouts immediately following a reset pulse (the start of the ramp) are affected by the reset and must be discarded. The amount of data to discard for each detector is specified in the LCDT calibration file. It is currently 55 ms for each detector reset.
- The last point of each ramp is deleted. This is to equalise the length of all ramps, since the last ramp in each telemetry format is slightly longer than the other ramps.
- Any readouts taken while the grating or FP are still moving should also be discarded. The LCDT file also contains the values for these discard times. The discard time for grating movements is 70 ms and the discard time for the FP movement is 5 ms.

The number of points discarded for the above reasons are written as keywords into the header of the LSPD file (see Section 7.2.5 for details).

### 4.3.3 Conversion of readouts to voltages

Before the raw detector readouts are converted into voltages, any invalid points which are outside the valid range for the analogue amplification chain are discarded (see more explanations about this in Section 5.8). The valid range is specified in the LCAL calibration file. Note that this is NOT the same as the saturation of the detector, which is corrected later in the processing chain.

The number of readouts discarded for this reason are written as keywords into the header of the LSPD file. See Section 7.2.5.

For each raw detector readout (in digital units; DN), the conversion to voltages is performed using the formula:

$$V = \frac{A(D - D_{off})}{G_{gain,det}} \quad (4.1)$$

Where:

- $V$  is the detector voltage at the input to the JF4 amplifier in volts.
- $A$  is the readout to voltage conversion factor in volts per readout unit.
- $D$  is the detector readout value.
- $D_{off}$  is an offset to the detector readout value.

- $G_{gain, det}$  is the analogue amplifier gain factor for the current gain level and detector. The gain level is in the range 0–7. The level is stored in bits 12–14 of the detector word.

The values for  $A$  and  $D_{off}$  can be found in calibration file LCVC (see Section 7.3.1 for details). The gain for the analogue amplification chain is read from calibration file LCGA (see Section 7.3.1) using the gain level (0–7) read from the detector word.

Finally the voltage as derived using Equation 4.1 is divided by the gain factor of the JF4 for the appropriate detector to reconstruct the voltage at the input of the JF4's. The JF4 gain factor can be found in calibration file LCJF (see Section 7.3.1).

#### 4.3.4 Flag saturated ramps

In previous versions of the pipeline saturated points had to be removed at this stage. A saturated point is one where the voltage exceeds the threshold where the model of the detector behaviour breaks down. This model has now been replaced by the  $\Delta V/\Delta t$  method, as described in Section 5.5. It is therefore no longer necessary to throw away saturated points. However, it was thought desirable to continue to flag any ramps which contain saturated points. This stage therefore checks all of the points in the ramp and if one or more points exceed the saturation threshold then the ramp is flagged as saturated in the LSPD status word (see Section 7.2.6). The saturation thresholds can be found in the LCDB calibration file (see Section 7.3.1).

The number of saturated points and the number of ramps containing one or more saturated points are written into the header of the LSPD file (see Section 7.2.5).

#### 4.3.5 First level deglitching

##### 4.3.5.1 Introduction to glitches and spikes

Glitches are caused by the effects of cosmic ray particles on the detectors (see Section 2.6). There is roughly one glitch every ten seconds per detector during the normal period of LWS operation. These energetic particles cause a sudden jump in the ramp voltage, due to a quantity of charge being dumped on the integrating amplifier. They also cause a change in the detector responsivity which affects the following ramps.

‘Slow’ glitches are glitches where the jump in voltage covers more than one readout value.

In addition to these ‘positive’ glitches, ‘negative’ glitches have also been found. These cause a sudden decrease in the ramp voltage, rather than an increase. They are thought to be due to hits on the FET. Negative glitches do not appear to affect the detector responsivity.

Before launch it was anticipated that ‘spikes’ in the analogue amplification chain may also need to be located and removed. They cause a single detector readout to have a much larger value than normal. Subsequent readouts are unaffected and there is no effect on subsequent ramps. However, no real spikes were seen in the data when the satellite was in-orbit. The spike removal was switched off as all of the spikes detected were actually caused by the effects of glitches. A modified spike detection remained operational, but it would be more accurate to describe it as an ‘anomaly’ detector, rather than a spike detector. The anomalies which were detected could be caused by real spikes, but they are more likely undetected glitches, or the effects following glitches above mentioned.

Statistics related to glitches and spikes are written into the header of the LSPD file. See Section 7.2.5 for details.

##### 4.3.5.2 Detection method

The following list describes how glitches and spikes were detected. Note that glitch detection is only performed on the section of ramp after the discarding of data due to the reset pulse etc. Any glitches

which occur in this discarded section of a ramp are not currently detected.

1. Perform point-by-point differentiation. This consists of finding the gradient in volts per ITK unit (ITK is the unit of time, defined in Section 7.2.1) between each point and the following point, and each point and the point two places away.
2. The mean and standard deviation of the first set of differentiated points are then calculated. The two largest values from the set are excluded from these calculations. This excludes any large jumps which may be caused by glitches.
3. Each point in the two sets of differentials is checked and those more than N standard deviations away from the mean are flagged as outliers. It is also recorded whether the point is an outlier above or below the mean. The value of N is specified in the LCD1 calibration file.
4. The outliers are searched to find the patterns expected from glitches or spikes. This is described in more detail in the following section.

If a glitch is detected by this step then the next three points are not checked for glitches. This is because it has been found that the effects of a glitch often caused a second, false glitch, to be detected shortly afterwards.

No spikes detection is done for the remainder of a ramp following a glitch. This is because it has been found that the effects of glitches caused lots of false spikes to be detected.

5. The heights of any glitches and spikes detected are estimated. The height of a spike is estimated by subtracting the voltage of the previous point from the voltage of the spiked point. The expected voltage increment due to the ramp slope is then subtracted from this value.

There is a special case for the first point in the ramp, since there will be no previous point. In this case the spike height is obtained by subtracting the voltage of the point following the spike from the voltage of the spiked point. The expected voltage increment due to the ramp slope is then ADDED to this height.

The height of a glitch is estimated by finding the difference between the point at the glitch location and a point 3 places ahead. This is to cope with slow glitches, or glitches that have noise. If the second point is beyond the end of the ramp then the last point in the ramp is used.

The expected nominal ramp increment over the time period between these two points is calculated and subtracted from the glitch height.

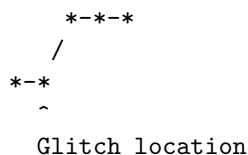
6. The heights are compared with the height of the ramp and any below a threshold height are rejected as described below. This is to reject genuine glitches and spikes which are insignificant with respect to the ramp. It also provides a method of rejecting spurious glitches and spikes.

For spikes the fractional height with respect to the height of the ramp is calculated. The height of the ramp is simply the voltage of the last point in the ramp minus the voltage of the first point in the ramp. Only those spikes with fractional heights above the threshold specified in the LCD1 calibration file are accepted.

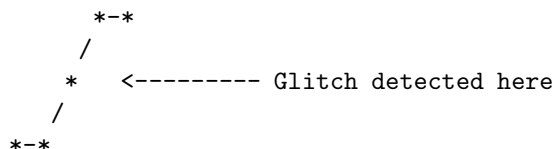
For glitches the same procedure is performed, except that the glitch height is also subtracted from the height of the ramp. This should give the height of the ramp as if no glitch has occurred. There is a separate threshold level specified in the LCD1 file for the fractional heights of glitches.

Note that these calculations have assumed that there is only one spike or glitch in the ramp.

Note that the ‘location’ of a glitch is understood to mean the point before the outlying point(s):



Using test data it has been found that ‘slow’ glitches are often detected only on the second point of the glitch:



In order to cope with this, the point at the glitch location is always discarded. For normal ‘fast’ glitches this will mean that one possibly good point is thrown away.

### 4.3.5.3 Patterns expected from spikes and glitches

This section details the patterns which identify spikes and glitches. The following conventions are used:

- OUT1 are the outlying points in the first differential array.
- OUT2 are the outlying points in the second differential array.
- A value of 1 indicates an outlier above N standard deviations from the mean.
- A value of -1 indicates an outlier below N standard deviations from the mean.
- An \* indicates that the value at this location is not checked, so it does not matter if it contains an outlier or not.
- The ramp point increases reading from left to right.

#### Glitches

Positive glitch at point n in ramp  
 =====

ramp point	n-1	n		ramp point	n-1	n
OUT1	*	1	OR	OUT1	*	1
OUT2	1	*		OUT2	*	1

The second of these checks tends to catch the ‘slow’ glitches, which cover more than one point. For the first point in the ramp only the second of these tests for positive glitches is done, as there are no previous points to check.

Negative glitch at point n in ramp  
 =====

ramp point	n-1	n		ramp point	n-1	n
OUT1	*	-1	OR	OUT1	*	-1
OUT2	-1	*		OUT2	*	-1

No check is done for negative glitches at the first point in the ramp. These will be recorded as a positive 'spike'. It remains to be checked whether this is the correct thing to do.

If the number of points in a ramp is NPOINTS, then these checks for glitches can only be done for  $n=1$  to  $NPOINTS-2$ , as there are only  $NPOINTS-2$  values for the second differential. This means that if the last point of a ramp is an outlier, then it will be reported as a spike, rather than a glitch. There is no way of telling the difference between a spike at the last point and a glitch.

### Spikes

Positive spike at point n in ramp  
 =====

ramp point	n-1	n
OUT1	1	-1
OUT2	*	*

There is a special case for the first point in the ramp, as there is no previous point to check. In this case if OUT1 is  $-1$  (i.e. a negative outlier) then this is regarded as a positive spike at this point.

Negative spike at point n in ramp  
 =====

ramp point	n-1	n
OUT1	-1	1
OUT2	*	*

It is not possible to distinguish between a negative spike at the first point in the ramp and a positive glitch at this point. Therefore, no check for negative spikes is performed for the first point. A negative spike at the first point will be reported as a positive glitch.

#### 4.3.5.4 Glitch handling

The glitches identified using the method described above are removed in the processing. The way in which this is done is controlled by the values in the LCD1 calibration file. Note that the removal of

glitched data is done after all glitches have been identified. This means that glitches which occur during ramps discarded because of glitches in previous ramps are still identified.

For positive glitches all of the ramp following the glitch is discarded, plus the two subsequent ramps. The section of ramp before the glitch occurred is still used, provided that it has at least the minimum number of points required for slope fitting (this value is specified in a file and is currently set to 10).

Negative glitches are handled in the same way as positive glitches, except that no ramps are discarded following the glitched ramp.

The deglitching performed during illuminator flashes is slightly different from the above description. See Section 4.3.7 for details.

The LSPD file also contains the ‘undeglitched’ data, i.e. the results when there is no discarding of data due to glitches. The photocurrent for ramps discarded following a glitch are still available in the LSPD file, but are flagged as ‘invalid’ in the status word.

Information about each glitch detected, including the time, the glitch height and the detector number, is written into the Glitch History file (LWGH). This file is for informational purposes only. It is not used as an input for any further processing steps.

### 4.3.6 Extraction of ramp slopes and conversion to photocurrent

Starting with OLP Version 7 the method used for the ramp extraction is the ‘ $\Delta V/\Delta t$ ’ method described below. A more detailed description can be found in Leeks 2000, [24].

For each ramp of each detector, the points which have not been discarded by previous stages are processed as follows:

- The ITK time key for each point is converted into time in seconds relative to the very start of the ramp (the point where the reset occurred).
- A second order polynomial is fitted to the set of time and voltage values for the ramp. This is done using a standard least-squares algorithm.
- The initial and final voltages,  $V_{initial}$  and  $V_{final}$  are then estimated as follows:

$$V_{initial} = \alpha + \beta t_{initial} + \gamma t_{initial}^2 \quad (4.2)$$

$$V_{final} = \alpha + \beta t_{final} + \gamma t_{final}^2 \quad (4.3)$$

Where:

- $t_{initial}$  is the time of the first point which has been fitted.
- $t_{final}$  is the time of the last point which has been fitted.
- $\alpha, \beta, \gamma$  are the coefficients of the second order fit.
- The value for  $\Delta V/\Delta t$  is then calculated using the following formula:

$$\Delta V/\Delta t = \frac{V_{final} - V_{initial}}{t_{final} - t_{initial}} \quad (4.4)$$

- The values of  $\Delta V/\Delta t$  are then converted into photocurrents as follows:

$$I_{ph} = (\Delta V/\Delta t) \cdot C_{JF4} \quad (4.5)$$

Where  $C_{JF4}$  is the capacitance of the JF4 for this detector, which is obtained from the LCJF file.

In addition to the detector photocurrent, the ‘rms of the detector ramp fit’ is also calculated. This gives a measure of how well the points in the ramp were fitted by the second order polynomial. In previous versions of SPL this value was called the ‘uncertainty’ in the photocurrent. However, this was an inaccurate description and this value should not be used as an uncertainty. The rms of the detector ramp fit is calculated as follows:

$$rms = C_{JF4} \sqrt{\frac{\sum [V(t_i) - F(t_i)]^2}{N_{points}}} \quad (4.6)$$

where:

- $V(t_i)$  is the voltage at time  $t_i$ .
- $F(t_i)$  is the value of the fit at time  $t_i$ .
- $N_{points}$  is the number of fitted points.
- $C_{JF4}$  is the capacitance of the JF4 for this detector.

The calculated photocurrent and rms of the fit are now written into the LSPD file, together with a time key, grating and FP positions and other information. The time key assigned is the ITK time value of the start of the ramp.

If for any reason the photocurrent has not been calculated for this ramp then both the photocurrent and uncertainty will be set to zero. The most common reason for this is a glitch which has caused all of the data to be discarded. The status word should also indicated that this point is not valid (see Section 7.2.6).

### 4.3.7 Illuminator processing

For calibration purposes each observation includes two or more periods when the internal illuminators are used. The data from these ‘illuminator flashes’ are identified by SPL, processed, and the results written into an LIPD file. This file is then used as an input to AAL.

Each illuminator flash consists of a ‘dark current’ measurement (which is strictly speaking a dark signal measurement, see Section 4.4.2), followed by a sequence in which different illuminators are flashed at one or more different levels, followed by another dark current measurement. For grating scans, at least two of the illuminator flashes are ‘closed’ flashes, where the FP is moved into the beam. This removes the source from the beam and means that the dark current measurement during the illuminator flash is a measure of the dark current/straylight. For FP scans all flashes will be ‘closed’ flashes.

The processing of the ramps in illuminator flashes is identical to the processing of ramps of science data, as previously described. The only difference is in the handling of glitches. The LCD1 file contains a separate set of parameters which control the handling of glitches during illuminator flashes. The current setting of these parameters (Version 8 of the LCD1 file) means that the whole of a glitched ramp will be discarded, but no subsequent ramps are discarded.

After each ramp in the illuminator flash has been processed it is written into the LIPD file. The LIPD file is analogous to the LSPD file, except that it contains data from illuminator flashes rather than science data. The LIPD file contains the photocurrents for each ramp for each detector, plus auxiliary information such as the value of the illuminator commanded status word and the illuminator current.

## 4.4 Auto-Analysis Processing Steps

### 4.4.1 Absolute responsivity correction and responsivity drift correction

The LWS photoconducting detectors usually drift upwards in responsivity with time owing to the impact of ambient ionising radiation. This drift in responsivity must be corrected for before co-adding of indi-

vidual scans. This is referred to as the responsivity drift correction.

The absolute flux calibration on the other hand, involves referring the responsivity of the detectors at the time of the observation to the responsivity at the time of the calibrator (Uranus) observation. This is referred to as the absolute responsivity correction.

Both corrections make use of the response to a standard illuminator flash sequence performed before and after each observation. The following sections describe how these corrections are performed.

From Version 7 of the pipeline onwards the responsivity drift correction was only performed for AOTs L01 and L03. This is because the correction did not work very successfully for L02 and L04 AOTs. The keyword LORELDN in the LSAN header indicates if the responsivity drift correction has been performed or not.

#### 4.4.1.1 Grouping of data

Before these corrections are applied, the data must be divided into ‘groups’. Each group will have a separate responsivity drift correction and absolute responsivity correction calculated and applied. The LGIF, group information file, contains one record for each group. The LGIF file identifies the start and end ITK of each group and also records information which is constant over the group. This includes the absolute responsivity and responsivity drift correction information for the group.

The grouping of data depends upon the AOT type. The easiest way of describing the grouping is to define the condition for the current group to end and a new group to start. A new group starts when:

1. An illuminator flash occurs.
2. A new raster position starts. This is checked for by looking for changes in the raster point ID. However, in the case of solar tracking observations the raster point ID is ignored as it can change even when the raster position is the same.
3. The observation is an L03 and the grating position changes. A small amount of variation in the grating position is allowed before it is regarded as ‘changed’. This is because only the grating measured position is available and this is subject to small fluctuations even when at the same nominal position.

For each group identified, a single reference time is calculated. This is the point at which the absolute responsivity correction will be calculated for the group. It is also the point where the responsivity drift correction will be normalised.

The reference time is simply half way between the time of the start and end of the group. This reference time is written into the LGIF file.

#### 4.4.1.2 Absolute responsivity correction

##### Processing of illuminator flashes

The first stage of the absolute responsivity correction is to process each illuminator flash in the observation. The aim is to find for each flash the ratio between the detector photocurrents from the flash and the reference photocurrents stored in the LCIR calibration file.

Only the ‘closed’ illuminator flashes are used for the absolute responsivity correction. However, all illuminator flashes are first processed using the same method. The results of processing each flash are written into the LIAC file. This file contains one record for each flash in the observation.

The data for all illuminator flashes in each observation are read from the LIPD data file produced by SPL. This file contains the detector photocurrents for each ramp in each flash, plus the illuminator commanded status word and other information.

Background determination

The first stage of processing an illuminator flash is to determine the background photocurrent for each detector. These backgrounds will also be used in the dark current/straylight subtraction stage (see Section 4.4.2). The background value for each detector for each flash is written into the LIAC file.

The method for determining the background is as follows:

1. Extract the set of detector photo currents in the LIPD file corresponding to the background measurement taken at the *start* of the flash.
2. Perform median clipping on the set of photo currents for each detector This is to remove spurious values due to undetected glitches. See below for a description of median clipping. The keyword LCIRNSDB in the LCIR file header gives the number of standard deviations to use for median clipping of the background.
3. Average the set of photo currents for each detector to determine a single background value for each detector.

The uncertainty to be associated with this value is given by  $\sigma/\sqrt{n}$  for the set of averaged photo currents. If there are less than three photo current values then the maximum of the individual photo current uncertainties is used.

Median clipping

The purpose of median clipping is to remove any outlying values from a set of measurements of the same value.

There must be at least five values for median clipping to be performed.

The method for median clipping is as follows:

1. Calculate the median value of the set of points.
2. Calculate the standard deviation of the set of points, omitting the highest and lowest values in the set.
3. Check each point and reject any that are more than a predetermined number of standard deviations above or below the median value. The number of standard deviations depends upon the data which is being median clipped.

Ratioing against reference data

For each illuminator flash a single absolute responsivity ratio is calculated for each detector. This is done by ratioing the photocurrents in the illuminator flash against reference flash data in the LCIR calibration file. The final ratio for each detector is written into the LIAC file.

The method for calculating the ratio for each detector depends on the kind of illuminator sequences performed in the observation. There was a major change in the on-board illuminator operations after ISO revolution 442. For all observations performed after revolution 442, the number of integrations performed for each illuminator were increased from 8 to 24.

Before revolution 442

Prior to ISO revolution 442 the removal of points affected by glitches sometimes left just three or four points for an individual illuminator, making it almost impossible to apply the OLP Version 10 weighted-average method (see below). Therefore, even in OLP Version 10, these data are still processed using the 'OLP 8' illuminator processing method.

This method relies on using the point-by-point ratio of detector photocurrents from the measured and references flashes. The following sequence of steps is performed:

1. Determine the ‘type’ of the illuminator flash for the current observation. The illuminator flash type is determined from the revolution number of the observation. The LCIR file header should describe each of the possible flash types and the range of revolution numbers in which they occur.
2. Locate the start of the data for the appropriate flash type in the LCIR file.
3. Locate the start of the illuminator flash data in the LIPD file. The data from the background measurement at the start of the flash are skipped.
4. For each photo current value for each detector in the LIPD file, subtract the appropriate background (see Section 4.4.1), then divide by the corresponding entry in the LCIR file. Continue until no more entries remain in the LCIR file.

Skip any photocurrent values which are set to zero in the LIPD file or the LCIR file. Skip any values for which the status word in the LCIR file indicates that it should be ignored.

If, while doing this, data are found to be missing from the LIPD file then jump to the start of the next illuminator level in the LIPD and LCIR files. Missing data are detected by a mismatch between the illuminator commanded status value in the LIPD and LCIR records. The warning message ‘LIMM’ is issued each time this occurs. Data may be missing from the LIPD file because of telemetry dropouts or frame checksum errors. The LCIR file should not have any missing data.

5. Perform median clipping on the set of ratios calculated for each detector. This is to discard outliers due to undetected glitches etc. See Section 4.4.1.2 for a details of median clipping. The value of the keyword LCIRNSDF in the LCIR file header gives the number of standard deviations for median clipping.
6. Find the average of the remaining ratios for each detector. The result is a single responsivity correction factor for each detector. The uncertainty for each value is calculated using the standard error formula ( $\sigma/\sqrt{n}$ ).

#### After revolution 442 (the ‘OLP 10’ method)

For observations performed after revolution 442, with the new illuminator scheme, the ‘OLP 10’ method is used. It calculates the detector response correction factor using weighted-averages of the photocurrent ratios. The key processing steps are as follows:

1. Calculate the point-by-point ratio of the photocurrent in the observed flash sequence and the reference flash sequence.
2. Group these ratios according to the illuminator in operation. Five such groups will occur because there are five illuminators.
3. Calculate the variance of each group of ratios.
4. Calculate the weighted-average of these ratios, using the variances of the groups as weights.
5. Repeat steps 1 to 4 for all other flashes in the observation.
6. Calculate the average of the correction factors from all flashes in the observation.

These steps can be expressed in the following equations:

$$R(d, j) = \frac{\sum_{i=1}^5 \left[ \frac{r(d, i, j)}{\sigma_r(d, i, j)} \right]^2}{\sum_{i=1}^5 \left[ \frac{1}{\sigma_r(d, i, j)} \right]^2} \quad (4.7)$$

$$R(d) = \frac{\sum_{j=1}^N R(d, j)}{N} \quad (4.8)$$

where  $r(d, i, j)$  and  $\sigma_r(d, i, j)$  are the response correction factor and standard deviation respectively for detector  $d$ , illuminator  $i$  and flash  $j$ ;  $R(d, j)$  represents the weighted average of the response correction factor for detector  $d$  and flash  $j$ ; and  $R(d)$  is the *final* response correction factor for detector  $d$  after averaging over the  $N$  flashes in the observation.

This method is expected to be an improvement on the ‘OLP 8’ method because the response of the LWS detectors is known to be transient (Fouks 2001, [16] and Caux 2001, [5]), leading to a characteristic signature of the detector photocurrent for each illuminator as shown in Figure 4.4. In other words the scatter of photocurrent ratios for a given illuminator is not just pure statistical noise but is instead a systematic feature of the given detector.

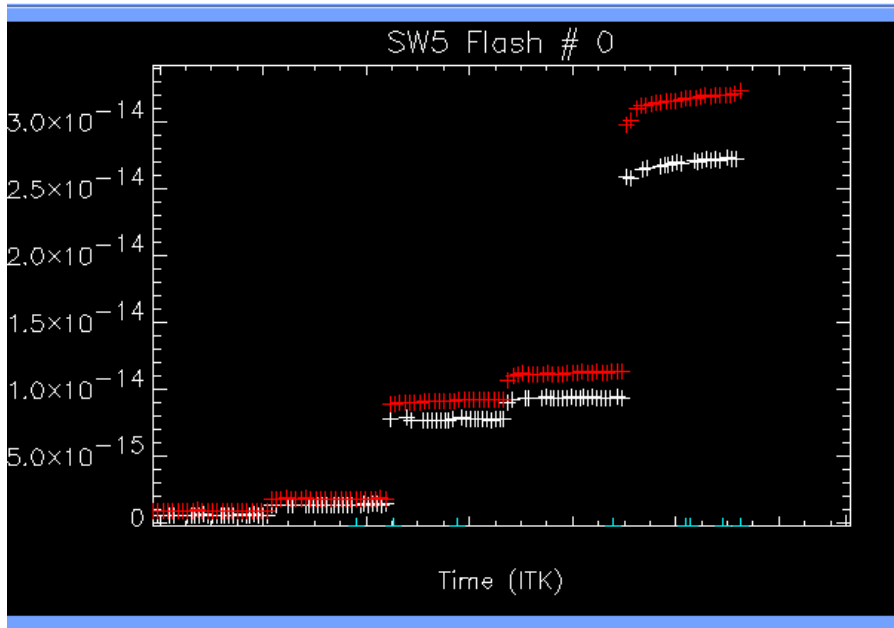


Figure 4.4: *Illuminator flash sequence photocurrents for detector SW5 in one observation carried out after ISO revolution 442 (white plus symbols). The reference illuminator flash data for this detector are shown as red plus symbols. The x-axis is a measure of the LWS on-board instrument time, ITK (Instrument Time Key).*

Figure 4.5 shows the spectrum of NGC 7027 respectively after application of both the ‘OLP 8’ and ‘OLP 10’ methods of illuminator processing. The level of continuity across the detectors in the ‘OLP 10’ method can be clearly seen. Numerous other test cases and examples have confirmed the superiority of this method. We therefore conclude that the new illuminator processing method as implemented in OLP Version 10 is superior to the one in OLP Version 8 and leads to better stitched spectra. For off-axis point sources in the LWS beam or for extended sources, any residual discrepancy present between adjacent detectors, especially in the SW detectors, is most likely to be the result of the asymmetric LWS beam profile (Lloyd 2001, [28]).

#### Performing correction

Once all illuminator flashes have been processed the absolute responsivity can be derived.

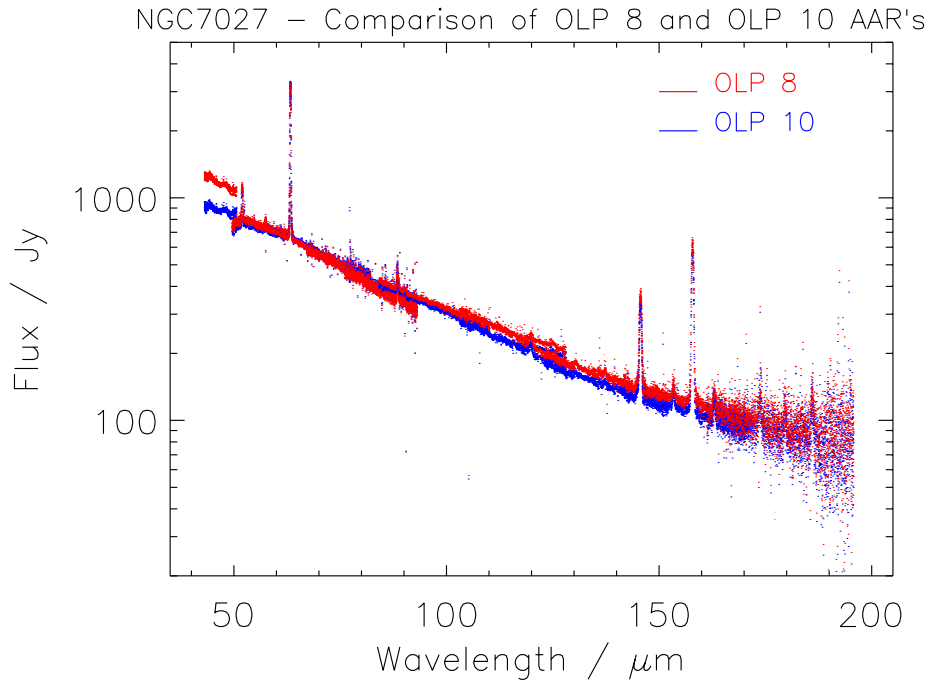


Figure 4.5: Comparison of ‘OLP 8’ and ‘OLP 10’ methods of illuminator processing for NGC 7027.

For each group identified in the LGIF file the absolute responsivity ratio for each detector at the reference time is calculated. This is done using the data from the two closed illuminator flashes which surround the reference time. For each detector the absolute responsivity correction factor is calculated by doing a linear interpolation in time between the values at the two surrounding closed illuminator flashes. The uncertainty in this value is calculated as the highest of the uncertainties for the two surrounding values. The value of the correction factor and its uncertainty are written into the LGIF file.

The absolute responsivity correction is then performed on all of the science data within the group by subtracting the dark current from the detector photocurrent and then simply dividing the result by the absolute responsivity correction factor.

#### 4.4.1.3 Responsivity drift correction

The responsivity drift correction corrects for the ‘drift’ in responsivity during an observation. The drift is obtained from the information in the LSCA scan summary file. The responsivity drift is calculated separately for each group of data identified in the LGIF file.

The responsivity drift correction is only performed for AOTs L01 and L03. No drift correction is performed for AOTs L02 and L04.

##### Generation of LSCA, scan summary file

The LSCA scan summary file contains summary information for every scan in the observation. This includes a value which represents the signal level over the whole scan. This is calculated by finding the average signal per point in the scan. The signal values used are the values from the LSPD file, before any further processing. Any values which are marked as ‘invalid’ in the LSA status word are not included in this average.

For each scan a reference time is also calculated. This is simply the mid point between the times of the start and end of the scan.

Note that for L02 photometric observations no LSCA file is produced. This is because no responsivity drift correction is needed on this data. Also, since AAL regards each point in a photometric observation as a single scan, the LSCA file would be very large and would contain the same information as the LSAN file.

#### Determination of drift slope

For each group of data identified in the LGIF file a separate drift slope is calculated for each detector. The method is as follows:

1. Identify the data in the LSCA scan summary file which lie within the time range of the group.
2. Discard any data from the LSCA file which does not correspond to a ‘full’ scan. The last scan in a measurement is often a ‘short’ scan where the mechanism only covers a fraction of the previous ‘full’ scans.

Short scans are identified by comparing the total number of points (ramps) in each scan with the number of points in the first scan in the group. The first scan of a group is assumed to be a full scan. If the number of points in a scan is below half of the number in a full scan then it is classified as a short scan and discarded.

Note that the total number of ramps in a scan can also vary because of missing frames of telemetry data.

3. For each of the full scans identified in the LSCA file, for each detector, fit a first order polynomial to the set of average signal values against reference times. This is done using a least squares fitting algorithm. The coefficients of the fitted slope are written into the LGIF file. The coefficients give the LSPD value at the reference time for the group and the gradient of the slope in LSPD units per time unit.

Note that in certain cases there may be insufficient valid data to determine a drift slope. This can happen for the inactive detectors in FP observations. The flag LGIFRSTA in the LGIF file indicates when this happens. In this case no responsivity drift correction is performed.

#### Performing correction

Once the drift slopes have been calculated for each detector in each group the responsivity drift correction can be applied.

For each group identified in the LGIF file the corresponding flux data are corrected. The method for correction is as follows:

1. Find the Y value of the drift slope for the appropriate detector at the time of the point to be corrected.
2. Divide this by the Y value of the drift slope at the reference time for the group. This gives the relative drift normalised to the reference time of the group.
3. Divide the flux value by the ratio determined above. The uncertainty in flux value is not changed.

### **4.4.2 Dark current/background straylight subtraction**

Each observation contains at least two ‘closed’ illuminator flashes. During these illuminator flashes the wheel is set to an opaque position, removing the flux contributions due to the source. This is achieved by placing one of the FPs in the beam with the etalons misaligned. For grating observations, at least the first and last flashes in the observation will be closed flashes. For FP observations, all flashes are closed

flashes since the FP is already in the beam and the etalons are misaligned before the illuminator flash is taken.

The background measurements during these closed illuminator flashes are a measure of the ‘dark signal’ at the time they were taken. (The ‘dark signal’ is the sum of the dark current and straylight). There is a separate background value for each detector. The values for the background measurements for the closed illuminator flashes are calculated using the information in the LIPD file. See Section 4.4.1 for details of how the background values are calculated. The backgrounds for each illuminator flash in the observation are written into the LIAC file. The closed illuminator flashes in the LIAC file are identified by the wheel absolute position field being set to either 0 (FPS) or 2 (FPL).

Between each pair of closed illuminator flashes in the observation a single dark current/straylight value is calculated for each detector. This is done by taking the mean of the two values from the surrounding flashes. The uncertainty in this value is given by the maximum of the two uncertainties from the surrounding flashes.

The dark current/straylight value is then subtracted from all of the detector photocurrent values between the pair of illuminator flashes. The uncertainty in the photocurrent is calculated by adding the uncertainties in the dark current/straylight and input photocurrent in quadrature. The dark current/straylight value subtracted from each scan is written into the scan summary file (LSCA). See Section 7.2.7.4 for details of the LSCA file.

From Version 8 onwards OLP uses a fixed dark current for processing of Fabry-Pérot data (AOTs L03 and L04). In OLP Version 10, for grating observations AAL checks each scan of each detector to see if the fixed dark current produces a better result (i.e. flux less negative) than the measured dark current. If this is the case then the fixed dark current is used instead of the measured dark current.

The values for this fixed dark current (one value per detector) have been determined as explained in Section 5.4 and are stored in the LCDK calibration file.

### 4.4.3 Grating scan wavelength calibration

The grating mechanism positions are converted into wavelengths at this stage. The input to this stage is the grating measured positions (LVDT readouts) and the calibration information in the LCGW file (see Section 7.3.2 for a description of the LCGW file). The conversion is performed by means of an algorithm. The coefficients required for the algorithm are stored in the LCGW file.

It has been found that the relationship between LVDT and wavelength changed over time. The LCGW file therefore contains different coefficients for different time periods.

The wavelength conversion is performed in two steps. The first step is to calculate the input beam angle to the grating,  $\Theta_i$ , for all ten detectors. This is calculated using the following formula:

$$\Theta_i = C_0 + C_1 \cdot LVDT + C_2 \cdot LVDT^2 + C_3 \cdot LVDT^3 \quad (4.9)$$

Where:

1. LVDT is the grating measured position.
2.  $C_0, \dots, C_3$  are the time varying coefficients of the fit. These are obtained from the LCGW file.

The input beam angle is then converted into wavelength for each detector by applying the grating equation and the geometry applicable to that detector. This is done using the following formula:

$$\lambda = \frac{\sin(\Theta_i) - \sin(\Theta_{det} - \Theta_i)}{Nlines \cdot Order} \quad (4.10)$$

Where:

1.  $\Theta_i$  is the input beam angle.
2.  $\Theta_{det}$  is the detector angle, obtained from the LCGW file.
3.  $N_{lines}$  is the number of lines per  $\mu\text{m}$  on the grating. This is a fixed value, obtained from the LCGW file.
4.  $Order$  is the fixed order number for the detector. This is 1 for the LW detectors and 2 for the SW detectors.

#### 4.4.4 Grating spectral responsivity calibration

The efficiency of the LWS as a spectrometer varies with wavelength, mainly due to the bandpass filtering incorporated into each detector unit and the spectral response of the detector itself.

The Grating Relative Responsivity Wavelength Calibration file, LCGR (see Section 7.3.2), contains a spectrum of the relative response of the instrument in grating mode (The way the file is derived is described in Section 5.2). The wavelength for each point in the spectrum is looked up in this table and the corresponding responsivity value read. If no exact wavelength match is found within the table then a responsivity value is calculated by linear extrapolation between surrounding wavelength entries. The responsivity corrected flux then is calculated by dividing the flux by the responsivity value.

From OLP Version 7 the wavelength range in the LCGR file was extended compared to the previous versions. This is to allow for wavelength identification of features on overlapping detectors (See Figure 2.5). The relative photometric calibration at the edges of the range is very poor. Many detectors have a ‘steep sided’ spectral response which makes the removal of the response uncertain. Also the steep sides enhance the effect of transient responses and the low throughput at the edges of the response curves leads to low signal-to-noise ratios. This region should therefore not be used for anything except wavelength identification of features. Data in this region can be identified by means of the ‘grating spectral responsivity warning’ flag in the LSAN status word (see Section 7.2.8). When this warning flag is set this indicates that the data point has poor calibration and should not be used for anything other than wavelength identification. The wavelength ranges for which the LCGR calibration is nominal are also specified by keywords in the LCGR header (see Section 7.3.2.)

#### 4.4.5 Spectral bandwidth correction

This correction only concerns grating scans. (For the corresponding correction for the FPs, see Section 4.4.7.)

The LCGB calibration file contains the spectral element size and uncertainty for each of the ten detectors. Auto-Analysis simply divides the flux for each detector by the appropriate spectral element size to perform the correction. The new flux uncertainty is calculated using the standard error formula.

The values of the spectral element sizes and uncertainties are written as keywords into the header of the LSAN file. Keywords LCGBddd contain the spectral element size for detector ddd (ddd=‘SW1’...‘LW5’), while keywords LCGBUddd contain the corresponding uncertainties.

#### 4.4.6 Fabry-Pérot scan wavelength calibration

The wavelength calibration of a FP scan is done using a parametrised algorithm for the FP wavelength calibration. The wavelength calibration for FP spectra is done as follows:

1. The grating position (LVDT value) is converted to wavelength using the algorithm specified above for the grating scan wavelength calibration (Section 4.4.3).

2. For every point in the scan the position value of the FP is converted into a gap of the two Fabry-Pérot etalons. This is done using the third order polynomial:

$$d = C_0 + C_1 \cdot POS + C_2 \cdot POS^2 + C_3 \cdot POS^3 \quad (4.11)$$

where  $d$  is the gap of the FP etalons,  $POS$  is the FP position value (as stored in the SPD product file (see Section 7.2.5), and  $C_0$ ,  $C_1$ ,  $C_2$  and  $C_3$  are the FP wavelength calibration parameters read from calibration file LCFW (see Section 7.3.2).

3. The first point of the scan is then used to determine the order the FP was working at for this scan. For this the wavelength determined from the grating position is taken as the approximate wavelength of the first point of the spectrum. The order is then calculated from:

$$m = INT\left(\frac{2d}{\lambda}\right) \quad (4.12)$$

where  $m$  is the order of the scan,  $d$  is the gap of the FP etalons and  $\lambda$  is the wavelength. INT means the integer part of this division.

4. Using the order calculated in the previous step, all Fabry-Pérot gaps for the points in the spectrum are converted to wavelength using:

$$\lambda = \frac{2d}{m} \quad (4.13)$$

#### 4.4.7 Fabry-Pérot throughput correction

From OLP Version 8 onwards, the FP spectral responsivity calibration has been replaced by the FP ‘throughput’ correction, which is the product of the FP transmission multiplied by the FP resolution element. The method of calibrating the total throughput of the FP’s has been devised using Mars as a calibration standard. This method uses a fitted polynomial between the wavelength and the FP throughput and the results are FP fluxes in units of  $W\text{ cm}^{-2}\ \mu\text{m}^{-1}$ .

The grating spectral responsivity calibration, described in Section 4.4.4, is also applied to FP data.

#### 4.4.8 Velocity correction to wavelength

The wavelengths calculated in the previous stages are corrected for the velocity of the spacecraft and earth towards the target. The header of the LSPD file contains keywords which specify this velocity at three points during the observation. These keywords are written by a subroutine written by ESA which is external to the LWS pipeline (TREFDOP1 to 3). The velocity at each mechanism position in a scan is calculated by interpolating in time between the three given values. A second order curve fit is used for the interpolation. Once calculated, the coefficients of this fit are written into the LSAN header as the keywords LVCOEFFn (n=0-2).

The wavelength at each mechanism position is then corrected using the following formula:

$$\lambda_{Corrected} = \lambda + \lambda \frac{V}{C} \quad (4.14)$$

Where:

- $\lambda$  is the wavelength to be corrected, in  $\mu\text{m}$ .
- $V$  is the velocity of the spacecraft and earth towards the target, in  $\text{km/s}$ .
- $C$  is the speed of light in  $\text{km/s}$ .

#### 4.4.9 Write LSNR data product (only in OLP versions earlier than 8)

Up to OLP Version 7, the absolute responsivity and the responsivity drift corrections were determined at the end of AAL. Therefore at this stage, before these corrections, the results of the previous calibration steps were written into the first product file produced by Auto-Analysis, named LSNR. This file was identical in structure to the final LSN file, apart from a few minor differences. This file was provided to give observers access to the data before the absolute responsivity correction and responsivity drift corrections were applied. In a few cases these corrections did not work successfully. The LSNR file provided an alternative product file for those cases. After OLP Version 8 the responsivity corrections are performed at the start of the pipeline.

#### 4.4.10 Calculation of uncertainties

The LSN file contains the field LSNFLXU which gives the estimation of the systematic flux error. The calculation of the uncertainty is detailed below, for the grating (AOTs L01 and L02) and the Fabry-Pérot (AOTs L03 and L04).

##### 4.4.10.1 Grating continuum flux error estimation

The grating flux is given by:

$$F(\lambda) = \frac{P(\lambda) - D}{f_R R(\lambda) \Delta\lambda(\lambda)} \quad (4.15)$$

where  $P(\lambda)$  is the photocurrent;  $D$  the dark current;  $f_R$  the responsivity correction factor from illuminator operation;  $R(\lambda)$  the detector responsivity from the LCGR file ( $A\text{ cm}^2\text{ W}^{-1}$ ) and  $\Delta\lambda(\lambda)$  the equivalent width of the grating resolution element at this wavelength.

We can write the associated uncertainty as:

$$\Delta F(\lambda) = \left( \Delta \left( \frac{P(\lambda)}{f_R R(\lambda) \Delta\lambda(\lambda)} \right)^2 + \Delta \left( \frac{D}{f_R R(\lambda) \Delta\lambda(\lambda)} \right)^2 \right)^{1/2} \quad (4.16)$$

where

$$\Delta \left( \frac{D}{f_R R(\lambda) \Delta\lambda(\lambda)} \right) = \left( \frac{\delta D^2}{D} + \frac{\delta f_R^2}{f_R} + \frac{\delta R(\lambda)^2}{R(\lambda)} \right)^{1/2} \times \left( \frac{D}{f_R R(\lambda) \Delta\lambda(\lambda)} \right) \quad (4.17)$$

and

$$\Delta \left( \frac{P(\lambda)}{f_R R(\lambda) \Delta\lambda(\lambda)} \right) = \left( \frac{\delta f_R^2}{f_R} + \frac{\delta R(\lambda)^2}{R(\lambda)} \right)^{1/2} \times \left( \frac{P(\lambda)}{f_R R(\lambda) \Delta\lambda(\lambda)} \right) \quad (4.18)$$

$\delta R/R$  is the statistical error in the LCGR file. Since this error does not depend on the observation, from OLP Version 10 it is left out of the error calculation. This term is thus set to zero. The user is referred to Section 5.2 for an estimate of the uncertainty of the relative response function (LCGR file). The value of  $\Delta F(\lambda)$  is thereby calculated absolutely using equation 4.16 and placed in the LSN.LSANFLXU tag.

##### 4.4.10.2 Fabry-Pérot continuum flux error estimation

For the Fabry-Pérot the flux is given by:

$$F(\lambda) = \frac{P(\lambda) - D}{f_R R_g(\lambda) G(\lambda) \eta_{FP}(\lambda) \Delta\lambda_{FP}(\lambda)} \quad (4.19)$$

where, in addition to the definitions above,  $R_g(\lambda)$  is the detector responsivity in grating mode at this grating setting (the RSRF value in  $A\text{ cm}^2\text{ W}^{-1}$ );  $G(\lambda)$  the relative height of the grating resolution element profile at this wavelength;  $\eta_{FP}(\lambda)$  the Fabry-Pérot efficiency at this wavelength and  $\Delta\lambda_{FP}(\lambda)$  the equivalent width of the Fabry-Pérot resolution element at this wavelength (in  $\mu\text{m}$ ).

We can write the associated uncertainty as:

$$\Delta F(\lambda) = \left( \Delta \left( \frac{P(\lambda)}{f_R R_g(\lambda) G(\lambda) \eta_{FP}(\lambda) \Delta\lambda_{FP}(\lambda)} \right)^2 + \Delta \left( \frac{D}{f_R R_g(\lambda) G(\lambda) \eta_{FP}(\lambda) \Delta\lambda_{FP}(\lambda)} \right)^2 \right)^{1/2} \quad (4.20)$$

where

$$\begin{aligned} \Delta \left( \frac{D}{f_R R_g(\lambda) G(\lambda) \eta_{FP}(\lambda) \Delta\lambda_{FP}(\lambda)} \right) = & \\ & \left( \frac{\delta D^2}{D} + \frac{\delta f_R^2}{f_R} + \frac{\delta R_g(\lambda)^2}{R_g(\lambda)} + \frac{\delta G(\lambda)^2}{G(\lambda)} + \frac{\delta \eta_{FP} \Delta\lambda_{FP}(\lambda)^2}{\eta_{FP} \Delta\lambda_{FP}(\lambda)} \right)^{1/2} \\ & \times \left( \frac{D}{f_R R_g(\lambda) G(\lambda) \eta_{FP}(\lambda) \Delta\lambda_{FP}(\lambda)} \right) \end{aligned} \quad (4.21)$$

Notice here that the error is quoted for the product  $\eta_{FP} \Delta\lambda_{FP}(\lambda)$ . This is because the new method of calibration for the FP throughput cannot distinguish between the contribution from the transmission of the FP and that of the resolution element of the FP. Also from Version 8 of the OLP onwards, the grating resolution element correction was not done; therefore,  $G(\lambda)$  drops out. The equivalent equations for the error arising from the photocurrent and dark current are therefore:

$$\begin{aligned} \Delta \left( \frac{D}{f_R R_g(\lambda) \eta_{FP} \Delta\lambda_{FP}(\lambda)} \right) = & \\ & \left( \frac{\delta D^2}{D} + \frac{\delta f_R^2}{f_R} + \frac{\delta R_g(\lambda)^2}{R_g(\lambda)} + \frac{\delta \eta_{FP} \Delta\lambda_{FP}(\lambda)^2}{\eta_{FP} \Delta\lambda_{FP}(\lambda)} \right)^{1/2} \\ & \times \left( \frac{D}{f_R R_g(\lambda) \eta_{FP} \Delta\lambda_{FP}(\lambda)} \right) \end{aligned} \quad (4.22)$$

and

$$\begin{aligned} \Delta \left( \frac{P(\lambda)}{f_R R_g(\lambda) \eta_{FP} \Delta\lambda_{FP}(\lambda)} \right) = & \\ & \left( \frac{\delta f_R^2}{f_R} + \frac{\delta R_g(\lambda)^2}{R_g(\lambda)} + \frac{\delta \eta_{FP} \Delta\lambda_{FP}(\lambda)^2}{\eta_{FP} \Delta\lambda_{FP}(\lambda)} \right)^{1/2} \\ & \times \left( \frac{P(\lambda)}{f_R R_g(\lambda) \eta_{FP} \Delta\lambda_{FP}(\lambda)} \right) \end{aligned} \quad (4.23)$$

All the terms except  $\delta \eta_{FP} \Delta\lambda_{FP}(\lambda)$  are known; this is calculated from a fit to the error values in the original derivation of the  $\eta_{FP} \Delta\lambda_{FP}(\lambda)$  parameters. The absolute flux error placed in the LSAN.LSANFLXU tag is therefore:

$$\Delta F(\lambda) = \left( \Delta \left( \frac{P(\lambda)}{f_R R_g(\lambda) \eta_{FP} \Delta\lambda_{FP}(\lambda)} \right)^2 + \Delta \left( \frac{D}{f_R R_g(\lambda) \eta_{FP} \Delta\lambda_{FP}(\lambda)} \right)^2 \right)^{1/2} \quad (4.24)$$

Note that in this case also  $\delta R/R$  is set to zero in OLP Version 10 (see last paragraph of Section 4.4.10.1).

## 4.5 Processing of the Parallel and Serendipity Modes

The approach to the processing of parallel and serendipity data is essentially the same as for the prime data and, whenever possible, the same algorithms and calibration files are applied (Swinyard et al. 1998, [40]; Burgdorf et al. 1998, [4]). For the SPD level product, the first stage of obtaining the slope of the ramp is not required. However the same engineering conversions are then applied to obtain a photocurrent. Only a small adjustment for the difference in slopes, obtained from 1 s (parallel/serendipity) and 1/2 s (prime mode) ramps, is also applied at this stage.

Table 4.1: *The LWS grating rest position wavelengths.*

Detector	Wavelength [ $\mu\text{m}$ ]	Width of resolution element [ $\mu\text{m}$ ]	Dark Current [ $\times 10^{-16}$ A]
SW1	46.2	0.29	4.35
SW2	56.2	0.29	1.89
SW3	66.1	0.29	1.91
SW4	75.7	0.29	0.86
SW5	84.8	0.29	1.21
LW1	102.4	0.6	2.22
LW2	122.2	0.6	0.03
LW3	141.8	0.6	0.29
LW4	160.6	0.6	1.74
LW5	178.0	0.6	1.28

### 4.5.1 Dark current subtraction and drift removal

Once the photocurrents have been obtained, the next stage is to remove the dark current. For prime mode grating data this is done by measuring dark current values prior to the illuminator flashes which take place at the start and end of each observation and subtracting the average. All dark current measurements were checked for trends and it was found that the dark current has remained at a stable value throughout each revolution of the ISO mission. The rare exception being that transient effects after observing bright sources sometimes led to higher than normal values. A similar monitoring exercise was done with parallel and serendipity data. The dark values were defined as the minimum photocurrents consistently obtained and these were implemented as one dark current value per detector. These values (see Table 4.1) were found to be lower than those found in prime mode (see Section 5.4) and were applied as a fixed dark removal in the parallel/serendipity pipeline.

From inspection of prime mode illuminator flashes, the responsivity of the LWS detectors is known to vary during a revolution, the net effect being a linear drift upwards, restored by a bias boost performed during the handover period in the middle of a revolution, and another linear drift in the second part of the revolution (Lim et al. 1998, [26]). The calibration of the detector responsivity relies on a simple ratio between the response to the illuminators found at the time of a particular observation and that used as a reference. However, as serendipity and parallel observations did not have dedicated illuminator flashes a different approach had to be found. For each half revolution all illuminator flashes were linearly fitted to obtain responsivity drift coefficients for that revolution. The parallel and serendipity data were then calibrated by using the interpolated responses of the detectors. For revolutions where there are no prime mode observations, a standard responsivity drift defined by averaging all revolutions, is applied.

In prime mode the grating or FP is moving constantly hence the detector receives a constantly changing signal. In parallel mode the grating remains at a fixed position and therefore it was possible to apply a

transient correction to the data. The wavelength determination was done by lookup table as all the data were taken at the grating rest position and this remained stable throughout the ISO mission. Each data point has a bandwidth of one grating resolution element (see Table 4.1). The units of both parallel and serendipity products are in  $\text{MJy sr}^{-1}$  as a correction is made for the beam profiles (see Section 5.9 or Lloyd 2000, [27]).



# Chapter 5

## Calibration and Performance

### 5.1 Introduction

We describe here the performance of the instrument together with the calibration processes conducted to convert the raw digitised signal into wavelength and absolute flux units, as well as those designed to derive any instrument characteristics needed to assess the quality of the data and the performance of the instrument.

Some of the calibration processes described here are meant to derive the calibration files which are used in the pipeline processing; others are used to characterise the instrument behaviour.

The calibration of the data comprises different steps:

- The conversion of the raw digitised signal from the detectors and mechanisms into photocurrent at each mechanism position is termed Derive-SPD (Standard Processed Data) (see Section 4.3); it was designed during ground testing and verified in the early phase of the ISO mission. The first stage of processing therefore requires no astronomical calibration and will in general not be discussed here.
- The conversions of mechanism position into wavelength on one hand, and of photocurrent into absolute flux units on the other hand, do require astronomical calibration. These conversions are performed as far as possible in Auto-Analysis (AAL - see Section 4.4).

However, the pipeline processing only derives the true flux for point like sources at the centre of the LWS field of view because it makes no attempt to correct for the angular response of the instrument, (i.e. the beam shape, see Section 5.9), or for any anomalous instrument behaviour such as the channel fringing seen on the spectra of extended or off-axis sources. The fringes and other unwanted effects are described in Chapter 6 and can be corrected for by using dedicated interactive software in LIA (LWS Interactive Analysis - see Section 8).

The accuracy achieved with the calibration and the derived instrument characteristics are given in the tables included in this chapter. Typical accuracy numbers are summarized in Table 5.1.

For a list and a description of the calibration files, we refer to Section 7.3.

### 5.2 Absolute Flux Calibration and Grating Relative Response

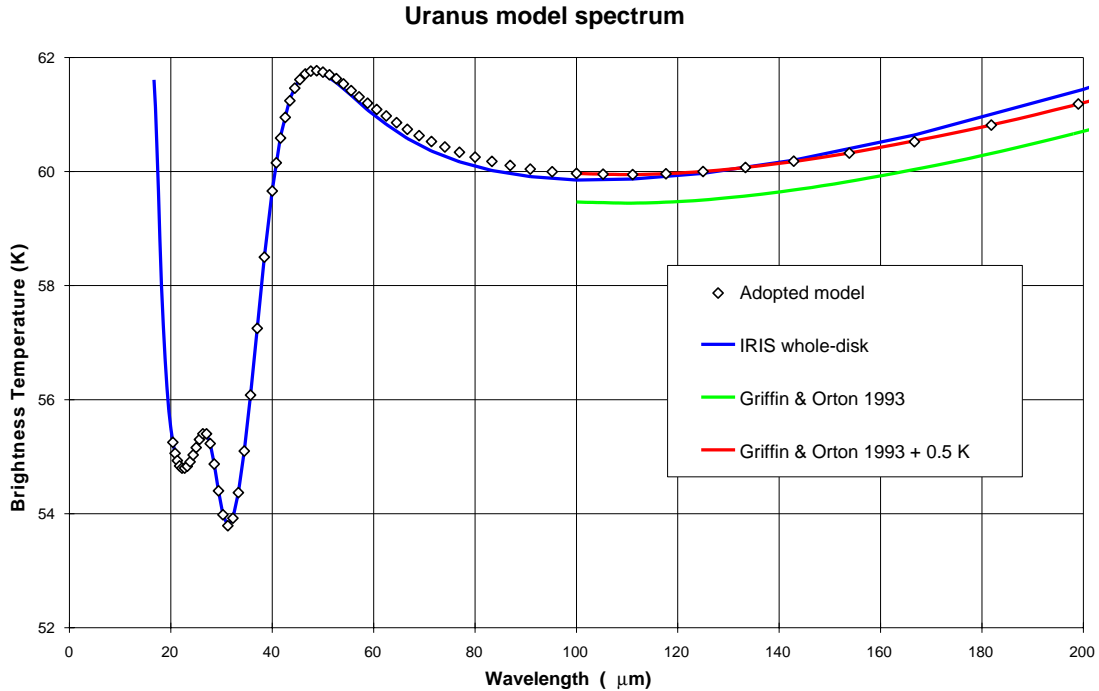
Both the absolute flux calibration and the relative spectral response function (RSRF), i.e. the relationship between flux and photocurrent in grating mode, have been established using observations of Uranus and a Uranus spectral model. The semi-empirical spectral model of Uranus, used as the LWS prime flux calibrator, originates from a synthesis of results from the Voyager Infra-Red Imaging Spectrometer (IRIS)(4–50  $\mu\text{m}$ ) and the JCMT near-millimetre UKT14  $^3\text{He}$  bolometer receiver (0.35–2.0 mm). The blue curve in Figure 5.1 represents the whole disk IRIS brightness temperatures extended to 200  $\mu\text{m}$

Table 5.1: *Typical accuracies of the different modes of the LWS*

Mode	Wavelength accuracy	Photometric accuracy
Grating (L01 & L02)	0.25 resolution elem. 0.07 $\mu\text{m}$ for SW1–SW5 0.15 $\mu\text{m}$ for LW1–LW5	point sources: 10%–20% depending on flux and detector extended sources: 50%
Fabry-Pérot (L03 & L04)	FPS: 6 $\text{km s}^{-1}$ FPL: 13 $\text{km s}^{-1}$	line intensity: within 20% continuum: to be scaled to the grating flux

using a radiative transfer atmospheric model (Conrath, private communication, 1996). This model had a composition of  $(85 \pm 3)\%$   $\text{H}_2$  with the remainder being He, apart from 2.3% of  $\text{CH}_4$  deep in the troposphere. Griffin & Orton 1993, [19] used JCMT data to extend their own atmospheric model down to far-infrared wavelengths (green curve). It can be clearly seen that in order to achieve consistency between these two results in the LWS wavelength range it is necessary to add a 0.5 K offset to the near-millimetre brightness temperatures (red curve). Since the calibration of Uranus data in the near-millimetre range is based on the Mars model of Wright 1976, [46] the introduction of a 1% offset is well within the estimated absolute calibration error.

Hence the adopted model of Uranus for calibrating LWS data, shown in Figure 5.1 as diamonds, is simply the Griffin & Orton 1993, [19] model with the 0.5 K offset. The smooth featureless continuum spectrum makes it ideal for calibrating LWS data. The error associated to the model is considered to be around 5%.

Figure 5.1: *Uranus model used in the LWS photometric calibration.*

The calibration spectrum is composed of scans from fifteen L01 observations of Uranus, obtained between revolutions 321 and 874.

Table 5.2: *Observations of Uranus used to derive the RSRF.*

TDT	Uranus angular diameter	Number of scans	Comments
32103705	2.439	4	OK
32803601	2.410	4	OK
33503801	2.360	4	OK
34901201	2.310	4	OK
34901605	2.310	4	OK
35601101	2.280	4	OK
53802611	2.375	4	OK
54403301	2.399	6	OK
55205305	2.410	6	OK
69800902	2.380	12	OK
70601702	2.340	6	affected by detector warm up, only used SW1–LW1
72002004	2.290	12	affected by detector warm up, only used SW1–LW1
73401302	2.230	12	OK
73800302	2.220	12	OK
87401402	2.210	10	OK

Scans were extracted from each observation so that the number of scans in each direction was equal; i.e., for an observation with 7 scans, only the first three forward scans were extracted. A standard dark current value was then subtracted from each scan. Each scan was scaled to the first scan in the revolution 321 using the mean of all the points in the scan as a scaling factor. The scans were averaged using a median clipped mean, clipping at  $3\sigma$  before division with the model.

### 5.2.1 Absolute flux calibration

The absolute flux calibration is performed by applying to all LWS observations the photocurrent to flux relationship derived from Uranus. It also involves referring the responsivity of the detectors at the time of the observation to the responsivity at the time of the calibrator (Uranus) observation. This is referred to as the absolute responsivity correction (described in detail in Section 4.4.1).

For each illuminator flash a single absolute responsivity ratio is calculated for each detector. This is done by taking the ratio between the signal measured when the illuminators were operated during an observation and the signal in the reference flash data in the LCIR calibration file. This reference flash calibration file was created as follows: previous versions of the RSRF file had relied on a special observation of Uranus taken in rev 317. Uranus was scanned many times, followed by five sequences of each of two types of illuminator flash (types 2 and 3; see Table 5.3). The two averaged sequences were then compared with the Uranus observations during those time periods to adjust them to the reference responsivity at the time of the first scan in revolution 321. These form the reference sequences in the LCIR calibration file. A further illuminator sequence (type 1) was used by LWS before the time Uranus was observed. To generate this entry in the LCIR file, sequences from observations of the HII region G298.228–0.331 during this time period were averaged together to form a reference sequence. This was then calibrated to the Uranus sequences using observations of the HII regions G298.228–0.331 and S106 and of the planetary nebula NGC 6302 taken during the three time periods denoted by different sequence types.

Table 5.3: *The three illuminator sequence types*

Illuminator sequence type	Revolutions used	Description
1	0–236	8 x 0.5 s ramps at levels 100 and 220
2	236–380	4 x 1 s ramps at levels 100 and 220
3	442–875	24 x 0.5 s ramps at level 180

To ensure that the power from the illuminators did not change during the course of the mission, weekly observations were made of a series of astronomical sources and the signal from these compared to that from the illuminators (Lim et al. 1998, [26]).

### 5.2.2 Relative spectral response function

The Uranus data described above are also used to establish the response of the instrument as a function of wavelength in grating mode - the Relative Spectral Response Function or RSRF. This is tabulated and stored in the LCGR calibration file, the content of which is shown for the 10 detectors in Figure 5.2. The basic conversion between photocurrent and flux for all LWS data is carried out using this calibration file.

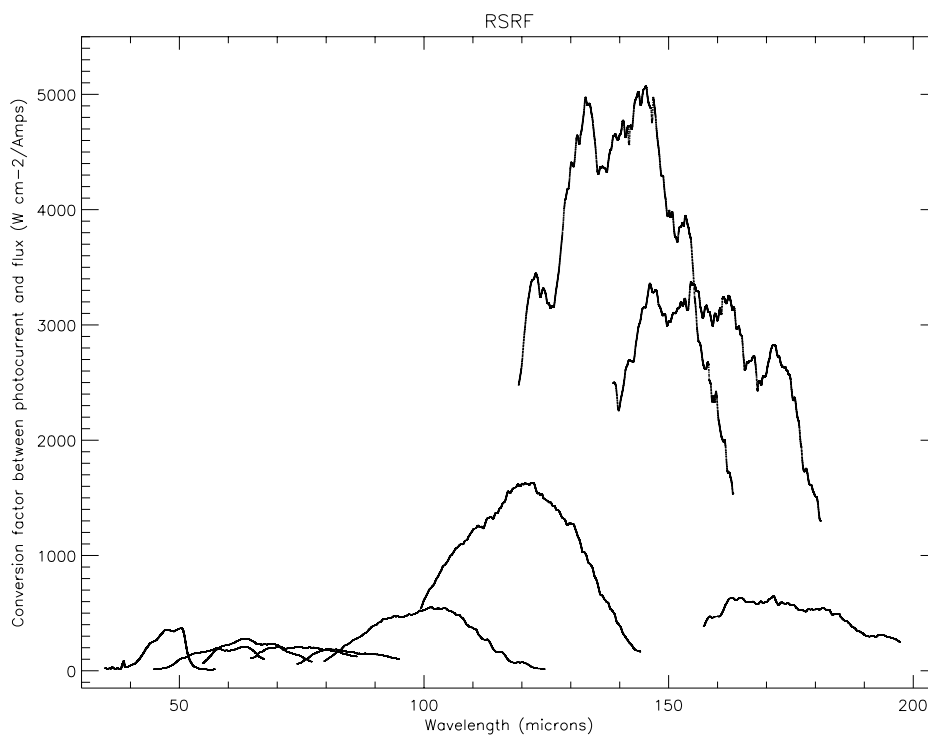


Figure 5.2: *Relative Spectral Response Function (RSRF) shown for the 10 detectors. This data is stored in the LCGR calibration file.*

### 5.3 Fabry-Pérot Flux Calibration

The flux calibration in Fabry-Pérot mode is more complex than for the grating. Ideally the relationship between photocurrent and flux for the Fabry-Pérot would have been directly established using observations of sources with known spectral characteristics. However, the transmission of the Fabry-Pérot is such that only the very brightest objects (Jupiter and Saturn) would have made suitable candidates for such observations. These have relatively poorly known far-infrared spectra and, even with sources as bright as these, the observations would have been prohibitively long. Therefore a boot strap method is used whereby the photocurrent is first converted to flux using the grating mode relationship and the signals from the illuminator operations; this also removes the signature of the instrument RSRF in grating mode.

From OLP Version 8 onwards, a ‘throughput correction’ is applied, thereby giving the FP flux in units of  $\text{W cm}^{-2} \mu\text{m}^{-1}$ . The throughput correction is the FP transmission multiplied by the FP resolution element, the two factors being undissociable in continuum observations; this has been derived using Mars as the calibrator.

The Fabry-Pérot photometric calibration is derived from observations of Mars made with the FPs set at a fixed gap and the grating scanned over its full range. In this observation mode the various order and wavelength combinations of the FP are selected as the wavelength falling onto the detectors changes due to the grating movement. An example of the output data are shown in Figure 5.3. The peaks of the orders represent the convolution of the instrument relative spectral response (RSRF), the spectrum of Mars and the product of the transmission efficiency  $T(\lambda)$  and effective spectral element width  $\eta(\lambda)$  of the FP used.

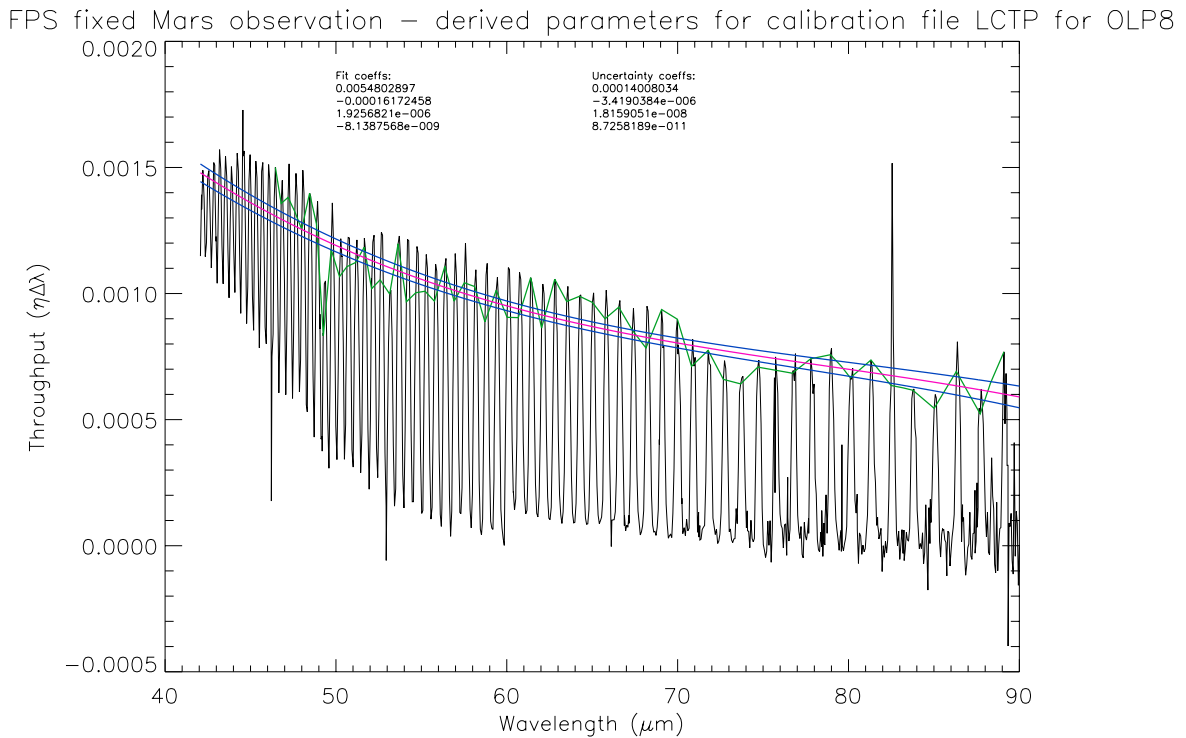


Figure 5.3: Derivation of the FPS throughput with Mars ‘mixed-mode’ observations. Red line: Third order polynomial fit to the peaks. Blue lines:  $\pm 1 \sigma$ .

With knowledge of the instrument spectral response from grating measurements and a model of the

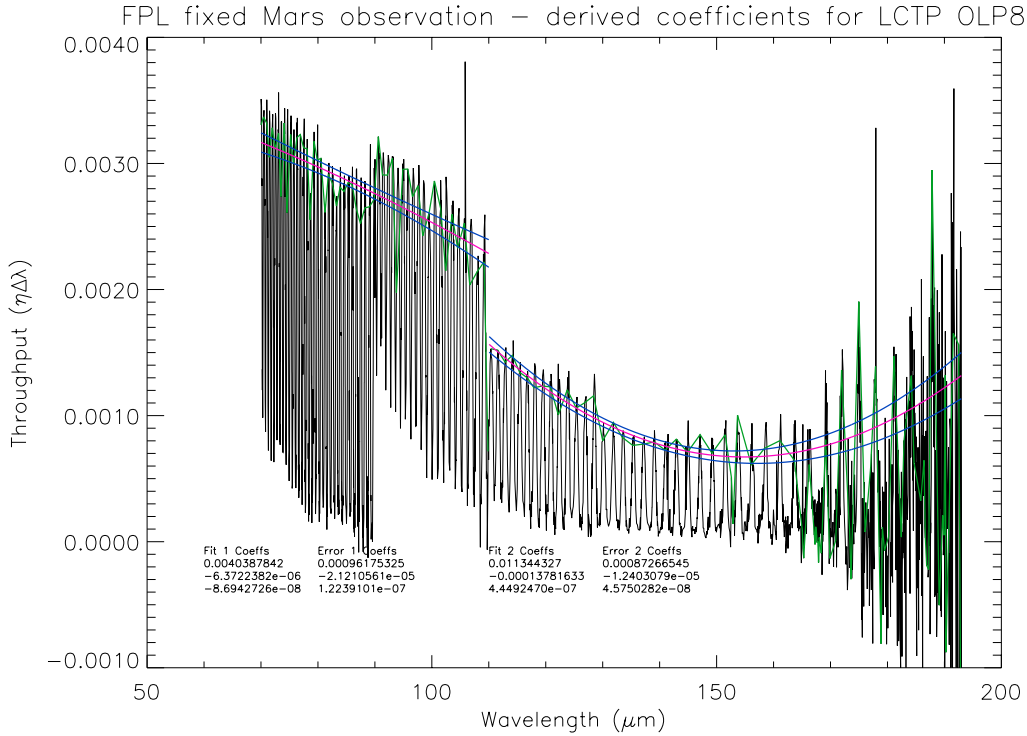


Figure 5.4: Derivation of the FPL throughput with Mars ‘mixed-mode’ observations. Note the break around  $110 \mu\text{m}$  between LW1 and LW2. Red line: Second order polynomial fit to the peaks. Blue lines:  $\pm 1 \sigma$ .

Martian spectrum the instrument and input spectrum can be removed giving the FP  $\eta T$  function versus wavelength which can be deduced by fitting the peaks with a low order polynomial (see Figure 5.3). In the case of the FPS this is a straightforward fit and there is no dependence on detector or grating order. For the FPL the situation is more complex as there is an apparent break between the detectors up to and including LW1 and from LW2 through LW5 (see Figure 5.4). This break has no explanation at present, but it is clearly present for all FPL observations and the derived calibration coefficients do correct for it. The derived coefficients of  $\eta T(\lambda)$  for FPS and the two sections of FPL (SW4–LW1 and LW2–LW5) are stored in the calibration file LCTP and used in Auto-Analysis to correct all FP data to  $\text{W cm}^{-2} \mu\text{m}^{-1}$ .

## 5.4 Dark Current Determination

In the pipeline processing, the dark current is taken as the average of the two dark current measurements performed respectively at the beginning and at the end of each observation. However, it is known that this estimate of the dark current can sometimes give erroneous results when subtracted from the data, due to an intrinsic uncertainty in the measurement of the dark current. This sometimes leads to negative flux values. In such cases, OLP Version 10 chooses either the dark current measurement attached to the observation, or a ‘fixed dark current’ that was determined in dedicated calibration observations, whichever gives the best result, i.e. the less negative values after the dark subtraction. There is also the possibility to redo the dark current subtraction in LIA with the dark current chosen by the user.

The fixed dark current has been determined by three independent methods:

- Two long measurements of the dark background were taken with one of the Fabry-Pérots in the beam with its etalons set non-parallel. The first measurement was taken straight after the mid-revolution detector curing procedure and the second in the last hour before the close of the LWS science window.
- Routine checks of the dark current were made near apogee in every revolution to monitor long term trends in the detector behaviour. As no long term drifts were found in the value of the dark currents, these measurements were combined to obtain an independent determination of the dark signal.
- When the LWS is not the prime instrument, useful data can still be obtained by recording the output of the detectors with low time resolution. Much of the time during these serendipity mode operations the LWS is viewing blank portions of the sky and the data can be used to determine the detector dark currents.

The results of the three independent means of measuring the dark currents are given in Table 5.4. They agree with each other to within one or two standard deviations. The low values for some detectors seen in the serendipity mode derivation are probably due to the lack of sampling of the pre-amplifier output and the different method used for deriving the photocurrent. The higher values derived from the hand-over illuminator operation reflect the fact that these are measured with a short integration time (8 s) and are therefore prone to problems of contamination by radiation hits. It is noteworthy that there appears to be no significant change in the level of the dark current between the middle and end of a revolution. This is in disagreement with predictions from tests made during pre-launch calibration (Price et al. 1992, [36]).

Table 5.4: *Detector dark currents for the ten LWS detectors determined from four different observations: the special long observations in revolution 650, the illuminator operations at apogee and the serendipity mode data. The dark currents are given in units of  $10^{-16}$  A. The quoted uncertainties are one standard deviation. The last two columns give the adopted ‘fixed dark currents’ in A and their uncertainty.*

Det.	Revolution 650 measurements		Apogee meas.	Serendipity mode	Adopted fixed dark current	dark current uncertainty
	Mid Rev.	End Rev.				
SW1	4.89±0.42	4.96±0.53	5.68±1.82	4.98±0.58	4.960E-16	5.447E-17
SW2	2.15±0.38	2.11±0.40	2.42±1.20	1.98±0.32	2.080E-16	4.255E-17
SW3	2.23±0.19	2.31±0.20	2.58±0.86	2.00±0.23	2.200E-16	2.085E-17
SW4	1.21±0.30	1.25±0.30	1.32±0.40	0.89±0.24	1.180E-16	3.404E-17
SW5	1.63±0.21	1.67±0.22	1.72±0.27	1.35±0.22	1.560E-16	2.383E-17
LW1	2.39±0.27	2.63±0.28	2.77±0.53	2.26±0.30	2.500E-16	2.936E-17
LW2	0.10±0.22	0.17±0.23	0.42±0.36	0.17±0.18	7.300E-18	2.723E-17
LW3	0.49±0.32	0.49±0.34	1.20±1.03	0.39±0.25	5.310E-17	3.915E-17
LW4	2.23±0.38	1.94±0.38	2.52±1.44	1.84±0.33	1.760E-16	4.213E-17
LW5	1.40±0.22	1.18±0.22	1.28±0.35	0.98±0.25	1.210E-16	2.511E-17

## 5.5 In-orbit Sensitivity of the LWS – Detector Performance

The sensitivity of the LWS is based on the knowledge of the noise equivalent power (NEP), which is defined for each detector as the noise obtained in dark current measurements with 0.5 s integration time divided by the detector responsivity  $S$  in A/W.

$$NEP = noise / S \quad [W/Hz^{-1/2}] \quad (5.1)$$

The noise figures are based on a measurement of the noise under dark conditions taken in revolution 650 (see Section 5.4). To obtain a noise figure 50 minutes of data were taken with the satellite pointing at a dark region of the sky and with a Fabry-Pérot in the beam with its etalons set non-parallel. The noise was estimated from the standard deviation of a Gaussian curve fitted to a histogram of the photocurrent values after deglitching. As most of the LWS observations, they have been performed using 0.5 s reset times, which is equivalent to a 1 Hz bandwidth.

To avoid making assumptions about the transmission of the telescope and instrument the LWS detector responsivity is not measured directly. Instead the instrument response is derived from the calibration source (Uranus) and its associated model spectrum; it is given as  $S_i(\nu)$  [ $A\text{ cm}^2\ \mu\text{m}\text{ W}^{-1}$ ]. We can calculate the Noise Equivalent Spectral Density (NESD) directly from this value:

$$NESD(\nu) = noise / S_i(\nu) \quad [W\text{ cm}^{-2}\ \mu\text{m}^{-1}\text{ Hz}^{-1/2}] \quad (5.2)$$

To convert this to NEP of the detectors requires knowledge of the telescope effective area and the instrument throughput. The instrument throughput was not directly measured on the ground and is complex to calculate. We therefore refer everything to the entrance aperture of the instrument by assuming knowledge of the instrument spectral resolution in grating mode and the effective area of the ISO telescope as a function of wavelength. This effective area has been calculated from an optical model of the ISO telescope and is given for the central wavelength of each detector in Table 5.5. The spectral resolution of the grating is measured from narrow emission line spectra. The calculated instrument NESD and NEFD (noise equivalent flux density) figures and the estimated instrument NEP are given in Table 5.5.

Table 5.5: *In-orbit sensitivity of the LWS instrument.*

Detector	Centre $\lambda$ [ $\mu\text{m}$ ]	Noise for 0.5 s resets [ $10^{-17}$ A]	NESD [ $10^{-19}\text{W cm}^{-2}$ $\mu\text{m}^{-1}\text{ Hz}^{-1/2}$ ]	Telescope eff. area [ $\text{cm}^2$ ]	NEP [ $10^{-16}$ $\text{W Hz}^{-1/2}$ ]	$\eta\tau$	cross over flux [Jy]
SW1	46.13	4.17	4.43	2460	3.16	0.0046	260
SW2	56.11	3.83	7.75	2431	5.47	0.0046	1460
SW3	66.03	1.91	3.00	2346	2.04	0.0095	710
SW4	75.61	2.98	5.40	2262	3.55	0.0044	1530
SW5	84.68	2.13	4.28	2205	2.74	0.0044	1330
LW1	102.25	2.68	0.849	1922	0.980	0.0095	360
LW2	122.04	2.26	0.231	1838	0.254	0.0095	42
LW3	141.63	3.19	0.122	1838	0.135	0.0142	28
LW4	160.38	3.83	0.202	1753	0.212	0.0108	80
LW5	177.74	2.21	0.691	1583	0.656	0.0033	360

The instrument NEPs increased by an average of a factor of four compared to pre-launch values. A factor of two increase was expected as 0.5 s amplifier resets were used in-orbit, whereas in the ground testing the NEP was measured using 2 s resets and the noise is proportional to the square root of the reset time for resets up to about 4 s (Shaver et al. 1983, [38]). The increased NEP was also due to the decreased responsivity which many of the detectors exhibited in-orbit, some of which was due to the decrease in detector bias voltage (to reduce spontaneous spiking) and the effects of ionising radiation on the detectors. For further analysis of the detector performance in-orbit compared to that on the ground see Leeks et al. 2001, [25].

If the power  $P$  falling on the detectors is low enough so that the noise is dominated by the detector read noise, then the signal-to-noise ratio  $\sigma$  expected in an integration time  $T$  is given by:

$$\sigma = \frac{P}{NEP} \sqrt{2T} \quad (5.3)$$

In the other extreme, when the power falling on the detectors is high enough such that the noise is dominated by the shot noise in the photon stream, the signal-to-noise  $\sigma$  is given by:

$$\sigma = \left( \frac{P}{4h\nu/\eta\tau} \right)^{0.5} \sqrt{2T} \quad (5.4)$$

The power at which the cross over between read noise and photon noise occurs has been derived in a study of the signal-to-noise ratio, performed using internal illuminators measurements (see Swinyard et al. 2000, [41] for more details). They are listed in Table 5.5.

## 5.6 Photometric Accuracy

The accuracy of the photometric calibration is determined by a number of factors:

- The measurements of Uranus that were used for the calibration result in a high S/N spectrum. However for sources brighter than Uranus that are observed long enough, the S/N of the resulting spectrum is limited by the S/N of the Uranus spectrum. The uncertainty in the RSRF is written in the calibration file containing it (see Section 7.3.2.4).
- Transients or memory effects may have an influence on the photometric accuracy of the data. The extent of their influence is not clear at this time.
- Ramp (non-)linearity will also influence the accuracy. It is believed that Derive-SPD is handling this reasonably well, except for really bright sources for which a correction is needed (see Section 5.7). However, comparison of planet and asteroids spectra with their models have suggested that some detectors (LW1, LW2 and LW3) could have a non-linearity behaviour resulting in a few % photometric errors in their ranges. This effect is still under investigation.
- The dark background removal will, especially for faint sources, be an important factor in the photometric accuracy. The effect depends on the source strength and the spectral shape (see Section 6.4). For very faint sources the drift correction applied in AAL may result in negative fluxes (see Section 4.4.1.3).
- Glitches also influence the photometric accuracy, since they have an effect on the responsivity of the detectors.

All these factors together lead to a photometric repeatability for LWS grating mode spectra of 10% between scans on the same detector (this is mainly due to the effect of responsivity changes), and 30% between adjacent detectors (mainly due to dark background removal problems for faint point sources and to the source extent for extended sources).

### 5.6.1 Calibration sources used for photometric purposes

To check the photometric calibration and the relative response calibration several sources were used during PV phase and during the routine calibration observations. Table 5.6 gives the sources used for different calibration purposes.

Table 5.6: Sources used for checking the photometric calibration and the relative response calibration of the LWS grating and Fabry-Pérot subsystems. The primary source for the grating flux calibration is Uranus, the other sources have been observed regularly for monitoring purposes. FG: Fixed Grating; FP: Fabry-Pérot.

Source	Type	Observation
<i>Absolute Flux Calibration and Relative Response Function</i>		
Uranus	planet	End to end grating scans (extended range)
<i>Absolute Flux Calibration: checking and monitoring</i>		
Uranus	planet	FG position On and Off source and full scan
Neptune	planet	FG position On and Off source and full scan
Ceres	asteroid	FG position On and Off source
Pallas	asteroid	FG position On and Off source
Vesta	asteroid	FG position On and Off source
Arcturus	star	FG position On and Off source and full scan
Aldebaran	star	FG position On and Off source and full scan
$\gamma$ Dra	star	FG position On and Off source
S106	HII region	FG and full scan
G298.288–0.331	HII region	FG and full scan
NGC 6543	PN	full grating scan
NGC 7027	PN	full grating scan
<i>Fabry-Pérot ‘throughput correction’ (transmission <math>\times</math> resolution element)</i>		
Mars	planet	Fabry-Pérot scans with fixed grating (mixed mode)

### 5.6.2 LWS photometric stability checked with observations of Mars

Sidher et al. 2000, [39] used ten LWS full grating scan observations (L01) of Mars to demonstrate that the observed  $\sim 3\%$  rotational modulation of the FIR disk-averaged brightness temperature can be detected with the LWS and that it compares very favourably with the predictions of the thermophysical model developed by Rudy et al. 1987, [37]. Figure 5.5 shows the observed and predicted modulation in each detector (except SW1 which is excluded because it suffers from memory effects) as well as a detector-averaged modulation. All these observations were processed as 1/4 s integration ramps by discarding the second-half of each 1/2 s ramp (see Section 5.8) in order to eliminate the non-linear behaviour seen in some LWS detectors for high fluxes. The absolute photometric accuracy evidenced by this figure is better than 10% for most detectors (observations and model differ by up to  $\sim 15\%$  in LW1 probably due to some residual non-linear effects). But what this figure shows primarily is that the LWS photometry is very stable, to a few % level, and that LWS can be used to detect variations as low as 3%. Mars is a very bright source (25 000 Jy at 100  $\mu\text{m}$ ) so the uncertainties due to dark current or background subtraction are minimal. For faint sources, such a high level of stability might be hidden due to dark current uncertainties.

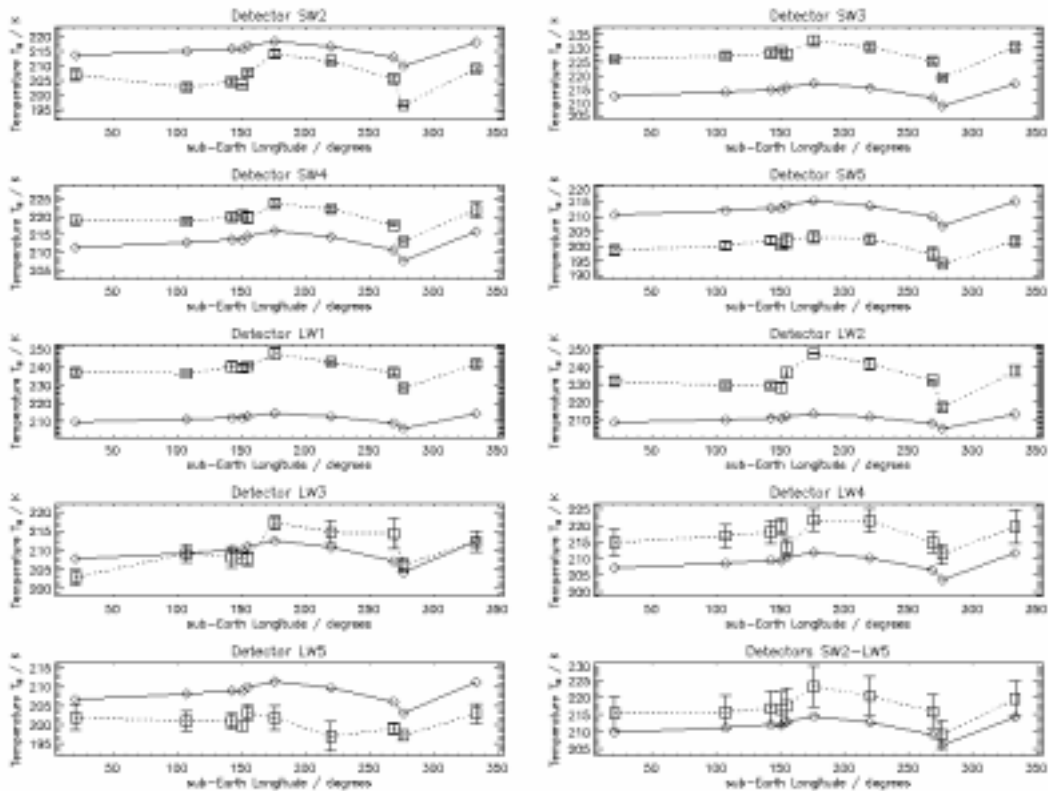


Figure 5.5: *The modulation of the brightness temperature as a function of sub-Earth longitude for detectors SW2 to LW5. The last panel shows the brightness temperature averaged over all nine detectors. The observations are shown as squares and the model as diamonds. The absolute photometric accuracy evidenced by this figure is better than 10% for most detectors but the LWS photometric stability is much better since it allows to detect the predicted variations of  $\sim 3\%$ .*

### 5.6.3 Comparison with IRAS fluxes

An extensive study comparing LWS and IRAS fluxes over a wide range of flux values has been performed by Chan et al. 2001, [6]. A summary of the study is given here highlighting the results concerning the photometric comparison between IRAS and LWS.

#### 5.6.3.1 Sample selection

The objects used for the comparison were selected among all LWS observations on the basis of the following criteria:

1. Objects included in the IRAS Point Source Catalogue (PSC) and observed with LWS with AOT L01
2. Non far-infrared variables
3. Non-fringed LWS data
4. IRAS flux density qualities  $\geq 2$  in the  $60\ \mu\text{m}$  and  $100\ \mu\text{m}$  bands

5.  $F_\nu(100\ \mu\text{m}) < 1000\ \text{Jy}$  – to avoid detector non-linearity
6.  $F_c/F_s < 0.5$  where  $F_c/F_s$  is the flux ratio of cirrus and source
7. IRAS ‘Point source correlation coefficients’ A (100%) or B (99%) in the  $60\ \mu\text{m}$  and  $100\ \mu\text{m}$  bands
8. Only source within  $2'$  search radius
9. IRAS CIRR3  $\leq 254\ \text{MJy/sr}$ , with no strong cirrus background at  $100\ \mu\text{m}$  on the IRAS Sky Atlas Map or on the LWS Parallel Map in the LW1 detector

The sample selected following the above criteria contains around 120 objects.

To check if the comparison of the IRAS and LWS fluxes is source-dependent (via the spectral shape for example), the sample was divided into six groups of different object types: group 1: dust stars; group 2: planetary nebulae; group 3: galaxies; group 4: interstellar medium; group 5: young stellar objects; and group 6: Vega-like stars.

### 5.6.3.2 Corrections applied

The LWS spectra were first corrected for the presence of near-infrared leak features when needed (see Section 6.7 for the description of the feature and the correction).

A ‘cirrus correction’ was applied to take out the contribution of the background flux due to the interstellar medium emission at the source position. Two different corrections were applied: either the IRAS flux was corrected using the CIRR2 value given in the IRAS PSC, or the LWS flux was corrected based on the IRAS CIRR3 value.

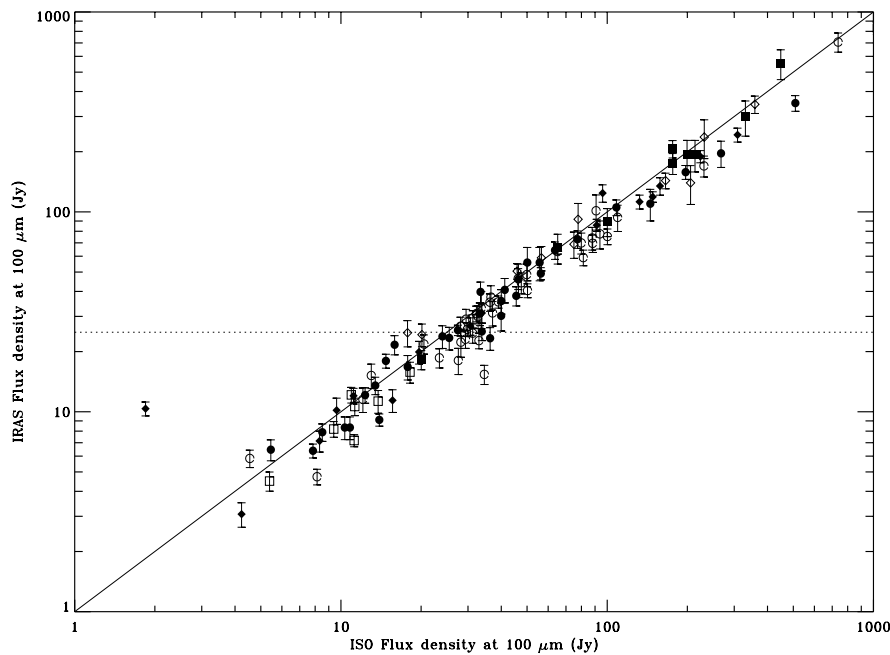


Figure 5.6: Comparison of IRAS and ISO LWS fluxes at  $100\ \mu\text{m}$  for a wide range of fluxes. The different symbols indicate the different groups (object types) listed in the text. No trend is seen with object type.

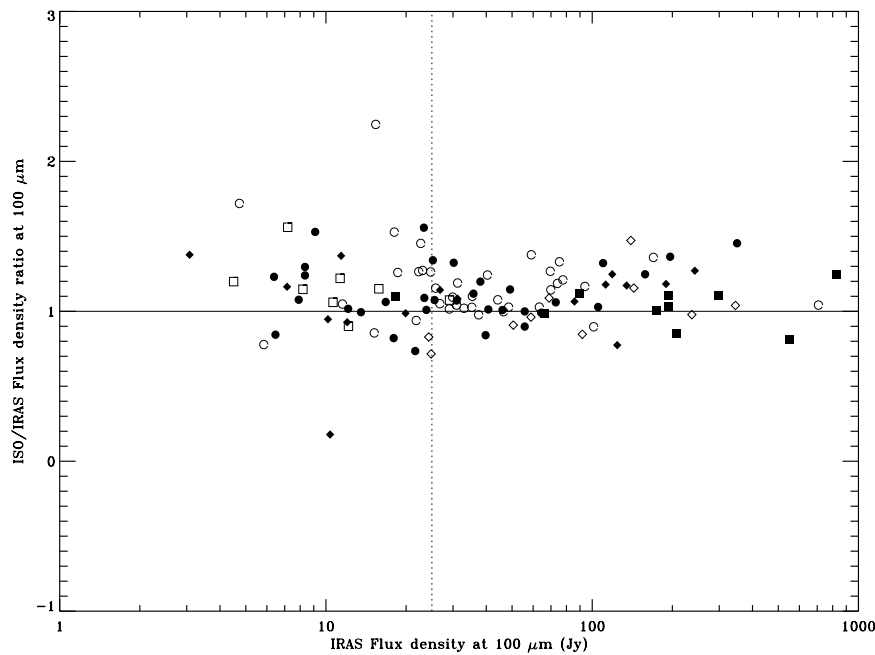


Figure 5.7: *Ratio of the IRAS flux to ISO LWS flux at 100  $\mu\text{m}$  for various source types.*

### 5.6.3.3 Results

Figure 5.6 shows the distribution of IRAS fluxes versus LWS fluxes at 100  $\mu\text{m}$ . Each type group is plotted with a different symbol, and one can check that there is no noticeable difference between the groups.

Figure 5.7 shows the same results, but this time the ratios of LWS to IRAS flux densities are presented.

First one should note that there is a reasonably good agreement between IRAS and ISO flux values (within 30%), in spite of the relatively large uncertainties associated with the needed correction factors.

However, the plots do evidence systematic effects that deserves more attention: in average ISO fluxes are 12.5% higher than IRAS fluxes and the differences seem to increase with increasing flux.

Therefore, to further investigate this behaviour, the flux comparison has been extended to the 60  $\mu\text{m}$  band and has been broadened by including other sources: on one hand, 23 sources used for cross-calibration between SWS and LWS in the context of the ISO cross-calibration (García-Lario 2001, [18]) and on the other hand, 155 galaxies observed with LWS, the fluxes of which were measured and compared to IRAS fluxes by Brauher & Lord 2001, [3]. At 60  $\mu\text{m}$ , the LWS observations do not cover the whole IRAS band. In the cross-calibration sample only sources that were observed also with SWS were used in order to reconstruct the ISO flux at 60  $\mu\text{m}$ ; for the extragalactic sample a small correction was applied in order to compensate for the fraction of the spectral energy distribution not covered by LWS. Complete details are given in García-Lario 2001, [18] and Brauher & Lord 2001, [3].

Figure 5.8 and 5.9 show the ISO versus IRAS fluxes for the three samples.

It is clear on these plots that there is a systematic difference between ISO and IRAS fluxes for bright sources. For faint sources, IRAS and ISO fluxes agree within a few % in average, with a high dispersion due to uncertainties in the dark current. However for brighter sources, ISO fluxes are systematically higher than IRAS fluxes, and the difference increases with flux level, from about 15% difference around 100 Jy, to a level of about 20% for sources up to 400 Jy, and 30–50% for sources brighter than 400 Jy.

The reason for this behaviour is not understood. It is not due to inaccurate dark current subtraction

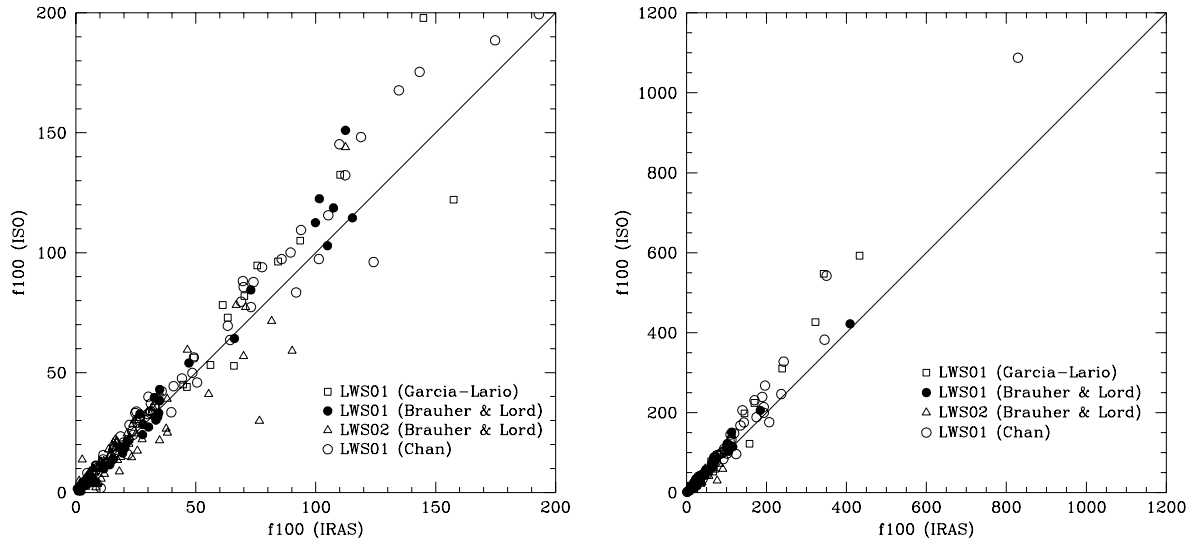


Figure 5.8: Comparison of IRAS and ISO LWS fluxes in Jy at  $100\ \mu\text{m}$  for the three samples described in the text. The first plot is a close-up of the second one at low fluxes.

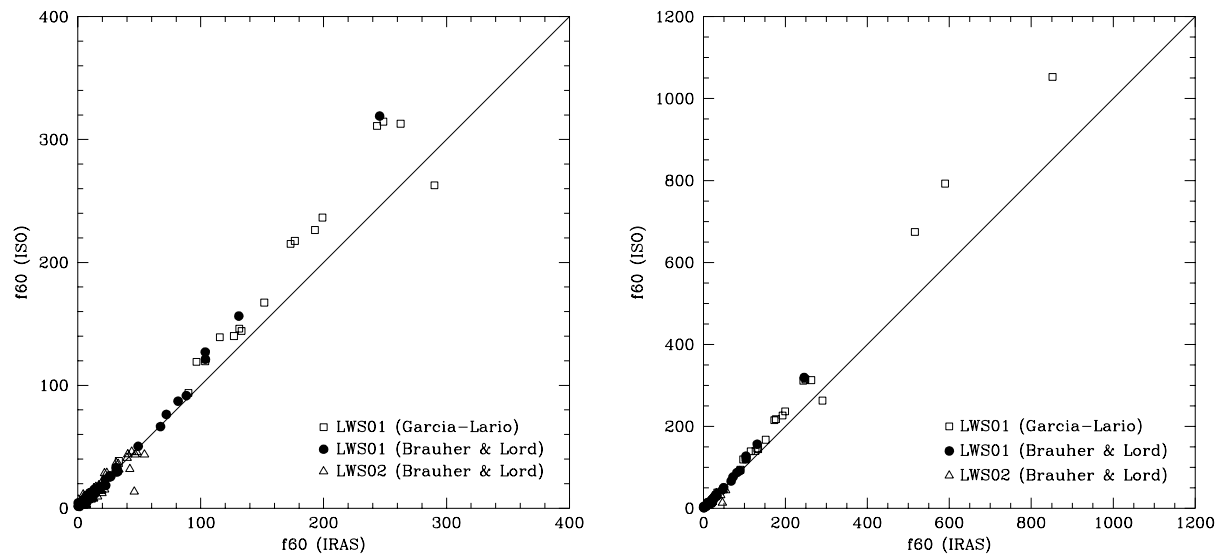


Figure 5.9: Comparison of IRAS and ISO LWS fluxes in Jy at  $60\ \mu\text{m}$ . The first plot is a close-up of the second one at low fluxes.

since this would affect the faintest sources unlike what we observe here. On the other hand it does not seem to be due to cirrus background contamination, since no trend is observed with the IRAS *CIRR2* parameter value.

A possible cause could be some non-linear effects in the IR detectors. However, the problem could be associated with IRAS and not with ISO.

Indeed, Figure IV.A.4.2 of the IRAS Explanatory Supplement, ([20]) does evidence detector non-linearity behaviour and Section VI.B.4.d quotes errors of respectively 30% and 70% at 60 and 100  $\mu\text{m}$  for sources above 100 Jy.

Further investigation is needed to decide if the systematic difference is imputable to IRAS or LWS calibration inaccuracies.

#### 5.6.4 Checking the Fabry-Pérot photometric accuracy

For the Fabry-Pérot mode, the photometric accuracy was determined by comparing the integrated line fluxes observed with the FP with the fluxes observed with the grating or line fluxes published in the literature. The sources and lines are given in Table 5.7. It was found that for strong lines accuracy is typically better than 30%. For faint lines however, the FP fluxes can be off by almost a factor two. This is mainly due to the removal of the dark current which is known to be problematic for low signal levels (see also Section 4.4.1.3 and 5.4).

Table 5.7: Sources and lines used for the determination of the photometric accuracy of the Fabry-Pérot data.

Source	Type	Lines
NGC 6543	PN	57.3, 88.4 $\mu\text{m}$
NGC 7027	PN	51.8, 63.2, 145.5, 157.7 $\mu\text{m}$
NGC 6357I	HII region	51.8, 57.3, 63.2, 88.4, 145.5, 157.7 $\mu\text{m}$
M 82	Galaxy	63.2, 88.4, 121.9, 157.7 $\mu\text{m}$

## 5.7 The Strong Source Correction

### 5.7.1 The reason for the correction

The responses of detectors LW1–LW4 are non-linear when they are exposed to strong sources. This non-linearity means that the photocurrent is lower than expected for the flux incident on the detectors. This occurs because the voltage produced by the radiation on the detectors de-biases them. This de-biasing lowers the responsivity hence an increase in the input signal does not produce the same increase in the output voltage, the value is lower and so the ramps are curved.

Figure 5.10 shows a curved ramp for a typical strong source. The gradient of the green line shows the value of  $\Delta V/\Delta t$  (see Section 4.3.6) for the ramp (the dashed lines show the change in voltage and time). The red line indicates the initial gradient of the ramp where the detector does not suffer from de-biasing. Thus, it can be seen that due to de-biasing the photocurrent obtained from the  $\Delta V/\Delta t$  method underestimates the true source flux of strong sources. This becomes worse with stronger sources as the ramp curves more and could eventually flatten off. For any detector the instrument transmission varies across the bandpass filter. At the edges of the detector filters there is a low response to any signal and the effects of non-linearity are correspondingly small. Where the instrument transmission is higher the signal suffers from more non-linearity as the flux on the detector is higher. This difference across the instrument transmission means that an individual detector spectrum is more non-linear near the centre of the wavelength range, where generally the transmission is high, than it is at the short and long wavelength cut-offs. This produces strange shaped (saggy) sub-spectra (see example in Figure 6.11).

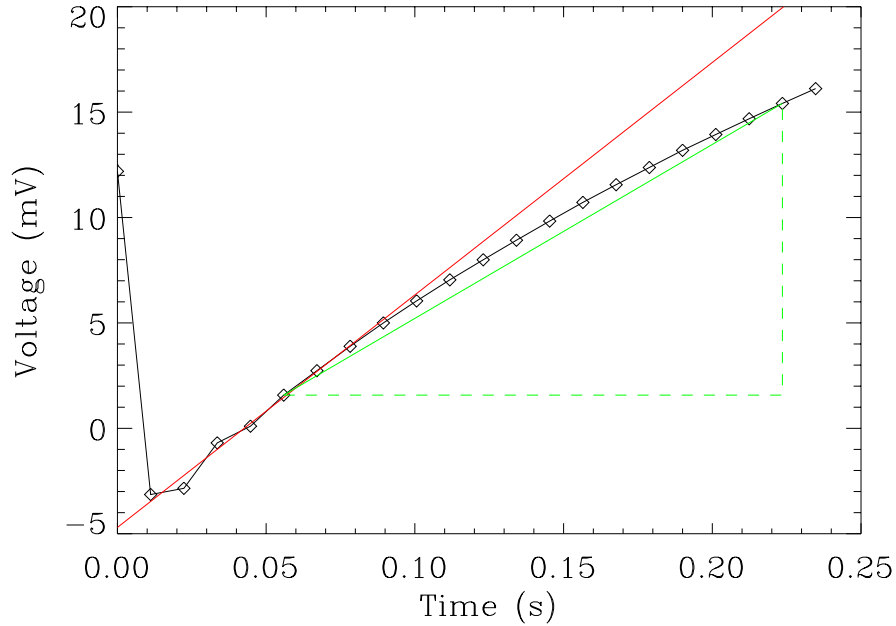


Figure 5.10: A curved ramp for a typical strong source. The green dashed lines show the change in voltage and time. The gradient of the green continuous line gives the value of  $\Delta V/\Delta t$ . The red line indicates a guess at the gradient of the ramp without de-biasing.

### 5.7.2 The correction

This non-linearity can be determined using the strong source Saturn, which is well modelled and is well calibrated in the short wavelength detectors (Davis et al. 1996, [13]). The flux model and the instrument transmission (RSRF) are used to find the photocurrents which we would expect for a linear system. These are then compared with the photocurrents found from the LWS observations of Saturn.

This comparison is shown in Figure 5.11 where the model versus LWS photocurrents ( $I_{\text{model}}$  and  $I_{\text{data}}$ ) are plotted as a function of wavelength. There is clearly a relationship between the two and we fit the second order polynomial (shown by the dashed line in Figure 5.11):

$$I_{\text{model}} = a I_{\text{data}} + b I_{\text{data}}^2, \quad (5.5)$$

where  $a$  and  $b$  are the first and second order coefficients. This is done for all of the detectors affected by non-linearity (LW1–LW4). The coefficients are then applied to any source photocurrents ( $I_{\text{source}}$ ) to produce the photocurrents corrected for the non-linearity ( $I_{\text{corrected}}$ ) using

$$I_{\text{corrected}} = a I_{\text{source}} + b I_{\text{source}}^2 \quad (5.6)$$

These corrected photocurrents are then calibrated using the LCGR file derived from Uranus as usual (see Section 5.2) to produce the flux spectrum.

Figure 5.12 shows the result of this correction for the HII region W28 A2 (the uncorrected spectrum is shown in Figure 6.11). To remove the scaling of individual sub-spectra that was introduced by the corrections, the sub-spectra were also scaled together using ISAP to produce a relative calibration.

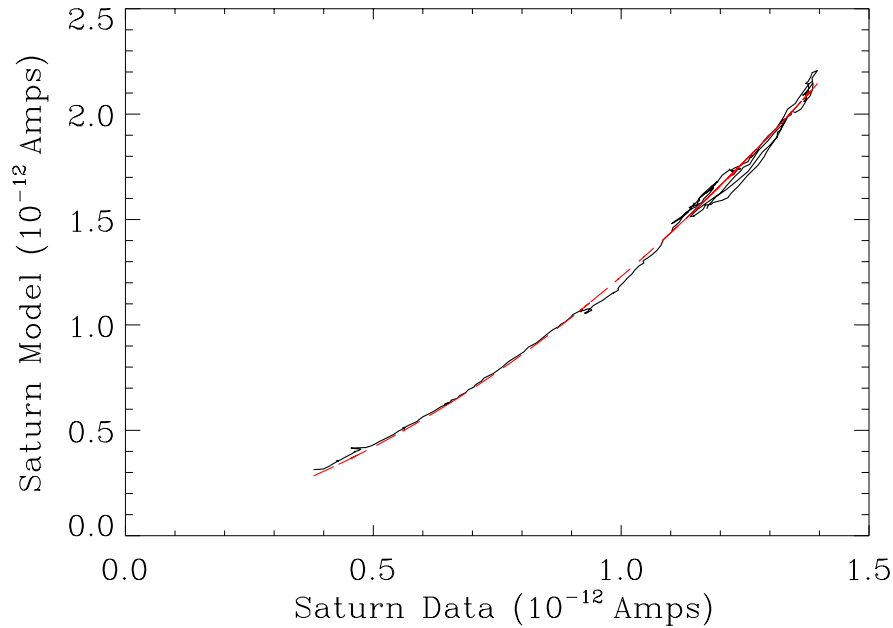


Figure 5.11: *Plot of the modelled versus observed photocurrents of Saturn for LW3. The dashed line shows the second order fit to the data.*

This shows that the sub-spectra now have similar shapes. From the figure it can be seen that the ‘saggy’ has been removed from the sub-spectra and they line up smoothly. Also fringing, which is seen in LWS observations of extended sources, is observed in the corrected W28 A2 spectrum (fringing is discussed in Section 2.3 and in Section 6.2).

This non-linear flux response correction is applied to LW1 and LW2–LW4, i.e. one unstressed detector and three of the four stressed detectors. Table 5.8 gives the instrument responsivity for each LWS detector, as reported in Swinyard et al. 2000, [41] grouped according to detector type (also see Section 2.6 for bias voltages). The responsivity of LW1 is 3–4 times greater than that of the other unstressed Ge:Ga detectors. This high responsivity is the cause of the non-linearity and explains why this detector requires the correction. The responsivities of detectors LW2–LW4 are also high, but that of the last stressed detector, LW5, is much lower (by a factor of 3–8). Due to this low responsivity, LW5’s data do not suffer noticeably from non-linearity and hence do not require the correction. Section 6.10 explains how to decide if your data need the correction, how to get them corrected and the procedure that is followed.

### 5.7.3 Future

Further investigations are underway, which should result in a new way of doing the strong source correction, which will be more reliable and produce better calibrated spectra. This will correct spectra for non-linearities seen in detector sub-spectra by their saggy (as described in Section 5.7 and 6.10). These non-linearities are due to the de-biasing of the detectors (LW1–LW4) which makes the integration ramps lower than expected, leading to an underestimation of the signal. Also the de-biasing of the detectors changes the relative spectral response of the detectors (the overall responsivity decreases and the spectral response shape changes). A new strong source correction to account for both of these should be available in a future release of LIA.

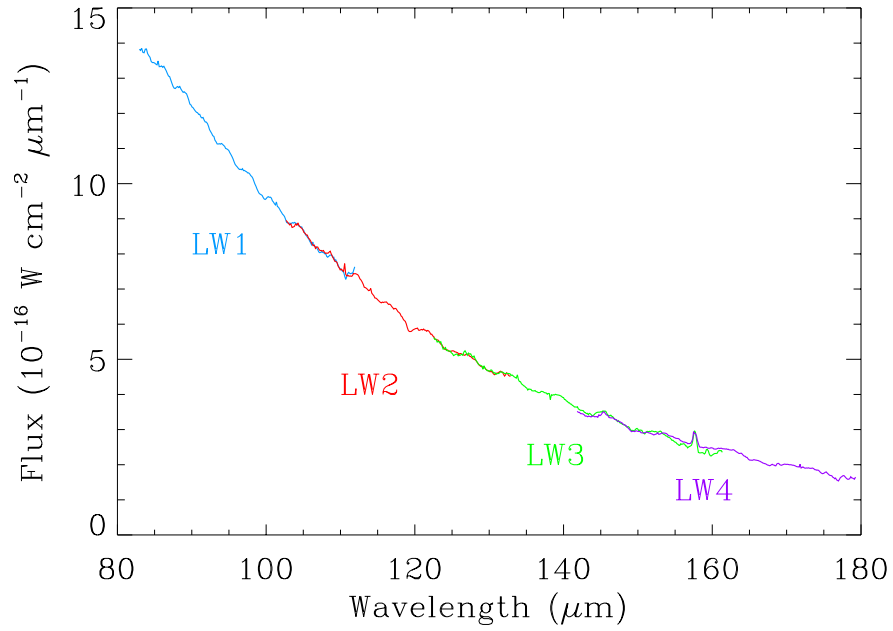


Figure 5.12: The plot shows part of the spectrum of the HII region W28 A2 with the strong source correction applied (the uncorrected spectrum is shown in Figure 6.11). The detector sub-spectra have been scaled together to assist comparison of the shapes of the overlaps.

Table 5.8: The in-orbit detector responsivities.

Detector	Type	Responsivity [A/W]
SW1	Ge:Be	0.132
SW2	Ge:Ga(u)	0.070
SW3	Ge:Ga(u)	0.094
SW4	Ge:Ga(u)	0.084
SW5	Ge:Ga(u)	0.078
LW1	Ge:Ga(u)	0.274
LW2	Ge:Ga(s)	0.886
LW3	Ge:Ga(s)	2.365
LW4	Ge:Ga(s)	1.803
LW5	Ge:Ga(s)	0.337

## 5.8 Quarter-Second Processing

The strong source correction (see Section 5.7) was made with Saturn quarter-second ramps. Applying this correction directly to observations of strong sources, where the ramp lengths are one half-second, does not remove the non-linearities as the data are de-biased more than corresponding quarter-second ramps. This is seen in Figure 5.13 where a non-linear half-second ramp is shown by the + symbols. The dotted vertical lines mark out the first quarter-second of the ramp and whole half-second ramp. It can be seen that the ramp curves over more as time increases. This de-biasing effect is even more apparent when one considers the  $\Delta V/\Delta t$  value of the first quarter-second and the whole half-second ramp (indicated by the slope of the long and short dashes respectively). This shows that there is a difference in calibration for quarter and half-second ramps, due to the de-biasing. Hence half-second data which suffer from ‘saggy’ should have their ramps reprocessed as if they are quarter-second ramps. This is done by discarding the 22 samples from the end of a ramp, which make up the extra quarter-second. Also, as in the normal processing, a further sample from the end is discarded because of the end of the format point and the usual amount is discarded from the start. This makes the ramps equivalent to the data used in real quarter-second ramps, by using exactly the same part of ramp. If any of the remaining points are unusable, such as being at the voltage limit of the ADC (see Figure 5.14), they are also discarded. [The illuminators however are processed as normal half-second ramps, as described in Section 4.3.6. This is done as their calibration is based on half-second length ramps and also their ramps should not be affected by non-linearity.] In doing this the non-linearity suffered will be to the same degree as those ramps of the correction source, Saturn, and the correction can be applied successfully to the photocurrents found from these ‘quarter-second ramps’.

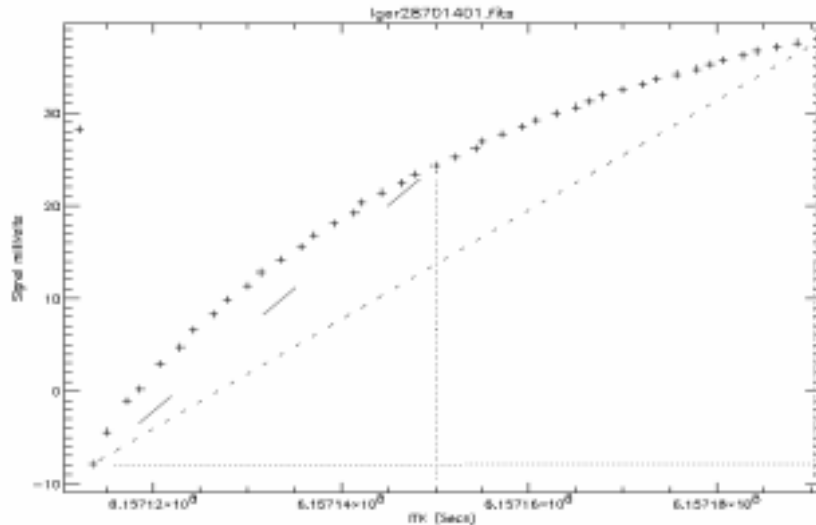


Figure 5.13: A half-second ramp of Sagittarius B2 from LW3. The gradient of the long dashed line shows the value of  $\Delta V/\Delta t$  from the first quarter-second of the ramp, marked out by dotted lines. The short dashed line gives  $\Delta V/\Delta t$  for the half-second ramp, also marked by dotted lines.

### 5.8.1 LW5: quarter- versus half-second processing

For LW5, with quarter-second ramps, the strong source correction is not needed as these ramps are linear. However, when strong sources are observed with half-second integrations the ramps may become non-linear. Hence for this detector the quarter-second and normal processed data (Figure 5.15 shows an

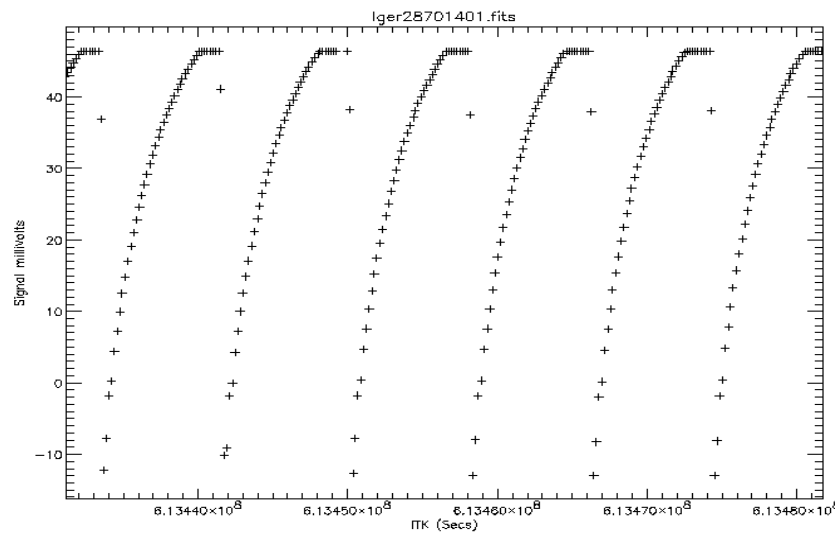


Figure 5.14: Half-second ramps of Sagittarius B2 from LW3 hitting the ADC rail.

example of these data) are compared with the corrected scaled LW4 data. The data which better match those of LW4 are used.

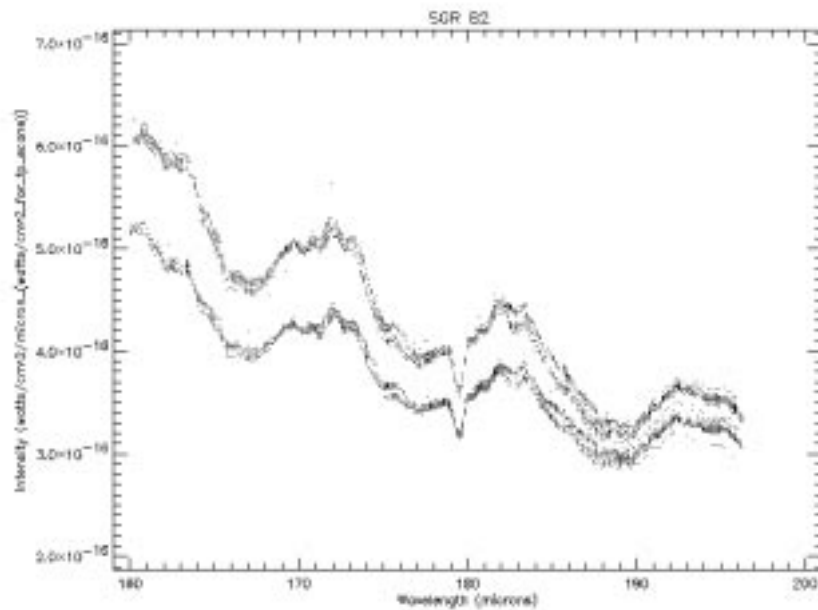


Figure 5.15: LW5 Sagittarius B2 with quarter-second processing (upper) and half-second processing (lower).

### 5.8.2 Summary of processing for various strength sources

- Weak sources have linear ramps and therefore quarter- and half-second ramps have the same calibration and do not need a correction.
- Strong sources with quarter-second ramps need to have the strong source correction applied to LW1–LW4. The other detectors do not need a correction.
- For strong sources with half-second ramps SW1–SW5 produce linear ramps and so they are processed using the usual amount of ramp. LW1–LW4 should be processed using only the first quarter-second of the ramps and have the strong source correction applied to them. LW5 should also be processed using both half- and quarter-seconds of the ramp and then be compared with the LW4 data (but they do not require a strong source correction).

## 5.9 Instrumental Field of View: The Beam Profile

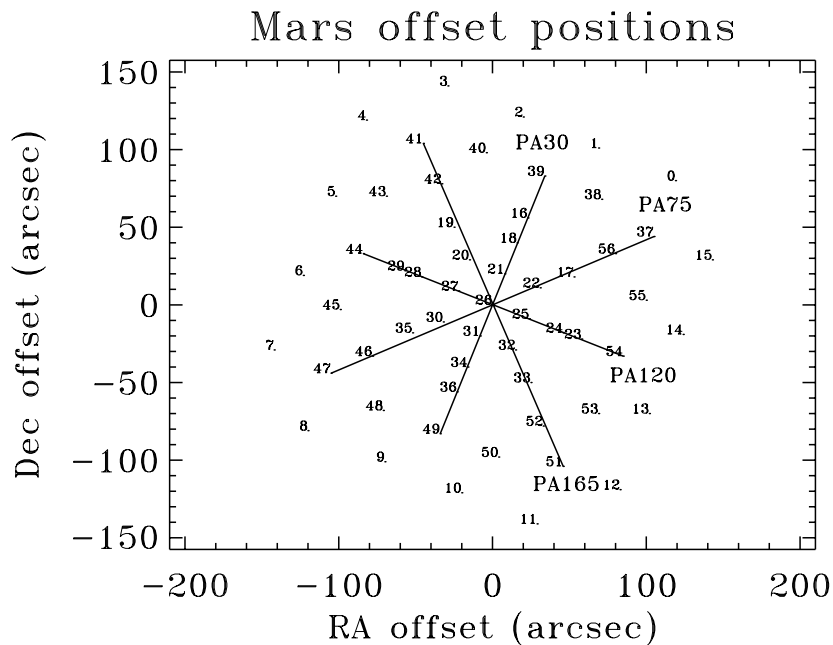


Figure 5.16: *Offset positions of the Mars beam profile observations.*

The beam profile has been derived from a series of standard bias, grating scan observations of Mars. One observation was made on-axis and the others were distributed around the field as shown in Figure 5.16. The flux at three wavelengths in each detector, at each of the raster positions, are used to describe the radial sensitivity of the instrument and a parameterisation defines the beam profile. In addition subsets of the data along the four radial alignments, which are labelled PA30, PA75, PA120 and PA165 on Figure 5.16, have been analysed to investigate possible asymmetries in the beam profile.

Before discussing the beam profile it is important to appreciate the properties of the optical path leading to the LWS detectors as these have a profound impact on the beam profile. The optical train of the LWS consist of the contour field mirror that allows a beam of  $\sim 120''$  to fall on the complex mirror M2, which is inclined at  $\sim 22^\circ$  to the incoming beam. M2 diverts the beam by  $\sim 44^\circ$  back through a semi-cylindrical

cut-out in the contour field mirror and then presents an elliptical beam of  $\sim 105 \times 97''$  (nominal FWHM) to the collimator, the LWS entrance pupil, the re-imaging mirror and detectors. Immediately in front of each detector is a rectangular aperture with rounded ends, which when projected onto the sky is approximately elliptical with dimensions of  $104 \times 157''$  at SW1 and  $138 \times 131''$  at LW5 in the directions along and across dispersion respectively. The long and short axes of M2 projected onto the sky are PA30 and PA120 (Y and Z axes) respectively.

As the detector apertures are nominally larger than the incoming beam from M2 it is, in fact, M2 that defines the aperture of the detectors, and the character of the optics determines the instrumental profile. Perversely, the substrate that supports M2 is also reflective, particularly at longer wavelengths, and is now believed to be responsible for the fringing that is seen in off-axis targets. A second consequence of this is that the instrumental profile will have weak wings out to  $\sim 120''$  diameter (the size of the contour field mirror).

The other feature of LWS grating spectra of objects observed off-axis is the poor stitching between adjacent detectors, which is often referred to as fracturing. The problem is apparently worse for objects in the part of the field that passes close to the cut-out in the contour field mirror. The origin of this problem is unknown but it introduces a complex, wavelength-dependent asymmetry into the instrumental profile. These problems are described in more detail in Sections 6.2 and 6.3.

### 5.9.1 The beam profile

The observed beam profile is the result of the convolution of the telescope PSF and the instrumental profile of each detector. Ideally the telescope PSF would be an Airy profile but the central obscuration and secondary supports, and any optical imperfections will conspire to redistribute power from the core of the profile to the Airy rings. Although a point source is being used to probe the structure of the beam, the width of the PSF, which is essentially an Airy profile, increases from  $\sim 25$  to  $100''$  (FWHM) between  $46 \mu\text{m}$  and  $178 \mu\text{m}$ , and at the longer wavelengths becomes comparable with the size of the beam. Due to the problems of fracturing and fringing the true shape of the instrumental profile is largely unknown.

To determine the effective beam size the observed fluxes at three wavelengths in each detector have been compared with those derived from a convolution of the telescope PSF with apertures of various sizes. The latest model of the telescope PSF includes the effects of the central obscuration and its supporting structure, and indicate that the power in the Airy rings is increased and that the wings of the profile contain 2-D structure. The asymmetry introduced into the profile is due to the three-legged secondary support. The aperture has been assumed to be circular with a rectangular profile.

It has previously been recognised that the effective apertures are significantly smaller than the nominal value of  $100''$ , based on the size of the beam from M2. The best value for most of the detectors lies close to  $80''$ , and for LW3, LW4 and LW5 is somewhat smaller than this. At the longest wavelengths the width of the telescope PSF is larger than the aperture itself which makes these determinations more difficult. An uncertainty of one arcsec in the radius corresponds to about 5% in the effective area of the aperture. Also, although a simple circular aperture has been adopted, more complex shapes can provide a better description of the asymmetries, under some circumstances. However, the range of possible shapes and number of free parameters makes this approach untenable.

The relative flux at each of the observed offset positions (see Figure 5.16) is shown for each detector in Figure 5.17 with the convolution of the telescope PSF and the best fit composite aperture superimposed. At shorter wavelengths the telescope PSF is narrow enough to probe the structure of the rectangular (top hat) instrumental profile and some indication of its shape can be seen. As the telescope PSF broadens towards longer wavelengths the details of the instrumental profile become washed out and the observed profile becomes more Gaussian.

The resulting estimates for the effective beam size for each detector are given in arcsec in Table 5.9.

The effective solid angle of the detectors is required to determine the point/extended source flux correction, for the conversion of observed flux to flux per steradian for extended sources and for the calibration

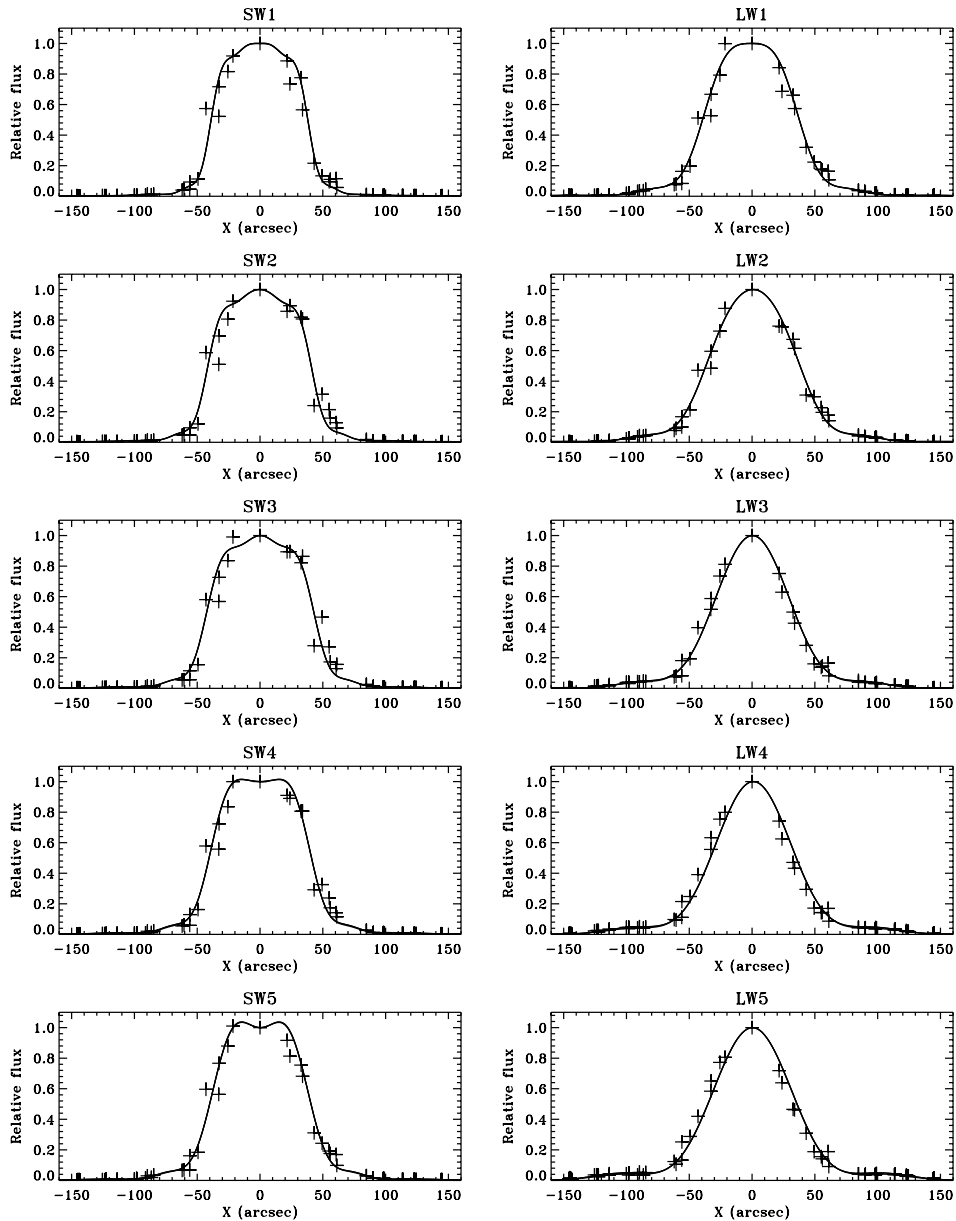


Figure 5.17: *The beam profiles for the central wavelength of each detector. The observed relative flux at each offset position is plotted against radius, with the sign taken from the RA offset in Figure 5.16. The line on each plot shows the calculated radial profile.*

of sources observed in parallel and serendipity mode (see Table 5.10).

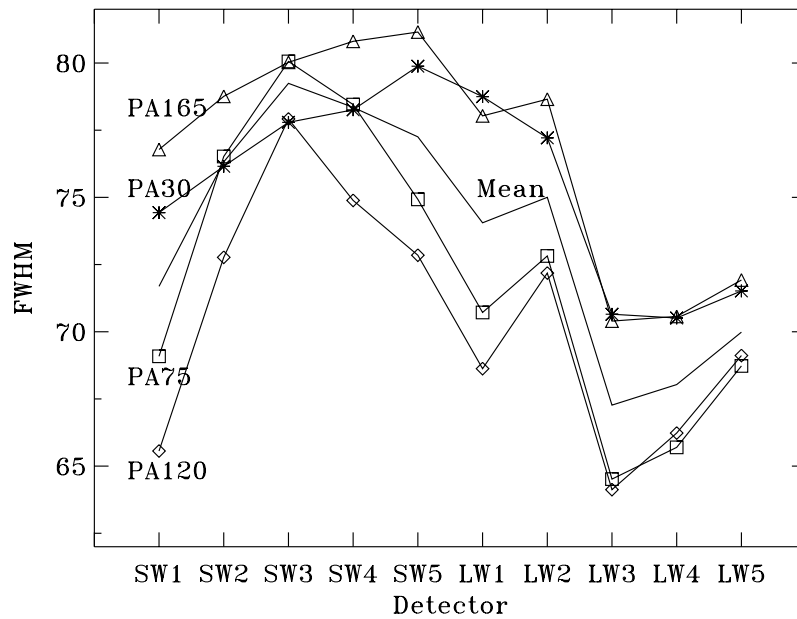
### 5.9.2 Asymmetry

It is already clear from Figure 5.17 there is some asymmetry in the beam profile, with groups of points lying systematically off the lines. The question of symmetry is not straightforward, and a simple analysis of the relative mean fluxes for the four radial alignments begins to show this.

Table 5.9: *Effective aperture of the detectors.*

Detector	Effective radius ["]	Detector	Effective radius ["]
SW1	39.4	LW1	38.6
SW2	42.3	LW2	38.9
SW3	43.5	LW3	35.5
SW4	40.9	LW4	34.7
SW5	39.5	LW5	33.2

Each of the radial alignments is a subset of the data which define the global mean profile. The four alignments are separated by approximately  $45^\circ$  to create two orthogonal pairs, with the PA30 set aligned along the Y axis, and the PA120 set aligned along the Z axis of M2. A Gaussian profile constrained to the optical axis was fitted to each set with the on-axis point and those with  $r > 65''$  excluded. Although each alignment contains nine points, only six points are used in the PA30 and PA120 solutions and only four points in the PA75 and PA165 solutions.

Figure 5.18: *FWHM vs. detector for the four alignments.*

Of the parameters derived from these solutions the FWHM is probably the most reliable, and this is shown in Figure 5.18 for the different detectors. Although there is considerable scatter the behaviour is fairly consistent. Each alignment shows an increase in FWHM through the SW detectors and then a subsequent decline, which reflects the behaviour of a Gaussian fit to all the data, and the run of effective aperture sizes in the table above. In more detail it can be seen that the alignments fall naturally into two pairs with very similar behaviour. PA75 and PA120 show much more variation than PA30 and PA165, and peak at SW3 as opposed to SW5. In particular PA75 and PA120 run through the fractured region;

see the spectra in Figure 6.3 of raster positions 27 and 30 in Figure 5.16.

### 5.9.3 Flux correction for extended sources

The LWS flux scale is based on a point source calibration, although beyond the diffraction limit at about  $110 \mu\text{m}$  a substantial fraction of the flux from an on-axis point source is diffracted out of the aperture. In fact there are significant diffraction losses for all LWS detectors but provided the calibration is applied to point sources observed on-axis these losses are irrelevant because they are cancelled out in the calibration process. However, for extended sources the diffraction losses do not occur and so a correction has to be applied to correctly place the derived fluxes on the point source calibration scale. The correction factor to apply to the fluxes in case of extended sources has been calculated at three wavelengths per detector. These factors are given as  $f$  in Table 5.10.

### 5.9.4 Extended source flux per unit area

To convert the observed flux of an extended source to flux per steradian requires both the extended source correction factor ( $f$ , see above) and the effective aperture in steradian explicitly.

The corrected extended source flux for an observed flux  $F$  given in Jy is  $S = F \times f / (\omega \times 10^6)$  MJy/sr, where  $f$  is the extended source correction and  $\omega$  is the effective solid angle of the beam in sr. These values are now given at three different wavelengths per detector (from Version 2.1 of this volume of the ISO Handbook on). As visible on Figure 5.19, for most detectors the resulting correction factor presents a gradient with wavelength. This has the positive consequence that with this correction there is a better agreement between the corrected fluxes of extended sources in the overlap regions between detectors.

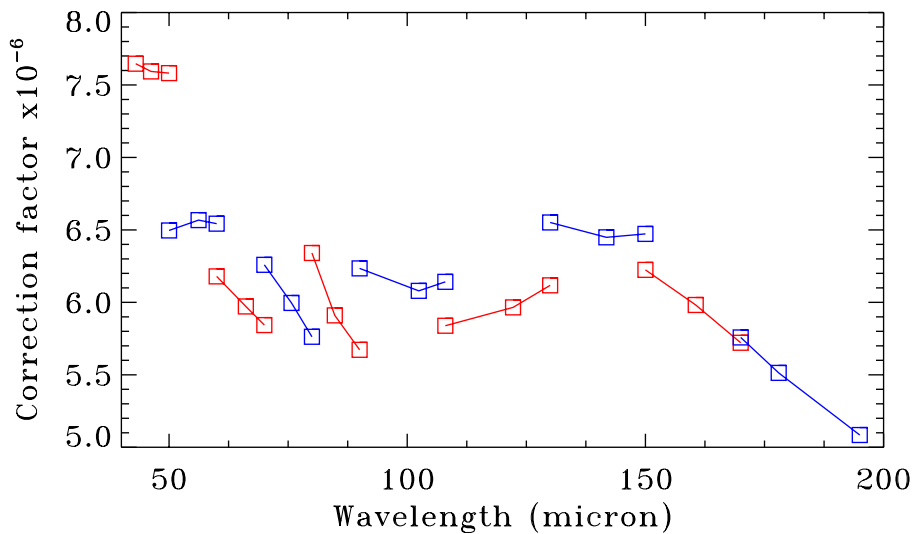


Figure 5.19: Correction factor for extended sources ( $f/(\omega \times 10^6)$ ) versus wavelength. The correction factor is given at three different wavelengths per detector. Detectors are given alternately in red and blue; red, SW1, SW3, SW5, LW2, LW4, and blue, SW2, SW4, LW1, LW3 and LW5.

An LIA routine has been provided that applies this correction to averaged, de-fringed LSAN files called EXTENDED\_FLUX. However, these corrections are derived under the assumption of a smooth and very

Table 5.10: Table of extended source correction ( $f$ ) and effective solid angle of the beam ( $\omega$ ) for the different LWS detectors, at three different wavelengths per detector. The effective aperture radius in arcsec ( $r_e$ ) is also given at the same wavelengths.

Detector	$\lambda[\mu\text{m}]$	$f$	$r_e ["]$	$\omega \times 10^6 [\text{sr}]$
SW1	43.0	0.8721	39.3	0.1140
	46.2220	0.8704	39.4	0.1146
	50.0	0.8691	39.4	0.1146
SW2	50.0	0.8705	42.6	0.1340
	56.2033	0.8677	42.3	0.1321
	60.0	0.8563	42.1	0.1308
SW3	60.0	0.8634	43.5	0.1397
	66.1173	0.8421	43.7	0.1410
	70.0	0.8127	43.4	0.1390
SW4	70.0	0.7845	41.2	0.1253
	75.6989	0.7334	40.7	0.1223
	80.0	0.7118	40.9	0.1235
SW5	80.0	0.6904	38.4	0.1088
	84.7977	0.6878	39.7	0.1163
	90.0	0.6803	40.3	0.1199
LW1	90.0	0.6753	38.3	0.1083
	102.425	0.6758	38.8	0.1111
	108.0	0.6757	38.6	0.1100
LW2	108.0	0.6761	39.6	0.1157
	122.218	0.6734	39.1	0.1128
	130.0	0.6557	38.1	0.1071
LW3	130.0	0.6445	36.5	0.0983
	141.809	0.6035	35.6	0.0935
	150.0	0.5623	34.3	0.0868
LW4	150.0	0.5727	35.3	0.0920
	160.554	0.5411	35.0	0.0904
	170.0	0.4855	33.9	0.0848
LW5	170.0	0.5002	34.3	0.0868
	177.971	0.4596	33.6	0.0833
	195.0	0.3749	31.6	0.0737

extended flux distribution. In the real world, structured or embedded sources could produce significant discrepancies from the ideal situation, and, with it, differences in flux.

LWS observations have been made at a number of positions in the Trumpler 14 and 16, and Galactic Centre fields and these have been compared with the IRAS 100  $\mu\text{m}$  fluxes at the same positions. Both fields contain a large area of extended emission, which although relatively smooth, does change by a factor of  $\sim 40$  over all. Figure 5.20 shows the comparison of the converted LWS and IRAS 100  $\mu\text{m}$  fluxes using the current LWS calibration. These measurements give a mean ratio, LWS/IRAS  $\sim 1.0 \pm 0.1$ . Ideally for this comparison the extended flux should be distributed as evenly as possible, and part of the uncertainty is probably due to unresolved structure within the beam.

For fields containing multiple sources the observed flux will depend critically on the precise positions of

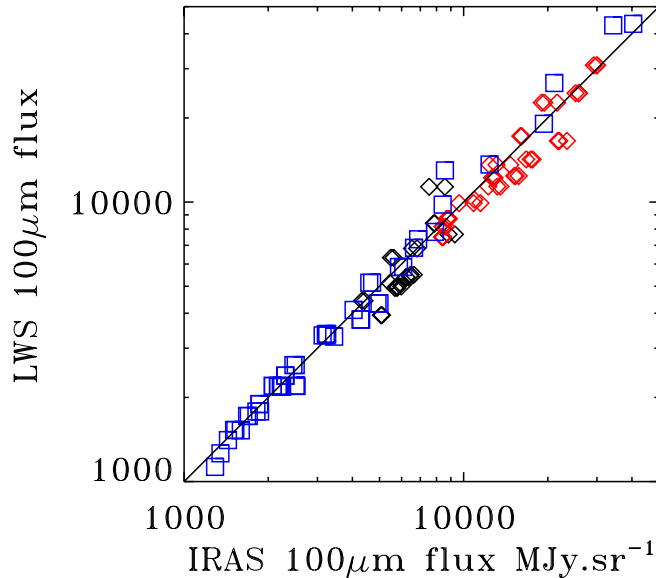


Figure 5.20: Comparison of LWS and IRAS 100  $\mu\text{m}$  fluxes in the Trumpler 14 (red diamonds) and 16 (black diamonds), and Galactic Centre (blue squares) fields.

the sources relative to the optical axis. To recover or model the observed flux will require positional information on the sources and a deconvolution with the telescope PSF and instrumental profile. Indeed, for single point sources observed off-axis a similar procedure will be required to recover the correct flux.

### 5.9.5 Effect of the ISO PSF at large distances: check of the straylight around Jupiter

A complete study of the beam profile of the LWS has been performed only for distances within  $150''$  of the central source. Rasters of larger extent would have been too time-consuming. There were, however, spot checks of the flux entering the instrument at even larger distances from a very strong source: The off-position spectra for Ganymede and Callisto. They provide us with the fluxes from Jupiter, when the aperture of the LWS was pointed at distances of  $5'$  and  $9'$  from this planet. The results are shown in Table 5.11 and compared to the fluxes expected from a model of the PSF by Okumura 2000, [30]; see Figure 5.21.

The significance of the correlation between the measured flux and the model PSF is  $2.4\sigma$  for detector SW2 at  $56\mu\text{m}$  and  $2.6\sigma$  for detector LW2 at  $122\mu\text{m}$ . The correlation between flux and distance or angle alone is much weaker, hence the model PSF reflects correctly the observed flux pattern up to a distance of  $9'$  from the source. On the other hand the measured fluxes are systematically higher than what is expected from the optical model, which could be due either to the fact that Jupiter is not a point source or to the existence of significant wings in the beam profile.

Table 5.11: Flux at a certain distance of Jupiter normalised by the flux of Jupiter: Comparison of LWS observations of Jupiter straylight with a model of the ISO PSF by Okumura 2000, [30].

Distance [arcsec]	Angle to S/C Z [°]	SW2	model	LW2	model
		$I_{off}^{SW2}/I_J$ $\times 10^{-6}$	$I_{off}^{PSF}/I_J$ $\times 10^{-6}$	$I_{off}^{LW2}/I_J$ $\times 10^{-6}$	$I_{off}^{PSF}/I_J$ $\times 10^{-6}$
282	38	860	77	1100	406
291	325	440	94	890	125
530	113	84	14	300	66
532	20	38	0.1	100	25
535	2	27	5.5	52	8
537	148	73	13	350	26
545	344	53	2.8	190	52

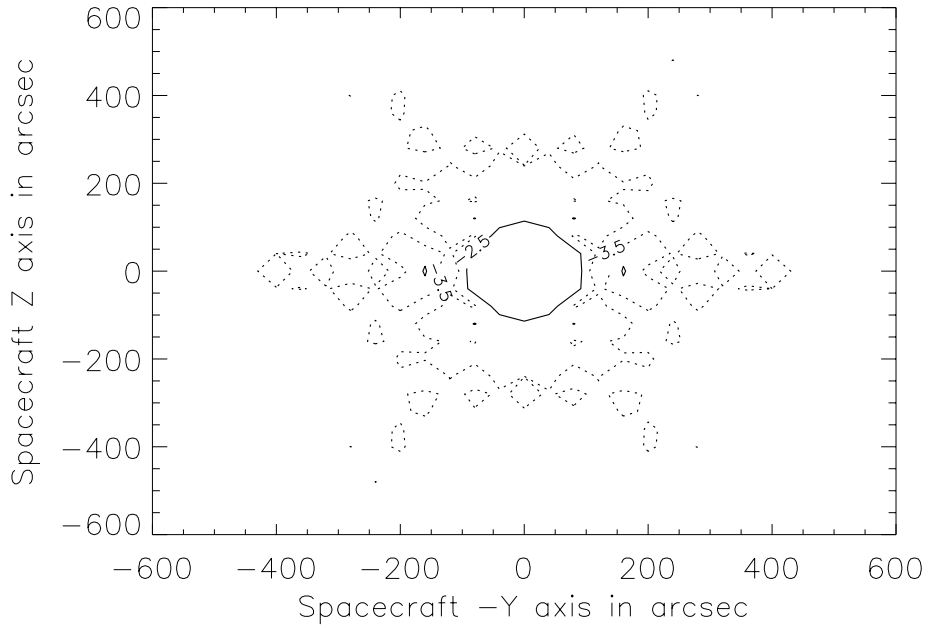


Figure 5.21: A model of the point spread function as sampled with the LWS. The contours show the drop in intensity by factors  $10^{-2.5}$  (continuous line) and  $10^{-3.5}$  (dotted line) compared to the on-source value.

## 5.10 Grating Wavelength Calibration

### 5.10.1 Basic principles and calibration strategy

The LWS diffraction grating was mounted in a scanning mechanism which rotated through  $\pm 7^\circ$ , allowing to cover the extended range of wavelengths of each detector. The wavelength corresponding to each scanning position was determined by the grating angle  $\theta_i$  (angle between the input aperture direction and the normal to the grating) and the detector angle  $\theta_d$  (angle between the input aperture direction and the detector direction), which was a constant for a given detector.

$$\lambda = (\sin\theta_i - \sin(\theta_d - \theta_i))/Nk \quad (5.7)$$

where  $N$  is the groove density of the grating (7.9 lines per mm) and  $k$  is the order: the grating was used in first order for the wavelength range 84–197  $\mu\text{m}$  with the five long wavelength detectors LW1 to LW5, and in second order for the wavelength range 43–93  $\mu\text{m}$  with the five short wavelength detectors SW1 to SW5.

In operations, the grating position was actually monitored via the engineering unit called LVDT (linear variable differential transformer). Therefore, once the ten detector angles were known, the wavelength calibration consisted in finding the relationship between the engineering units LVDT and the actual grating angle  $\theta_i$ .

This was done by fitting a third order polynomial to a large database consisting of the measurements of emission line centroids in terms of LVDT units associated with the expected wavelengths of the lines for a number of calibration sources observed throughout the ISO mission.

### 5.10.2 Calibration sources and types of observations

The wavelength standards are mainly planetary nebulae and HII regions. They were chosen so as to provide the largest possible sample of lines and so that several of them were visible from ISO as much as possible during the mission (see Table 5.12 and Figure 5.22). The lines used had to be strong enough to give good signal-to-noise and to be unresolved by the grating.

The observations were performed weekly with end-to-end grating scans and provided measurements of seven different emission lines, spread between 51  $\mu\text{m}$  and 158  $\mu\text{m}$ , appearing on two detectors each.

Note that there were no measurements for SW4 and LW5, as no strong lines were found in their wavelength range. However, the relationship is in principle independent of the detector and all measurements of all lines were used together.

### 5.10.3 Detector angles

The wavelength calibration was first derived by adopting the detector angles measured before launch. Then the plot of the residuals (normalised differences between the expected wavelengths and the wavelengths derived from the LVDT with the polynomial relationship) showed systematic offsets for some detectors, suggesting that some of the detector angles had changed after launch. Therefore their values have been slightly adjusted until minimising the residual offsets for all detectors. The new angles used from OLP Version 6.0 onwards are listed in Table 5.13 together with the corresponding shifts relative to the pre-launch angles. The angle shifts for detectors SW4 and LW5 were adopted from the neighbouring detectors.

### 5.10.4 Time dependence

The stability of the system was checked by monitoring the measured LVDT at the line centres in the weekly observations. It is found to be remarkably stable for measurements performed close to the rest

Table 5.12: *Lines from astronomical sources used for grating wavelength calibration.*

line id. $\lambda$ [ $\mu m$ ]	det.	LVDT mean( $\sigma$ )	# obs	sources
[O III]51.815	SW1	1327(3)	171	NGC 6543 NGC 6826 G298.228 IRAS 15408 NGC 7027
[O III]51.815	SW2	2783(3)	196	NGC 6543 NGC 6826 G298.228 IRAS 15408 NGC 7027 NGC 6302
[N III]57.330	SW2	1993(2)	161	NGC 6543 NGC 6826 G298.228 IRAS 15408 NGC 6302
[N III]57.330	SW3	3376(5)	152	G298.228 IRAS 15408 NGC 6302
[O I]63.184	SW2	1124(3)	88	G298.228 IRAS 15408 NGC 7027 NGC 6302 NGC 7023 IRAS 23133
[O I]63.184	SW3	2584(3)	97	G298.228 IRAS 15408 NGC 7027 NGC 6302 NGC 7023 IRAS 23133
[O III]88.356	SW5	1579(3)	185	NGC 6543 NGC 6826 G298.228 IRAS 15408 NGC 7027 NGC 6302
[O III]88.356	LW1	3142(4)	189	NGC 6543 NGC 6826 G298.228 IRAS 15408 NGC 7027, NGC 6302
[N II]121.889	LW2	2176(2)	7	NGC 6302
[O I]145.525	LW3	1878(4)	76	G298.228 IRAS 15408 NGC 7027 NGC 7023 IRAS 23133
[O I]145.525	LW4	3250(5)	80	G298.228 IRAS 15408 NGC 7027 NGC 6302 NGC 7023 IRAS 23133
[C II]157.741	LW3	945(4)	90	G298.228 IRAS 15408 NGC 7027 NGC 6302 NGC 7023 IRAS 23133
[C II]157.741	LW4	2374(3)	91	G298.228 IRAS 15408 NGC 7027 NGC 6302 NGC 7023 IRAS 23133

Table 5.13: *Detector angles adopted for wavelength calibration. The second line lists the shift of the new angle respective to the angle measured on the ground. Both sets of numbers are in degrees.*

	SW1	SW2	SW3	SW4	SW5	LW1	LW2	LW3	LW4	LW5
angle	67.80	58.74	49.71	40.73	31.72	63.26	54.29	45.27	36.275	27.32
shift	-0.10	-0.01	0.00	0.00	+0.02	+0.02	+0.01	+0.01	+0.04	+0.04

(central) position of the grating (LVDT $\sim$ 2100). But elsewhere, a little jump happened in revolution 346. The jump was bigger the farther away the grating was from its rest position, and the jump had opposite signs for opposite angles (see Figure 5.23). After the jump, only a very slow drift was observed in the LVDT measurements. This jump implied that the relationship between grating angle and LVDT reading had changed on revolution 346 for an unknown reason and it was decided to derive a time-dependent wavelength calibration, which considers two distinct periods, i.e. pre- and post-revolution 346.

In Table 5.14 the values of the coefficients used by the pipeline are reported.

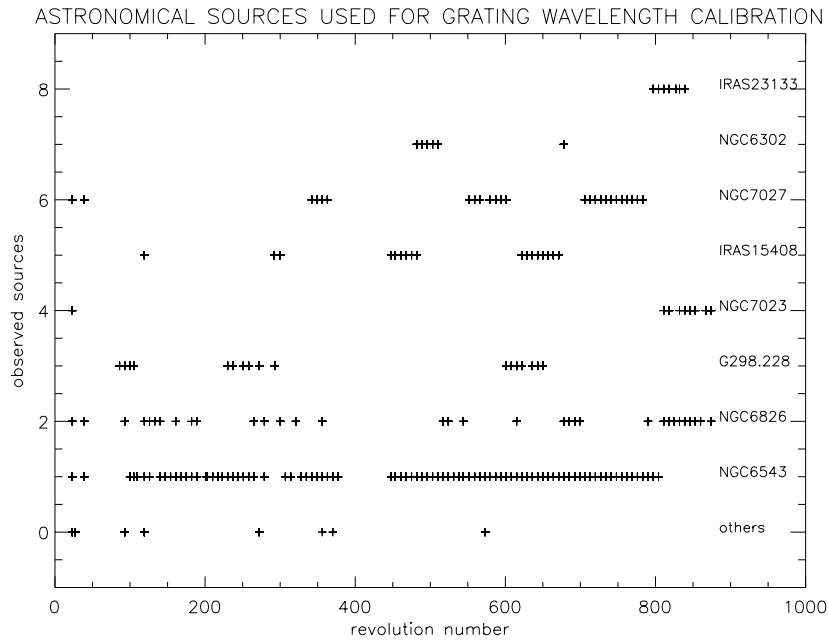


Figure 5.22: Main LWS grating wavelength standards observed during the mission. The gap between revolutions 378 and 442 corresponds to the period when LWS was not used because of a problem with the FP interchange wheel.

Table 5.14: Grating wavelength coefficients.

revs	0th order	1st order	2nd order	3rd order
1–345	69.624422	$-5.16459527 \cdot 10^{-3}$	$5.02618935 \cdot 10^{-7}$	$-8.20047303 \cdot 10^{-11}$
346–875	69.554848	$-5.13190430 \cdot 10^{-3}$	$5.02794834 \cdot 10^{-7}$	$-8.18631699 \cdot 10^{-11}$

### 5.10.5 Assessment of the achieved wavelength accuracy

The accuracy of the grating wavelength calibration has been checked by measuring the central wavelengths of the lines observed in a large number (65) of Auto-Analysis results from observations of NGC 7027, NGC 6543, S106 and W Hya. This check has shown that in an individual observation the wavelength calibration is measured with an accuracy better than 1/4 of a resolution element (i.e.  $0.07 \mu\text{m}$  for SW detectors and  $0.15 \mu\text{m}$  for LW detectors). Only in one case the errors were slightly higher for an observation performed in a revolution just preceding the jump, when the noise on the LVDT reading was the highest, but in most of the cases the wavelength determination was better than 0.1 resolution elements.

It has to be mentioned that, because of the effect illustrated in Figure 5.23, the wavelength accuracy is higher near the centre of a detector. Therefore a slight wavelength error can be observed for a line detected at a detector edge. In this case, the measurement of the line should be performed on the adjacent detector, where it is likely to fall more near the centre.

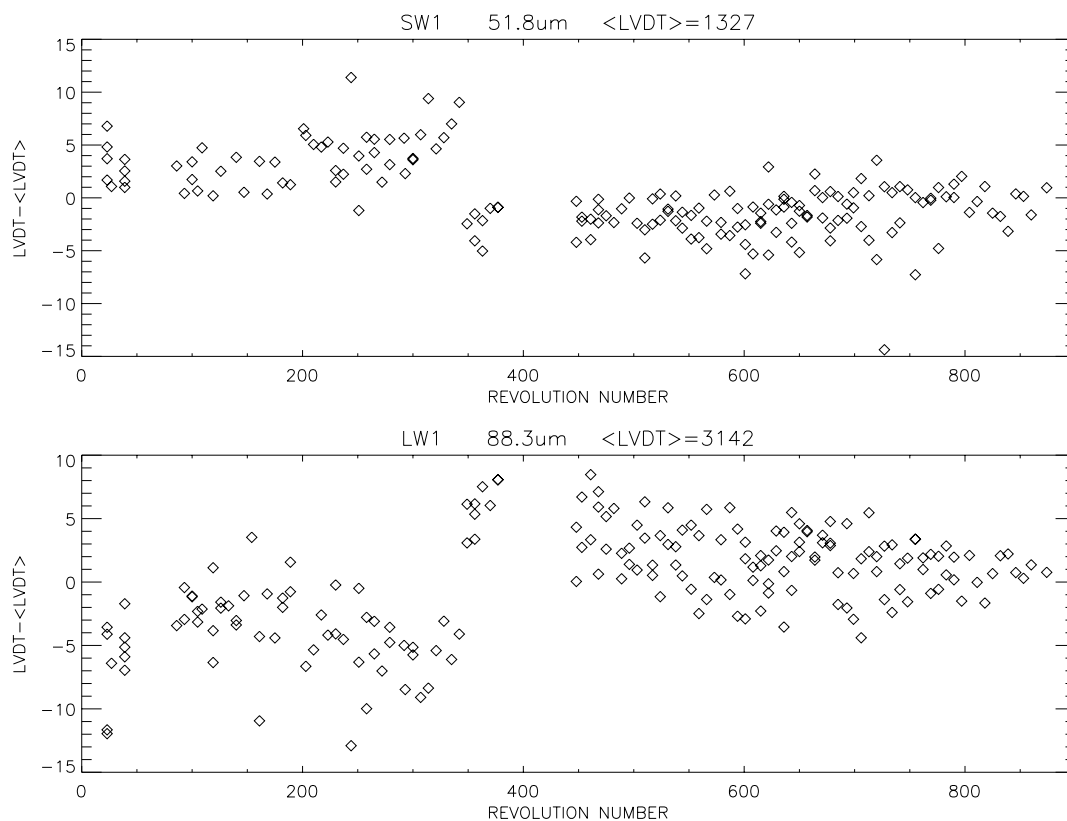


Figure 5.23: Deviation of the measured line centre (in engineering units LVDT) from the average value as a function of time, for two lines recorded at opposite grating directions relative to the rest position. 40 LVDT units correspond to 1 resolution element of the grating.

Table 5.15: Wavelength calibration accuracy for an LWS grating spectrum. These accuracies are based on actual measurements.

Mode	Accuracy
grating	~25% of a resol. element 0.07 $\mu\text{m}$ for SW detectors 0.15 $\mu\text{m}$ for LW detectors

## 5.11 Grating Resolution and Characterisation of the Line Profiles

### 5.11.1 Preparation of the data

The study of the grating profile was performed with data obtained over the ISO lifetime for wavelength calibration (see Table 5.12 and Figure 5.22). In order to have a homogeneous sampling, only those data obtained with AOT L01, an oversampling of 8, 6 scans of the full grating range and the same number of forward and backward scans were used.

The data processing was performed with the ISAP software. The standard processing of the selected observations is summarized by the following scheme:

- For each object we selected up to 20 observations well spread all over the mission.
- Each individual scan was checked for the presence of glitches or any anomalous feature. Glitches were removed and anomalous scans discarded.
- Each scan was rebinned to 32 points per resolution element.
- Forward and backward scans were averaged separately.
- In the case of extended sources, the resulting scans were corrected for the presence of fringes.
- The continuum was fitted by a polynomial and subtracted off.
- The profile was normalised so that the peak of all profiles was one.
- The resulting spectra were re-centred to the laboratory wavelength, so that profiles from different velocity sources can be compared.

The products were thus one spectrum per scan direction per spectral line per detector per observation per object.

### 5.11.2 Stability of the line profiles

In order to define as general a profile as possible, parameters susceptible of inducing profile variations were looked for in a step by step approach. When a parameter had proved not to induce any significant variation, the profiles were averaged over this parameter for the subsequent study.

- **Stability with time.** All observations of the same line on the same detector for the same object were plotted together to look for time variations. The peak to peak variations in the peak height of the line were as low as 2% for the strong lines and always less than 20% in the worst cases corresponding to the faintest lines used. No trend was found with time so these numbers are representative of the photometric accuracy of the LWS detectors. The variation of the line width with time is in general much smaller than the sampling interval of the observations (8 points per resolution element). We concluded that there are no significant time variations in the instrumental profiles.
- **Search for transient effects: comparison of forward and backward scans.** Slight differences do exist between the forward and backward scans of the same line from the same object due to transient or memory effects. In the short wavelength detectors the difference in the peak is always less than 2%, while in the long wavelength detectors it can be up to 6%. There is no trend with the flux level. In the base of the line some broadening can be observed, in general on the short wavelength side for forward scans and on the long wavelength side for backward scans. The opposite case is also seen though, possibly due to errors in placing the continuum.

Because the effect is symmetrical when adding the forward and backward scans together, and because most of the differences between forward and backward scans are seen in the feet of the line, where they are confused with continuum features and thereby will be removed by the baseline subtraction process, our recommendation, as long as no formal transient correction is available, is to use both scan directions together. We have thus averaged forward and backward profiles for the rest of the study.

- **Variation of line profile with object and detector.** In general the profiles show very little difference from object to object (the differences are less than 4%) and they show no significant differences between lines coming from different detectors.

There is one exception with the clearly anomalous line at  $57 \mu\text{m}$  on detector SW2. It shows a strong asymmetry towards the short wavelengths for some objects. The asymmetry is clearly not real because it does not appear when the same line is observed with the detector SW3. It is not due to the detector either, as two other lines falling on SW2 (at  $52 \mu\text{m}$  and  $63 \mu\text{m}$ ) do not show any anomaly. The  $57 \mu\text{m}$  line on detector SW2 has thus been excluded from the derivation of the mean profile obtained by averaging all lines from all detectors in all objects.

- **Difference in line profiles from point and extended sources.** The profiles from extended sources and from point sources were kept separate to check whether off-centred emission was creating any distortion in the line profiles. The comparison of the mean profiles shows that, if anything, the profiles from the extended sources are more symmetrical and more similar to Gaussians than the point source profiles. We thus concluded that there is no distortion coming from the source extension or off-centring and we have averaged all profiles from point sources and extended sources together.

In conclusion, we have created two mean grating profiles (one for SW and one for LW detectors) which are the average of all lines listed in Table 5.12 except the  $57 \mu\text{m}$  line on SW2.

### 5.11.3 Characteristics of the profiles. Comparison to Gaussians.

When considering all the LWS optical elements and detector characteristics, the wavelength response function is not expected to be Gaussian. It is however always convenient when measuring a line intensity to be able to use a Gaussian approximation.

Figure 5.24 shows the comparison of the measured mean profiles with a Gaussian function fitted to them. It also shows the residuals, i.e. the differences between the two profiles.

Table 5.16 lists the line flux, full width at half maximum (FWHM) and peak heights both for the measured profiles and for the fitted Gaussian. This shows that the error made on the determination of the flux with a Gaussian fit is only of the order of 2%.

Table 5.16: *Parameters of the measured grating profiles compared with the results of Gaussian fits.*

	Observed mean profile			Gaussian fit to the mean profile		
	FWHM [ $\mu\text{m}$ ]	line flux (normalised to peak=1)	height	FWHM [ $\mu\text{m}$ ]	line flux (normalised to peak=1)	height
SW detectors	$0.308 \pm 0.005$	$0.314 \pm 0.008$	1.00	$0.283 \pm 0.009$	$0.322 \pm 0.010$	$1.06 \pm 0.02$
LW detectors	$0.611 \pm 0.014$	$0.637 \pm 0.014$	1.00	$0.584 \pm 0.015$	$0.644 \pm 0.016$	$1.04 \pm 0.02$

The line full widths at half maximum that we measure on our profiles are slightly larger than those measured before launch: 0.31 instead of 0.29 for the short wavelength detectors, and 0.61 instead of 0.60 for the long wavelength detectors. This is likely due to the broadening effect of transients.

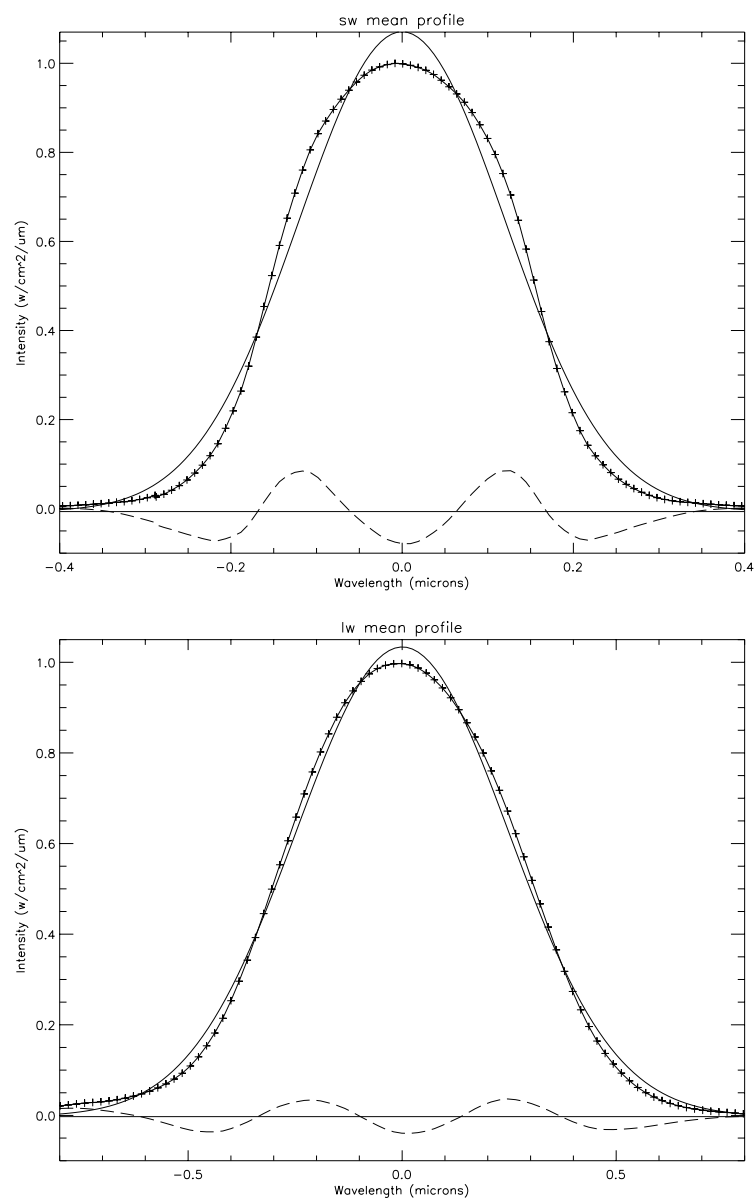


Figure 5.24: Measured grating profiles (plus signs) and comparison with a Gaussian fit (solid line). The residuals, *i.e.* the difference between the measured profile and the Gaussian fit, are also shown (dashed line). Up: profile for short wavelength detectors (SW1 to SW5) ; down: profile for long wavelength detectors (LW1 to LW5).

### 5.11.4 Effect of a lower spectral sampling

The above study of the line profile has been conducted with the highest oversampling permitted in the observations, an oversampling of 8, i.e. eight points per spectral element. However, in AOTs L01 and L02, four different oversamplings were permitted: 8, 4, 2 and 1. Following the Nyquist theorem, an oversampling of two or higher allows derivation of the line flux with a precision better than 5% (a sampling of 1 point per spectral resolution element would be clearly insufficient). However, we would like to warn the user that a Gaussian fit to observations obtained with an oversampling of 2 or even 4 might give results with a higher error than the one quoted above for an oversampling of 8. This is due to the fact that when a line is scanned quickly, the transient effects are more important and tend to broaden the line. This effect should be reduced once a transient correction (Section 6.9) is available.

## 5.12 Fabry-Pérot Wavelength Calibration

### 5.12.1 Introduction

The LWS Fabry-Pérot interferometers are fully described in Davis et al. 1995, [12] but for this section, which explains the adopted strategy and the results of the wavelength calibration, we can simply think of a Fabry-Pérot as two partially transmitting mirrors facing each other, a distance  $d$  apart.

Under simplifying assumptions the FP transmission has a maximum at wavelength  $\lambda$  when:

$$\frac{\lambda m}{2} = d \quad (5.8)$$

where  $m$  is a positive integer called the 'order'. Note that at separation  $d$  there are an infinity of transmitted wavelengths, namely  $2d$ ,  $d$ ,  $2/3d$  and so on. To avoid contamination by undesired wavelengths the LWS FP used the grating as an order sorter.

In Equation 5.8 there are no free parameters so that once  $d$  and  $m$  are known we can easily derive  $\lambda$  without needing a calibration. But the separation between mirrors was read out by the on-board electronics in terms of a quantity, the FP encoded position, whose relation with  $d$  is known from ground calibration to be a cubic function. So Equation 5.8 turns into:

$$\frac{\lambda m}{2} = A + Bx + Cx^2 + Dx^3 \quad (5.9)$$

Being the result of a digital measurement,  $x$  is an integer running from 0 to 4095. Wavelength calibration means then deriving the four coefficients of the above polynomial.

### 5.12.2 Strategy of calibration

Let us assume that we have observed a number of lines at wavelengths  $\lambda_i$  and found their centres<sup>1</sup>  $x_i$ . We can not directly invert Equation 5.9 to find the unknown coefficients because we still miss the orders  $m_i$ . So that the first step is to observe the same line in at least two adjacent orders, say  $m$  and  $m + 1$ .

The AOT logic selected for each wavelength one single order, so to observe the same line at different orders we executed special dedicated observations (COIF). Having determined the centres  $x_1$  and  $x_2$  for the two orders we recast Equation 5.9 in a different form:

$$\frac{\lambda}{2} = B(x_2 - x_1) + C(x_2^2 - x_1^2) + D(x_2^3 - x_1^3) \quad (5.10)$$

---

<sup>1</sup>Note that the position of a centre, being the result of a fitting procedure, is no longer an integer but a decimal number.

After observing lines in different orders a first estimate of the coefficients is obtained with a least squares fit. Now we rewrite Equation 5.9 in the following way:

$$m_{i,j} = \frac{2}{\lambda_i} (A + Bx_{i,j} + Cx_{i,j}^2 + Dx_{i,j}^3) \quad (5.11)$$

where  $i$  refers to a given wavelength observed at order  $j$ . All the  $m$ 's must be integer so that the value of  $A$  which minimises the differences  $\|m_{i,j} - \text{INT}(m_{i,j})\|$  is looked for. Once  $A$  is found Equation 5.9 is used to determine the order  $m$  and finally all four coefficients can be derived at the same time, again using a least squares fit.

### 5.12.2.1 The line fitting algorithms

To find the centre of a line three algorithms can be used and are now briefly described.

The three techniques are completely independent of each other and give us a better estimate of the centre position and its error, defined as  $\max\|x_i - \bar{x}\|$  with  $\bar{x}$  being the average of the three values  $x_i$ .

However, the FP wavelength calibration was carried out according to the procedure described in the previous section and uses only the first method described below. All three techniques have been used for the monitoring programme discussed later.

- **Determination of the centroid**

The background is estimated, and then subtracted, by fitting a low order ( $\leq 3$ ) polynomial to the ends of the FP scan, far from the line. The line profile is divided into a number of points, usually 10, avoiding the wings and the peak where the profile could be distorted, e.g. by memory effects.

At each point the segment that intersects the line is found and the half-power point computed. The 10 half-power points are then averaged. The procedure, fully described in the LWS Calibration File Derivation Procedure, gives as output:

- the peak position and its error;
- the peak flux in term of photocurrent;
- the full width at half maximum (FWHM).

- **Fourier interpolation**

The background is estimated as in the previous method. The line is then Fourier transformed and all the high frequencies filtered out. After an inverse transformation the obtained smoothed line profile is reconstructed to find the peak position and intensity as well as the FWHM.

- **Gaussian fitting**

The IDL procedure `GAUSSFIT` has been used. It simultaneously fits the background and the line profile so from this point of view it is the best of the three methods presented. The procedure gives the line centre, peak height and FWHM. In all cases the FP line profile is definitively not Gaussian, being the convolution of the source intrinsic profile and an Airy function so that only the centre position is reliable.

Experience has shown that even at low signal-to-noise ratio, the three line centres very rarely differ by more than one FP encoded position.

### 5.12.3 Calibration for OLP Version 10

Lines and sources observed to calibrate the short wavelength FP (FPS, covering from 46.764  $\mu\text{m}$  to 71.892  $\mu\text{m}$ ) and for the long wavelength FP (FPL, covering from 70.186  $\mu\text{m}$  to 197.094  $\mu\text{m}$ ) are reported in Table 5.17. The derived coefficients are written in Table 5.18.

Table 5.17: *Lines and sources used to calibrate the FP's. Rev. is the revolution number.*

	Source	Rev.	Ion	Line [ $\mu\text{m}$ ]	Orders
FPS	NGC 7027	168	[O I]	63.2	87, 88
	G 36.3+0.7	300	[O III]	51.8	104, 105, 106
	G 0.6–0.6	321	[O III]	51.8	105, 106
	NGC 7027	370	[O I]	63.2	88, 89
FPL	NGC 7027	175	[O I]	145.5	69, 70
	G 0.6–0.6	287	[O III]	88.4	114, 115
	G 36.3+0.7	300	[O III]	88.4	114, 115

In Figure 5.25 the relation between encoded position and gap between plates is shown as a solid line for both FPS and FPL. Asterisks mark the positions where a particular combination  $(\lambda, m)$  falls. The combinations actually selected by the AOT logic are indicated. All wavelengths observable with FPS correspond to a particular position inside the portion of the curve delimited by two vertical segments.

Table 5.18: *FPS and FPL wavelength calibration coefficients (see Equation 5.9).*

	FPS	FPL
A	2713.2569	5010.6224
B	0.023870650	0.031654363
C	$4.1581366 \cdot 10^{-7}$	$7.3574580 \cdot 10^{-8}$
D	$-2.4636391 \cdot 10^{-11}$	$5.1097999 \cdot 10^{-11}$

#### 5.12.4 Monitoring the Fabry-Pérot wavelength calibration

To check the stability of the calibration against possible temporal trends, weekly observations have been performed on a number of selected sources, chosen according to their luminosity, visibility and with as small FWHM as possible. Lines and sources used for this task are listed in Table 5.19.

Table 5.19: *Lines and sources used to monitor the FP calibration.*

Ion	Line [ $\mu\text{m}$ ]	FP	Source
[O III]	51.8	S	G 0.6–0.6, G 36.3–0.7, NGC 7027, NGC 7538
[N III]	57.3	S	NGC 3603, G 0.6–0.6, NGC 6302
[O I]	63.2	S	NGC 7023, NGC 7027, NGC 7538, S106
[O III]	88.4	L	G 0.6–0.6, G 36.3–0.7, NGC 3603, NGC 7538
[N II]	121.9	L	G 0.6–0.6
[O I]	145.5	L	NGC 7023, NGC 7027
[C II]	157.7	L	G 0.6–0.6, NGC 6302, NGC 7023, NGC 7027, NGC 7538, S106

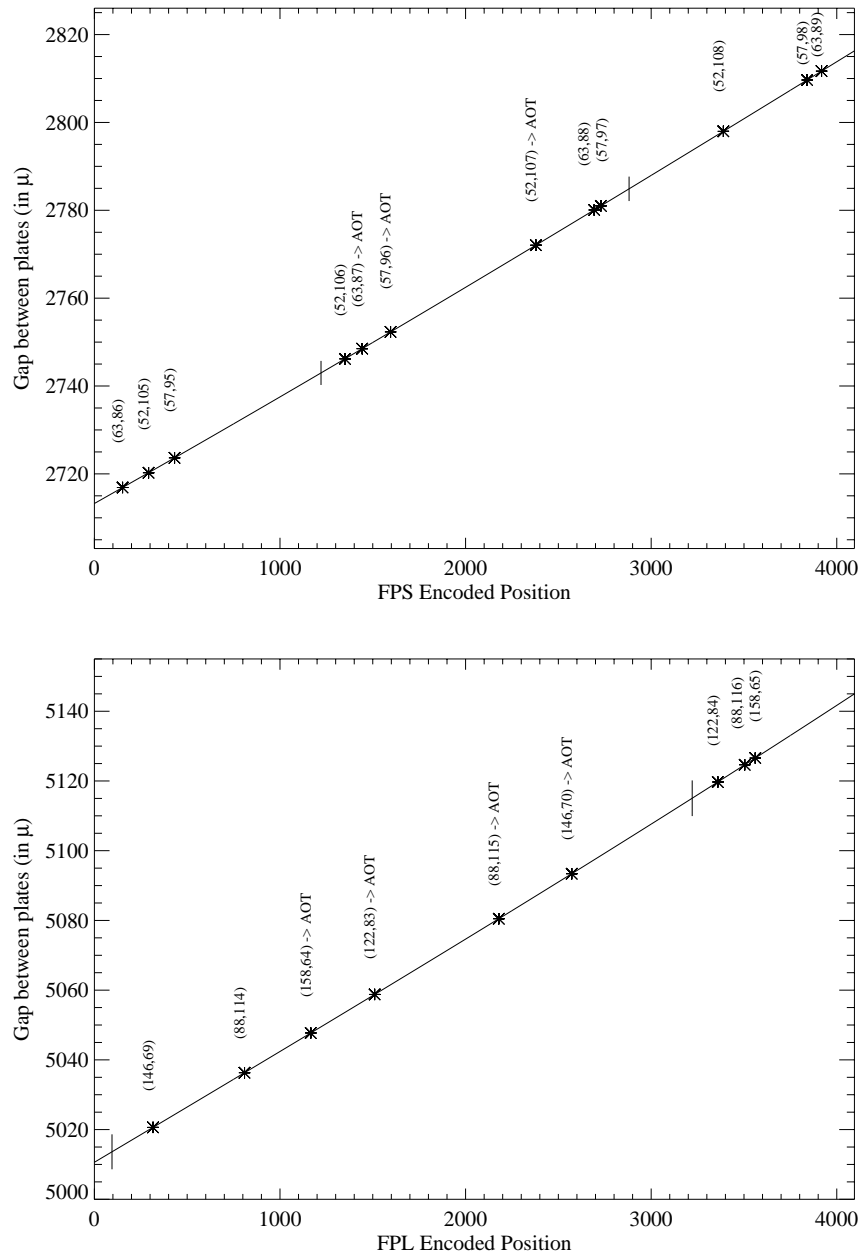


Figure 5.25: Distance between plates versus encoded position for FPS (top) and FPL (bottom) wavelength calibration coefficients. The instrument was always operated in the range delimited by the two small vertical segments. Note the larger interval of positions used for FPL. The asterisks mark the position corresponding to a particular combination (wavelength, order). To calibrate the instrument some other combinations were used, also shown in the figure.

Each line has been fitted with the methods previously described so that its centre is the average of three values. It has been converted into wavelength using Equation 5.9 and taking into account the relative motion of the source with respect to the satellite.

#### 5.12.4.1 Results for FPS

The calibration looks stable with no temporal trend. Note that the [N III] line was not used to derive the calibration coefficients, so that we can use our data to measure its rest wavelength. Combining all 11 measurements we get  $\lambda \pm 1\sigma = 57.32952 \pm 0.00072 \mu\text{m}$ , in perfect agreement with the quoted value in the literature ( $57.33 \mu\text{m}$ ). In Table 5.20 the rms error for each wavelength is reported.

Table 5.20: *The rms calibration errors for each line observed as part of our monitoring programme for FPS.*

Ion	Line	Error	
		[ $10^{-4} \mu\text{m}$ ]	[ $\text{km s}^{-1}$ ]
[O III]	51.8	9.5	5.5
[N III]	57.3	7.2	3.8
[O I]	63.2	8.7	4.1

#### 5.12.4.2 Results for FPL

Figure 5.26 illustrates the monitoring of the FPL wavelength accuracy. As can be seen, especially in the plot corresponding to the [O I] line at  $145.5 \mu\text{m}$ , the calibration seems to be affected by systematic errors. But even in the worst case errors are lower than half a spectral resolution element.

The rms errors are reported in Table 5.21. Note that when the measured wavelength is systematically shifted with respect to the rest wavelength, the rms is a measure of the average displacement and not a true scatter around the mean.

Table 5.21: *The rms calibration errors for each line observed as part of our monitoring programme for FPL.*

Ion	Line	Error	
		[ $10^{-3} \mu\text{m}$ ]	[ $\text{km s}^{-1}$ ]
[O III]	88.4	1.5	5.1
[N II]	121.9	2.2	5.4
[O I]	145.5	6.6	13.6
[C II]	157.7	3.0	5.6

### 5.12.5 Fabry-Pérot wavelength accuracy

As is clear from Equation 5.8 or 5.9 in Section 5.12, what we measure is the distance  $d$  and not the wavelength  $\lambda$ . For this reason the accuracy of the calibration depends on which FP position range was used to observe a given line. This information is written in LSPD files.

Looking at Figure 5.25 (top) and Table 5.20 we conclude that the accuracy of the wavelength calibration for FPS is  $\sim 4 \text{ km s}^{-1}$  at positions  $x < 2000$ , slightly increasing to  $\sim 6 \text{ km s}^{-1}$  at larger values of  $x$ . A reasonable choice for error over the range of positions is then  $\Delta\lambda = 2.00 \cdot 10^{-5}\lambda$ .

In the case of FPL the range covered by the instrument is larger. From Figure 5.25 (bottom) and Table 5.21 it is evident that a systematic error is present in the calibration, increasing towards larger  $x$  values.

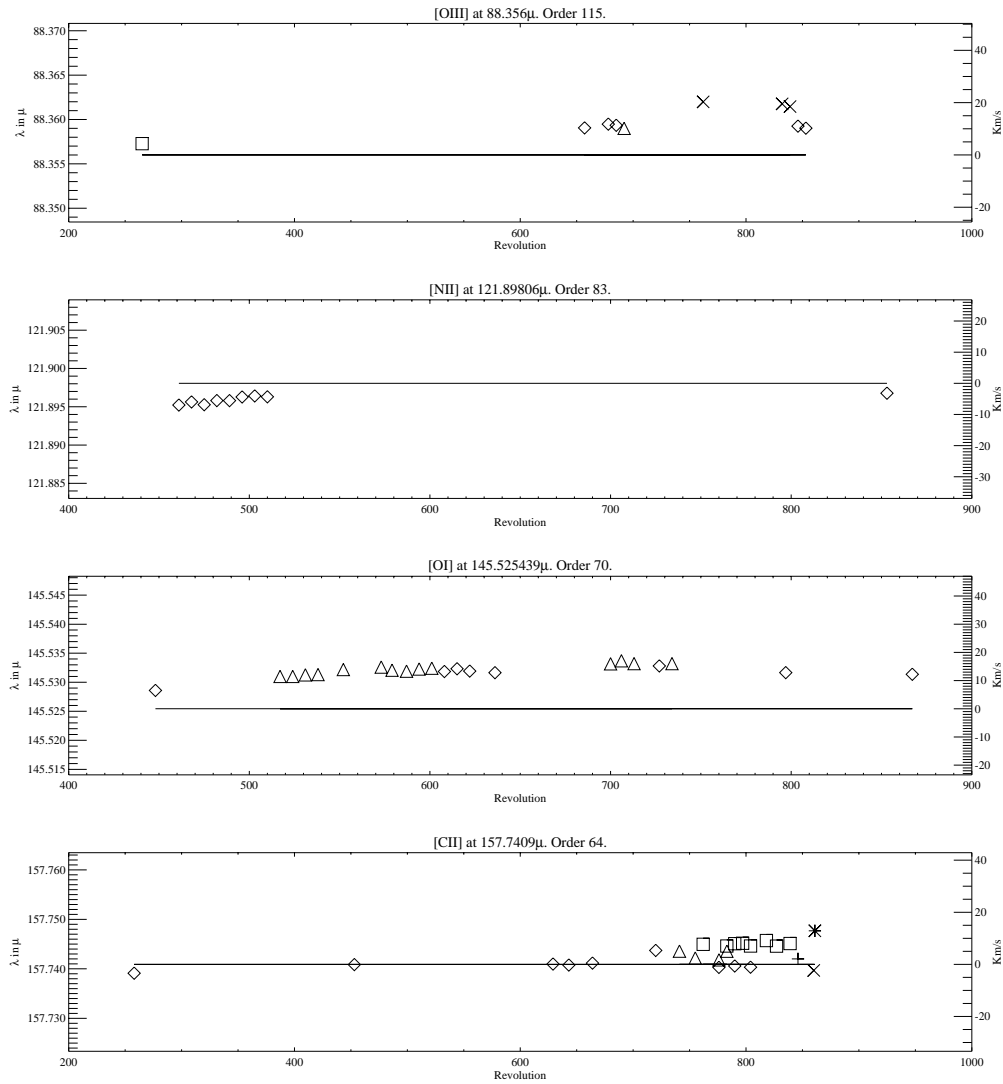


Figure 5.26: Monitoring data for FPL. Solid line: rest wavelength. Left ordinate: wavelength in microns; right ordinate: difference from rest position in  $\text{km s}^{-1}$ . Symbols:  $\diamond$  G 0.6-0.6 (first 2 plots), NGC 7023 (second 2 plots);  $\triangle$  G 36.3-0.7 (first), NGC 7027 (third and fourth);  $\square$  NGC 3603 (top), NGC 7538 (last);  $\times$  NGC 7538 (first), S 106 (last); for the last plot + G 0.6-0.6 and \* NGC 6302.

For the validation of OLP Version 10 data, the accuracy of lines was studied in NGC 7027 for 21 observations. Excluding the  $145.5 \mu\text{m}$  [O I] line, the overall rms error was  $2.69 \text{ km s}^{-1}$ . Measurements of the  $145.5 \mu\text{m}$  line were made during orbits 601, 706, 713 and 734. If the rest wavelength is taken to be  $145.525 \mu\text{m}$  then the velocity residuals of these measurements are  $+16.1$ ,  $+20.7$ ,  $+18.2$  and  $+18.2 \text{ km s}^{-1}$ , which makes the overall rms error  $4.42 \text{ km s}^{-1}$ . However, if a value of  $145.535 \mu\text{m}$  is used, the velocity residuals are  $-4.50$ ,  $+0.11$ ,  $-2.37$  and  $-2.37 \text{ km s}^{-1}$ , and the overall rms error is only  $2.65 \text{ km s}^{-1}$ .

This discrepancy in the measurement of the  $145.5 \mu\text{m}$  line of NGC 7027 suggests that either:

- this line arises from a region which has a different velocity signature compared to the other lines measured in NGC 7027. This is plausible given the complex nature of NGC 7027 (see Phillips et al.

1991, [32]). However, the [O I] line at  $63.2 \mu\text{m}$  observed with FPS did not show such high residuals in FPS, which makes this hypothesis difficult to believe.

- the  $145.525 \mu\text{m}$  rest wavelength, the value used when deriving the wavelength calibration, is inaccurate.

A literature search has shown there are two different values recorded as the rest wavelength for the  $145.5 \mu\text{m}$  [O I] line:

- $145.525 \mu\text{m}$ , from the NASA's Jet Propulsion Laboratory Spectral Catalog — see <http://spec.jpl.nasa.gov/> and Zink et al. 1991, [47]
- $145.535 \mu\text{m}$ , from The National Institute of Standards and Technology — see <http://www.nist.gov/>.

The difference of  $0.010 \mu\text{m}$  between both values is equivalent to  $21 \text{ km s}^{-1}$ . In any case, until this ambiguity is resolved, users should view their line velocity measurements of the  $145.5 \mu\text{m}$  [O I] line with caution.

Another systematic check of the accuracy of the FPL calibration was made using 16 CO lines observed in Orion BN/KL between revolutions 699 and 873. The systematic error indicated above was evident, but to a lesser extent. Once the source velocity was subtracted ( $+9 \pm 1.9 \text{ km s}^{-1}$ , Knapp et al. 1981, [23]), the residual velocity differences (i.e. observed wavelength minus rest wavelength, expressed as velocity) have an rms of  $6 \text{ km s}^{-1}$  and are never worse than  $\pm 11 \text{ km s}^{-1}$ , as shown in Figure 5.27. This figure can provide some guidance to users on the magnitude and time-dependent nature of systematic errors observed in well calibrated LWS FPL data.

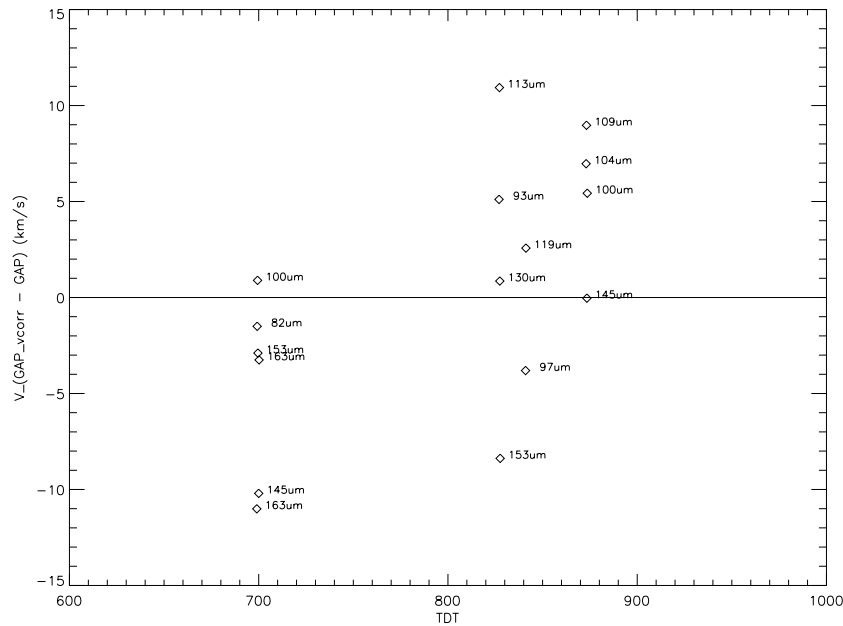


Figure 5.27: Velocity residuals measured for 16 CO lines in Orion. The dispersion of these residuals gives an idea of the wavelength accuracy for FPL.

For the accuracy of FPL measurements, we therefore adopted the most conservative value, half of the spectral resolution element or  $13 \text{ km s}^{-1}$  even if the internal scatter of data points seem to imply that a better accuracy could potentially be achieved. For FPS data the accuracy adopted is  $1/3$  of a spectral resolution element or  $6 \text{ km s}^{-1}$ .

## 5.13 Fabry-Pérot Resolution and Line Profiles

Measurements of the Fabry-Pérot efficiency and resolving power were made during ground testing using a far-infrared laser at a number of spot wavelengths (Emery et al. 1993, [15]). It has proved difficult to confirm these measurements in-orbit owing to an absence of emission lines that are sufficiently narrow so that the intrinsic width of the line can be ignored with respect to the resolution element of the Fabry-Pérot. The presence of transient effects (Section 6.9) also causes the lines to be artificially broadened. The resolving power as derived from ground testing are listed in Table 5.22.

Table 5.22: *Fabry-Pérot resolving power and resolution values for each detector, as measured on the ground before launch.*

FP	Det.	$\lambda$ [ $\mu\text{m}$ ]	res. power	res. element [ $\mu\text{m}$ ]
FPS	SW1	47.00	8600	0.0055
	SW2	56.17	8450	0.0066
	SW3	66.09	8200	0.0081
FPL	SW4	75.68	7800	0.0097
	SW5	84.80	9200	0.0092
	LW1	102.42	9700	0.0105
	LW2	122.19	9600	0.0127
	LW3	141.78	9250	0.0153
	LW4	160.59	8900	0.0180
	LW5	178.00	8500	0.0209

## 5.14 Accuracy of the Parallel and Serendipity Mode Calibration

The calibration of the parallel and serendipity modes can be checked in various ways:

1. when the parallel data is taken at the same position as an independent prime pointing
2. before the instrument becomes prime there is some serendipity data at that pointing
3. by looking at overlapping parallel rasters taken on different revolutions

### 5.14.1 Prime mode observations coincident with parallel observations

Table 5.23 lists five L01 observations which were selected to provide a direct cross-check between parallel and prime mode. All L01 positions lie within the parallel rasters with the two Galactic Centre pointings being exactly coincident with one of the raster positions.

Figure 5.28 shows the Galactic Centre background position where the pointing is the same for the prime and parallel mode observations. For all positions the agreement is generally better than 20%. This result was obtained by comparing the fluxes from each detector at the parallel wavelengths with the prime data at those specific wavelengths. The best agreement was in the Galactic Centre position with the maximum flux. The first position in  $\rho$  Oph, which is in a low flux region, showed the worst agreement. The uncertainties in dark current affect the quality of the data; hence, this result meets expectations. There were no systematic differences found, although detectors SW1 and SW2 could be more than a factor of two higher or lower than the prime mode. For the interpolated positions all other detectors were well within a factor of two of the prime mode.

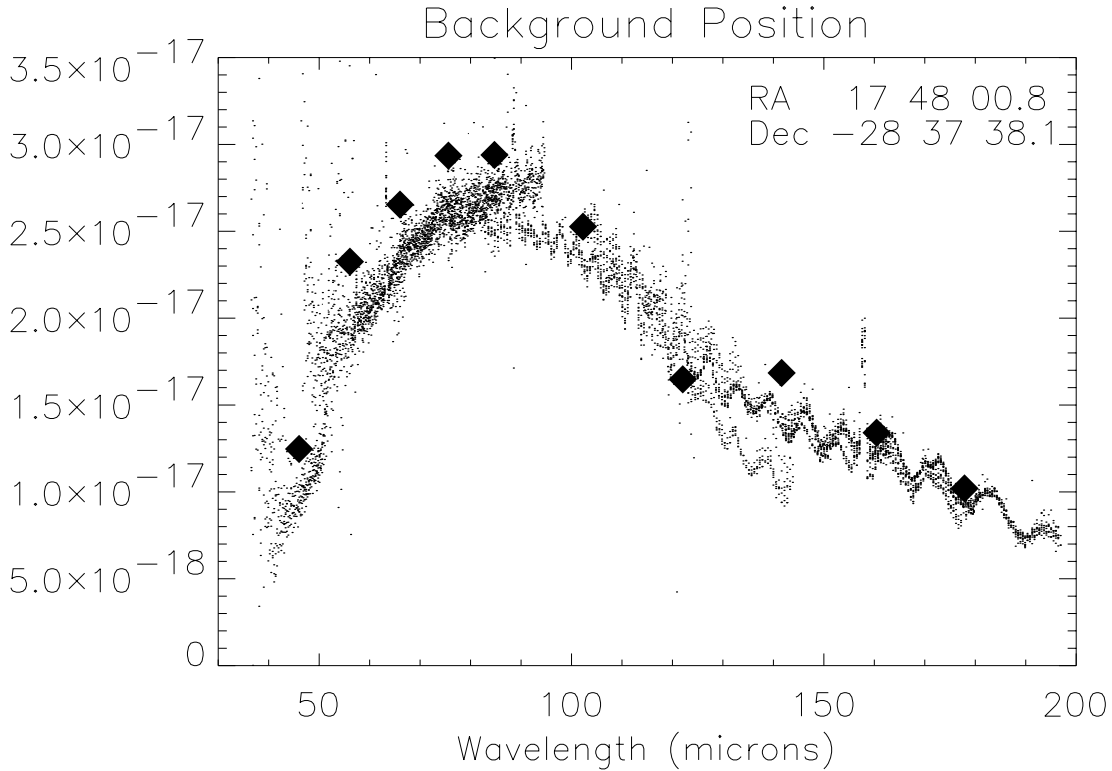


Figure 5.28: *The L01 full grating spectrum of a background position near the Galactic Centre. The diamonds are fluxes from an observation done in parallel mode at the same position.*

Table 5.23: *L01 observations concurrent with parallel observations.*

TDT	RA	Dec	Source
29502313	16 25 43.5	-24 11 39.8	$\rho$ Oph
48400517	16 27 02.0	-24 37 25.6	$\rho$ Oph
29200534	16 26 26.3	-24 24 29.9	$\rho$ Oph
69601005	17 48 00.8	-28 37 38.1	Gal. Centre background
69600801	17 46 42.5	-28 49 01.3	Gal. Centre

### 5.14.2 Comparison with prime mode from stabilisation periods

Before LWS prime mode observations are performed, there are between 10–20 ramps in the previous serendipity product, for which the on-target flag is OK, the pointing is stabilised and serendipity mode is still active. The fluxes obtained from these ramps can be compared to those obtained from the prime mode at the same grating position to check on how accurately the serendipity fluxes are being derived. In principle this can be done for every prime grating mode observation of a non-moving source. This check was performed on ten observations selected to have varying properties e.g. flux, source extent, etc. The agreement is very good when looking at bright point sources (see Figure 5.29; TDT 28701825) but less good when looking at bright extended sources (see Figure 5.29; TDT 28701401) and faint sources. It

is also interesting to note that in the latter case, the LW2–LW4 detectors are saturated in prime mode and saturation effects are also present in the stabilisation period. The parallel flux is usually within 20% of the prime mode flux and there are no systematic deviations except for detector LW1 which was often about 30–40% lower in serendipity mode than in prime mode.

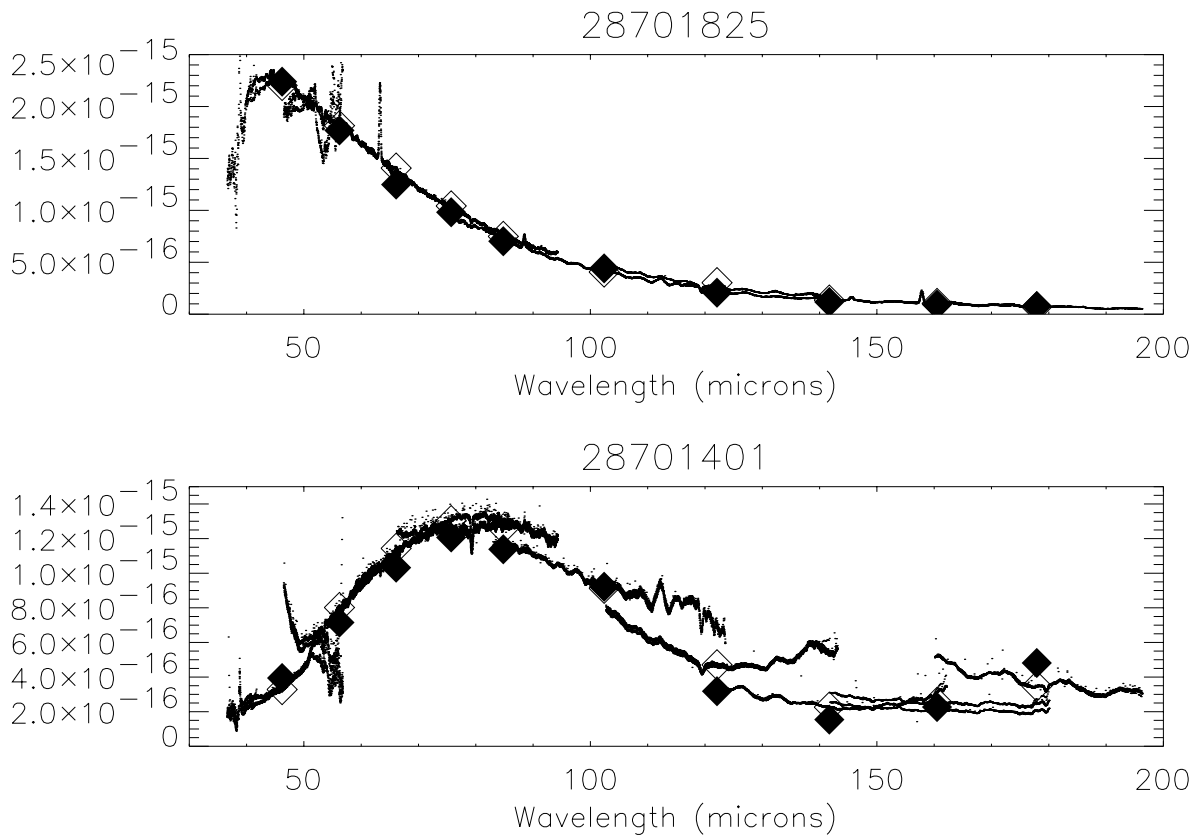


Figure 5.29: Two comparisons between serendipity mode just before an observation (filled diamonds) and averages at grating rest position during that observation (open diamonds).

### 5.14.3 Comparison between overlapping parallel rasters

The parallel mode interactive analysis (LPIA) enables the building of a map from constituent product files using linear interpolation to form a uniform grid. Figure 5.30 shows one example where a map has been generated from about 15 large ( $\geq 30$  points) rasters and 32 other parallel observations. The raster pointings superposed on this map are from TDT 31300236 and the fluxes obtained at each point, both in the map and the constituent raster are shown in Figure 5.31. Each individual point from the raster was ratioed with the nearest point in the map (i.e. for TDT 31300236, 401 ratios were obtained per detector) and these were averaged to get one comparison value for that detector per observation. This comparison was tried in three other areas (TDTs 32201917, 31201606 and 64102109) and the average ratio was always found to be within 20% with the majority of ratios well within 10%.

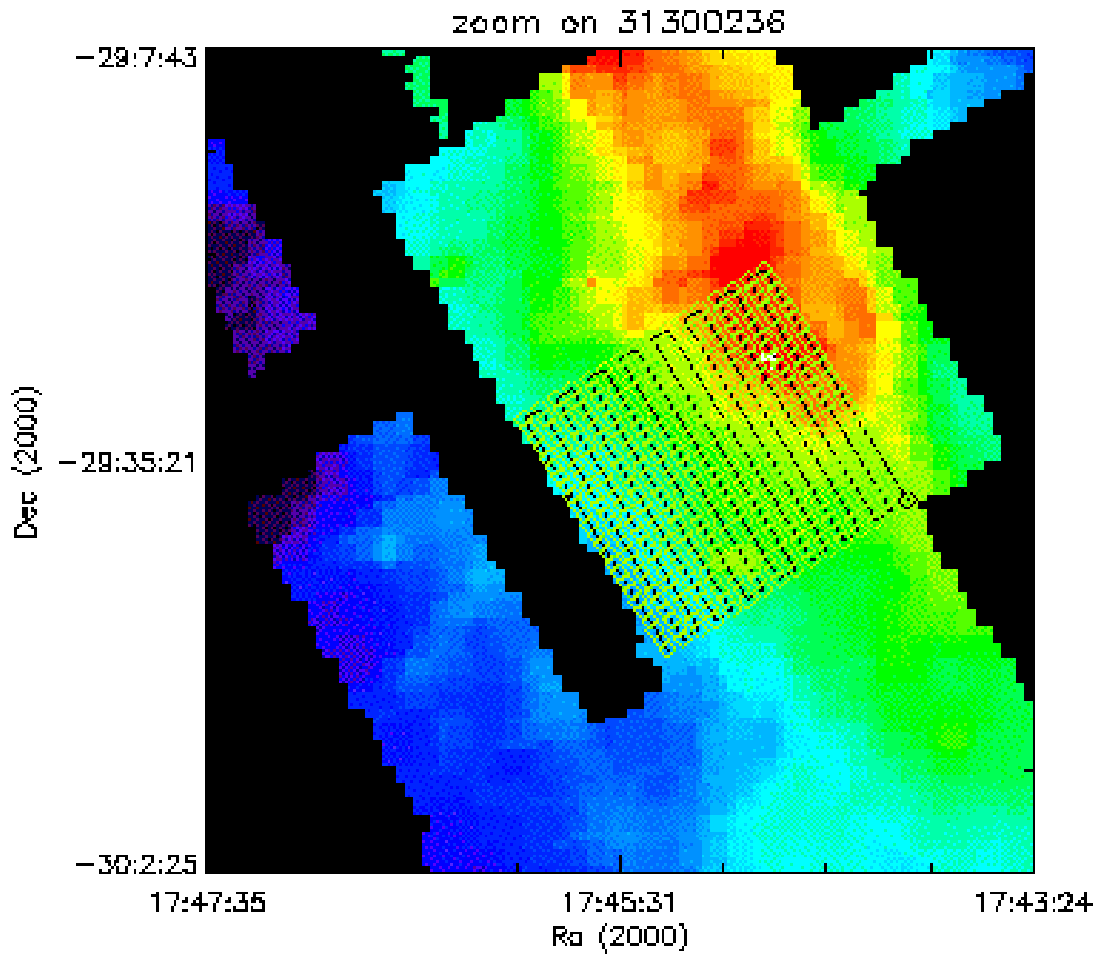


Figure 5.30: A parallel map produced from several rasters in the Galactic Centre region. The pointings of one of the constituent raster observations, TDT 31300236, are shown.

#### 5.14.4 Comparison with other instruments

In addition to checking the internal calibration, comparisons can be made also with IRAS and ISOPHOT. For each of these other instruments the comparison is difficult to interpret as the flux obtained from LWS parallel observations covers a very narrow spectral band whereas the other instruments are observing a much broader spectral range. In spite of this, one important aspect which can be addressed by comparing LWS parallel data with data from other instruments, and which cannot be discerned with the internal checks, is to see if the beam shapes used for the conversion from  $W \text{ cm}^{-2} \mu\text{m}^{-1}$  to  $M\text{Jy sr}^{-1}$  are reasonable. Maps were generated covering the  $\rho$  Oph region and compared with IRAS High-Res maps, at  $60 \mu\text{m}$  (with those of SW2 at  $56.2 \mu\text{m}$  and SW3 at  $66.1 \mu\text{m}$ ) and  $100 \mu\text{m}$  (with SW5 at  $84.8 \mu\text{m}$ , LW1 at  $102.4 \mu\text{m}$  and LW2 at  $122.1 \mu\text{m}$ ). The comparison was made by selecting linear strips across  $\rho$  Oph and looking at the profiles along those strips. The difference between the instruments was no more than 10%. At  $60 \mu\text{m}$  SW2 profiles almost exactly matched the IRAS profile and the SW3 profile was always higher indicating that the effective wavelength of the IRAS filter may be nearer the SW2 wavelength than SW3. At  $100 \mu\text{m}$  LW1 gave a very good match (difference  $\leq 5\%$ ) and SW5 ( $84.8 \mu\text{m}$ ) was higher,

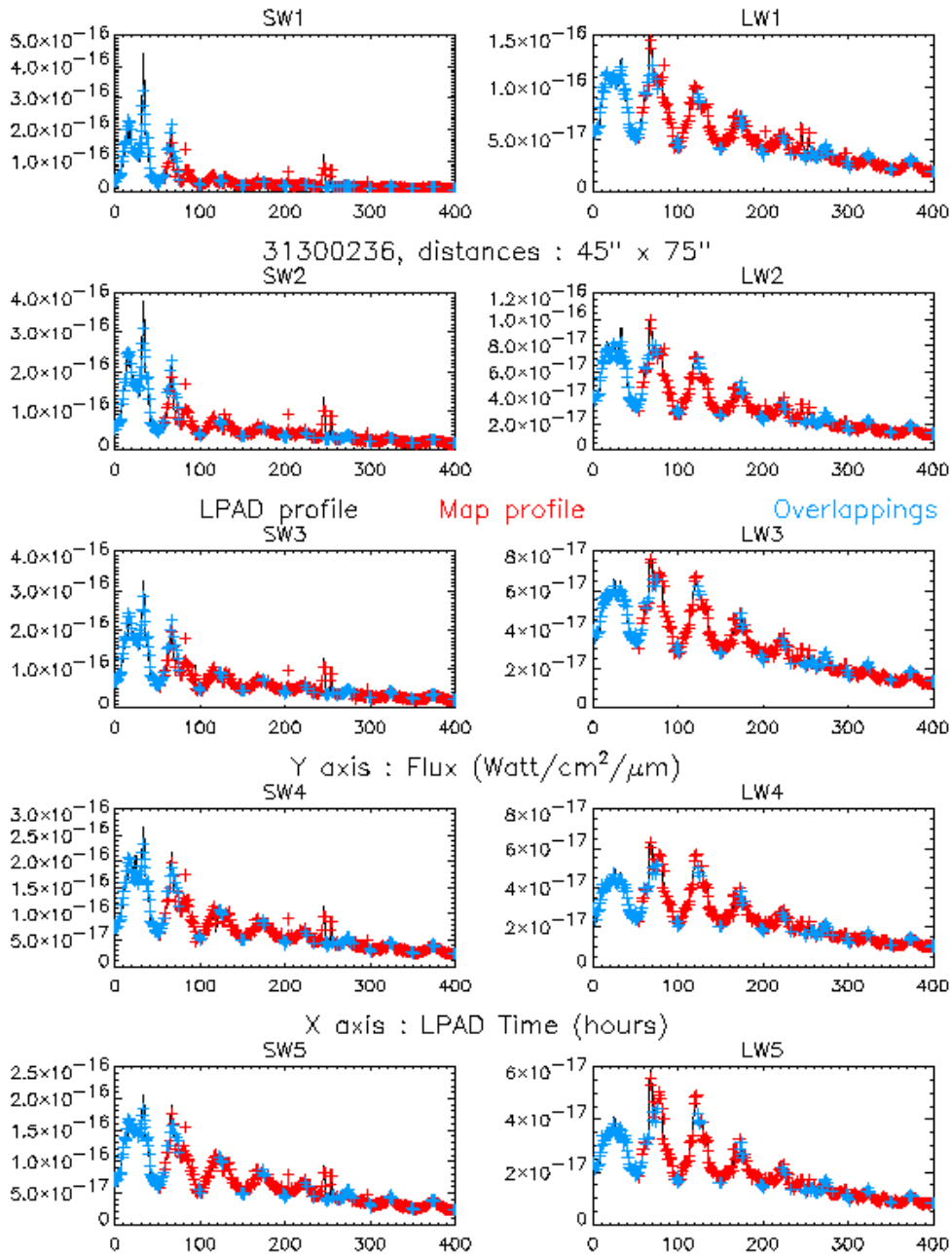


Figure 5.31: The comparison between the map fluxes and the raster fluxes for the ten LWS detectors in the pointing sequence of TDT 31300236. The map fluxes are shown in blue and the raster fluxes are shown in red.

while LW2 (122.1  $\mu\text{m}$ ) and the PHOT (80–120  $\mu\text{m}$ ) filter were lower. LW2 is the only detector in parallel mode where the wavelength is coincident with a strong ([N II]) line; therefore, we do not expect good agreement with IRAS as the IRAS 100  $\mu\text{m}$  filter only has a 20% transmission at 120  $\mu\text{m}$ .



## Chapter 6

# Caveats and Unexpected Effects

In-orbit the LWS was generally a well behaved and linear instrument, therefore the only persistent problem many users will find with their data is the presence of glitches (Section 6.1) and often a small difference between the two scan directions due to transients (Section 6.9). Spurious spectral features are fairly rare but those known are covered in Sections 6.7 to 6.11.

The 10 sub-spectra may not completely match photometrically (Section 6.5) for various reasons, such as statistical errors in the dark current (Section 6.4) and responsivity determination during processing (Section 4.4.1). The instrument also becomes non-linear when exposed to high fluxes (Sections 5.7 and 6.10).

For observers with data from extended sources, the LWS optics caused fringing and fracturing in the beam and these effects are described in Sections 6.2 and 6.3. As the LWS photometric calibration is based on a point source, these effects combined with diffraction will mean that the matching between sub-spectra will be worse for extended sources than point sources.

There are a further two caveats specific to the FPs, an unexplained systematic error in the wavelength calibration which nevertheless remains within the accuracy specifications (Section 6.12) and a problem, mainly concerning L03 observations, where the grating element is not placed accurately enough for the FP scan to be in the centre of the grating profile (Section 6.13).

### 6.1 Glitches

The deglitching performed by Derive-SPD is believed to remove the majority of the glitches in the data. However, some glitches may still remain undetected as illustrated in Figure 6.1. In particular, any glitch which occurs during the period of time discarded at the beginning of each ramp is not currently detected.

In addition it has been found that some (large) glitches have a long lasting effect on the detector responsivity. They can cause one scan for one detector to be significantly higher for some period of time. It is recommended to look carefully at the data scan by scan and discard dubious data points. This can be done easily within ISAP (see Section 8.2.2).

### 6.2 Response to Off-axis and Extended Sources: Fringes in the Data

Channel fringes are seen on all LWS spectra of extended or off-axis point sources, as is illustrated in Figure 6.2.

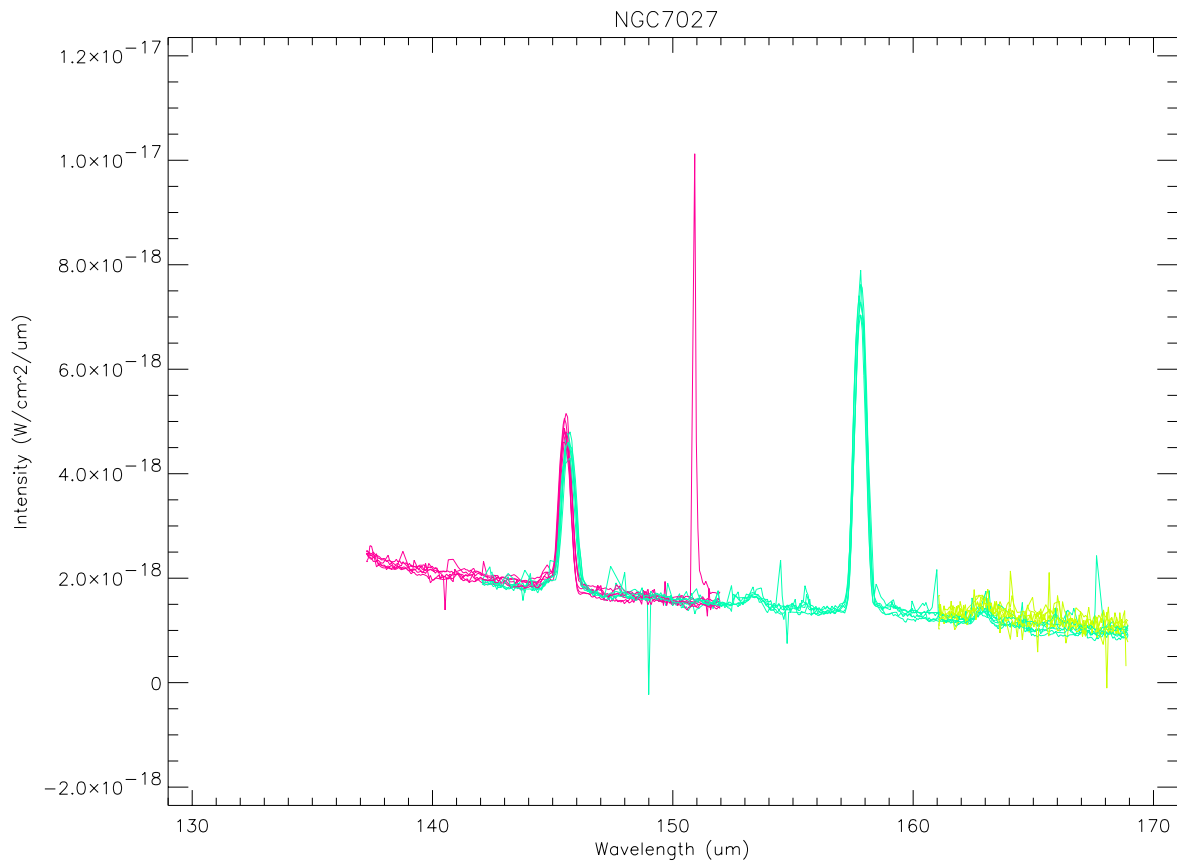


Figure 6.1: *Example of a remaining glitch in the calibrated data. This figure shows the individual scans (7 scans) plotted on top of each other. It partly covers three detectors: LW3 (violet), LW4 (green) and LW5 (yellow). The highest point in the spectrum (near 151  $\mu\text{m}$ ) is due to a glitch occurred during one scan on detector LW3.*

Extensive modelling of the response of the instrument has shown that the channel fringing is caused by Mirror 2 which was stepped, as explained in Section 2.3 and Section 5.9, causing interference between the reflecting surface of the LWS field mirror and its support structure as the diffraction pattern from the source falls off the edge of the field mirror itself.

The distance between any two fringe antinodes is predicted to be  $(\sigma_1 - \sigma_2) \sim \frac{1}{2h} = 0.33 \text{ cm}^{-1}$  in frequency space. As is evident in many observed source spectra (see for example Figure 6.2), the amplitude of this parasitic fringing increases with wavelength. Further, the diameter of the Airy pattern from the telescope also increases with wavelength because of diffraction, so it is more likely that the detector will view the annular part of Mirror 2. The contour field mirror controlled the illumination of this annulus. Modelling (Section 5.9) has determined that a  $120''$  diameter beam fell onto Mirror 2 and the annulus.

The reflectivity of the support structure material is not known well enough at these wavelengths to permit the production of an exhaustively quantitative model that would allow the removal of the channel fringes given knowledge of the spatial structure of the source. Instead a method has been devised that performs a multivariate fit for the period, amplitude and phase of the sinusoid in wavenumber space and removes it from the spectrum by division or subtraction. This has proved successful in removing the channel fringing from the continuum spectrum of most sources whilst preserving the shape and intensity

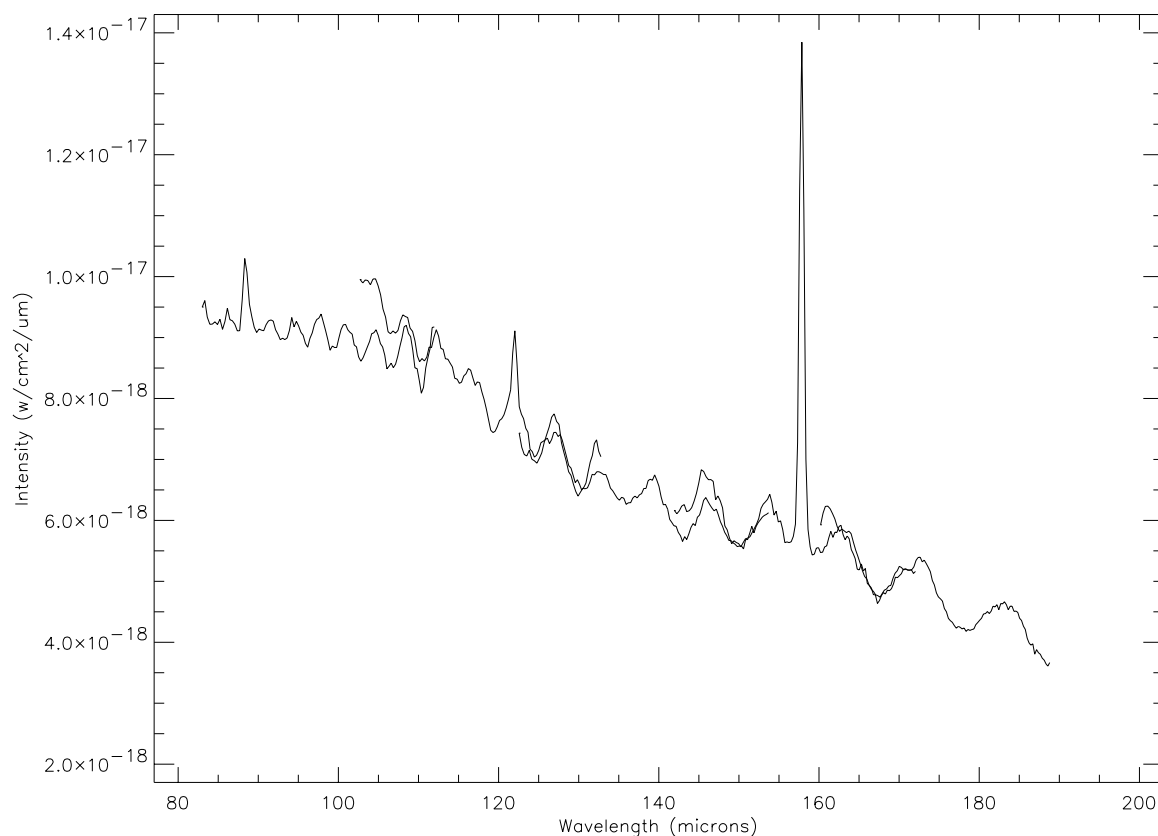


Figure 6.2: *Example of fringes in the spectrum of an extended source. Only the long wavelength detectors are shown here, as they are the most affected by the problem.*

of the unresolved spectral features. A special command is available in ISAP (see Chapter 8) to apply this defringing method to LWS grating spectra.

High frequency fringing also occurs on Fabry-Pérot spectra, although this is much more rarely seen. The spacing of the fringes in wavenumber is known:  $0.0095 \text{ cm}^{-1}$ . As for the grating, the fringes are stronger for longer wavelengths and undetectable for short wavelengths; their origin is probably the same as the one for the grating and related to Mirror 2. The `DEFRINGE` routine in LIA (see Chapter 8) allows the application of the defringing method to all three AOTs L01, L03 and L04.

### 6.3 Response to Off-axis and Extended Sources: Spectrum Fracturing

For point sources observed off-axis, and to a lesser extent extended sources, the stitching between adjacent detectors breaks down when the source lies in a particular part of the beam (see Figure 6.3). The reason for this is unknown but the part of the beam affected is the edge that passes close to the cutout in the contour field mirror, between Mirror 2 and the collimator. At shorter wavelengths the flux levels are generally higher in this region compared to similar radii in other parts of the beam, and at longer wavelengths the effect of fringing is reduced. The spectrum takes on a broken or fractured appearance

with large discontinuities between detectors. The effect is worse at shorter wavelengths and for the SW detectors it introduces a strong gradient in the flux with wavelength. The variation of the mean flux in the fractured region is the main cause of the asymmetry in the beam, and of the difficulty in modelling it. Two routines in LIA, `CORRECT_SPECTRUM` for point sources and `EXTENDED_FLUX` for extended sources, can be applied to reduce this effect in the spectra.

## 6.4 Dark Current Subtraction

As explained in Section 4.4.2, in the pipeline processing of the two grating AOT's (L01 and L02), the dark current is taken either as the average of the two dark current measurements performed respectively at the beginning and the end of each observation, or as a 'fixed' dark current that was determined in dedicated calibration observations (see Section 5.4). For the majority of sources, i.e. those above about 20 Jy at 60  $\mu\text{m}$ , the dark current is negligible. For faint sources however, the uncertainty in the dark current measurement can become large relative to the source flux level and can lead to sub-spectra being misaligned or even to a negative sub-spectrum if the dark current determined is higher than the on-target flux. In such cases, it is better to revisit the dark current subtraction in LIA. The user can then choose to use the 'fixed' dark current or a dark current previously interactively derived within LIA (for LIA see Section 8.2.3).

Processing of Fabry-Pérot data (L03 and L04) systematically uses the fixed dark current.

## 6.5 Differences between Overlapping Sub-spectra

In some cases there is a difference between the sub-spectra from different detectors in their overlapping regions, where they should in principle be at the same flux level. As an example see Figure 6.4 where the SW3 detector is obviously misaligned compared to the rest of the detectors. Each sub-spectrum has an independent calibration and this misalignment is most probably due to uncertainty in the responsivity of the detectors, estimated independently for each observation.

The LWS calibration is based on Uranus, which is a point source within the LWS beam. The output of the automatic processing assumes the observed object is also point like in the LWS beam. Therefore for most point sources there is almost no difference between the levels of the detectors with the small differences being due to the uncertainty in the determination of the responsivity of that detector for that observation. For extended sources the sub-spectra are not expected to match. This is because LWS has a different effective beam size for different detectors due to fringing. A full description of the LWS beam and the fringing along with information on how to correct for these effects can be found in Section 6.2.

Another uncertainty, which can have an impact on the relative levels of the sub-spectra, is that of the determination of the dark current. On this subject, see Section 6.4.

It should be noted that SW1 has the least reliable photometric calibration of the LWS detectors, due to a long time constant which makes it visibly affected by long term transient behaviour (Section 6.9).

From a photometric point of view, it is strongly recommended that users should not attempt to merge the sub-spectra together. Nevertheless, the spectra can be fitted back together within ISAP (see Section 8.2.2).

## 6.6 Spurious Features Introduced by the RSRF

The calibration of any source is achieved by dividing the observed photocurrents for that source by the Relative Spectral Response Function (RSRF) i.e. the overall responsivity of the instrument for each detector, in terms of current per unit flux-density (Section 5.2.2). Clearly, any spurious features in the RSRF will be transferred to the calibrated spectrum. The signal-to-noise ratio obtained in the calibration

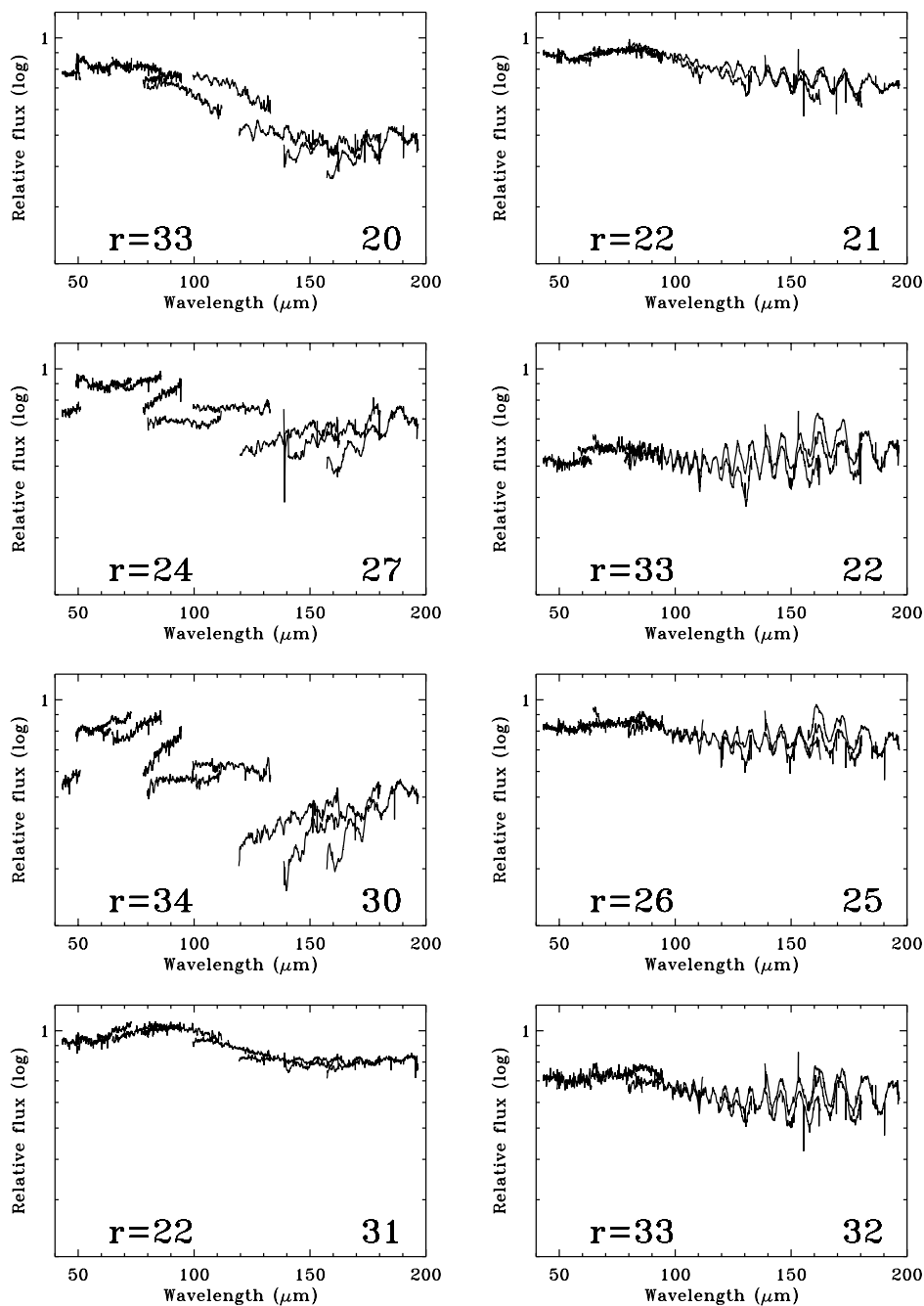


Figure 6.3: Spectra of Mars observed at various positions off-axis corresponding to those in Figure 5.16. The fracturing of the spectra can be seen on one side of the field, and the effects of fringing at longer wavelengths.

observations of Uranus – and therefore in deriving the RSRF – is comparatively modest and thereby limits the signal-to-noise ratio on the calibrated spectrum of any other source, no matter how strong.

An eventual lack of precision in the Uranus model used to define the RSRF would also be propagated to

all LWS observations, creating possible spurious features in the calibrated spectra.

A good example of spectral features induced by uncertainties in the RSRF is a double-peaked profile visible in OLP Version 10 data products of all SW1 spectra of strong-continuum sources, as illustrated in Figure 6.4.

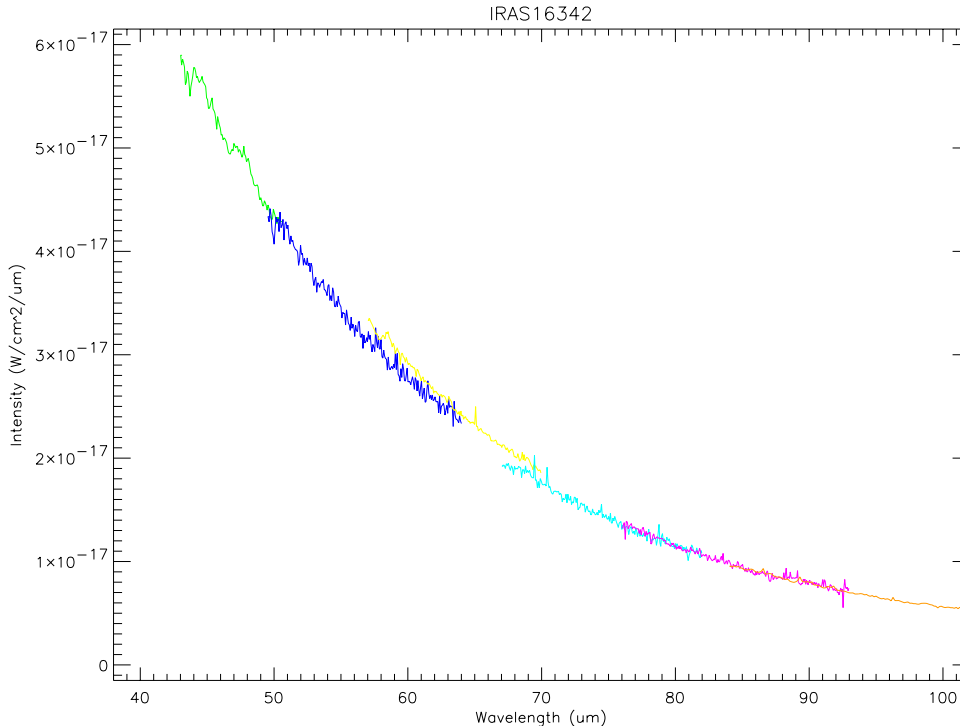


Figure 6.4: *The double-peaked feature in SW1 visible here (around 44 and 47  $\mu\text{m}$ ) is a probable example of spurious features due to an uncertainty in the Uranus model used to derive the RSRF.*

Therefore observers should be very circumspect in picking out unknown features in their spectra: these should be checked against the published RSRF (in the LCGR file). This can be done with the LWS Interactive Analysis software (LIA – see Section 8.2.3).

## 6.7 The Near-Infrared Leak

LWS spectra of stars that are bright in the near-infrared (NIR) sometimes contain features which resemble broad spectral features, but which do not occur at the same wavelength in detectors which cover the same range (see an example in Figure 6.5). The origin of these features is believed to be a near-infrared leak in the blocking filters located in front of the detectors. This supposition is supported by a statistical test, which showed a correlation between these features and the brightness in the J, H, and K near-infrared photometric bands. The strength of these features is best correlated with the strength of the sources in the H-band (1.6  $\mu\text{m}$ ). In a small sample of post-main-sequence stars observed in the Core Programme, all those which had an H-band emission brighter than about 2.2 magnitudes (around 140 Jy) were seen to exhibit these spurious features.

Follow-up observations of one of the affected sources gave results consistent with a near-IR leak as the origin of the features. The spurious features are now known to be reproducible, in terms of wavelength,

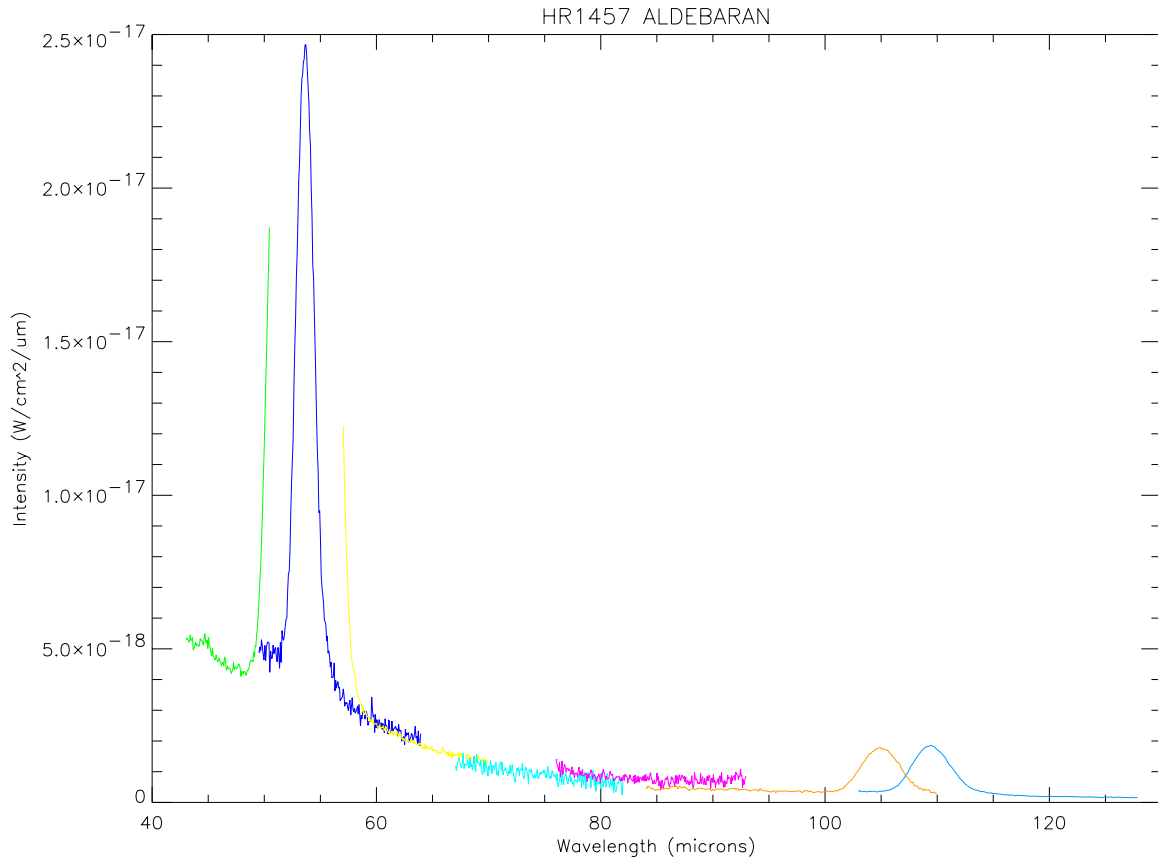


Figure 6.5: *Example of features due to the near-IR leak in the spectrum of Aldebaran.*

shape and FWHM from one source to another and for repeated observations of the same source. This means that a template profile can be created which observers can fit to their data and use to remove the spurious features. To first order the profile is Gaussian for each of the three most-affected detectors: SW2, LW1 and LW2. The short-wavelength wing of a similar feature also affects the longest-wavelengths of detector SW1's range, while the long-wavelength wing of a spurious feature affects the shortest wavelengths of detector SW3's range. The best estimates of central wavelength and FWHM of the Gaussians are given in Table 6.1.

Using these parameters, it has proved possible to effectively remove these spurious features and to detect narrow emission lines that were undetectable before.

Based on the small number of affected sources in the Core Programme, we can offer the following estimates:

1. The spurious features become noticeable when the H-band emission of the observed source is brighter than 2.2 magnitudes, and the ratio of flux densities  $F(1.6 \mu\text{m})/F(60 \mu\text{m}) \geq 4$ .
2. A zero magnitude source at the H-band (roughly  $F(1.6 \mu\text{m}) = 1050 \text{ Jy}$ ) gives a feature with peak flux  $1.5 \cdot 10^{-18} \text{ W cm}^{-2} \mu\text{m}^{-1}$  in detector SW2.

LWS observations affected by the near-IR leak have now been corrected from the features and the corrected spectra are available as 'Highly Processed Data Products' (HPDP) from the ISO Data Archive.

Table 6.1: *This table gives the characteristics of the features that are observed due to the near-IR leak of the blocking filters of the LWS detectors. The values for SW1 and SW3 are rather unreliable as only one wing of the feature is visible on either of these detectors.*

Detector	Peak wavelength [ $\mu\text{m}$ ]	FWHM [ $\mu\text{m}$ ]
SW2	53.60	1.86
LW1	105.08	4.30
LW2	109.39	3.91
SW1	51.6	2.4
SW3	52.2	4.0

## 6.8 ‘Detector Warm-up Features’ in the Long Wavelength Detectors

Spurious emission features appear on the LWS spectra from the longest wavelength detectors (LW3, LW4 and LW5) in observations taken towards the end of the mission. An example of a spectrum affected by these features is shown in Figure 6.6.

A systematic investigation by the LWS Instrument Team led to the identification of the features in the following observations (TDT numbers):

65401108, 65601407, 66401804, 66500305, 66500306, 66801524, 66801525, 67100301, 67301203, 67301222, 67301223, 67501340, 67501357, 68500805, 68501504, 68701144, 68900805, 68900806, 70301315, 70302001, 70302002, 70302104, 70302105, 70302225, 70601702, 70601904, 71301708, 73700762, 73701360, 73701459, 74601203, 74802710, 74802912, 74803403, 74901722, 74901723, 75002331, 75002332, 75002333, 75400423, 75601535, 79000702, 80401605, 81301224, 81301225, 81301226, 81301227, 81301228 81301301, 81601413.

Note however that this list is not exhaustive; in particular the features have been recognized only in L01 spectra, since the wavelength ranges covered in L02 and L04 spectra are too small to be able to distinguish these features. For L03 data no systematic search for the presence of these features has been carried out.

The features are broad (a few  $\mu\text{m}$ ) emissions centred near  $155\ \mu\text{m}$  on detector LW3,  $159\ \mu\text{m}$  on detector LW4, and  $163\ \mu\text{m}$  on detector LW5. In addition to them, a rise in flux can be seen on the LW5 detector longward of  $180\ \mu\text{m}$ . The features are more visible on rather faint sources (typically less than a few  $10^{-18}\ \text{W cm}^{-2}\ \mu\text{m}^{-1}$  at  $160\ \mu\text{m}$ ), since the peak strength of the features is a few times  $10^{-19}\ \text{W cm}^{-2}\ \mu\text{m}^{-1}$ . The biggest problem of these features is that the one on the LW4 detector blends with the  $157\ \mu\text{m}$  [C II] line.

A detailed examination of the cause of these anomalies has shown that they are associated with a simultaneous increase in dark current, noise and spontaneous spiking on the stressed detectors and a decrease in the current required to maintain the temperature of the stressed detector mount. This all indicates that the temperature of the stressed detector mount, which is connected to the helium tank, did not recover to the nominal value following the illuminator flash at the beginning of the observations. An increase of only a few hundred milli-Kelvins is sufficient to radically change the dark current and noise performance of the stressed detectors. The straylight features themselves appear to be due to radiation from a source of 8 K located somewhere in the vicinity of the detector block - possibly radiating through the holes in the back of the instrument. The theory advanced to explain the change in the thermal balance of the instrument is that the liquid helium film in the tank broke periodically in the vicinity of the LWS strap location as the tank came close to exhaustion. The radiation and conducted heat from the illuminators then caused the detector block to warm up with little or no cooling power available from the LHe tank. As the observations progressed the detectors can be seen to return to their nominal state but, unfor-

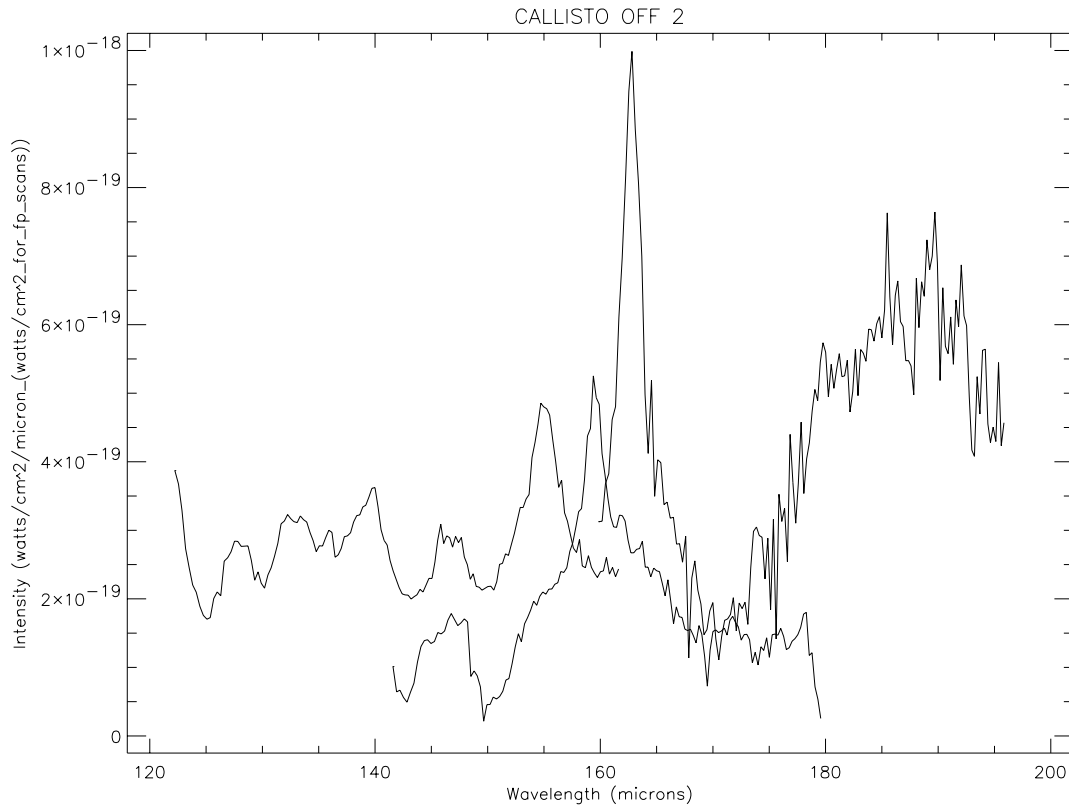


Figure 6.6: *The straylight features on LWS detectors LW3 (at 155  $\mu\text{m}$ ), LW4 (at 159  $\mu\text{m}$ ) and LW5 (at 163  $\mu\text{m}$ ). Note also the strong rise in flux beyond 180  $\mu\text{m}$ .*

tunately, the stressed detector data from the observations affected are effectively useless as the changes in responsivity, dark current and the spontaneous spiking mean that they cannot be calibrated in any meaningful way.

## 6.9 Transients and Memory Effects

### 6.9.1 Description

All LWS detectors presented some level of memory effects, also called transient effects, due to the slow response times (typically tens of seconds) to changes in illumination (Church et al. 1992, [7]). These non-linear effects were more severe for the Ge:Be detector (SW1) and some of the stressed Ge:Ga detectors (LW2–LW5). The response of the detectors depended not only on illumination level, but also on the illumination history. The transient effects could be enhanced by intrinsic spectral characteristics of the observed astronomical source, but also by strong glitches or fringes. A good illustration of the response times of the detectors is given by the time series of L02 fixed grating observations, where each detector remains at one wavelength and thus sees the same flux for a long time. Figure 6.7 (from Müller 2001, [29]) shows typical examples of transients in such fixed grating observations. In this mode of operations, the transients are easy to correct for, but it is much more difficult for a normal scanning mode, where the illumination experienced by each detector changed every half-second and the detectors never had time to

stabilise.

The best way to correct the transient effects in spectra would have been to handle a complete physical model of each detector as well as a complete knowledge of the detector illumination in all observing conditions (see Coulais & Fouks 2001, [10]). However, there was no such model available for LWS detectors.

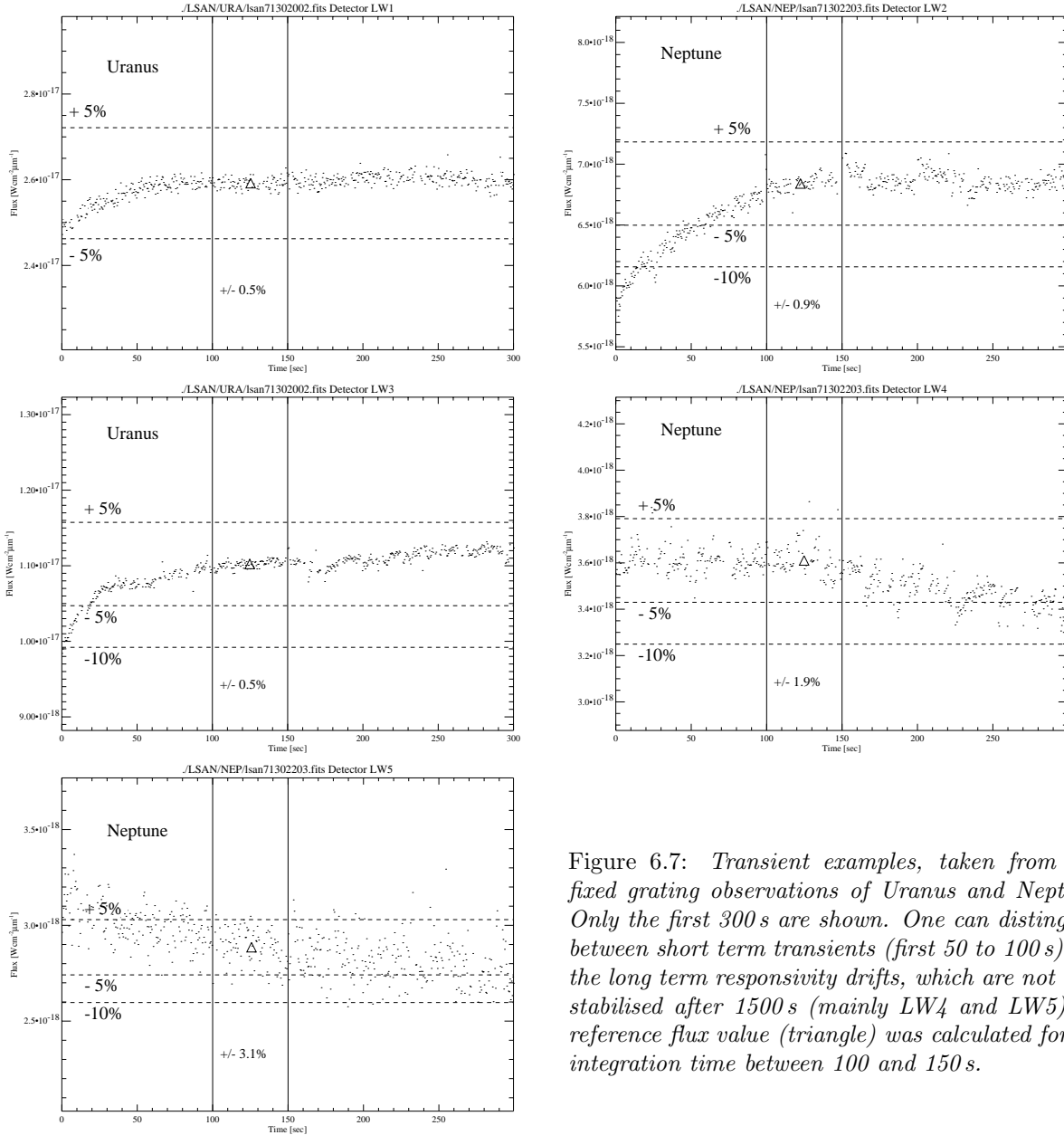


Figure 6.7: *Transient examples, taken from L02 fixed grating observations of Uranus and Neptune. Only the first 300 s are shown. One can distinguish between short term transients (first 50 to 100 s) and the long term responsivity drifts, which are not even stabilised after 1500 s (mainly LW4 and LW5). A reference flux value (triangle) was calculated for the integration time between 100 and 150 s.*

Some attempts to derive a physical model of Ge:Ga photo-conductors were done in the PHT and LWS teams before ISO launch, which were not conclusive. The use of an empirical solution has been proposed, based on the standard Fouks-Schubert model (see Fouks & Schubert 1995, [17] and references therein) derived for Si:Ga detectors, and used with success for CAM and PHT-S detectors (Coulais & Fouks 2001, [10]; Coulais et al. 2001, [11]) and for some SWS detectors (Kester 2001, [22]). The detailed report of the transient study in LWS is given in Caux 2001, [5].

In order to implement this solution the formalism of the usual Fouks-Schubert model (Fouks & Schubert 1995, [17]), has first been adapted to the specific LWS case. The original Fouks-Schubert model is written for semi-stationary fluxes. For photometric instruments, as CAM and PHT, this assumption is valid. This is not really the case for the LWS spectrometer, for which the flux varies almost continuously. However, generally the flux change from one step to the other is small and one can consider the semi-stationary state valid, assuming each step of the spectrometer to be a new constant flux level. The original Fouks-Schubert formula can then be rewritten into a more suitable form for LWS as:

$$J_n(t) = \beta J_n^\infty + \frac{(1 - \beta)(J_n^{ini} - \beta J_n^\infty)J_n^\infty}{J_n^{ini} - \beta J_n^\infty + (J_n^\infty - J_n^{ini})e^{-\frac{(t-t_n)}{\tau}}} \quad (6.1)$$

Where  $J_n(t)$  is the observed signal at the instant  $t$ ,  $J_n^\infty$  is the expected signal if no transient effects were present,  $J_n^{ini}$  is the observed flux just after the change at the time  $t_n$  and  $\tau$  is a time ‘constant’ which depends on the detector (we will see later that in the LWS case,  $\tau$  is not constant). We also have the continuity equation:

$$J_n^{ini} = J_{n-1}^{final} + \beta(J_n^\infty - J_{n-1}^\infty) \quad (6.2)$$

We have tried different forms of  $\tau$  and the best results, in terms of quadratic difference between forward and backward scans, were obtained with:

$$\tau = \frac{E}{abs(J_n - J_{n-1})^\alpha} \quad (6.3)$$

where  $E$ ,  $\alpha$  and  $\beta$  are free parameters which are intrinsic for each detector. One can note that the main difference with the original Fouks-Schubert relation is the dependence of  $\tau$  with the signal gradient and not with the signal value. The second order equation implies two solutions for the transient corrected intensity, among which we always chose the one closest to the non-corrected value as for most observations we do not expect a very strong correction.

In order to fully calibrate the transient-corrected spectra, we have derived a transient-corrected RSRF, derived as the original RSRF (Section 5.2) but based on transient-corrected observations of Uranus (see Caux 2001, [5] for more details). The differences between the transient-corrected RSRF and the original RSRF are of the order of  $\pm 2\%$ .

### 6.9.2 The correction procedure

A dedicated LIA routine has been written to allow the user to correct LWS spectra for transient effects in the case of grating observations. It is not yet implemented in the current LIA (Version 10.1) but will be in one of the next LIA releases. This routine uses the SPD products as the correction should be applied on the time series. It requires to average previously the scans (forward and backward scans separately) to ensure a good signal-to-noise level of the data to be corrected. We have checked that generally the differences seen on scans performed in the same direction are only due to noise. Sometimes, the first forward and backward scans are affected by long term transient effects (due to a prior observation of a very bright source for example), and require to be entirely zapped. It also requires a previous very careful deglitching of the data as the presence of remaining glitches can seriously hampered the correction process.

The best  $\alpha$ ,  $\beta$  and  $E$  parameters are computed for each observation, using the criterion that the signal recorded on forward and backward scans should be equal. The observed difference is hence supposed to be the signature of the transient effects which are different in the two scanning directions, due to the asymmetrical spectral shape of the bandpass filters located in front of the detectors or to a gradient in the spectrum.

The procedure then applies the correction simultaneously to the forward and backward averaged scans, and produces two transient-corrected spectra, one forward and one backward, which can be compared to judge how well the correction performed, and which have to be further averaged together to produce the final transient-corrected spectrum.

The LIA routine that finds the best Fouks-Schubert parameters has been tested on a wide set of different observations and was found to be stable. We have used all available Uranus observations to check if

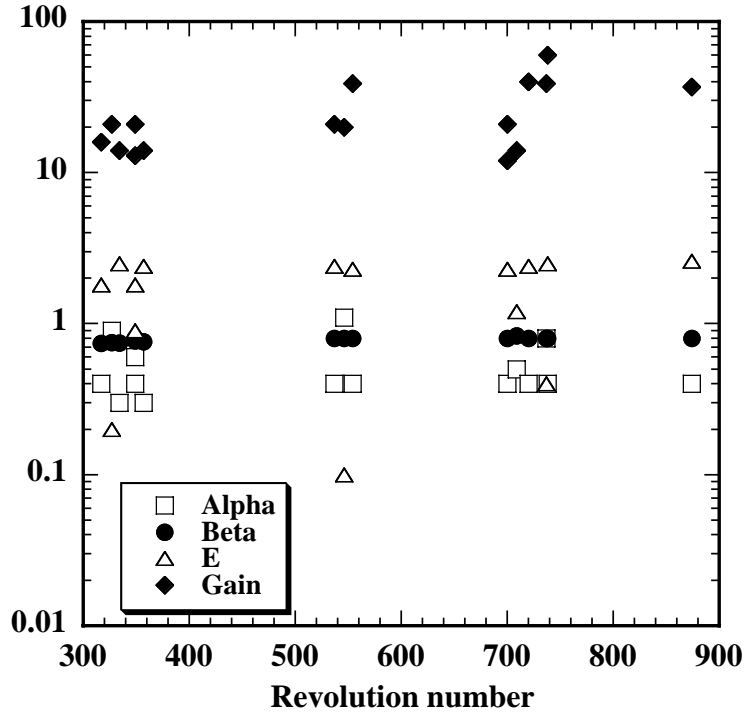


Figure 6.8: Variation, with the revolution number, of  $\alpha$ ,  $\beta$ ,  $E$  and gain (in terms of quadratic difference between forward and backward scans) for Uranus observations (detector LW2).

the three tunable parameters vary for a given source. We have found all parameters rather constant for all observations taken with the same detector bias and the same oversampling factor, as is illustrated in Figure 6.8. The variation with bias and sampling factor is expected because the intrinsic properties of the detectors vary with the applied bias and because the parameter  $\tau$  is proportional to the signal gradient, which varies with the oversampling factor for the same input flux. As an illustration of the parameter values, the mean Uranus values for  $\alpha$  and  $\beta$  are listed in Table 6.2. They are used as starting values in the transient correction procedure but are expected to vary with the object because they depend on the spectrum gradient. ( $E$  is coupled to  $\alpha$  and the starting value is set to 1.0)

Table 6.2: Mean transient correction parameter values for Uranus, used as starting values in the correction procedure.

Detector	SW1	SW2	SW3	SW4	SW5	LW1	LW2	LW3	LW4	LW5
$\alpha$	0.6679	0.5161	0.7788	0.7707	0.7000	0.5224	0.5382	0.4251	0.4412	0.5346
$\beta$	0.82	0.8971	0.9233	0.9033	0.9367	0.94	0.774	0.74	0.7942	0.9491

The data improvement (in terms of quadratic difference between forward and backward scans) is important for detectors presenting large memory effects (SW1, LW2 and LW3), and is smaller for the others, particularly for non-stressed Ge:Ga detectors. This improvement depends as well on the type of source observed: extended sources with large fringing are subject to a much larger improvement than point sources.

The validity of the correction has been tested on different types of astronomical sources. Figure 6.9 shows the effect of the correction on an extended source (galactic line of sight). One can note a small improvement at small scale, the remaining effects at large scale are supposed to be due to the imperfect defringing. One can also note the difference in the absolute level of the flux, which has an incidence on the stitching of the detectors. Figure 6.10 shows the improvement obtained on strong lines for a

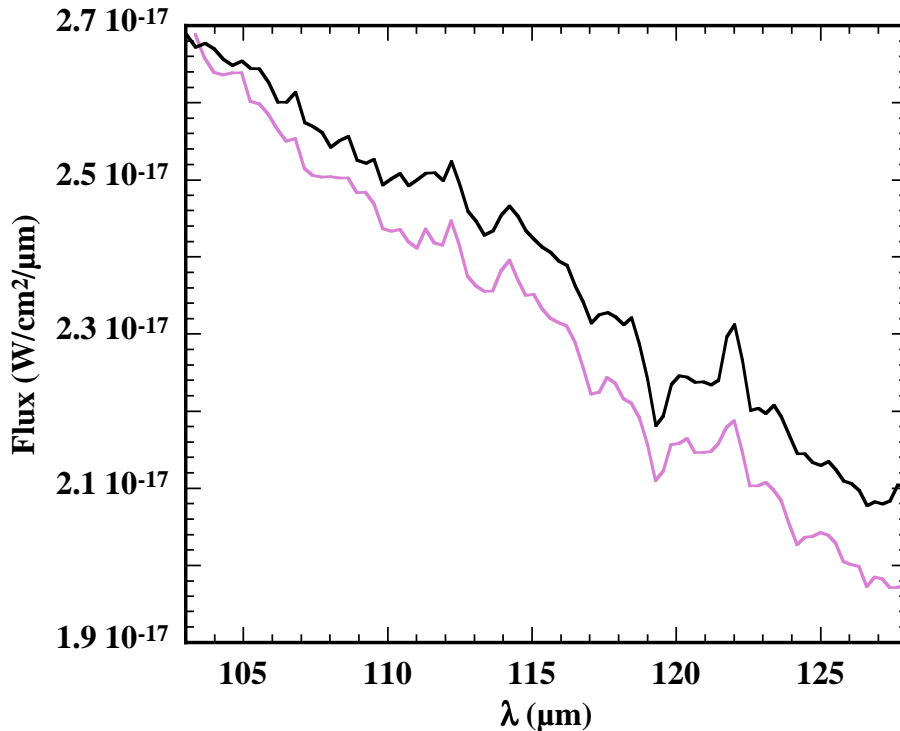


Figure 6.9: *Result of the transient correction obtained for an extended source (detector LW2). Grey line: original data - black line: transient effect corrected data.*

non-extended source (a compact HII region) relative to the LWS beam. For a detector having small transient effects (LW1; Figure 6.10a), the difference on the computed line fluxes is small (a few %) while for a detector presenting larger transient effects (LW4; Figure 6.10b), it can be of the order of 10%. One can also note the more symmetrical shape of the lines after the correction, as well as a line width closer to the standard value. Finally, it can be noted that the wavelength calibration for transient effect corrected data is slightly different than the original one.

Fabry-Pérot observations with LWS were always performed (for routine observations) by scanning the spectrum in only one direction. This prevents the use of the forward and backward scan differences to derive the correction parameters. We are presently working on a dedicated LIA routine to correct FP observations interactively, which will require some inputs from the observer, as the astronomical source line shape and width. This will always make the correction observer-dependent.

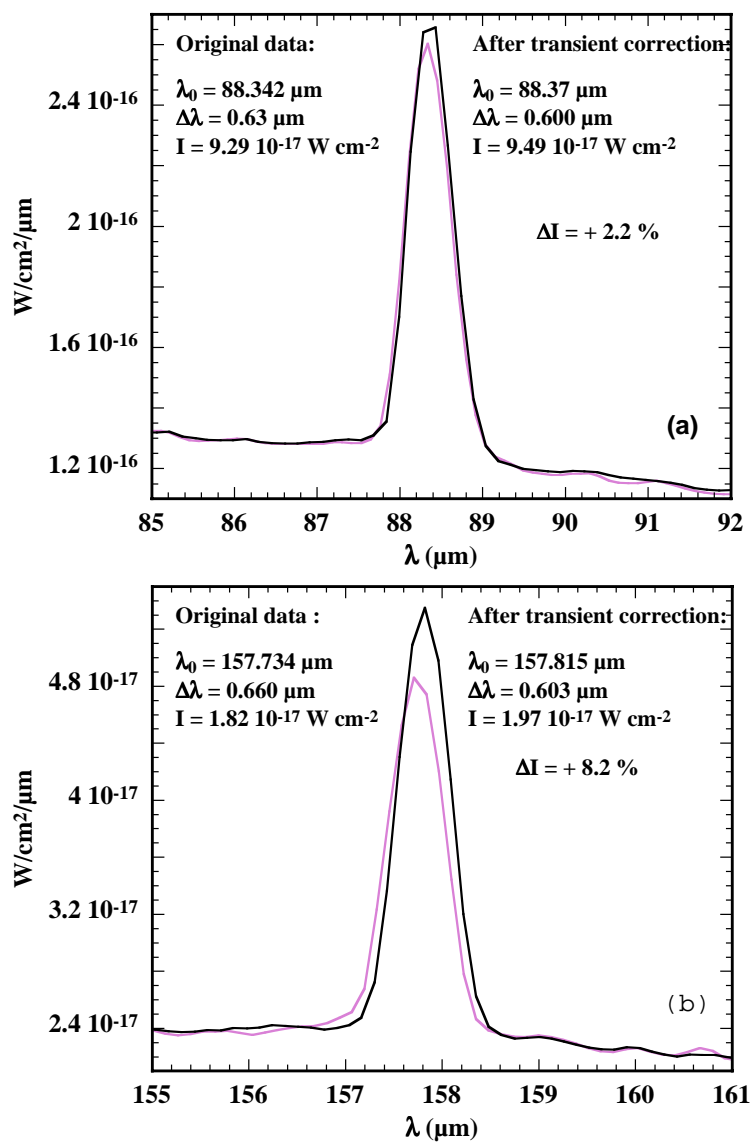


Figure 6.10: Result of the transient correction obtained for a non-extended source. Grey line: original data - black line: transient effect corrected data. (a) detector LW1; (b) detector LW4.

## 6.10 Detector Non-linearity: the Strong Source Correction

### 6.10.1 Does your data require the correction?

The strong source correction is described in Section 5.7. To see if the strong source correction needs to be applied to your data, you should look at your LSAN data in ISAP: this is best done by examining the overlapping sub-spectra (in units of  $\text{W cm}^{-2} \mu\text{m}^{-1}$ ) of detectors LW1–LW4 with their neighbours to see if their spectral shapes agree. LW3 is the most non-linear detector so it is best to check that one first. If some of the detectors do not agree on spectral shape (and their spectra are ‘saggy’) then the detector sub-spectra are affected by non-linearity. Figure 6.11 shows an example of a strong source that has ‘saggy’ sub-spectra and requires the strong source correction. In particular you should check your data for this if the saturated data flag comes up when data are loaded into ISAP.

A rough flux guide in Janskys: for data with a flux of less than 500 Jy at  $150 \mu\text{m}$  the correction will not be necessary (it is also unlikely that data in the range of 500 to 1000 Jy will need the correction). For data in the flux range of 1000 to 10000 Jy at  $150 \mu\text{m}$  the correction might be required and the above steps should be followed for further confirmation. Above 10000 Jy it is very likely that the correction should be applied to the data.

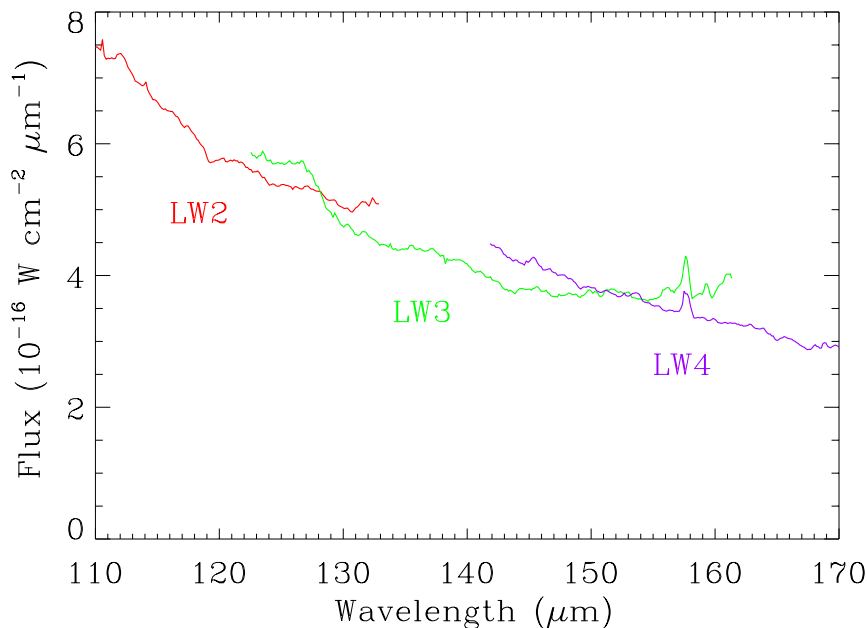


Figure 6.11: An example of a spectrum of a strong source, where the sub-spectra are ‘saggy’, i.e. the spectra of overlapping detectors have different shapes.

If any of your detector sub-spectra look saggy, the strong source correction needs to be applied to the data (the calibration of these saggy data is wrong, and cannot be trusted). The reason for, and the description of, the correction are exposed in Section 5.7.

### 6.10.2 Getting the correction applied to your data

If you have data requiring the strong source correction you can contact the UK ISO Data Centre via `isouk@r1.ac.uk`. The data will then be corrected by experts and the resulting data files sent to you.

If you wish to carry out the correction procedure yourself, you can use the `SS_CORR` routine available in LIA (see Section 8.2.3), followed by the `SHORT_AAL` procedure to process the corrected LSPD file into an LSAN file. The strong source correction has been made using Mars, as well as Saturn. Both corrections should be applied to your data and you have to decide which is best by looking at the agreement of the sub-spectra shapes of the LSAN files. In some cases the decision is not easy so if you require help in deciding please contact `isouk@r1.ac.uk` for assistance.

The new LSAN and LSPD files can then be used in ISAP and LIA to do any further data reduction. On reading into ISAP you should see that the data are no longer saggy. You should not rely on the absolute fluxes of this LSAN file. The absolute calibration of the linear detectors can be trusted however and hence the sub-spectra of detectors LW1–LW4 can be scaled to one of these to produce a relative calibration. In doing this it should be seen that now the detectors agree on the shape of the spectrum.

Ideally the observations of strong sources were carried out using quarter-second ramps (integrations), however if they are half-second ramps the correction should not be applied directly to ramps of this length (see Section 5.8). You will need to contact `isouk@r1.ac.uk` to have your data processed as quarter-second ramps. Then the strong source correction will be carried out on the data (as described above) and all the relevant data files will be sent on.

In the near future, a table listing the observations that have already been corrected for strong-source effects will be available. The data from these corrected observations will be made available as 'Highly Processed Data Products' (HPDP) for download from the ISO Data Archive.

## 6.11 57.16 $\mu\text{m}$ SW2 Feature in the Fabry-Pérot Spectra

An unidentified feature has been observed on several sources (Orion, 30 Dor, G 298.228–0.331) at 57.16  $\mu\text{m}$ , about 0.17  $\mu\text{m}$  shortwards of the [N III] 57.33  $\mu\text{m}$  line on detector SW2. This line cannot be real because it is not seen on detector SW3. It is believed to be related to the line asymmetry seen on the grating spectrum for the 57  $\mu\text{m}$  line on SW2 only, however the wavelength shift needed to make the asymmetry observed on the grating in the cases of 30 Dor and G 298.228–0.331 is higher (0.35  $\mu\text{m}$ ) than that observed on the FP spectrum. What causes this feature is not known.

## 6.12 FP Wavelength Calibration

Although the FP wavelength calibration accuracy meets the specifications (see Section 5.12), the velocity difference observed between different lines in a given object is substantially higher than the velocity dispersion measured on repeated observations of the same line, as illustrated in Figure 6.12. This aspect shows that the wavelength measurements by the Fabry-Pérot are very stable but the absolute wavelength accuracy is hampered by an unknown effect, which could be the uncertainty on the theoretical wavelength of some fine-structure lines, as discussed in Section 5.12.5.

## 6.13 Removal of the Grating Resolution Element in FP Observations

Fabry-Pérot observations with the LWS were implemented as a series of mini-scans. For each mini-scan, the grating was set to a fixed position and the selected interferometer was scanned over a range of gap values. At the end of the interferometer scan, the grating was moved to a different position and the next

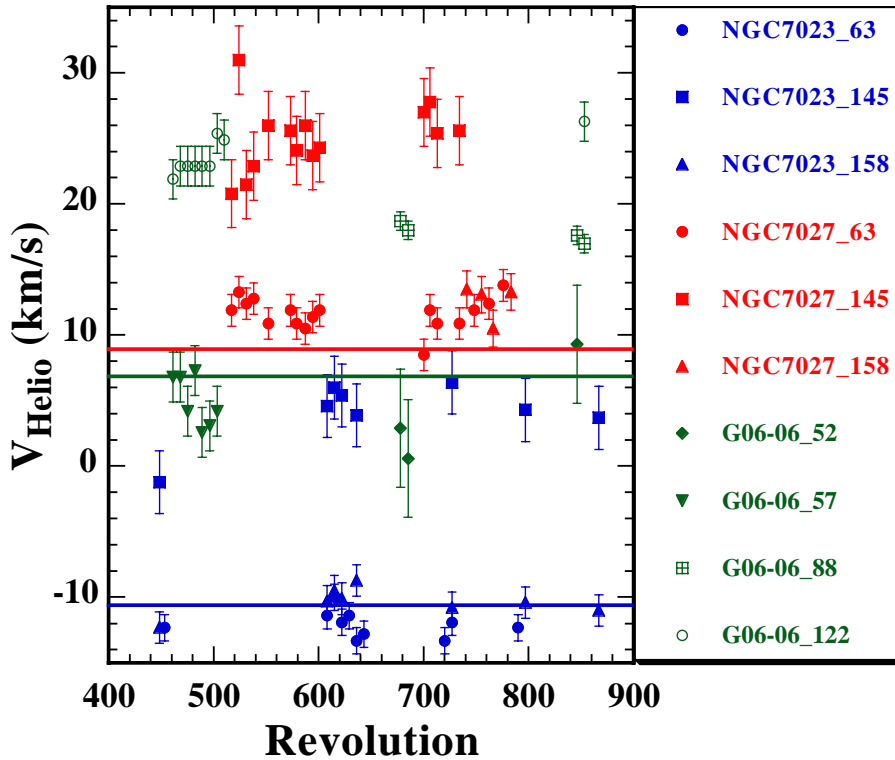


Figure 6.12: *This plot illustrates the good wavelength stability of the Fabry-Pérots together with the uncertainty in the absolute calibration. Central velocities are plotted for each line and each object as a function of revolution number. It shows that although for the same line/object the velocity is very stable, the velocities derived from different lines are different. This evidences a systematic uncertainty in the calibration which is not yet understood but which in any case is never higher than half a resolution element.*

mini-scan began. Each mini-scan therefore sampled the grating response profile, which must be removed from the data. Removal of the grating response profile has proved difficult because of a non-repeatability of unknown origin in the grating position (Section 5.10). For high-resolution observations this non-repeatability corresponds to an uncertainty in the wavelength at which the grating profile was centred. Before OLP Version 8 the standard pipeline processing did not take into account this uncertainty: it just assumes that the grating response profile was centred at exactly the wavelength specified by the grating wavelength calibration. When the grating profile is removed from the Fabry-Pérot data, the result can be a spectrum that is significantly skewed. The unpredictable nature of the grating setting, combined with the fact that there is no independent means of determining the grating position, means we are forced to infer the grating position directly from the data.

For this reason, from OLP Version 8 onwards, the underlying grating profile is not removed in the standard pipeline processing. For L04 data, where the FP scans were quite short, the effect should be very small. For L03, however, there may be some effect on the slope of the continuum, depending on the extent of the FP scan at each grating position.

The user is recommended to refer to FP\_PROC, the LWS Interactive Analysis (LIA) FP processing tool which removes the grating profile. For L04 spectra the user can remove the skewness interactively, thereby deducing the actual grating position. For L03 observations, the grating transmission profile is removed from each mini-scan separately and can be shifted for each one until it matches best with its neighbours.

This can either be done interactively for each mini-scan or via an automatic least squares routine which minimises the difference between overlap on adjacent mini-scans.

New grating profiles have been derived, which are better characterised away from the maximum and thus have more accurate wings than the profiles used in the OLP calibration files. They allow to remove the grating shape across the entire mini-scans.

## 6.14 Use of ‘Non-prime Data’ in FP Observations

During each L03 and L04 observation the LWS FP and grating settings were optimised for the detector whose bandpass filter included the wavelength range of interest. This was designated as the ‘prime’ detector. However, all ten LWS detectors recorded data simultaneously in their own spectral ranges. The other nine detectors are known as ‘non-prime’ and often recorded useful data that can complement the prime data. These data could not be processed within the old version of FP\_PROC, which only dealt with prime detector data. This procedure has been updated to allow the use of the non-prime detectors, as described in detail in Polehampton 2001, [34].

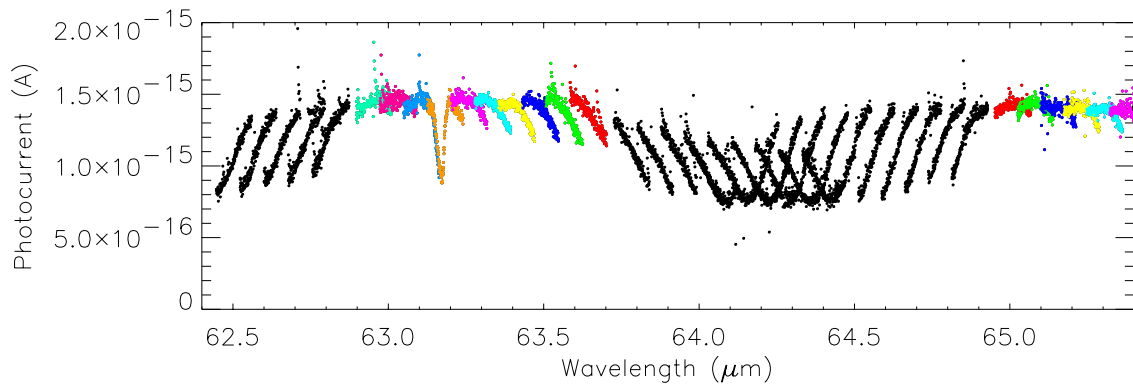


Figure 6.13: *Example of the raw data (after wavelength calibration) recorded on a ‘non-prime’ detector during an L03 observation. There are clearly useful mini-scans present in the data (in colour).*

In the LIA routine FP\_PROC all ten detectors appear in a menu bar at the top of the screen. This allows non-prime data to be selected and processed in the same way as prime data. In order to process all non-prime detectors the FP throughput calibration was extended to cover wavelengths outside each FP’s nominal range. The detectors within each FP’s nominal range are shown in Table 6.3.

Table 6.3: *Detectors within each FP’s nominal range.*

FPS	SW1	SW2	SW3
FPL	SW4	SW5	LW1 LW2 LW3 LW4 LW5

As a general guide to know how good a mini-scan is (see Figure 6.14), we define it as ‘useful’ if it had at least one data point located above 90% of the maximum transmission of the grating. Assuming that the grating profile was approximately Gaussian, the 90% level occurred at a distance from the profile centre of:

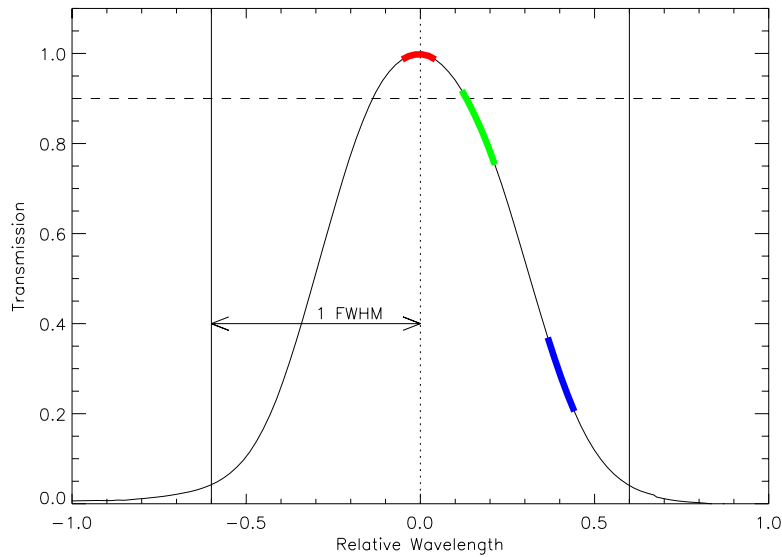


Figure 6.14: The grating profile shape (solid line) is shown with the limits used to define ‘useful’ data. The red and green mini-scans are classed as ‘useful’ whereas the blue mini-scan is not.

$$x^2 = -\ln 0.9 \left( \frac{FWHM}{2(2\ln 2)^{1/2}} \right)^2 \quad (6.4)$$

where  $FWHM$  is the full width at half maximum of the grating profile. This gives a cut-off distance of  $x=0.195 FWHM$  from the profile centre. This limit ensures that most of the prime data are defined as having good signal-to-noise. This limit is nevertheless only meant to give an indication. Some mini-scans might not meet the ‘useful’ data criteria and still be good to use, only with a slightly lower signal-to-noise ratio.

A good demonstration of the improvement that can be achieved using non-prime data is illustrated in Figure 6.15 showing a comparison of prime and non-prime data for the  $53 \mu\text{m}$  OH lines in Sgr B2 (from Polehampton 2002, [33]).

## 6.15 Side Order Contamination in FP Data

When the FP orders are so close together that more than one order is included in the range of wavelengths transmitted by the grating, the photocurrent recorded is an over-estimate of the true value. This is a particular problem on detector LW1 using the long wavelength FP (FPL) and SW2 using the short wavelength FP (FPS).

Therefore a correction to compensate for FP side order contamination is automatically applied in the LIA routine `FP_PROC`.

If more than one FP order occurred within the wavelength range transmitted by the grating the measured photocurrent was due to the combined flux in these orders (see Figure 6.16). If the FP throughput, detector response and intrinsic source flux did not change significantly between one FP order and the next then the relative contribution from each order can be calculated from the value of the grating transmission at each order wavelength.

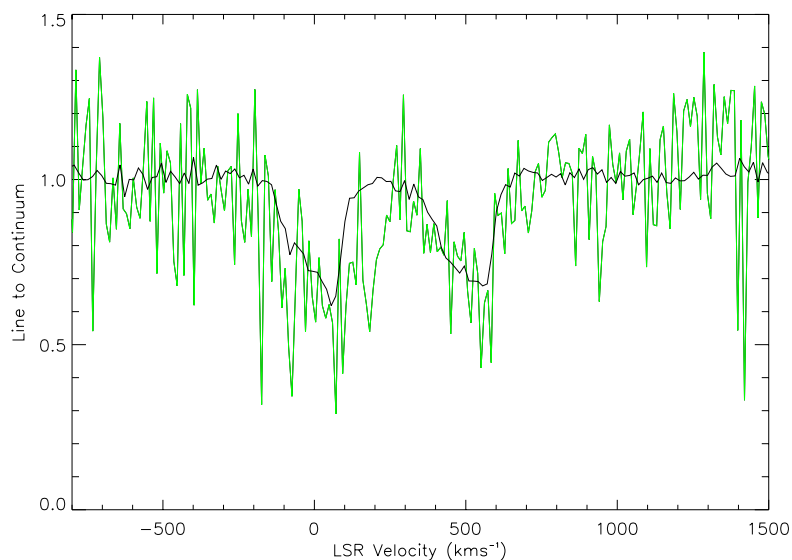


Figure 6.15: Comparison of prime and co-added non-prime data for the  $53\ \mu\text{m}$  OH lines in Sgr B2. Prime FPS observation is in green and co-added non-prime observations (FPL) are in black.

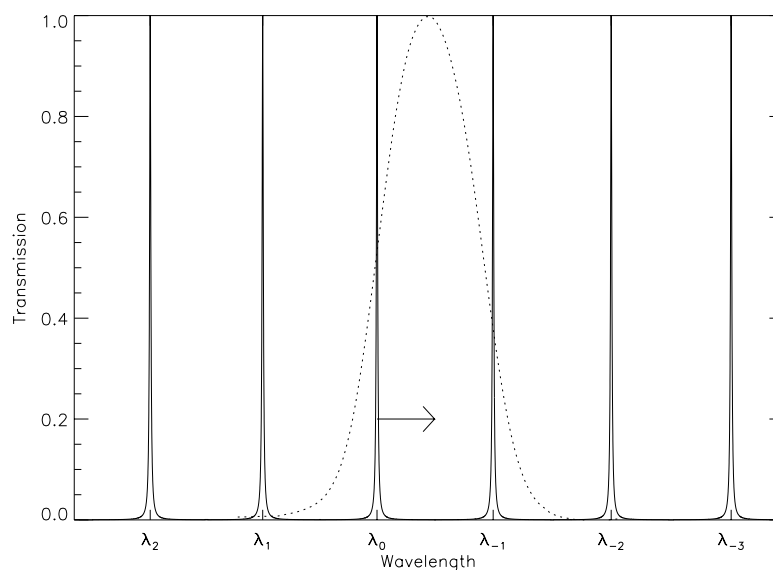


Figure 6.16: FP transmission for orders at wavelengths from  $\lambda_2$  to  $\lambda_{-3}$ . The order at  $\lambda_0$  moves across the grating spectral response profile (dotted line) creating one mini-scan. The photocurrent recorded at each point in this mini-scan also has a contribution from the adjacent order at  $\lambda_{-1}$ .

This is (automatically) carried out in a routine in FP\_PROC that modifies the shape of the profile that is removed from the data. This is done individually for each mini-scan based on the separation of FP orders during that scan. Figure 6.17 shows an example of the extra transmission due to adjacent FP

orders at each point on the grating profile. The corrected profile compensates for the transmission in the side orders.

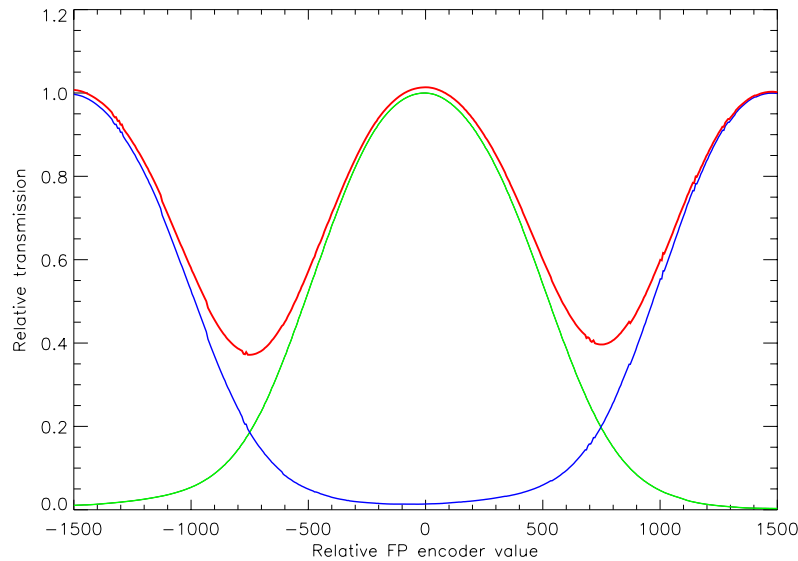


Figure 6.17: Grating profile shown in green with the contribution from the two FP orders either side shown in blue. The combined profile in red compensates for the flux from the side orders.

The correction works well for the general continuum level where the source spectrum was relatively flat over several FP orders. However, when an adjacent FP order occurred at the wavelength of a strong line, it can result in a false line detection. This is separated from the real line by the distance between FP orders. These are known as ‘ghost’ lines and are not corrected for.

## 6.16 Responsivity Drift in Long FP Observations

The responsivity of the LWS detectors increased with time during each ISO half revolution. After each half revolution a bias boost was performed to return the detector responsivity to the nominal level. In L03 observations where a large range in wavelength was covered the drift causes a gradient in the continuum across the observation.

A routine to correct for the responsivity drift during L03 observations has been added at the absolute responsivity correction stage in the LIA routine `FP_PROC`. This is based on the illuminator flashes performed before and after every observation. These recorded the response of the ten detectors to a standard illumination level and therefore traced the drift in responsivity. The illuminator flashes from all LWS observations have been combined to produce an average gradient in responsivity during each half revolution for use with the LWS parallel mode observations which did not have their own illuminator flashes (Section 4.5). This gradient is used to calculate a drift in responsivity for L03 observations by tying its absolute level to the observation’s own illuminators. This can produce much improved stitching of observations in a long L03 dataset and means that each observation reflects the true continuum slope more accurately. The responsivity drift correction is not applied to L04 observations as they were made up from many repeated scans over a small range in wavelength and therefore the responsivity drift of the detectors did not affect their overall shape.



## Chapter 7

# Guide to Instrument Related Data Products

### 7.1 Inventory and Naming Convention

When an observer receives data from the ISO Data Archive, the set of files will mainly consist of files prefixed by the letter 'L' followed by a three letter code giving the product type (see below). Other product files e.g. EOHI are general files which are not needed for most purposes. Each product file will also consist of an 8 figure number which is unique for each observation. The first three digits refer to the revolution number, the next three to the sequence within the revolution and the final two is a number defined by the observer.

e.g. file LSAN74201208.fits:

'L' indicates that it is an LWS file

'SAN' is the code for the Auto-Analysis product (see below)

742 is the revolution number

012 indicates that this is the 12th observation in the revolution

08 was the number assigned by the observer

The convention for the product code is

LC**	-	LWS Calibration file	(These are not observation-dependent)
LGER	-	LWS Grating ERD file	
LGIF	-	LWS Auto-Analysis group information file	
LIAC	-	LWS Auto-Analysis illuminator summary file	
LIER	-	LWS Illuminator ERD file	
LIPD	-	LWS Illuminator processed data	
LLER	-	LWS Long-wavelength Fabry-P\erot ERD file	
LPAA	-	LWS Parallel AAR file	
LPAD	-	LWS Parallel reduced AAR file	
LPSP	-	LWS Parallel SPD file	
LSAA	-	LWS Serendipity AAR file	
LSAN	-	LWS Auto-Analysis product file	(this file contains the calibrated spectra)
LSCA	-	LWS Auto-Analysis scan summary file	
LSER	-	LWS Short-wavelength Fabry-P\erot ERD file	
LSPD	-	LWS SPD file	
LSSP	-	LWS Serendipity SPD file	

LSTA - LWS Compact Status History file  
LWGH - LWS Glitch History file  
LWHK - LWS Housekeeping ERD file  
(LSNR) - LWS Auto-Analysis product file without responsivity corrections  
(this file is no longer produced since OLP Version 8)

The details about the LWS calibration files LC\*\* are given in Section 7.3. Depending on the observing mode that has been used, different sets of files have been produced.

- For Grating observations (AOTs L01 and L02):

Raw data:  
LGER  
LIER  
LSTA  
LWHK  
Standard processed data:  
LIPD  
LSPD  
LWGH  
Auto-Analysis results:  
LSAN  
LIAC  
LSCA  
LGIF

- For Fabry-Pérot observations (AOTs L03 and L04):

Raw data:  
LIER  
LLER or LSER (depending whether FPL or FPS was used)  
LSTA  
LWHK  
Standard processed data:  
LIPD  
LSPD  
LWGH  
Auto-Analysis results:  
LSAN  
LIAC  
LSCA  
LGIF

- For parallel and serendipity modes:

LPSP  
LSSP  
LPAA  
LSAA  
LPAD

## 7.2 Product Files – Description of Content and Use

This section gives for every product file a short description of the content and the use of the file. The most common starting point for data reduction is LSAN file (Section 7.2.7.1) which is the final output file from the automated processing of standard observations (L01, L02 and L04). If an observer wishes to re-process their data with interactive analysis then they will require the SPD level files LSPD (Section 7.2.5.1) and LIPD (Section 7.2.5.2), the Glitch History file LWGH (Section 7.2.5.3) is not needed as it is not used in Auto-Analysis stage.

Note: at present the L03 data is only scientifically validated to SPD level due to the problem relating to the placement of the grating resolution element (Section 6.13) therefore L03 observers must start their reduction with this data and it is recommended that they use LWS interactive analysis. It is unlikely that any observer will wish to use ERD level products (Section 7.2.4) however these are included in this chapter in order to give a complete set of information.

### 7.2.1 Timing information in the products: the ITK

The LWS Instrument Time Key (ITK) is the main source of timing information in the products for one AOT, and is therefore extremely important for the processing. The LWS ITK is unique over an orbit. It is given in units of  $2^{-14}$  of a second. The ITK for science record  $n$  can be calculated using:

$$ITK_n = ITK_{ref} + 2^{14}(UTK_f - UTK_{ref})/24 + T_d + nD(L_s)2^{14}/\omega \quad (7.1)$$

where:

- $ITK_n$  is the ITK for this science record (number  $n$ )
- $ITK_{ref}$  is the ITK for the start of the revolution, which can be found in the header of each product
- $UTK_f$  is the UTK for this format
- $UTK_{ref}$  is the UTK corresponding to  $ITK_{ref}$
- $T_d$  is the time delay after the start of a format (=248 ITK units)
- $D(L_s)$  is the number of ticks of the spacecraft clock (taken from housekeeping frame 17).
- $\omega$  is the spacecraft clock frequency (=2<sup>18</sup>)

### 7.2.2 General FITS header keywords for LWS data

Table 7.1 gives the general keywords that are used in the header of every data product. Some of these are general FITS keywords, others are specific for ISO data.

### 7.2.3 Transparent data

Transparent data are AOT specific data that are not processed by the satellite, but are passed directly from the uplink side of the ground station to the down link side ('transparent' in this case thus means bypassing the satellite). The Transparent Data (TDATA) contains information generated during the processing of the observer's input which may be required when processing the data for an observation, but is not required by the instrument to execute the observation on the satellite. The TDATA messages either relate to a complete observation (or AOT) or to the execution of a particular Instrument Command Sequence (ICS) and are written to the EOHA and EOHI files respectively. The main TDATA information

appears as the fields EOHAOTV and EOHIMSG1 in the EOHA and EOHI files. Their contents are shown in Tables 7.2 and 7.3.

As the TDATA is not sent to the satellite it is not synchronised accurately with the execution of ICSs by the instrument, or to the telemetry stream from the instrument. A counter has therefore been implemented in the LWS housekeeping which increments when each relevant ICS is executed allowing the data produced to be associated with the correct TDATA information by the ISO data processing software.

## 7.2.4 Edited Raw Data (ERD files)

### 7.2.4.1 LSTA: The LWS Compact Status History

**Type of File:** FITS binary table

**Contents:** For every period where the instrument is in the same status this file holds a record giving information on the begin and end time of that period and on the status of the instrument. The record structure can be found in Table 7.4.

LSTATYPE is Integer\*2 variable consisting of a high byte which identifies the sub-system and a low byte that subdivides different types within the sub-system. The sub-system values are:

```
'0100'X Illuminator sub-system
'0200'X Grating sub-system
'0300'X FPS sub-system
'0400'X FPL sub-system
'0000'X Other
```

Using this and the LSTASTAT field the status of the instrument at any given time can be determined (Table 7.5).

The sample list is used to tell the instrument which sub-systems have to be readout. Table 7.6 gives the possible sample lists for LWS.

In principle the only things that are of interest to the general user of LWS are the detector readouts, the positions of grating and FP, and the illuminator status. The temperatures are put here as well for use by the LWS instrument team.

Table 7.1: *The general keywords that are used in the headers of all product files.*

Name	type	contents
SIMPLE	L	general FITS keyword
BITPIX	I	general FITS keyword
NAXIS	I	general FITS keyword
EXTEND	L	general FITS keyword
ORIGIN	C	European Space Agency
TELESCOP	C	Infrared Space Observatory
INSTRUME	C	Instrument used
FILENAME	C	File name in ISO archive
DATE	C	Creation date 96/115
FILEVERS	C	Version ID in ISO archive
OLPVERS	C	SOC OLP system version
USERNAME	C	Unofficial data product
VERS1	C	Version ID of each input file
OBJECT	C	Target ID as given by proposer
OBSERVER	C	Proposer ID in ISO Mission DB
EQUINOX	R	Equinox
TMRATE	I	Telemetry rate in kbps (kbits/sec)
EOHAUTCS	C	Approx. UTC of start of observation
EOHAUTCE	C	Approx. UTC of end of observation
EOHAAOTN	C	AOT name
EOHAPLID	C	Proposal ID
EOHAOSN	C	Observation sequence number
EOHAPSN	C	Pointing sequence number
EOHAPCAT	C	Proposal category
EOHACIND	C	Calibration indicator
EOHATTYP	C	Target type
AOTVERS	C	AOT-to-OCT logic version
ATTUTCSL	C	UTC of start time of slew to intended target
ATTUTCS	C	UTC of time of first arrival at intended target
ATTOTFTH	R	On-target flag threshold (arc secs)
ATTRA	R	Intended Right Ascension of instrument viewing
ATTDEC	R	Intended DEClination (with ATTRA)
ATTTYPE	C	Type of attitude operation (P/R/T)
ATTGUIDE	R	Guide star reference number
ATTSAANG	R	Solar aspect angle (degrees)
ATTERROR	I	Contingency flag(0=success; 1=target not acq'd)
TREFUTC1	I	UTC (whole seconds since 01-01-1989)
TREFUTC2	I	UTC (remaining fraction of second)
TREFUTK	I	ISO Uniform Time Key (UTK)
TREFITK	I	ISO Instrument Time Key (ITK)
TREFITKU	R	ITK unit length in seconds
XTENSION	C	Binary table FITS extension
BITPIX	I	general FITS keyword
NAXIS	I	general FITS keyword
NAXIS1	I	general FITS keyword
NAXIS2	I	general FITS keyword
PCOUNT	I	general FITS keyword
GCOUNT	I	general FITS keyword
TFIELDS	I	general FITS keyword

Table 7.2: *The contents of the AOT variable TDATA message contained in the EOHA file. If no type is given, the variables are stored as ASCII characters.*

Offsets (bytes)	Length (bytes)	Type	Description
0-3	4	2 I*2	Raster Dimensions
4-8	5		Observation duration (seconds) not including slew
9-19	11		Date of AOT to OCT logic processing as YYDDHMMSS
20-29	10		unused
30	1		FPS used flag (0: no, 1: yes), blank for grating AOTs
31	1		FPL used flag (0: no, 1: yes), blank for grating AOTs
32-33	2		spare
34-35	2	I*2	Total number of spectra (number of lines for line scan AOTs, number of spectra to build up the range for wavelength range AOTs)
36-37	2	I*2	Detector used for the start wavelength (only AOT L01)
38-39	2	I*2	Detector used for the end wavelength (only AOT L01)
			OR
36-39	4	I*4	Start zone of the series of zones (only AOT L03)
40-43	4	I*4	End zone of the series of zones (only AOT L03)
44-47	4	I*4	First zone number corresponding to FPL (breakzone) (only AOT L03)
48-55	8	F8.4	Start wavelength of requested range (AOTs L01 and L03)
56-63	8	F8.4	End wavelength of requested range (AOTs L01 and L03)

Table 7.3: *Contents of the TDATA message 1 as contained in the EOHI file.*

Offsets (bytes)	Length (bytes)	Type	Description
0-3	4	I*4	Requested S/N for this line or range
4-15			unused
16-17	2	I*2	Spectrum number (line number or part of range)
18-23	6	I*6	Current scan number
24-27	4	I*4	Current zone number (only AOTs L03 and L04, see below)
28-35	8	F8.4	Wavelength (current line for line spectra or reference line that determined integration time for range spectra)
36-43	8	E8.3	Incident power (for line in line spectra or for reference line for range spectra)
44-47	4	I*4	Maximum scan half width (only for line spectra)
48-49	2	I*2	Active detector (line spectra: detector for current line; Range spectra: detector for reference line)
50-55	6	I*6	Total number of scans to be completed
56-59	4	I*4	Total number of measurements
60-63	4	I*4	Number of scans between illuminator flashes

Table 7.4: *LWS Compact Status record structure.*

Field	Number	Type	Description
CSGPUKST	1	I*4	UTK start time
CSGPUKEN	1	I*4	UTK end time
CSGPIKST	1	I*4	ITK start time
CSGPIKEN	1	I*4	ITK end time
CSGPUTST	2	I*4	UTC start time
CSGPUTEN	2	I*4	UTC end time
CSGPOSN	1	I*1	Observation Sequence Number
CSGPFILL	15	I*1	Spare
LSTASMP1	1	I*2	Sample list word 1
LSTASMP2	1	I*2	Sample list word 2
LSTASMP3	1	I*2	Sample list word 3
LSTASMP4	1	I*2	Sample list word 4
LSTASMP5	1	I*2	Sample list word 5
LSTASMP6	1	I*2	Sample list word 6
LSTASMP7	1	I*2	Sample list word 7
LSTALTYP	1	I*2	Sample list type
LSTASPA1	1	I*2	Spare
LSTAGRSN	1	I*2	Grating scan number
LSTAGRSD	1	I*2	Grating scan direction (0:forward; 1:reverse)
LSTASTAT	1	I*2	Instrument status
LSTAFPSN	1	I*2	FP scan number
LSTAFPSD	1	I*2	FP scan direction (0:forward; 1:reverse)
LSTAXTRA	1	I*4	Spare

Table 7.5: *Meaning of the LSTASTAT field*

LSTATYPE	LSTASTAT	Meaning
Grating	0	Grating sample list, grating not scanning
Grating	1	Grating sample list, grating scanning
FPS	0	FPS sample list, FP not scanning
FPS	1	FPS sample list, FP scanning
FPL	0	FPL sample list, FP not scanning
FPL	1	FPL sample list, FP scanning
Illuminator	0	Illuminator sample list, illuminators off
Illuminator	1	Illuminator sample list, illuminators on
Other	n/a	Other sample list

Table 7.6: *LWS sample list.*

Sample list	Sampled data
Grating	10 detectors, grating position (LVDT), grating coil current, grating structure temperature, grating electronics temperature, grating commanded position
FPS	10 detectors, grating LVDT position, 3 FPL error signals FPS commanded position, grating
FPL	10 detectors, grating LVDT position, 3 FPL error signals FPL commanded position,
Illuminator	10 detectors, illuminator current, grating structure temperature, detector temperature A or temperature B, FPL temperature, illuminator status

## 7.2.4.2 LIER: LWS illuminator ERD file

**Type of File:** FITS binary table

**Contents:** For every readout this contains the timing data for that readout, the raster point information plus the raw science data for the 15 sampled science channels of LWS.

The record structure can be found in Table 7.7.

Table 7.7: *LWS illuminator ERD file record structure.*

Field	Offset	Number	Type	Description
GPSCTKEY	0	1	I*4	Instrument Time Key
GPSCRPID	4	2	I*1	Raster point ID (also for single pointing)
GPSCFILL	6	1	I*2	Spare
LIERDSW1	8	1	I*2	SW1 detector readout
LIERDSW2	10	1	I*2	SW2 detector readout
LIERDSW3	12	1	I*2	SW3 detector readout
LIERDSW4	14	1	I*2	SW4 detector readout
LIERDSW5	16	1	I*2	SW5 detector readout
LIERDLW1	18	1	I*2	LW1 detector readout
LIERDLW2	20	1	I*2	LW2 detector readout
LIERDLW3	22	1	I*2	LW3 detector readout
LIERDLW4	24	1	I*2	LW4 detector readout
LIERDLW5	26	1	I*2	LW5 detector readout
LIERGST	28	1	I*2	Grating structure temperature
LIERDTA	30	1	I*2	Detector temperature A
LIERLTMP	32	1	I*2	FPL temperature
LIERICUR	34	1	I*2	Illuminator current
LIERICS	36	1	I*2	Illuminator commanded status
LIERFIL2	38	1	I*2	Spare

### 7.2.4.3 LGER: LWS grating ERD file

**Type of File:** FITS binary table

**Contents:** For every readout this contains the timing data for that readout, the raster point information plus the raw science data for the 15 sampled science channels of LWS.

The record structure can be found in Table 7.8.

Table 7.8: *LWS grating scan ERD file record structure.*

Field	Offset	Number	Type	Description
GPSCTKEY	0	1	I*4	Instrument Time Key
GPSCRPID	4	2	I*1	Raster point ID (also for single pointing)
GPSCFILL	6	1	I*2	Spare
LGERDSW1	8	1	I*2	SW1 detector readout
LGERDSW2	10	1	I*2	SW2 detector readout
LGERDSW3	12	1	I*2	SW3 detector readout
LGERDSW4	14	1	I*2	SW4 detector readout
LGERDSW5	16	1	I*2	SW5 detector readout
LGERDLW1	18	1	I*2	LW1 detector readout
LGERDLW2	20	1	I*2	LW2 detector readout
LGERDLW3	22	1	I*2	LW3 detector readout
LGERDLW4	24	1	I*2	LW4 detector readout
LGERDLW5	26	1	I*2	LW5 detector readout
LGERGLVP	28	1	I*2	Grating LVDT position
LGERGCUR	30	1	I*2	Grating current
LGERGST	32	1	I*2	Grating structure temperature
LGERGET	34	1	I*2	Grating electronics temperature
LGERGCP	36	1	I*2	Grating commanded position
LGERFIL2	38	1	I*2	Spare

## 7.2.4.4 LSER: LWS short-wavelength Fabry-Pérot ERD file

**Type of File:** FITS binary table

**Contents:** For every readout this contains the timing data for that readout, the raster point information plus the raw science data for the 15 sampled science channels of LWS. The record structure can be found in Table 7.9.

Table 7.9: *LWS FPS scan ERD file record structure.*

Field	Offset	Number	Type	Description
GPSCTKEY	0	1	I*4	Instrument Time Key
GPSCRPID	4	2	I*1	Raster point ID (also for single pointing)
GPSCFILL	6	1	I*2	Spare
LSERDSW1	8	1	I*2	SW1 detector readout
LSERDSW2	10	1	I*2	SW2 detector readout
LSERDSW3	12	1	I*2	SW3 detector readout
LSERDSW4	14	1	I*2	SW4 detector readout
LSERDSW5	16	1	I*2	SW5 detector readout
LSERDLW1	18	1	I*2	LW1 detector readout
LSERDLW2	20	1	I*2	LW2 detector readout
LSERDLW3	22	1	I*2	LW3 detector readout
LSERDLW4	24	1	I*2	LW4 detector readout
LSERDLW5	26	1	I*2	LW5 detector readout
LSERGLVP	28	1	I*2	Grating LVDT position
LSERSCP	30	1	I*2	FPS commanded position
LSERSEC1	32	1	I*2	FPS error signal 1
LSERSEC2	34	1	I*2	FPS error signal 2
LSERSEC3	36	1	I*2	FPS error signal 3
LSERFIL2	38	1	I*2	Spare

## 7.2.4.5 LLER: LWS long-wavelength Fabry-Pérot ERD file

**Type of File:** FITS binary table

**Contents:** For every readout this contains the timing data for that readout, the raster point information plus the raw science data for the 15 sampled science channels of LWS. The record structure can be found in Table 7.10.

Table 7.10: *LWS FPL ERD file record structure.*

Field	Offset	Number	Type	Description
GPSCTKEY	0	1	I*4	Instrument Time Key
GPSCRPID	4	2	I*1	Raster point ID (also for single pointing)
GPSCFILL	6	1	I*2	Spare
LLERDSW1	8	1	I*2	SW1 detector readout
LLERDSW2	10	1	I*2	SW2 detector readout
LLERDSW3	12	1	I*2	SW3 detector readout
LLERDSW4	14	1	I*2	SW4 detector readout
LLERDSW5	16	1	I*2	SW5 detector readout
LLERDLW1	18	1	I*2	LW1 detector readout
LLERDLW2	20	1	I*2	LW2 detector readout
LLERDLW3	22	1	I*2	LW3 detector readout
LLERDLW4	24	1	I*2	LW4 detector readout
LLERDLW5	26	1	I*2	LW5 detector readout
LLERGLVP	28	1	I*2	Grating LVDT position
LLERLCP	30	1	I*2	FPL commanded position
LLERLEC1	32	1	I*2	FPL error signal 1
LLERLEC2	34	1	I*2	FPL error signal 2
LLERLEC3	36	1	I*2	FPL error signal 3
LLERFIL2	38	1	I*2	Spare

#### 7.2.4.6 LWHK: LWS housekeeping ERD file

**Type of File:** FITS binary table

**Contents:** The LWHK file contains the contents of the housekeeping frames 1 and 17 from each telemetry format. These frames contain important information about the instrument status, which are used during the data processing. Each record in the LWHK file contains the data from a single telemetry format. The LWHK data are therefore only available once per format (every two seconds at the nominal telemetry rate). This compares with the contents of the LGER, LLER, LSER and LIER files, which are sampled at a much higher rate.

The record structure can be found in Table 7.11.

Table 7.11: *LWS housekeeping ERD file record structure.*

Field	Offset	Number	Type	Description
GEPRTKEY	0	1	I*4	Instrument Time Key
GEPRQUAL	4	2	I*1	Frame quality flag (see note)
LWHKFR01	8	128	I*2	Housekeeping Frame 1
LWHKFR17	264	128	I*2	Housekeeping Frame 17

The frame quality flag is set to 0 for perfect data, and is non-zero for imperfect quality data (i.e. frame 1 or 17 are bad). The housekeeping frames 1 and 17 contain the essential housekeeping of the instrument and are used in the processing. The most important parameters that can be found in these housekeeping frames are given in Tables 7.12, 7.13, 7.14 and 7.15.



Table 7.13: *Location of the most important amplifier parameters in the housekeeping frames.*

Parameter	Frame	bytes
Current sample number	17	172–173
Current number of resets from step	17	174–175
Number of resets after saturation	17	176–177
Commanded number of resets per step	17	170–171
Commanded number of samples per reset	17	168–169

Table 7.14: *Location of the most important grating parameters in the LWS housekeeping frames.*

Parameter	Frame	bytes
Grating commanded position	17	44–45
Grating LVDT position	17	62–63
Grating requested scan mode	17	64–65
Grating current scan number	17	56–57
Grating requested start position	17	46–47
Grating requested step size	17	50–51
Grating requested number of steps	17	48–49
Grating current step number	17	52–53

Table 7.15: *Fabry-Pérot parameters: Location of Fabry-Pérot parameters in the housekeeping frames.*

Parameter	Frame	bytes
FP requested scan mode	17	88–89
FP S or L commanded selection	17	72–73
FP requested start position	17	76–77
FP requested step size	17	80–81
FP requested number of steps	17	78–79
FP current scan number	17	86–87
FP current step	17	82–83
FP current commanded position	17	74–75
FPS power ON/OFF	17	90–91
FPS offset 2	17	92–93
FPS offset 3	17	94–95
FPS coil current 1	17	102–103
FPS coil current 2	17	104–105
FPS coil current 3	17	106–107
FPS error coil 1	17	96–97
FPS error coil 2	17	98–99
FPS error coil 3	17	100–101
FPL power ON/OFF	17	108–109
FPL offset 2	17	110–111
FPL offset 3	17	112–113
FPL coil current 1	17	120–121
FPL coil current 2	17	122–123
FPL coil current 3	17	124–125
FPL error coil 1	17	114–115
FPL error coil 2	17	116–117
FPL error coil 3	17	118–119

## 7.2.5 Standard Processed Data (SPD product files)

### 7.2.5.1 LSPD: LWS standard processed data

**Type of File:** FITS binary table

**Contents:** The LWS SPD contains the detector photocurrents for all ramps taken at all grating or Fabry-Pérot positions. The information contained in the SPD includes:

- timing information
- the mechanism position
- detector photocurrents for all ten detectors (uncalibrated against the internal illuminators, including their uncertainties
- detector photocurrents for all ten detectors without deglitching, and their uncertainties

For FP spectra only a subset of those (for certain detectors) will contain scientifically usable data. The SPD contains sufficient information which identifies the data specifically requested by the observer.

The photocurrents for one detector at all mechanism positions in one scan will constitute one LWS ‘mini-spectrum’.

The units for the LWS Derive-SPD data are:

- The photocurrents contained in an SPD record are in units of amps
- The mechanism positions contained in an SPD record are raw values
- The timing information is expressed as LWS ITK

Table 7.16 gives the record structure for the LWS SPD product file.

The header of the LWS SPD file contains the general FITS keywords described in Section 7.2.2. It also contains the additional, LWS specific, keywords listed in Table 7.17. Keywords with the prefix ‘LEI’ are copied from the EOHI TDATA information. Keywords with the prefix ‘LEOH’ are copied from the EOHA TDATA information (see Section 7.2.3 for more details about TDATA).

In addition to these keywords, the SPD header also contains various statistics on the data. These are intended more for diagnostics, so they should be treated with caution by observers. They are listed in Table 7.18. The letter ‘n’ at the end of the keyword is used to indicate that there is a set of keywords with one keyword per detector. The value of n ranges from 0 to 9, with 0 representing detector SW1, etc. See also the description of the processing performed by Derive-SPD in Section 4.3.

Table 7.16: *LWS SPD file record structure.*

Field	Offset	Number	Type	Unit	Description
GPSCTKEY	0	1	I*4	–	General prefix: ITK
GPSCRPID	4	2	I*1	–	General prefix: Raster Point ID
GPSCFILL	6	1	I*2	–	General prefix: Spare
LSPDTYPE	8	1	I*4	–	Record type
LSPDADET	12	1	I*4	–	Active detector flags. Bit 0 = SW1, bit 1 = SW2... (bit 0=LSB)
LSPDLINE	16	1	I*4	–	Line number
LSPDSCNT	20	1	I*4	–	Scan count
LSPDSDIR	24	1	I*4	–	Scan direction (0=forward; 1=reverse; –999=error)
LSPDGCP	28	1	I*4	–	Grating commanded position
LSPDGLVP	32	1	R*4	–	Grating LVDT position (average over mechanism position)
LSPDGLVU	36	1	R*4	–	Uncertainty in grating LVDT position
LSPDFPOS	40	1	I*4	–	FP position
LSPDPHC	44	10	R*4	A	Detector photocurrents
LSPDPHCU	84	10	R*4	A	rms of detector ramp fit
LSPDDPUD	124	10	R*4	A	Detector photocurrent without deglitching
LSPDDUUD	164	10	R*4	A	rms of undeglitched detector ramp fit
LSPDSTAT	204	10	I*1	–	Detector status bytes
LSPDMAUX	214	1	I*2	–	Auxiliary data for this mechanism position

Table 7.17: *LWS SPD file header keywords.*

Keyword	Type	Unit	Description
LBIAS <sub>xxx</sub>	I	none	Bias level for each detector
LCD1*	*	none	Various values from LCD1 calibration file
LCF*	*	none	Processing options selected. For pipeline these are fixed at standard values
LEIWAV <sub>nn</sub>	R	$\mu m$	For line AOTs give the expected wavelength for line nn. For wavelength range AOTs gives the wavelength of the reference line which determined the integration time for part nn of spectrum
LEOHFPS	L	none	Indicates if FPS was used. (FP observations only)
LEOHFPL	L	none	Indicates if FPL was used. (FP observations only)
LEOHSPCT	I	none	Number of spectra obtained
LEOHSDET	I	none	Detector used for start wavelength (L01 only)
LEOHEDET	I	none	Detector used for end wavelength (L01 only)
LEOHSZNE	I	none	Start zone (L03 only)
LEOHEZNE	I	none	End zone (L03 only)
LEOHBZNE	I	none	Break zone (L03 and L04 only)
LEOHSWAV	R	$\mu m$	Start wavelength of requested range. (L01 and L03 only)
LEOHEWAV	R	$\mu m$	End wavelength of requested range. (L01 and L03 only)
LPHOTOM	L	none	Flag indicating if observation was done in photometric mode (fixed grating)
LSVERS <sub>nn</sub>	C	none	LWS version information for each calibration file used by SPL

Table 7.18: *LSPD statistics keywords.*

Keyword	Type	Unit	Description
LSRNDAT	I	none	Total number of raw data points read from ERD per detector
LSRNRMP	I	none	Total number of ramps read from ERD per detector
LSRNITKJ	I	none	Number of jumps in ITK (indicated missing data caused by telemetry dropouts etc.).
LSRNSPKn	I	none	Number of anomalous points found. See description of first level deglitching.
LSRUNRn	I	none	Number of points rejected due to detector resets and mechanism movements.
LSRDNRn	I	none	Number of points rejected as having invalid raw values.
LSRDG1Rn	I	none	Number of points rejected due to glitches detected by first level deglitching.
LSRDG1Nn	I	none	Number of glitches found by first level deglitching.
LSRDG1An	I	none	Number of ramps affected by glitches found by first level deglitching. (Ramp could contain more than one glitch.)
LSRFIT1n	I	none	Number of ramps fitted with first order slope fit.
LSRFIT2n	I	none	Number of ramps fitted with second order slope fit.
LSRFEWRn	I	none	Number of points rejected because too few points remained in ramp for slope to be fitted.
LSRVLTRn	I	none	Number of saturated points.
LSRSATRn	I	none	Ramps containing 1 or more saturated points.
LSRNPNTn	I	none	Number of data points actually processed into SPD.
LSRMAXPn	R	A	Maximum photocurrent
LSRMINPn	R	A	Minimum photocurrent
LSRMAXGn	R	A	Maximum goodness of fit of slopes
LSRMINGn	R	A	Minimum goodness of fit of slopes
LSRMAXDn	R	1/V	Maximum calculated de-biasing parameter. Only calculated for second order slope fits. Set to zero if not calculated.
LSRMINDn	R	1/V	Minimum calculated de-biasing parameter. Only calculated for second order slope fits. Set to $1.0 \cdot 10^9$ if not calculated.
LSRPERn	R	none	Percentage of raw data points actually used to calculate SPD results.
LSRGRATn	R	s <sup>-1</sup>	Estimated glitch rate per detector.
LSRGRTOT	R	s <sup>-1</sup>	Estimated total glitch rate.

### 7.2.5.2 LIPD: LWS illuminator processed data file

**Type of File:** FITS binary table

**Contents:** The LIPD is similar to the LSPD file, but contains the results of processing the ramps of an illuminator flash rather than a grating or FP scan. This file contains the following information:

- Timing information
- The value of the illuminator commanded status word
- Detector photocurrents for all ten detectors, plus their uncertainties
- Other auxiliary information

The units are as follows:

- The timing information is expressed as LWS ITK
- The photocurrents are in units of amps

The LIPD has two principal purposes. Firstly it is used by Auto-Analysis to perform the absolute responsivity correction. This is done by comparing the photocurrents in the LIPD file against reference photocurrents in the LCIR calibration file. Secondly the ramps at the start of ‘closed’ illuminator flashes provide a measure of the background and straylight at that time.

The header of the LIPD file contains the same keywords as the header of the LSPD file. The LIPD file contains the same detector status word as the LSPD file (see Section 7.2.6).

### 7.2.5.3 LWGH: LWS Glitch History file

**Type of File:** FITS binary table

**Contents:** The LWGH file contains a record of all glitches detected by SPL during an observation (including the illuminator flashes). Each record of the LWGH file contains the information for a single glitch. The information stored includes the time of the glitch, the detector number and the height of the glitch. The full layout of the LWGH file is given in Table 7.19.

The FITS header for the file must contain, in addition to the mandatory keywords, at least the additional keywords given in Table 7.20.

The keywords TREFUTC1, TREFUTC2, TREITK, and TREFUTK are copied from the header of the ERD file being processed.

The keyword LWGHMORE gives the number of glitches which occurred after the maximum size of the LWGH file was reached. In practice this should always be zero as the maximum size has been set to a sufficiently large value to cope with all observations.

Table 7.19: *LWGH file record structure.*

Name	offset	num	type	Description
LWGHITK	0	1	I*4	ITK time of start of glitch
LWGHRITK	4	1	I*4	ITK time of start of glitched ramp
LWGHDET	8	1	I*2	Detector number (0–9)
LWGHRAT	10	1	I*2	Estimated glitch height to ramp height ratio expressed in multiples of 0.01
LWGHHI	12	1	R*4	Estimated height of glitch, in volts

Table 7.20: *LWS Glitch History file keywords.*

Name	Type	Description
TREFUTC1	I	The Universal time, in seconds, of an arbitrary format during the observation. The field LWGHTIME specifies the time of the glitch relative to this point
TREFUTC2	I	Remaining fractions of a second of time specified by TREFUTC1
TREFITK	I	ITK time corresponding to TREFUTC1
TREFUTK	I	UTK time corresponding to TREFUTC1
LWGHMORE	I	Number of additional glitches found after maximum number of glitch records allowed in file had been exceeded. Should always be zero.
LSVERS <sub>n</sub>	C	LWS version information for each calibration file used (n=1,2,3,...)
LCD1*	*	Various keywords which detail how first level deglitching functioned. These are copied from the LCD1 calibration file used (see Table 7.38)

**7.2.5.4 LPSP: LWS parallel Standard Process Data****Type of File:** FITS binary table**Contents:** The LPSP file contains the Standard Process Data for parallel mode observations.Table 7.21: *LPSP file record structure.*

Field	Dimension	Format	Description
GPSCTKEY	1	I*4	Instrument Time Key
GPSCRPID	2	I*1	Raster point ID
GPSCFILL	1	I*2	Spare
UTK	1	I*4	UTK time
LWINTKEY	1	I*4	LWS window time key (seconds since beginning of lws parallel observation window in current revolution) TUNIT=sec
FLUX	10	R*4	Detector photocurrent TUNIT=amps
PROCFLGS	10	I*2	Processing flags
OTF	1	I*2	On Target Flag (Star Tracker flag)
STABLE	1	I*2	Stability flag (computed)
RA	1	R*8	RA coordinates TUNIT=degree
DEC	1	R*8	DEC coordinate TUNIT=degree
ROLL	1	R*8	Roll angle TUNIT=degree

**7.2.5.5 LSSP: LWS serendipity Standard Process Data****Type of File:** FITS binary table**Contents:** The LSSP file contains the Standard Process data for serendipity mode observations.Table 7.22: *LSSP file record structure.*

Field	Dimension	Format	Description
GPSCTKEY	1	I*4	Instrument Time Key
GPSCRPID	2	I*1	Raster point ID
GPSCFILL	1	I*2	Spare
UTK	1	I*4	UTK time
LWINTKEY	1	I*4	LWS window time key (seconds since beginning of lws parallel observation window in current revolution) TUNIT=sec
FLUX	10	R*4	Detector photocurrent TUNIT=amps
PROCFLGS	10	I*2	Status word (Processing flags)
OTF	1	I*2	On Target Flag (Star Tracker flag)
STABLE	1	I*2	Stability flag (computed)
RA	1	R*8	RA coordinates TUNIT=degree
DEC	1	R*8	DEC coordinate TUNIT=degree
ROLL	1	R*8	Roll angle TUNIT=degree

## 7.2.6 LSPD and LIPD status words

### 7.2.6.1 Detector status word

Each LSPD and LIPD record contains a status word for each of the ten detectors for the current ramp. This has been implemented as the field LSPDSTAT or LIPDSTAT, which are arrays of ten words, with one word for each detector.

The detector status word contains the fields (Bit position 0 is the least significant bit) given in Table 7.23.

Table 7.23: *The contents of the detector status word.*

Bit	Description
0	Glitch flag
1	Saturation warning flag
2	Invalid data flag (new in OLP Version 8)
3	Discarded following glitch flag (new in OLP Version 8)
5-7	Percentage of available data used

These fields are described in more detail below.

- Glitch flag: this flag is set if one or more glitches occurred.
- Saturation warning flag: this flag is set if the ramp contains one or more saturated points. Saturated points are still processed. See Section 4.3.4 for details.
- Invalid data flag: indicates that the point is invalid and should not be used.
- Discarded following glitch flag: indicates that the point has been declared invalid because it is deemed to be affected by a glitch occurring in a previous ramp. Whenever this flag is set the ‘invalid data’ flag will also be set.
- The percentage of available data used refers to the number of detector readouts from this detector for this ramp which were used to calculate the photocurrent value. This is expressed as a percentage of the available data points.

The number of ‘available’ data points is defined as the number of sampled detector readouts for this ramp, minus the number of points discarded because of detector resets and mechanism movements.

The following table gives the meaning of each of the possible values of this bit field:

Bit value	Meaning
0	$data = 0\%$
1	$0\% < data \leq 10\%$
2	$10\% < data \leq 20\%$
3	$20\% < data \leq 40\%$
4	$40\% < data \leq 60\%$
5	$60\% < data \leq 80\%$
6	$80\% < data < 100\%$
7	$data = 100\%$

### 7.2.6.2 Mechanism status word

Each record of the LSPD file contains a single integer\*2 field called LSPDMAUX. This word contains various status information associated with the current mechanism position.

The meaning of each of the bits in this word are given in Table 7.24

Table 7.24: *The contents of the mechanism status word.*

Bit	Description
0–3	NRESETS
4–13	NSAMPLES
14	Grating LVDT error
15	Spare

These fields are described in more detail below.

- NRESETS is the commanded number of ramps per mechanism position. It is copied from the LWS housekeeping data file (LWHK).
- NSAMPLES is the commanded number of samples per ramp. It is copied from the LWS housekeeping data file (LWHK).
- Grating LVDT error is defined as the grating LVDT position differing by more than a given amount from the grating commanded position for the current ramp. The value of this threshold is specified in the configuration file. This value is also written into the header of the LSPD file as the keyword LCFGRWAR.

## 7.2.7 Auto-Analysis results (AAR product files)

### 7.2.7.1 LSAN: LWS Auto-Analysis results

**Type of File:** FITS binary table

**Contents:**

This product contains the set of individual spectra for each detector including the range required by the observer. Each spectrum consists of calibrated flux and wavelength, together with their uncertainties, and has been derived from data gathered from a single detector during a single scan whilst observing a single point on the sky (could be one point of a raster) in a single AOT.

The user is reminded that within the LWS off-line Processing chain there will be:

- no averaging of data points at the same grating or FP position
- no joining together of spectra from adjacent detectors
- no generation of maps for raster scans
- no subtraction of the local astronomical background

For some information on these additional processing steps that could be made we refer to Chapter 8.

The units for the data in this product are:

- The fluxes are in  $\text{W cm}^{-2} \mu\text{m}^{-1}$  for grating and Fabry-Pérot scans. The uncertainties in these values cannot be calculated by the pipeline. However, the LSAN file does contain the fractional systematic error due to the calibration, which forms part of the overall uncertainty.

Table 7.25: *LWS Auto-Analysis product file record structure.*

Field	Offset	Number	Type	Unit	Description
LSANUTK	0	1	I*4	–	UTK time
LSANRPID	4	2	I*1	–	Raster Point ID
LSANFILL	6	1	I*2	–	Filler
LSANLINE	8	1	I*4	–	Line number
LSANDET	12	1	I*4	–	Detector ID
LSANSDIR	16	1	I*4	–	Scan direction
LSANSCNT	20	1	I*4	–	Scan count
LSANWAV	24	1	R*4	$\mu m$	Wavelength
LSANWAVU	28	1	R*4	$\mu m$	Uncertainty in wavelength
LSANFLX	32	1	R*4	$W cm^{-2} \mu m^{-1}$	Flux on detector
LSANFLXU	36	1	R*4	none	Flux uncertainty
LSANSTAT	40	1	I*4	–	Status word
LSANITK	44	1	I*4	–	ITK time

- The wavelengths and their uncertainties are in microns
- Timing information is given as both UTK and ITK.

Each record of the LSAN contains:

- General Auto-Analysis record prefix (including UTK)
- Detector ID
- Wavelength and uncertainty
- The flux falling on the detector.

The record structure is given in Table 7.25. The header of the LSAN file contains information about the calibration that was used to derive the product, in particular the flux calibration and the velocity correction. Table 7.26 gives the keywords that contain this information.

Table 7.26: *LWS Auto-Analysis file keywords.*

Name	Type	Description
LSVERS <sub>n</sub>	C	LWS version number for each SPL calibration file (n=1,2,3.....)
LVERS <sub>n</sub>	C	LWS version number for each AAL calibration file (n=1,2,3.....)
LPHOTOM	L	Flag indicating if observation is done in photometric mode (fixed grating).
LCGBdet	R	Grating spectral bandwidth correction factor for detector det (det=SW1...LW5) from LCGB file
LCGBUdet	R	Uncertainty in grating spectral bandwidth correction factor for detector det (det=SW1...LW5) from LCGB file
LCFWFLC <sub>n</sub>	R	4 double precision numbers (n=0,1,2,3) giving FPL wavelength conversion coefficients (FP observations only)
LCFWFSC <sub>n</sub>	R	4 double precision numbers (n=0,1,2,3) giving FPS wavelength conversion coefficients (FP observations only)
LCGWCON	R	(n=0,1,2,3,4) Coefficients used during conversion of grating LVDT to wavelength
LCGWLINE	R	Number of lines per $\mu\text{m}$ on grating. Used during conversion of grating LVDT to wavelength
LCGWA <sub>det</sub>	R	(Det='SW1'...'LW5') Angle for each detector used during conversion of grating LVDT to wavelength
LSTRNOM <sub>n</sub>	R	(n=0–9) Start of wavelength range for which GR RSRF is valid for each detector
LENDNOM <sub>n</sub>	R	(n=0–9) End of wavelength range for which GR RSRF is valid for each detector
LOWRTALL	L	Flag indicating whether LSAN file contains all data Should always be 'T'
LODRKOPT	L	Dark current option: 0=off; 1=use measured value; 2=use standard (fixed) value; 3=autoselect
LOSKP <sub>THP</sub>	L	True if FP throughput correction was omitted
LOSKP <sub>VEL</sub>	L	Indicates if FP velocity correction stage was omitted Should always be 'F'
LOABSOPT	I	Abs. responsivity option, 0=off; 1=on; 2=select Should always be 2
LORELOPT	I	Rel. responsivity option, 0=off; 1=on; 2=select Should always be 2
LVCOEF <sub>n</sub>	R	Coefficients of 2nd order fit for the velocity correction (n=0,1,2).
LOABSDN	L	Indicates if absolute responsivity correction was done
LORELDN	L	Indicates if relative responsivity correction was done
LEOH*	*	Copy of EOHA information from LSPD header (see Table 7.17)
LEI*	*	Copy of EOHI information from LSPD header (see Table 7.17)

### 7.2.7.2 LSNR: LWS Auto-Analysis results without responsivity correction

**Type of File:** FITS binary table

**Contents:** The LSNR file contains the same results as the LSN file, but without the absolute responsivity and responsivity drift corrections applied. The layout is identical to the LSN file, except that the field names have the prefix ‘LSNR’ rather than ‘LSAN’. The keywords in the header of the LSNR file are identical to those in the LSN file. See description of LSN file for more details. The LSNR file contains the same status words as the LSN file (see Section 7.2.8).

**Note:** This file is no longer produced from OLP Version 8 onwards

### 7.2.7.3 LIAC: LWS illuminator summary file

**Type of File:** FITS binary table

**Contents:** This file contains the final results of processing the illuminator flashes. One record is written to this file for each illuminator flash in the observation. Note that only the information from ‘closed’ illuminator flashes are actually used in the processing. However, the LIAC file will contain the results for all illuminator flashes, regardless of whether they are open or closed. Each record of the LIAC file contains the following fields:

- Timing information in both ITK and UTK units
- The wheel position during the flash. Wheel positions are: 0=FPS; 1=Grating; 2=FPL; 3=blank (not used). A value of 0, 2 or 3 indicates that the flash is ‘closed’
- The photocurrent backgrounds measured at the start of the flash for each detector, in amps
- The ratio between the flash data and the calibration reference data in the LCIR file for each detector
- Other auxiliary information

Table 7.27: *LIAC product file record structure.*

Field	Number	Format	Description
LIACIKS	1	I4	ITK of start of flash
LIACIKE	1	I4	ITK of end of flash
LIACUKS	1	I4	UTK of start of flash
LIACUKE	1	I4	UTK of end of flash
LIATYPE	1	I4	Illuminator flash type identifier (0,1,...)
LIACWHAP	1	I4	Wheel absolute position 0=FPS; 1=GR; 2=FPL
LIACRES	10	R4	Absolute responsivity correction factors
LIACRESU	10	R4	Uncertainty in absolute responsivity correction
LIACBK	10	R4	Background photocurrent for each detector
LIACBKU	10	R4	Uncertainty in background photocurrent
LIACNR	10	I4	No. of points used in calculation of correction
LIACNB	10	I4	No. of points used in calculation of background

**7.2.7.4 LSCA: LWS scan summary file****Type of File:** FITS binary table**Contents:** This file contains summary information for each scan processed by Auto-Analysis. The main purpose of this file is to enable the correction for the drift in responsivity to be performed. Each record of the LSCA file contains:

- The average photocurrent for each detector for a single scan
- The ITK times of the beginning, middle and end of the scan
- The dark current/straylight value subtracted from the scan in AAL.
- Other information which is constant over the scan

Table 7.28: *LSCA product file record structure.*

Field	Number	Format	Description
LSCARPID	2	I1	Raster point ID
LSCAADET	3	I1	Active detector as string
LSCAFILL	3	I1	Filler (Record must be multiple of 4 bytes)
LSCAITKS	1	I4	ITK of start of scan
LSCAITKE	1	I4	ITK time of end of scan
LSCAITKR	1	I4	ITK time of reference point in scan
LSCAFLX	10	R4	Average detector flux for scan for each detector
LSCANRMT	1	I4	Total number of ramps in scan
LSCANRMF	10	I4	Number of ramps used in calculation of average
LSCALINE	1	I4	Line number (L02 and L04 only)
LSCAGPOS	1	I4	Grating measured position at start of scan (L03)
LSCASCNT	1	I4	Scan count (0,1...)
LSCASDIR	1	I4	Scan direction (0=forward; 1=reverse; -999=error)
LSCAORD	10	R4	Order numbers (L03, L04)
LSCABK	10	R4	Background/straylight subtracted from scan
LSCABKU	10	R4	Uncertainties in background/straylight

### 7.2.7.5 LGIF: LWS Group Information File

**Type of File:** FITS binary table

**Contents:** The LGIF file provides information about the absolute responsivity correction and responsivity drift correction applied to the final LSA data. It contains one record for each ‘group’ of data in the LSA file. A group is a time interval during which a single absolute responsivity correction factor and drift correction factor is applied for each detector. Each record of the LGIF file contains:

- The start and end times of this group, in ITK units
- The reference time of the group in ITK units. This is the point at which the absolute responsivity correction factors are calculated and at which the responsivity drift is normalised
- The absolute responsivity correction factor and its associated uncertainty for each detector
- A set of flags indicating if responsivity drift information has been calculated for each detector
- The coefficients of the drift slope applied to correct for the responsivity drift for each detector. The coefficients give the LSPD value at the ITK reference time for the group and the gradient of the slope in LSPD units per ITK unit
- Other information which is constant for the group

Table 7.29: *LGIF product file record structure.*

Field	Number	Format	Description
LGIFITKS	1	I4	ITK of start of group
LGIFITKE	1	I4	ITK of end of group
LGIFITKR	1	I4	Reference ITK at which correction is calculated
LGIFABS	10	R4	Absolute responsivity correction factor
LGIFABSU	10	R4	Uncertainties in absolute responsivity correction
LGIFRSTA	10	I4	Relative responsivity status flag
LGIFREL1	10	R4	1st coefficient of relative responsivity correction
LGIFREL2	10	R4	2nd coefficient of relative responsivity correction
LGIFNSCD	1	I4	Number of scans used for calculation of drift correction
LGIFNSCG	1	I4	Total number of scans in group
LGIFLINE	1	I4	Line number for group (for L02 and L04)
LGIFGPOS	1	I4	Grating measured position for group (L03)
LGIFADDET	3	I1	Active detector, as string (only valid for L02 and L04)
LGIFFILL	3	I1	Filler (Record must be multiple of 4 bytes)
LGIFRPID	2	I1	Raster point ID for group

**7.2.7.6 LPAA: LWS parallel Auto-Analysed data****Type of File:** FITS binary table**Contents:** The LPAA file contains the Auto-Analysis data for parallel mode observations.Table 7.30: *LPAA product file record structure.*

Field	Dimension	Format	Description
GPSCTKEY	1	I*4	Instrument Time Key
GPSCRPID	2	I*1	Raster point ID
GPSCFILL	1	I*2	Spare
UTK	1	I*4	UTK time
LWINTKEY	1	I*4	LWS window time key (seconds since beginning of LWS parallel observation window in current revolution) TUNIT=second
FLUX	10	R*4	Detector Data TUNIT= $\text{W cm}^{-2} \mu\text{m}^{-1}$
PROCFLGS	10	I*2	Processing flags
OTF	1	I*2	On Target Flag (Star Tracker flag)
STABLE	1	I*2	Stability flag (computed)
RA	1	R*8	RA coordinates TUNIT=degree
DEC	1	R*8	DEC coordinate TUNIT=degree
ROLL	1	R*8	Roll angle TUNIT=degree

**7.2.7.7 LSAA: LWS serendipity Auto-Analysed data****Type of File:** FITS binary table**Contents:** The LSAA file contains the Auto-Analysis data for serendipity mode observations.Table 7.31: *LSAA product file record structure.*

Field	Dimension	Format	Description
GPSCTKEY	1	I*4	Instrument Time Key
GPSCRPID	2	I*1	Raster point ID
GPSCFILL	1	I*2	Spare
UTK	1	I*4	UTK time
LWINTKEY	1	I*4	LWS window time key (seconds since beginning of LWS parallel observation window in current revolution)
FLUX	10	R*4	Detector Flux TUNIT= (MJy/sr)
PROCFLGS	10	I*2	Processing flags
OTF	1	I*2	On Target Flag (Star Tracker flag)
STABLE	1	I*2	Stability flag (computed)
RA	1	R*8	RA coordinate TUNIT=degree
DEC	1	R*8	DEC coordinate TUNIT=degree
ROLL	1	R*8	Roll angle TUNIT=degree
SPEED	1	R*8	Speed TUNIT=degree/s.

## 7.2.7.8 LPAD: LWS parallel averaged data

**Type of File:** FITS binary table

**Contents:**

Table 7.32: *LPAD product file record structure.*

Field	Dimension	Format	Description
GPSTKEY	1	I*4	Instrument Time Key
GPSCRPID	2	I*1	Raster point ID
GPSCFILL	1	I*2	Spare
UTK	1	I*4	UTK time
LWINTKEY	1	I*4	LWS window time key (seconds since beginning of LWS parallel observation window in current revolution) TUNIT=second
FLUX	10	R*4	Averaged data ( $W\text{ cm}^{-2}\mu\text{m}^{-1}$ )
STDEV	10	R*4	Standard deviation on Flux
WEIGHT	10	I*4	Number of samples effectively used
PROCFLGS	10	I*2	Processing flags
OTF	1	I*2	On Target Flag (Star Tracker flag)
STABLE	1	I*2	Stability flag (computed)
RA	1	R*8	Average RA coordinate TUNIT=degree
RAERR	1	R*8	Error on RA coordinate
DEC	1	R*8	Average DEC coordinate TUNIT=degree
DECERR	1	R*8	Error on DEC coordinate TUNIT=degree
ROLL	1	R*8	Average Roll angle TUNIT=degree
ROLLERR	1	R*8	Error on Roll angle TUNIT=degree

### 7.2.8 LSAN status words

The LSAN file contains one record **per detector** for each ramp. The status words in the LSNR files are identical in layout and content to the status words in the LSAN file.

Each record of the LSAN file contains one 32 bit status word per record. Eight bits of this status word are simply a copy of the status word for the appropriate detector from the LSPD file.

The layout of the LSAN status word for each detector is as given in Table 7.33.

Table 7.33: *Contents of the Auto-Analysis status word.*

Bit	Meaning
0–7	Copy of detector status word from LSPD file
8	Invalid data flag
9	Spectral responsivity error flag
10	Active detector flag
11	Grating spectral responsivity warning flag
12–14	Spare
15	FP flag. Set to 1 if FPL is in use; 0 otherwise
16–23	Spare
24	Invalid photocurrent flag

The invalid data flag indicates that the flux value is not valid. This flag will be set if the SPD contained no data for this point, or an error occurred during the spectral responsivity correction stage (see below), or if the invalid photocurrent flag is set (see below). If the ‘percentage data’ field in the SPD status word is set to 0 then there was no SPD data for this point. This is usually due to data being discarded due to glitches.

The spectral responsivity error flag indicates that either no responsivity value could be found in the calibration files for this point, or that the responsivity value found was set to zero.

The active detector flag indicates for L02 and L04 AOTs if this detector is the ‘active’ detector. For these AOTs only one detector can be active at any one time. For L01, L03 and photometric L02 AOTs this flag is not applicable and will not be set for any detector.

The grating spectral responsivity warning flag indicates data points which are poorly calibrated. **Any points with this flag set should only be used for wavelength identification of features.** See Section 4.4.4 for more details.

The invalid photocurrent flag indicates that the value of the detector photocurrent from the SPD data was outside the acceptable range for this observation. This flag is set when the photocurrent value is a negative value which is less than  $-1$  times the absolute value of the dark current/straylight. Invalid photocurrent values may be caused by glitches which have not been detected.

## 7.3 Calibration Files

This section gives a description of all the calibration files used during the automated pipeline processing of LWS data. The contents of these files are fixed for each version of the processing and can only be updated when a new OLP version is issued.

The SPD level files are mainly concerned with how LWS output is turned from engineering units to photocurrent at each grating position and much of this information has remained unchanged since before launch although parameters such as discard times have been updated in-orbit. The files LCD2, LCFP and LCD3 are no longer used.

The Auto-Analysis level files are concerned with the astronomical calibration of LWS and have evolved with various versions of the LWS pipeline processing as the understanding of instrument calibration has improved. In particular the photometric and spectral response calibration of LWS has changed with each version. The LCTP and LCDK files have only been in existence since OLP Version 8.

### 7.3.1 SPD calibration files

The contents and usage of the SPD calibration files have changed as the pipeline has developed. Some of the calibration files still read by SPL are no longer used during the processing. Other files contain information which is no longer used. In the following sections only the information which is actually used is identified.

Each SPD calibration file contains a version number and date for identification purposes. The version numbers are contained in the keywords named XXXXVER, where XXXX is the four letter name of the calibration file. The date is contained in the keyword LDATE. The date and version numbers of the calibration files used by Derive-SPD are written into the header of the SPD and AAR files as a series of keywords named LSVERSn (n=1,2,...).

#### 7.3.1.1 LCDT: Discard times file

**Type of File:** FITS Header

**Contents:**

- The amount of time to be discarded following each detector reset, in ms. The LCDT file from OLP Version 7 onwards effectively contains only a single discard time which applies to all ramps of all detectors. However, due to requirements for previous versions of the pipeline, this is implemented as two separate discard times for each of the ten detectors. One discard time is for ‘short’ (high signal) ramps, the other discard time for ‘long’ (low signal) ramps. Since the introduction of the  $\Delta V/\Delta t$  method of slope fitting in OLP Version 7, all discard times are set to the same value.
- Two keywords specifying the time period that must be discarded after a movement of the grating or Fabry-Pérot. These times are not in use as the amount of time discarded after each detector reset has been found to be sufficient to cover mechanism settling times as well.

Table 7.34: *LCDT calibration file keywords.*

name	type	unit	description
LCDTNSAM	I	none	Threshold for switching from standard set of detector reset discard times to alternate set.
LCDTTRTn	R	ms	Standard discard time for detector n (n=0...9) following detector reset. Only used if number of samples in ramp is less than or equal to LCDTNSAM.
LCDTTRAN	R	ms	Alternate discard time for detector n (n=0...9) following detector reset. Only used if number of samples in ramp is greater than to LCDTNSAM.

**Use:** To determine how much of every integration ramp has to be discarded. Used in Derive-SPD processing step ‘Construct ramps and discard unusable readouts’, see Section 4.3.2.

### 7.3.1.2 LCAL: Readout limits for the analogue electronics

**Type of File:** FITS header

**Contents:**

- Ten values specifying for each detector the minimum readout value below which the analogue amplification chain does not respond. All readouts which are below this value are discarded. See Table 7.35 for the keywords.
- The following ten keywords specify for each detector the maximum readout value above which the analogue amplification chain saturates. All readouts above this value are discarded. See Table 7.35 for the keywords.

Table 7.35: *LCAL calibration file keywords.*

name	type	unit	description
LCALDMI0	I	–	Detector SW1 minimum readout
LCALDMI1	I	–	Detector SW2 minimum readout
LCALDMI2	I	–	Detector SW3 minimum readout
LCALDMI3	I	–	Detector SW4 minimum readout
LCALDMI4	I	–	Detector SW5 minimum readout
LCALDMI5	I	–	Detector LW1 minimum readout
LCALDMI6	I	–	Detector LW2 minimum readout
LCALDMI7	I	–	Detector LW3 minimum readout
LCALDMI8	I	–	Detector LW4 minimum readout
LCALDMI9	I	–	Detector LW5 minimum readout
LCALDMX0	I	–	Detector SW1 maximum readout
LCALDMX1	I	–	Detector SW2 maximum readout
LCALDMX2	I	–	Detector SW3 maximum readout
LCALDMX3	I	–	Detector SW4 maximum readout
LCALDMX4	I	–	Detector SW5 maximum readout
LCALDMX5	I	–	Detector LW1 maximum readout
LCALDMX6	I	–	Detector LW2 maximum readout
LCALDMX7	I	–	Detector LW3 maximum readout
LCALDMX8	I	–	Detector LW4 maximum readout
LCALDMX9	I	–	Detector LW5 maximum readout

**Use:** To determine which readouts are outside the limits of the electronics. Note that this is not the same as the ‘saturation’ limits. These limits are specified in the LCDB file.

### 7.3.1.3 LCVC: Detector voltage conversion file

**Type of File:** FITS header

**Contents:** Two keywords are used in the conversion of raw detector readouts into voltages. The conversion is done using the formula:

$$V = (\text{raw detector value} - \text{LCVCVOFF}) * \text{LCVCVFAC}$$

where the keywords are:

LCVCVFAC= Conversion factor, Volts per raw value  
LCVCVOFF= Offset to be subtracted from raw value

The conversion factor and the offset value are REAL values.

**Use:** To convert the readouts into voltages.

### 7.3.1.4 LCGA: Analogue amplification gains

**Type of File:** FITS header

**Contents:** Eighty keywords (all REAL values) specify the analogue amplification gain for each gain setting of each detector. Each keyword has the format: LCGADG<sub>detector</sub><sub>gain</sub>, where <sub>detector</sub> specifies the detector as a number between 0 and 9, and <sub>gain</sub> specifies the gain setting as a number between 0 and 7.

**Use:** In Derive-SPD for the conversion of readouts to voltages.

### 7.3.1.5 LCJF: JF4 amplifier parameters

**Type of File:** FITS Header

**Contents:** Ten keywords specifying the fixed gain of the JF4 amplifier for each detector. Followed by ten keywords specifying the capacitances associated with each of the JF4 amplifiers. See Table 7.36 for the keyword names.

Table 7.36: *LCJF calibration file keywords.*

name	type	unit	description
LCJFJG0	R	–	Detector SW1 JF4 gain
LCJFJG1	R	–	Detector SW2 JF4 gain
LCJFJG2	R	–	Detector SW3 JF4 gain
LCJFJG3	R	–	Detector SW4 JF4 gain
LCJFJG4	R	–	Detector SW5 JF4 gain
LCJFJG5	R	–	Detector LW1 JF4 gain
LCJFJG6	R	–	Detector LW2 JF4 gain
LCJFJG7	R	–	Detector LW3 JF4 gain
LCJFJG8	R	–	Detector LW4 JF4 gain
LCJFJG9	R	–	Detector LW5 JF4 gain
LCJFJC0	R	farad	Detector SW1 JF4 capacitance
LCJFJC1	R	farad	Detector SW2 JF4 capacitance
LCJFJC2	R	farad	Detector SW3 JF4 capacitance
LCJFJC3	R	farad	Detector SW4 JF4 capacitance
LCJFJC4	R	farad	Detector SW5 JF4 capacitance
LCJFJC5	R	farad	Detector LW1 JF4 capacitance
LCJFJC6	R	farad	Detector LW2 JF4 capacitance
LCJFJC7	R	farad	Detector LW3 JF4 capacitance
LCJFJC8	R	farad	Detector LW4 JF4 capacitance
LCJFJC9	R	farad	Detector LW5 JF4 capacitance

**Use:** In Derive-SPD for the conversion of readouts to voltages.

### 7.3.1.6 LCDB: Saturation voltage thresholds for slope fitting

**Type of File:** FITS Header

**Contents:**

This file contains the maximum allowable voltage before a point is regarded as being saturated. See Section 4.3.4 for a description of how saturated points are handled.

This file also contains values for the ‘de-biasing’ parameters and the thresholds for switching between first and second order slope fitting. These values have not been used since the introduction of the  $\Delta V/\Delta t$  method of slope fitting in OLP Version 7.

Table 7.37: *LCDB calibration file keywords.*

name	type	unit	description
LCDBVM0	R	Volts	Detector SW1 maximum readout
LCDBVM1	R	Volts	Detector SW2 maximum readout
LCDBVM2	R	Volts	Detector SW3 maximum readout
LCDBVM3	R	Volts	Detector SW4 maximum readout
LCDBVM4	R	Volts	Detector SW5 maximum readout
LCDBVM5	R	Volts	Detector LW1 maximum readout
LCDBVM6	R	Volts	Detector LW2 maximum readout
LCDBVM7	R	Volts	Detector LW3 maximum readout
LCDBVM8	R	Volts	Detector LW4 maximum readout
LCDBVM9	R	Volts	Detector LW5 maximum readout

**Use:** In Derive-SPD for identifying saturated points.

## 7.3.1.7 LCD1: First level deglitching parameters

**Type of File:** FITS Header

**Contents:** See Table 7.38 for the contents of this file.

Table 7.38: *LCD1 calibration file keywords.*

name	type	unit	description
LCD1GFRA	R	none	Glitches whose height is below this fraction of the ramp height will be rejected
LCD1SPRA	R	none	'Spikes' whose height is below this fraction of the ramp height will be rejected
LCD1SDRJ	R	none	Number of standard deviations from mean for point to be marked as an outlier.
LCD1PGRJ	I	none	Number of ramps to discard after a positive glitch.
LCD1NGRJ	I	none	Number of ramps to discard after a negative glitch.
LCD1GRRJ	L	none	Indicates if the whole of the glitched ramp should be discarded.
LCD1PGRI	I	none	For illuminator flashes, the number of ramps to discard after a positive glitch.
LCD1NGRI	I	none	For illuminator flashes, the number of ramps to discard after a negative glitch.
LCD1GRRJ	L	none	For illuminator flashes, indicates if the whole of the glitched ramp should be discarded.

**Use:** Contains various parameters which control the detection and removal of glitched points by first level deglitching.

### 7.3.1.8 LCGH: Glitch History file parameters

**Type of File:** FITS Header

**Contents:** The first keyword (LCGHGHR) gives the maximum number of records that can be written to the LWS Glitch History file. This was introduced because of early fears that this file might grow uncontrollably. In fact this has not proved to be the case and this value is set to a high enough value to cope with all observations.

Table 7.39: *LCGH calibration file keywords.*

name	type	unit	description
LCGHGHR	I	–	Maximum number of records

**Use:** For writing data to the LWS Glitch History file.

### 7.3.1.9 LCD2: Second level deglitching parameters

**Type of File:** FITS Header

**Contents:** This file relates to a deglitching stage used during early versions of the pipeline. This file is still currently read by SPL, but its contents are not used.

**Use:** Not used

### 7.3.1.10 LCFP: Parameters for electronic filters

**Type of File:** FITS Header

**Contents:** Ten keywords containing the time constants for the high pass filter for each detector. The times are specified in seconds.

These values have not been used since the introduction of the  $\Delta V/\Delta t$  method of slope fitting in OLP Version 7.

**Use:** Not used

### 7.3.1.11 LCD3: Third level deglitching parameters

**Type of File:** FITS Header

**Contents:** This file relates to a deglitching stage used during early versions of the pipeline. This file is still currently read by SPL, but its contents are not used.

**Use:** Not used

## 7.3.2 Auto-Analysis calibration files

### 7.3.2.1 General information

All Auto-Analysis calibration files contain a set of standard keywords in their header to identify the version and validity of the file. These keywords can be used to check that the calibration files are valid for the data that is being processed. The keywords are checked during the automatic processing of the data in the OLP pipeline.

The keywords can be found in Table 7.40

Table 7.40: *Auto-Analysis calibration files general keywords.*

name	type	unit	description
LDATE	C	–	date of creation or update
LVER	I	–	version number
LMODEL	C	–	identifies instrument model (always FM)
LVLSTART	I	–	UTK of start of validity
LVLEND	I	–	UTK of end of validity
LVLBIAn	I	–	indicates the bias level for which the file is valid for each detector (0–9). If LVLBIA0 is set to –1 file is independent of bias, other bias levels are then not present

The version number and date of all the calibration files used by Auto-Analysis are written into the header of the LSAN file as a series of keywords named LVERS<sub>n</sub> (n=1,2,...).

### 7.3.2.2 LCIR: Illuminator reference file

**Type of File:** FITS binary table

**Contents:** The LCIR file is a calibration file which contains a reference photocurrent value for each ramp in an illuminator flash for each detector. The LCIR is a FITS binary table extension file of shape 1, i.e. there is only one LCIR file which covers the whole mission.

The file contains an illuminator ‘type’ number as part of each record, allowing it to contain reference data for more than one ‘type’ of illuminator flash. The comments in the LCIR file header should describe each flash type stored in the file.

For each flash type the LCIR file contains only the data starting from when the first illuminator was switched on and ending when the last illuminator was switched off. **The background measurements at the beginning and end of the flash are not contained in the LCIR file.** The reference photocurrent values in the LCIR file have had the background photocurrent already subtracted.

Each LCIR record contains a status flag which allows selected points to be ignored when ratioing against the flash data. This can be used to mask out data from illuminator levels which do not provide useful data. Any photocurrent value in the LCIR file which is set to zero will also be ignored in the same way. Values may be zero because of glitches in the reference data.

The header of the LCIR file contains keywords which specify NSD, the number of standard deviations for median clipping the data. These keywords are: LCIRNSDB (Number of Standard deviations to use for median clipping of background) and LCIRNSDF (Number of Standard deviations to use for median clipping of flash data).

The record structures is given in Table 7.41

Table 7.41: *LCIR calibration file record structure.*

name	offset	Number	type	unit	description
LCIRTYPE	0	1	I*4	–	Number identifying type of illuminator flash
LCIRPHC	4	10	R*4	A	Reference photocurrent, with background subtracted
LCIRPHCU	44	10	R*4	A	Uncertainty in reference photocurrent
LCIRSTAT	84	1	I*4	–	Status word. 1=use this value; 0=ignore this value
LCIRICS	88	1	I*4	–	Illuminator commanded status

**Use:** For the flux calibration of the data.

### 7.3.2.3 LCGW: Grating position to wavelength conversion parameters

**Type of File:** FITS binary table.

**Contents:** This file contains the parameters required for converting the grating LVDT readout values into wavelength. Since the wavelength calibration changes over time this file contains different sets of coefficients for different time periods. Each record of the LCGW file contains one set of coefficients, which are valid for a particular time period. Rather than use a time key directly, the LCGW file uses the revolution number to identify which record is valid for which time period. Each record contains the start and end revolution numbers for which it is valid.

The record structure of the LCGW file is shown in Table 7.42.

The header of the LCGW file also contains keywords which contain fixed values for use in the conversion. These keywords are shown in Table 7.43.

Table 7.42: *LCGW calibration file record structure.*

name	Offset	number	type	unit	description
LCGWSREV	0	1	I*4	-	Revolution number of start of validity for this record
LCGWEREV	4	1	I*4	-	Revolution number of end of validity for this record
LCGWCOEF	8	5	R*4	-	Conversion coefficients
LCGWADET	28	10	R*4	deg	Angle for each detector

Table 7.43: *LCGW keywords.*

name	type	unit	description
LCGWLINE	R	-	Number of lines per $\mu m$ on grating
LCGWodet	I	-	Order number for each detector (det='SW1'...'LW5')

**Use:** Wavelength calibration of the grating.

### 7.3.2.4 LCGR: Grating relative response file

**Type of File:** FITS primary array

**Contents:** This FITS file contains the grating relative wavelength responsivities for each detector at selected wavelengths. The file applies for a particular bias level. The data are normalised to the wavelength at which the absolute responsivity is measured. The relative responsivity includes a correction for the aperture size of the instrument, assuming the source is a point source in the centre of the beam. The unit of the relative responsivity therefore is  $\text{cm}^2$ . The file is written as a FITS primary array with three axis (NAXIS=3). The axis are defined as given in Table 7.44.

Table 7.44: *LCGR calibration file structure.*

name	Number of elements	type	unit	description
NAXIS1	4	R*4	$\mu\text{m}$	Wavelength
		R*4	$\mu\text{m}$	Uncertainty in wavelength
		R*4	$\text{cm}^2$	Relative Responsivity
		R*4	$\text{cm}^2$	Uncertainty in responsivity
NAXIS2	10	R*4	–	Detector number
NAXIS3	4096	R*4	–	Grating LVDT value

The header of the file contains keywords which specify the range of grating positions which are used within the file and the ‘nominal’ wavelength range for each detector. The nominal range is where the calibration is of acceptable quality. Everything outside the nominal range has poor calibration and is flagged with a warning flag in the L<sub>SA</sub>N status word. These keywords are shown in Table 7.45.

Table 7.45: *LCGR keywords.*

name	type	unit	description
LSTARPOS	I	-	First valid grating position in file
LENDPOS	I	-	Last valid grating position in file
LSTRNOM <sub>n</sub>	R	$\mu\text{m}$	Start of nominal wavelength range for detector n (n=0...9)
LENDNOM <sub>n</sub>	R	$\mu\text{m}$	End of nominal wavelength range for detector n (n=0...9)

**Use:** Relative responsivity correction for grating mode.

### 7.3.2.5 LCFW: Fabry-Pérot wavelength calibration parameters

**Type of File:** FITS Header

**Contents:** This FITS file contains the parameters required for converting FP position into wavelength. The parameters are the coefficients for the third order polynomial that is used to describe the dependence of the wavelength on the position of the FP etalons. Because of the precision of the FP wavelength calibration, these values should be read into real\*8 variables. Table 7.46 gives the keywords for this file.

Table 7.46: *LCFW calibration file keywords.*

name	type	unit	description
LCFWFLC0	D	–	FPL zeroth order coefficient
LCFWFLC1	D	–	FPL first order coefficient
LCFWFLC2	D	–	FPL second order coefficient
LCFWFLC3	D	–	FPL third order coefficient
LCFWFSC0	D	–	FPS zeroth order coefficient
LCFWFSC1	D	–	FPS first order coefficient
LCFWFSC2	D	–	FPS second order coefficient
LCFWFSC3	D	–	FPS third order coefficient

**Use:** Wavelength calibration of Fabry-Pérot data.

### 7.3.2.6 LCGB: Grating spectral bandwidth correction factors

**Type of file:** FITS binary table

**Contents:** The correction factor for the grating spectral bandwidth for each of the ten LWS detectors. For each detector the factor and its uncertainty is given. The record structure can be found in Table 7.47.

Table 7.47: *LCGB calibration file record structure.*

name	offset	number	type	unit	description
LCGBDET	0	1	C*3	–	Detector
LCGBSPAR	3	1	I*1	–	Filler
LCGBSB	4	1	R*4	1/ $\mu$ m	Bandwidth
LCGBSBU	8	1	R*4	1/ $\mu$ m	Uncertainty in bandwidth

**Use:** In Auto-Analysis to correct fluxes for the spectral bandwidth for grating spectra.

**7.3.2.7 LCDK: Fixed dark current calibration file**

**Type of file:** binary extension FITS file

**Contents:** The file contains the dark current values for each detector.

**7.3.2.8 LCTP: Fabry-Pérot throughput correction calibration file**

**Type of file:** FITS header

**Contents:** The file contains the coefficients of the polynomial fits of  $\eta \times T(\lambda)$  (product of the transmission efficiency  $T(\lambda)$  and the effective spectral element width  $\eta(\lambda)$ ) for FPS and the two sections of FPL (SW4-LW1 and LW2-LW5)

## Chapter 8

# Getting Started with LWS Data

LWS data are supplied via `ftp`<sup>1</sup> from the ISO Data Archive (IDA) in the form of FITS files.

Although the main product, the LSWAN files, are in a suitable format for any astronomical package, a dedicated software package for analysing both SWS and LWS data exists: the ISO Spectrometer Analysis Package (ISAP) (see section 8.2.2).

For some data sets, observers may want to re-run the Auto-Analysis processing stage interactively before proceeding with the ISAP reduction. The LWS Interactive Analysis (LIA) package is produced for this purpose (see Section 8.2.3).

### 8.1 Retrieving and Reading the Data

LWS data, as any other ISO data, can be retrieved from the ISO Data Archive (IDA) at the following address:

`http://www.iso.vilspa.esa.es/` → Access the Archive

We refer to the ISO Handbook Volume I, [21] for more information on the ISO Data Archive and how to use it.

The ISO data files obtained can either be general, applying to all instruments e.g. satellite pointing, housekeeping etc., or instrument specific. A full description of the general file types are also given in the ISO Handbook Volume I, [21], along with a description of the data layout for each of these files. The LWS specific files are fully described in Chapter 7 in the present handbook volume.

A recommendation for new users is to request the data files using the default 'basic science' retrieval option. This option allows an observer to retrieve a basic set of files for the requested observation although it is expected that most users will only require the final LSWAN product file (see Section 7.2.7). However, for most options of the LWS Interactive Software (LIA), the user will need to retrieve the data at SPD level.

All ISO product files are in FITS format and almost all, including all LWS specific product files, have the data stored in a FITS binary extension.

They can be read for example with the 'mrdfits' command in IDL.

The following is an example to read wavelength and flux in the file `lsan63901302.fits`:

```
new=mrdfits('lsan63901302.fits',1,h1)
wavelength=new.lsanwav
flux=new.lsanflx
```

---

<sup>1</sup>Archive products can also be downloaded directly from the 'Latest Results' screen by clicking on the 'Retrieve' button after IDA Version 5.2, released in July 2002

## 8.2 Analysing the Data

To help you in analysing and processing further the LWS data we recommend that you make use of the two packages especially developed for this purpose: ISAP and LIA. The user is also referred to the LWS data reduction recipes.

### 8.2.1 LWS data reduction recipes

The recipes are available from:

<http://www.iso.vilspa.esa.es/> → ISO Explanatory Library → LWS

The recipes are structured as worked examples for the following AOT types:

- LWS01 - Grating wavelength range
  - Faint source
  - Medium brightness source
  - Bright source
- LWS02 - Grating line spectrum
- LWS04 - Fabry-Pérot Line scans

### 8.2.2 The ISO Spectral Analysis Package (ISAP)

This is a software package that was specifically written for LWS and SWS data. The package was written jointly by the LWS Instrument Team, the SWS Instrument Team and IPAC. It can read in the product files and write as output FITS files, ASCII files or IDL save files. This package requires an IDL licence and the IDL path should also include the IDL astronomy library which is available at:

<http://idlastro.gsfc.nasa.gov/>

The routines in ISAP have been tailored to reduce LWS data. ISAP allows the user to **flag** or **delete** data points that are clearly wrong (due to undetected glitches for instance) and to perform most of the basic operations for spectral analysis like **averaging** scans with different averaging routines, **scaling** the detectors to make smooth spectra, **rebinning** spectra to a standard wavelength scale, **adding** a constant, **averaging** spectra, **subtracting** a background spectrum from a spectrum, **measuring** line intensities and **fitting** line profiles, as well as some LWS specific operations like **defringing** the data.

A full set of documentation, including cookbooks for reducing each observation type is available with ISAP.

ISAP can be downloaded from the ISO website in IPAC:

<http://www.ipac.caltech.edu/iso/> → ISAP

or

<http://www.iso.vilspa.esa.es/> → ISO Data Analysis Software → ISAP

### 8.2.3 The LWS Interactive Analysis (LIA)

This package is written as a set of IDL routines, to be used together with ISAP. The routines are written to allow users to **inspect**, **reprocess** and **recalibrate** their LWS data with the possibility of interactively customizing the various data reduction stages to their particular set of data. It also allows some extra functionalities, like the interactive FP responsivity correction. LIA is a joint development of the ISO-LWS Instrument Team at Rutherford Appleton Laboratories (RAL, UK - the PI Institute) and the Infrared Processing and Analysis Center (IPAC/Caltech, USA).

As of June 2003 the current version of LIA is version 10.1. LIA can be downloaded from the UKIDC web site:

<http://jackal.bnsc.rl.ac.uk/isouk/>

or

<http://www.iso.vilspa.esa.es/> → ISO Data Analysis Software → LIA

A full set of documentation is available at this web site. If you need further help with LIA, you can contact the UK ISO National Data Centre ([isouk@rl.ac.uk](mailto:isouk@rl.ac.uk)).

The following lists the routines included in LIA together with a short description.

- **Inspection Routines:** designed to allow the LWS data user to inspect his/her pipeline products as produced through the Standard Processing stage (SPD) and the Auto-Analysis stage (AAR).
  - **INSPECT\_SPD:** Displays SPD results before and after the application of the standard deglitching algorithm. A two panel plot with a Graphical User Interface (GUI) appears on the screen. The user can display the data in LWS instrument time key (ITK) units, or in seconds from the start of the observation. The display can be zoomed to look in more detail at the effects of the glitches. Various glitch statistics are reported.
  - **INSPECT\_IPD:** Displays illuminator flash sequence data for closed flashes. The dark currents as measured at the start of each closed flash are also displayed. The user can get an impression here whether the calculated dark currents are in line with the latest best estimates from the PV phase/Handover flashes. Dark currents in flux units are also listed.
  - **INSPECT\_DRIFT:** Displays the SPD results before and after the detector responsivity drift correction is applied. Only suitable for displaying grating LWS01 data.
  - **INSPECT\_ABS:** Displays the absolute responsivity correction factors (the ratio of closed illuminator flash data referenced to the illuminator flash data at the time of flux calibration observation).
  - **INSPECT\_RSRF:** Displays the SPD data (LSPD file), the Relative Spectral Response Function (RSRFs in the LCGR file) and the AAR data (LSAN - the LWS Auto-Analysis results file) in wavelength units. A two panel plot with a GUI appears on the screen. The upper panel shows the LSPD and the RSRF (normalised to the LSPD data at the grating rest position). Only suitable for grating AOTs, i.e. LWS01 and LWS02. This routine is expected to be useful for verifying the existence, or otherwise, of some of the more interesting features present in the LSAN file.
  - **INSPECT\_RASTER:** Displays the pointing directions for raster observations, as well as for single pointings.
- **Interactive Routines:** designed to allow the user to customize the data reduction process and to tune the algorithms used in the data reduction.
  - **IA\_DARK:** Dark Current (DC) subtraction. The estimate and subtraction of the DC is a critical point particularly for faint sources and for FP observations in general; in these cases signal received is at the detector noise level and hence an incorrect DC subtraction may lead to negative photocurrents; as these are later divided by the instrumental transmission profiles (RSRF) the resulting calibrated spectrum will be potentially difficult to interpret.
  - **IA\_DRIFT:** Responsivity Drift (RD) correction. It is well known that the LWS detectors present a temporal drift in responsivity. Its removal is based on the evaluation of the time series of averages of spectral scans; the obvious requirement is that the scan range and the source's intrinsic signal does not vary. The sole case in which this requirement is met is with single pointing L01 AOTs (fortunately the majority of LWS observations).

- **IA\_ABSCORR**: Absolute Responsivity Correction (ARC) factors. ARCs are the values used to scale the detector responsivities to the values measured when the LWS primary calibrator (Uranus) was observed, and on which the instrumental transmission profiles of the instrument have been derived.
  - **FP\_PROC** (for FP data only): An interactive tool which produces calibrated LSAN files for FP observations. It can handle both L03 and L04 AOTs and allows important functions such as i) realignment of scans in an L03 AOT; ii) correction for incorrect grating positioning in an L04 AOT; or iii) reprocessing using either a default or a user supplied set of dark currents (for this reason **FP\_PROC** also belongs to the third routine class - see below).
  - **GUI\_FPMF** An interactive tool to perform FP multi-Gaussian fitting of a single blended line.
  - **DEFRINGE(L01, L03 and L04)**: This tool is written for interactive defringing of LWS data. It requires an LSAN file containing data which has been averaged across each separate detector (for L01 AOT) or mini-scan (for L03 AOT), or line (for L04 AOT). This is because the fringes change with wavelength and therefore the routine removes the fringing by detector (L01), mini-scan (L03) or line (L04). If the data is not averaged in this manner, the GUI will not work.
- **Recalibration Routines**: designed to allow the user to recalibrate the data reprocessed using the interactive routines, or to make a complete non-interactive reprocessing using defaults other than those used by the automatic OLP.
    - **SHORT\_AAL** (for Grating data only): utility to recalibrate an L01 or L02 observation. It essentially performs wavelength and flux calibration using interactively reprocessed data (see above) as input. It can also perform a general reprocessing (without using the interactive routines) using default settings which are different from those used by the OLP. There are a number of keywords which need to be used when calling **SHORT\_AAL**, depending on which of the interactive routines have previously been used.
    - **FP\_PROC** (for FP data only, same routine as in second class): utility to recalibrate an L03 or L04 observation. It essentially performs wavelength and flux calibration using interactively reprocessed data (see above) as input. It can also perform a general reprocessing (without using the interactive routines) using default settings which are different from those used by the OLP. It also allows interactive manipulation of the data (for this reason **FP\_PROC** also belongs to the second routine class, see above). A number of keywords should be used when calling **FP\_PROC**, depending on which of the interactive routines have previously been used. In LIA Version 10 **FP\_PROC** was extensively modified to include non-prime data, extend the grating profiles, improve the throughput coefficients and remove side-order contamination.
    - **CORRECT\_SPECTRUM** - corrects an averaged, de-fringed off-axis *point source* spectrum to the flux and spectral shape that would be seen had the source been observed on-axis.
    - **EXTENDED\_FLUX** - re-calibrates an averaged, de-fringed spectrum of an extended source to flux per steradian or MJy/sr. The routine corrects the flux and spectral shape and corrects for the effective beam of the instrument. However, the re-calibration assumes a smooth extended source, which rarely applies in practice.
    - **SS\_CORR** - corrects for strong-source effects, which occur in detectors LW1 to LW4 (see Section 5.7). The routine produces a corrected LSPD file, that the user has to process through **SHORT\_AAL** to create the corrected LSAN file for further analysis. Two different sets of correction coefficients are available, based on models of Mars and Saturn respectively. The resulting spectra need to be checked to see which coefficients give the better result. Further work is currently being undertaken to determine a uniform approach for applying this correction, to eliminate the need to select coefficients or perform subsequent processing. In the meantime, users who require assistance with applying this correction to their data should contact experts at the UK ISO Data Centre (see Section 6.10).

In 2003 and 2004, it is planned to introduce a few new LIA routines.

- **GR\_TRANSIENT** - applies a transient correction for grating data only. The GUI-based routine, to be included in a future version of LIA, will perform the transient correction on L01 grating data, starting at SPD level. The responsivity drift correction and deglitching are carried out prior to the transient correction being applied. The routine applies the transient correction using the Fouks-Schubert method as described in Section 6.9. The routine looks for the three tunable parameters  $\alpha$ ,  $\beta$  and E that minimize the quadratic differences between forward and backward scans. The output is one forward and one backward scan, that the user can compare to one another to see how well the correction performed. The starting values for  $\alpha$  and  $\beta$  are given in Table 6.2. For E the starting value is 1.0.
- **NIR\_LEAK** - work has been completed on correcting the LWS data known to be affected by the near-infrared light leak, with corrected data imported to the ISO Data Archive. A LIA routine may however be released for performing this correction in a future version.

### 8.3 Analysing Parallel/Serendipity Mode Data

Several interactive analysis packages, written in IDL, are available at the UK LWS web site:

`http://jackal.bnsc.rl.ac.uk/isouk/ → Software`

`→ LWS parallel mode products and analysis tools`

to analyse the products of parallel and serendipity observations. They can either be run interactively from the command line or via a GUI. These allow combining individual rasters and pointings into uniformly gridded maps. There are also routines which allow potential point sources to be extracted from serendipity mode and maps to be produced from serendipity mode observations. Further analysis can then be done on the maps with other packages.

### 8.4 Where to Find the Calibration Parameters

Table 8.1 gives in alphabetical order the calibration files where the observer can find the calibration parameters that are used in the data processing. The **instrumental** calibration parameters are used in the Derive-SPD process and the **astronomical** calibration parameters are used in the Auto-Analysis process. The table also give the reference to the table that describes the calibration file in this document. The descriptions of these calibration files are given in Section 7.3.1 and Section 7.3.2.

Table 8.1: *List of instrumental and astronomical calibration parameters used respectively in Derive-SPD and in Auto-Analysis.*

Type	Parameter	File	Table or Section
Instrumental	Analogue amplification gains	LCGA	Section 7.3.1.4
	Detector amplifier (JF4) capacitances	LCJF	Table 7.36
	Detector amplifier (JF4) gains	LCJF	Table 7.36
	Detector readout to voltage conversion	LCVC	Section 7.3.1.3
	First level deglitching parameters	LCD1	Table 7.38
	Maximum voltages on the detectors	LCDB	Table 7.37
	Readout limits of the electronics	LCAL	Table 7.35
	Time periods to be ignored after a reset	LCDT	Table 7.34
Astronomical	FP wavelength calibration coefficients	LCFW	Table 7.46
	Grating relative response curves	LCGR	Table 7.44
	Grating spectral bandwidth correction	LCGB	Table 7.47
	Grating wavelength calibration table	LCGW	Table 7.42
	Standard illuminator photo currents	LCIR	Table 7.41
	Fixed dark current values	LCDK	Section 7.3.2.7
	Fabry-Pérot throughput correction	LCTP	Section 7.3.2.8

## 8.5 Useful Web Addresses

- The ISO Data Archive:  
<http://www.iso.vilspa.esa.es/> → Access the Archive
- The LWS homepage at the ESA ISO Data Centre (IDC) in Vilspa:  
<http://www.iso.vilspa.esa.es/> → ISO Explanatory Library → LWS
- The general ISO LWS homepage at the UK ISO Data Centre at RAL:  
<http://jackal.bnsc.rl.ac.uk/isouk/>
- The LWS homepage at the US ISO Science Support Center at IPAC:  
<http://www.ipac.caltech.edu/iso/>

# Appendix A

## List of Acronyms

**AAI** Acronym to indicate the LWS Auto-Analysis programme.

**AAR** Auto-Analysis Result. This is a generic name for the results of the Auto-Analysis programme. For LWS it usually refers to the LSN product file, but it can also include the other product files generated by Auto-Analysis (LSNR, LGIF, LSCA, LIAC).

**ADC** Analogue to Digital Converter

**AMAG** Anamorphic Magnification (the ratio of the diameter in the dispersion direction to that in the non-dispersion direction)

**APU** Analogue Processing Unit

**AOT** Astronomical Observation Template: the standard observing modes for the ISO instruments.

**COIF** Calibration Observation Implementation File. Such files were used to define an observation which had to be performed in a non-standard mode, i.e. not using the AOTs

**CSH** Compact Status History

**DPU** Digital Processing Unit

**ERD** Edited Raw Data. This is a generic name for the raw data files used as an input to the Derive-SPD programme. In the LWS case it usually refers to the LGER, LLER, LSER or LIER files.

**EOHA** Executed Observation History per AOT: this file gives for every performed AOT the timing and some information about that AOT (see full description in the ISO Handbook Volume I.

**EOHC** Continuous Executed Observation History. Essentially a copy of EOHA

**EOHI** Edited Observation History per ICS: This gives for every ICS that was sent to the satellite the timing and some information for that ICS (see full description in the ISO Handbook Volume I.

**FET** Field-Effect Transistor

**FITS** Flexible Image Transport System

**FOV** Field Of View

**FP** Fabry-Pérot.

**FPL** Long wavelength Fabry-Pérot.

- FPS** Short wavelength Fabry-Pérot.
- FPU** Focal Plane Unit
- FWHM** Full Width Half Maximum.
- GUI** Graphical User Interface.
- HPDP** Highly Processed Data Products.
- ICS** Instrument Command Sequence: command that is translated by the on-board software of the instrument to a sequence of actions. This is the normal way to command the ISO instruments.
- IDA** ISO Data Archive.
- IDUM** Instrument Data Users Manual.
- ISAP** ISO Spectral Analysis Package: software package developed specifically for analysis of data obtained with the two ISO spectrographs (LWS and SWS).
- ITK** Instrument Time Key ( $= 2^{-14}$  sec)
- JCMT** James Clerk Maxwell Telescope
- LIA** LWS Interactive Analysis: package of IDL routines written to allow the user to interactively inspect, reprocess, and recalibrate their LWS data.
- L01-4** names attributed to the four observing modes (also called AOTs) , L01 and L02 are grating modes and L02 and L03, Fabry-Pérot modes. They are sometimes noted LWS01 - LWS04
- LHe** Liquid Helium
- LW1-5** labels for the 5 long wavelength LWS detectors
- NEP** Noise Equivalent Power
- NEFD** Noise Equivalent Flux Density
- NESD** Noise Equivalent Spectral Density
- NIR** Near Infrared
- M2** the second mirror in the LWS optical path (see Figure 2.2).
- OCT** Observatory Command Template: template used to transfer the commands (instrument or other) to the satellite. This also includes e.g. the pointing requests.
- OLP** Off-Line Processing, also referred to as the 'pipeline'. It refers to the software that automatically processes the LWS data from the raw telemetry data up to calibrated spectra.
- OTF** On-Target Flag
- PSF** Point Spread Function
- PV** Performance Verification: the initial phase of two months of the ISO operations, when the instrument performance in orbit was tested and characterised.
- rms** Root Mean Square
- RSRF** Relative Spectral Response Function

**SCP** Spacecraft Commissioning Phase: The first three weeks of ISO in orbit operations when all the systems of the satellite and instruments were functionally tested.

**SOC** Science Operations Centre

**SPD** Standard Processed Data: The result of the first stage of the ISO data processing. This is one of the products that is sent to the observers.

**SPL** Acronym for LWS Derive-SPD programme.

**SW1-5** labels for the 5 short-wavelength LWS detectors

**TDATA** Transparent Data: information about the observation that does not need to be uplinked to the satellite but that is needed to process the data.

**TDF** Telemetry Distribution File: The file format in which the data is received from the satellite at the ground station.

**TDT** Target Dedicated Time. It is the entire time spent to perform all observations of a concatenated group (in many cases, just one observation).  $TDT = \text{observation time} + \text{overhead time}$ .

**UTC** Universal Time (Coordinated)

**UTK** Uniform Time Key: the time key that is used as a timekey for all ISO data products (for details see the ISO Handbook Volume I)



# Bibliography

- [1] Born M. & Wolf E. 1970, *Principles of Optics*, Pergamon Press, 4<sup>th</sup> edition
- [2] Bratt P.R. 1977, *Semiconductors and Semimetals*, Vol. 12, Chapt. ‘Impurity Germanium and Silicon Infrared Detectors’, 39
- [3] Brauher J. & Lord S. 2001, *The ISO LWS-IRAS cross-calibration of extragalactic sources*, in ‘The Calibration Legacy of the ISO mission’. Eds. L. Metcalfe & M.F. Kessler, ESA SP-481 (in press)
- [4] Burgdorf M.J., Harwood A.S., Trams N.R. et al. 1998, *Automatic data processing and quality control: experiences from ISO LWS*, SPIE 3349, 359
- [5] Caux E. 2001, *Transient effects correction for LWS detectors*, in ‘The Calibration Legacy of the ISO mission’. Eds. L. Metcalfe & M.F. Kessler, ESA SP-481 (in press)
- [6] Chan S.J., Lloyd C., Swinyard B.M. & Lim T. 2001, *Comparison between IRAS and ISO LWS*, in ‘The Calibration Legacy of the ISO mission’. Eds. L. Metcalfe & M.F. Kessler, ESA SP-481 (in press)
- [7] Church S.E., Price M.C., Griffin M.J. et al. 1992, *Non-linear effects in doped-Germanium photoconductors for the ISO Long Wavelength Spectrometer*, in ‘Photon Detectors for Space Instrumentation’, ESA SP-356, 261
- [8] Church S.E. 1993, *Fitting a second-order polynomial to JF<sub>4</sub> ramps to compensate for saturation effects*, LWS/QMC/N/2064.03
- [9] Clegg P.E., Ade P.A.R., Armand C. et al. 1996, *The ISO Long-Wavelength Spectrometer*, A&A 315, L38
- [10] Coulais A. & Fouks B.I. 2001, *Current status of modelling of point sources transient response for LW-ISOCAM*, in ‘The Calibration Legacy of the ISO mission’. Eds. L. Metcalfe & M.F. Kessler, ESA SP-481 (in press)
- [11] Coulais A., Sée J., Giovannelli J.-F. et al. 2001, *Transient correction for ISOPHOT C-100 detector*, in ‘The Calibration Legacy of the ISO mission’. Eds. L. Metcalfe & M.F. Kessler, ESA SP-481 (in press)
- [12] Davis G.R., Furniss I., Towlson W.A. et al. 1995, *Design and performance of cryogenic, scanning Fabry-Pérot interferometers for the Long-Wavelength Spectrometer on the Infrared Space Observatory*, Appl. Opt. 34, 92
- [13] Davis G.R., Griffin, M.J., Naylor, D.A. et al. 1996, *ISO LWS measurement of the far-infrared spectrum of Saturn*, A&A 315, L393
- [14] Duncan W.D. 1983, *Efficiency of optical systems with diffraction-image-sized Fabry optics*, Infrared Phys. 23, 333

- [15] Emery R.J., King K.J., Swinyard B.M. & Church S.E. 1993, *Testing the Long Wavelength Spectrometer for ISO*, in 'Infrared Detectors and Instrumentation'. Ed. A. Fowler, SPIE 1946, 272
- [16] Fouks B.I. 2001, *Physical approach to the problems of space low-background detectors*, in 'The Calibration Legacy of the ISO mission'. Eds. L. Metcalfe & M.F. Kessler, ESA SP-481 (in press)
- [17] Fouks B.I. & Schubert J. 1995, *Precise theoretical description of photoresponse for detectors of ISOPHOT's Si:Ga array*, SPIE 2475, 487
- [18] García-Lario P. 2001, *Cross-Calibration Final Report*, SAI/2001-030/Rp, Version 1.0
- [19] Griffin M.J. & Orton G. 1993, *The near-millimeter brightness temperature spectra of Uranus and Neptune*, Icarus 105, 537
- [20] 'Infrared Astronomical Satellite (IRAS) Catalogs and Atlases Explanatory Supplement' Vol. 1, 1998. Eds. C.A. Beichman, G. Neugebauer, H.J. Habing, P.E. Clegg & T.J. Chester. NASA RP-1190
- [21] Kessler, M.F., Müller T.G., Leech K. et al. 2002, *The ISO Handbook: Volume I, ISO - Mission & Satellite Overview*, ESA SP-1262, SAI-2000-035/Dc, Version 2.0
- [22] Kester D. 2001, *Memory effects and their correction in SWS Si:Ga detectors*, in 'The Calibration Legacy of the ISO mission'. Eds. L. Metcalfe & M.F. Kessler, ESA SP-481 (in press)
- [23] Knapp G.R., Phillips T.G., Redman, R.O. & Huggins, P.J. 1981, *High-velocity gas in the Orion BN/KL region - Observations of the carbon monoxide /2-1/ and sulfur dioxide /13/1,13/-12/0,12/ lines*, ApJ 250, 175
- [24] Leeks S.J. 2000, *The Long Wavelength Spectrometer: Reduction and interpretation of data on W28 A2, a high-mass star-forming region*, Ph.D. Thesis, Queen Mary & Westfield College, London, UK
- [25] Leeks S.J., Swinyard B.M., Lim T.L. & Clegg P.E. 2001, *The in-orbit performance of the LWS detectors*, in 'The Calibration Legacy of the ISO mission'. Eds. L. Metcalfe & M.F. Kessler, ESA SP-481 (in press)
- [26] Lim T.L., Burgdorf M.J., Swinyard B.M., et al. 1998, *Long term performance of doped Ge:Ga photoconductors in the space environment*, in 'Infrared Astronomical Instrumentation', SPIE 3354, 347
- [27] Lloyd C. 2000, *An investigation of the ISO LWS beam profile and fringing*, in 'ISO Beyond Point Sources: Studies of Extended Infrared Emission'. Eds. R. Laureijs, K. Leech & M.F.Kessler, ESA SP-455, 21
- [28] Lloyd C. 2001, *Fringing and spectrum fracturing in ISO LWS observations*, in 'The Calibration Legacy of the ISO mission'. Eds. L. Metcalfe & M.F. Kessler, ESA SP-481 (in press).
- [29] Müller T.G. 2001, *Non-linear detector response of LWS LW-detectors*, SAI/2001-042/Rp
- [30] Okumura K. 2000, *The ISO point spread function and CAM beam profiles*, in 'ISO Beyond Point Sources: Studies of Extended Infrared Emission'. Eds. R. Laureijs, K. Leech & M.F.Kessler, ESA SP-455, 47
- [31] Petti L., 1989, *ISO LWS Critical Design Review*, Optical Design Specialist Panel
- [32] Phillips J.P., Mampaso A., Williams P.G. & Ukita N. 1991, *The CO structure of NGC 7027 - A bipolar nebula in the making*, A&A 247, 148
- [33] Polehampton E.T. 2002, *The ISO LWS high resolution spectral survey of Sagittarius B2*, Ph.D. Thesis, Oxford, UK

- [34] Polehampton E.T., Swinyard B.M., Sidher S.D., Baluteau J.-P. 2001, *Recovery and calibration of non-prime Fabry-Pérot data in the LWS*, in 'The Calibration Legacy of the ISO mission'. Eds. L. Metcalfe & M.F. Kessler, ESA SP-481 (in press)
- [35] Price M.C. 1993, *Non-linear behaviour of doped germanium photoconductors: Inherent and ionising radiation Induced Effects*, Ph.D. Thesis, Queen Mary & Westfield College, London, UK
- [36] Price M., Griffin M.J., Church S., Murray A. & Ade P.A.R. 1992, *Ionising radiation-induced effects in doped germanium FIR photoconductors*, in 'Photon Detectors for Space Instrumentation', ESA SP-356, 309
- [37] Rudy D.J., Muhleman D.O., Berge G.L. et al. 1987, *Mars - VLA observations of the northern hemisphere and the north polar region at wavelengths of 2 and 6 cm*, Icarus 71, 159
- [38] Shaver P.A., McGee R.X., Newton L.M., Danks A.C. & Pottasch S R. 1983, *The galactic abundance gradient*, MNRAS 204, 53
- [39] Sidher S.D., Griffin M.J., Davis G.R. et al. 2000, *ISO LWS observations of Mars-detection of rotational modulation in the far infrared*, Icarus 147, 35
- [40] Swinyard B.M., Burgdorf M.J., Clegg P.E., et al. 1998, *In-orbit performance of the ISO Long Wavelength Spectrometer*, SPIE 3354, 888
- [41] Swinyard B.M., Clegg P.E., Leeks S., Griffin M.J., Burgdorf, M.J. & Lim T. 2000, *Space operation and performance of doped germanium photoconducting detectors in the far infrared: experience from the ISO LWS*, ExA 10, 157
- [42] Teitsworth S.W. & Westervelt R.M. 1986, *Non-linear current-voltage characteristics and spontaneous current oscillations in p-Ge*, Physica D 23, 181
- [43] Teitsworth S.W., Westervelt R.M. & Haller E.E. 1983, *Non-linear oscillations and chaos in electrical breakdown in Ge*, Phys. Rev. Lett. 51, 825
- [44] Ungar S., Mangin J., Lutz M., Jeandel G. & Wyncke B., 1990, *Infrared black paints for room and cryogenic temperatures*, in 'Infrared Technology XV'. Ed. I.J. Spiro, SPIE 1157, 369
- [45] Wang J.-Q., Richards P.L., Beeman J.W. & Haller E.E. 1987, *Stressed photoconductive detector for far-infrared space applications*, Appl. Opt. 26, 4767
- [46] Wright E.L. 1976, *Recalibration of the far-infrared brightness temperatures of the planets*, ApJ 210, 250
- [47] Zink L.R., Evenson K.M., Matsushima F., Nelis T. & Robinson R.L. 1991, *Atomic oxygen fine-structure splittings with tunable far-infrared spectroscopy*, ApJ Lett. 371, L85



# Index

- AAL, 33, 42, 57
- AAR , see Auto-Analysis
- absolute flux calibration, 57, 59
- absolute responsivity correction, 42, 43, 59, 175
- analogue processing unit, 5
- AOTs, 26
- aperture sizes, 12, 77, 80
- Auto-Analysis, 31, 33, 42, 128, 151, 159, 167, 175, 177
  
- beam profile, 77
- bias boosts, 23, 125
  
- calibration files, 159, 177
  - Auto-Analysis, 167
    - LCDK, 33, 49, 159, 172, 178
    - LCFW, 33, 51, 171, 178
    - LCGB, 33, 50, 171, 178
    - LCGR, 33, 50, 52, 60, 110, 170, 175, 178
    - LCGW, 33, 49, 169, 178
    - LCIR, 33, 43, 44, 59, 168, 178
    - LCTP, 33, 62, 159, 172, 178
  - SPD, 160
    - LCAL, 32, 36, 161, 178
    - LCD1, 32, 38, 40, 42, 165, 178
    - LCD2, 159, 166
    - LCD3, 159, 166
    - LCDB, 32, 37, 164, 178
    - LCDT, 32, 36, 160, 178
    - LCFP, 159, 166
    - LCGA, 32, 37, 162, 178
    - LCGH, 32, 166
    - LCJF, 32, 37, 41, 163, 178
    - LCVC, 32, 37, 162, 178
- calibration sources, 65, 85
- CAM, 1
- CSH, 31, 35
  
- dark current, 42, 44, 48, 54, 62, 108, 172, 175
- dark signal, 49, 63
- de-biasing, 22, 71, 75
- Derive-ERD, 31
- Derive-SPD, 31, 32, 35, 57, 177
  
- detectors, 17
  - angles, 85
  - background, 44
  - bias levels, 18
  - integration ramps, 22, 25, 36, 37, 41, 75
  - LW1, 66, 72, 110, 119, 123
  - LW2, 72, 110, 113, 117, 119
  - LW3, 72, 112, 113, 117, 119
  - LW4, 72, 112, 113, 119
  - LW5, 29, 73, 75, 85, 112, 113
  - non-linearities, 71, 119
  - redundancy, 8
  - spikes, 37, 39
  - SW1, 29, 108, 110, 113, 117
  - SW2, 29, 89, 110, 120, 123
  - SW3, 110, 120
  - SW4, 85
- digital processing unit, 5
  
- EOHA, 35, 129, 130
- EOHI, 35, 129, 130
- ERD, 31, 32, 35, 128, 130
- extended sources
  - correction, 81, 82, 176
  - fracturing, 107
  - fringes, 105
  
- Fabry-Pérot
  - description, 14
  - flux calibration, 61
  - flux error estimation, 52
  - grating profile removal, 120
  - line profiles, 99
  - non-prime data, 122
  - photometric accuracy, 57, 71
  - responsivity drift correction, 125
  - side order contamination, 123
  - spectral resolution, 99
  - spurious features, 120
  - throughput correction, 51, 61, 172
  - wavelength accuracy, 57, 96
  - wavelength calibration, 50, 92, 120, 171
- field of view, 5, 77, 80, 82

- filters
  - transmission, 8
- FITS keywords, 129
- focal plane unit, 5
- FPL, 16, 28, 122, 123, 138
  - spectral coverage, 16
  - spectral resolution, 99
  - throughput correction, 61
- FPS, 16, 28, 122, 123, 137
  - spectral coverage, 16
  - spectral resolution, 99
  - throughput correction, 61
- fracturing, 107
- fringes, 6, 78, 105, 107, 176
- glitches, 23, 37, 39, 40, 42, 105, 148, 165, 166, 175
- grating
  - description, 8
  - efficiency, 13
  - flux error estimation, 52
  - line profiles, 88–90, 92
  - photometric accuracy, 57, 66
  - responsivity drift correction, 54, 175
  - spectral bandwidth correction, 50
  - spectral coverage, 8
  - spectral resolution, 25, 88, 90
  - spectral responsivity, 50, 170
  - spurious features, 108, 112
  - wavelength accuracy, 57, 87
  - wavelength calibration, 49, 85, 169
- IDA, 1, 173
- illuminator flashes, 23, 24, 29, 30, 42–44, 46, 48, 59, 175
- interactive analysis, 2, 31, 57, 73, 107, 108, 110, 115, 120, 121, 123, 125, 173–176
- IRAS, 67, 82
- ISAP, 2, 105, 107, 108, 119, 120, 173, 174
- L01 , see LWS01
- L02 , see LWS02
- L03 , see LWS03
- L04 , see LWS04
- LCAL , see calibration files
- LCD1 , see calibration files
- LCD2 , see calibration files
- LCD3 , see calibration files
- LCDB , see calibration files
- LCDK , see calibration files
- LCDT , see calibration files
- LCFP , see calibration files
- LCFW , see calibration files
- LCGA , see calibration files
- LCGB , see calibration files
- LCGH , see calibration files
- LCGR , see calibration files
- LCGW , see calibration files
- LCIR , see calibration files
- LCJF , see calibration files
- LCTP , see calibration files
- LCVC , see calibration files
- LGFR , see product files
- LGIF , see product files
- LIA , see interactive analysis
- LIAC , see product files
- LIER , see product files
- line profiles, 88–90, 92, 99
- LIPD , see product files
- LLER , see product files
- LPAA , see product files
- LPAD , see product files
- LPSP , see product files
- LSAA , see product files
- LSAN , see product files
- LSCA , see product files
- LSER , see product files
- LSNR , see product files
- LSPD , see product files
- LSSP , see product files
- LSTA , see product files
- LWGH , see product files
- LWHK , see product files
- LWS, 1
  - LWS01, 26, 43, 47, 107, 128, 129, 174
  - LWS02, 26, 27, 43, 47, 128, 129, 174
  - LWS03, 27, 35, 43, 47, 49, 107, 120, 122, 125, 128, 129
  - LWS04, 27, 43, 47, 49, 107, 120, 122, 128, 129, 174
- near-infrared leak, 68, 110, 177
- NEP, 63
- observing modes, 25
  - narrow-band photometry, 27
  - parallel mode, 27, 29, 54, 99, 101, 128, 149, 157, 158, 177
  - serendipity mode, 27, 29, 54, 63, 99, 100, 128, 149, 157, 177
- off-axis observations
  - fracturing, 107
  - fringes, 105
  - interactive correction, 176
- OLP, 31

- optics, 5
- particle hits, 23
- photometric accuracy, 57, 65–67, 71
- PHT, 1
- product files, 128, 143, 151
  - Auto-Analysis
    - LGIF, 33, 43, 46, 48, 127, 156
    - LIAC, 33, 43, 44, 49, 127, 154
    - LPAA, 127, 157
    - LPAD, 127, 158
    - LSAA, 127, 157
    - LSAN, 33, 43, 52, 127, 129, 151, 159, 173
    - LSCA, 47, 127, 155
    - LSNR, 52, 127, 154, 159
  - ERD
    - LGER, 35, 127, 136
    - LIER, 35, 127, 135
    - LLER, 35, 127, 138
    - LSER, 35, 127, 137
    - LSTA, 31, 35, 127, 130
    - LWHK, 35, 127, 139
  - SPD
    - LIPD, 32, 33, 35, 42, 43, 45, 49, 127, 129, 147, 150
    - LPSP, 127, 149
    - LSPD, 35–37, 41, 42, 127, 129, 143, 150, 175
    - LSSP, 127, 149
    - LWGH, 32, 35, 41, 127, 129, 148
- PSF, 78, 83
- quality check, 35
- ramps, 25
  - discarded readouts, 36
  - quarter-second processing, 75
  - saturation, 37
  - slope extraction, 41
- readout electronics, 20
- readouts
  - conversion to voltages, 36
  - selection, 36
- relative spectral response function, see RSRF
- responsivity, 8, 42, 50, 51, 57, 73, 108, 170
  - drift correction, 42, 47, 54, 125, 175
- rest position wavelengths, 54
- RSRF, 57, 60, 108, 115, 175
- sensitivity, 63
- solid angles, 81
- spatial resolution, 5
- SPD, 31, 32, 128, 143, 160, 175
- spectral bandwidth correction, 50
- spectral coverage, 8, 18
- spectral resolution, 5, 25, 88, 99
- SPL, 32, 35
- spurious features, 108, 112, 120
- straylight, 42, 44, 48, 83
- strong source correction, 71, 77, 119, 176
- SWS, 1, 174
- TDF, 31
- throughput correction, 51
- transient effects, 89, 92, 99, 113, 115, 117, 177
- transparent data, 129
- Uranus model, 57
- velocity correction, 51
- warm-up features, 112
- wavelength accuracy, 57, 87, 96
- wavelength calibration, 49–51, 85, 92, 120, 169, 171